Controlled Synthesis and Characterization of Templated, Magneto-Responsive Nanoparticle Structures

by

Harpreet Singh

B.Tech. Chem. Eng., Indian Institute of Technology, Kharagpur, India (1999)

M.S.C.E.P. Chem. Eng., Massachusetts Institute of Technology, Cambridge, MA (2003)

Submitted to the Department of Chemical Engineering in partial fulfillment of the requirements for the degree of
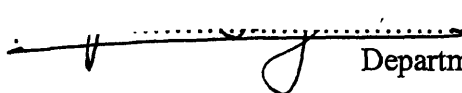
Doctor of Philosophy

at the
Massachusetts Institute of Technology
August 2006
[September 2006]
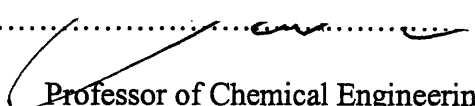
Signature of Author... ....
Department of Chemical Engineering
August 7, 2006

Certified by..
T. Alan Hatton
Ralph Landau Professor of Chemical Engineering Practice
Thesis Supervisor

Certified by..
Paul E. Laibinis
Professor of Chemical Engineering, Vanderbilt University
Thesis Supervisor

Accepted by..
William M. Deen
Professor of Chemical Engineering
Chairman, Committee for Graduate Students
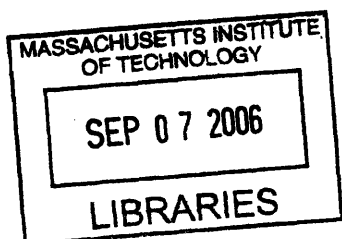
Controlled Synthesis and Characterization of Templated, Magneto-Responsive Nanoparticle Structures

by

Harpreet Singh

Submitted to the Department of Chemical Engineering on August 6, 2006
in partial fulfillment of the requirements for the degree of
Doctor of Philosophy in Chemical Engineering

Abstract

Magnetic fluids are colloidal dispersions of magnetic nanoparticles that are stable with respect to gravitational and moderate magnetic fields because of their small particle size, and to unbounded aggregation due to their surface coatings. The interaction between individual magnetic nanoparticles in a suspension is negligible even under applied magnetic fields. However, when they are incorporated into composite structures they act in concert to provide the desired magnetic response. The dynamic response of such composite structures can be exploited in a wide range of applications including high energy absorption scenarios. The goal of this thesis was to use magnetic nanoparticles as building blocks to create 3D magneto-responsive nanostructures and manipulate their behavior in the presence of an external magnetic field for various applications.

Two approaches were followed to create composite structures. In the first approach, rigid magnetic chains composed of magnetic nanoparticles were synthesized. The layer-by-layer technique was used to coat polystyrene beads with magnetic nanoparticles to create novel core-shell structures. The behavior of these structures under an applied magnetic field was modeled and the results were verified experimentally. These magnetic polystyrene beads were then aligned within a microchannel by an external magnetic field and linked together using sol gel chemistry to yield *rigid* superparamagnetic chains. Linking the magnetically aligned beads with a flexible linker yielded *flexible* superparamagnetic chains. These permanently-linked magnetic chains can be used as micro-mixers in a microfluidic channel under a rotating magnetic field. The reorientation dynamics of these chains under an external magnetic field was modeled. Microcontact printing was employed to tether the flexible chains in a desired pattern on a glass surface. Tethered flexible magnetic chains have potential applications in microfluidics and separations.

Rings and icosahedra shaped electrostatically charged templates were generated from the self-assembly of mixtures of surfactants in an aqueous solution and were investigated for their application in the synthesis of non-spherical magnetic structures. The magnetic response of the magnetic rings was modeled and the results were verified experimentally. "Templateless" aggregation of magnetic nanoparticles using radiation crosslinking was also investigated. Aqueous magnetic nanoparticles stabilized with a radiation crosslinkable polymer resulted in magnetic gels at high dosage amount of the ionizing radiation. Magnetic gels can have potential applications in biological areas.

2

Different size monodisperse magnetic nanoparticles were synthesized via an organic synthesis route, and the effect of size on the Néel relaxation behavior of the fixed magnetic nanoparticles was investigated. Theoretical analysis suggested that incorporation of magnetic nanoparticles with high relaxation times in a matrix can be used to absorb energy. The energy penalty associated with the deflection of the magnetic dipole against the field should result in the stiffening of the matrix. This was demonstrated both experimentally and theoretically. Drop ball impact test was performed on foam embedded with infinite Néel relaxation nanoparticles and the deflection profile of the foam was monitored both in the presence and in the absence of a magnetic field. The deflection of the foam by the ball was modeled to calculate the strain profile developed by the foam, which was then converted into the equivalent amount of energy absorbed by the foam and the magnetic nanoparticles. A method of electrospinning was used to encapsulate magnetic nanoparticles in a polymeric matrix to create field responsive nanofibers for various applications. The magnetization properties of the nanofibers were also characterized and their behavior under an applied magnetic field was modeled.

Thesis Supervisor: T. Alan Hatton
Title: Ralph Landau Professor of Chemical Engineering Practice

Thesis Supervisor: Paul E. Laibinis
Title: Associate Professor of Chemical Engineering, Vanderbilt University

Acknowledgements

"It is good to have an end to journey toward; but it is the journey that matters, in the end." (Ursula Le Guin).

There are many people I am grateful to, who made the tenure of my Ph.D. something I would cherish for the rest of my life. I am indebted to my advisors Alan Hatton and Paul. E. Laibinis for giving me the opportunity to work in their group and the independence that I was allowed to pursue my ideas. I have imbibed a lot from Alan's penchant for details and his in depth analysis style and this has made me a better researcher. I would also like to thank my thesis committee members, Professors Doyle and Gast and Dr. Shuguang, for all of their contributions during my committee meetings. Your opinions really helped me to explore new ideas.

In addition, I would like to thank those researchers who assisted me, including Mike Frongillo of the MIT CMSE, Monique Dubois of CEA, France, Dr. Sun and Zhang at IBM T.J. Watson Research Insitute, and Suraj Deshmukh, Dr. Mao Wang and Professor Rutledge at MIT. It goes without saying that I need to thank Hatton group members past and present for their help. In particular, I need to thank Lino Gonzalez and Marco Lattuada for sharing their mathematical knowledge with me, Sanjoy Sircar for keeping the computers, and Sonja Sharpe and Smeet Deshmukh for keeping the lab, running smoothly. I am also grateful to Beth Tuths for all her help and cheerful chats, which were a good break from research. I must also say thanks to all of my friends in the department with whom I discussed my research.

Without the blessing of my parents I wouldn't have made so far. I would like to thank my father Rajender Singh, my mother Dalgeet Kaur and my brothers Jasvinder Singh, Paramjeet Singh and Armit singh for always being there when I needed them. Biggest thanks to my wife Preeti Chhabra during the last phase of my Ph.D. for being so understanding and caring. Special thanks to my friend Richa Kumar for her unrelenting emotional support during my stay at MIT and proof reading my papers and thesis with her zero knowledge of engineering. Without these people support, I would never have been able to make it to this point.

Table of Contents

Chapter 4: Synthesis of Flexible Magnetic Nanowires of Permanently-Linked Core-Shell Magnetic Beads Tethered to a Glass Surface Patterned by Microcontact Printing 111

Chapter 5: Other Aggregation Techniques 128

Chapter 6: Nanoparticle Size and Energy Absorption Applications ... 162

List of Figures

10

11

12

List of Tables

Chapter 1

Introduction

1.1 Motivation and Approach

Over the past decade, there has been a surge of interest in nanomaterials, which include structures with at least one dimension under 100 nm. The ability to control the composition, structure, properties and function of materials with manipulability on the nanometer scale can lead to the production of nanomaterials that exhibit interesting properties, which may be applicable in broadly ranging domains such as chemistry, electronics, sensors, and biotechnology [1]. A major hurdle in the application of nanomaterials is the limited number of strategies available to assemble them into macrostructures that can be physically handled. The aim of the research presented in this thesis is to develop techniques to bridge this gap between the nanoworld and the physical world — to create macrostructures which can be physically manipulated while still exhibiting the properties of nanomaterials.

This work focuses on using magnetic nanoparticles as building blocks to create 3D magneto-responsive structures. Magnetic nanoparticles have been the focus of increasing interest due to their extensive technological applications in data storage [2], magneto-optical areas [3, 4], biomedicine [5-10] and catalysis [11, 12]. Creating complex hierarchal structures from magnetic nanoparticles can not only improve their performance in existing applications but also extend their applications to newer fields like microfluidics, separations, and energy absorption. We will explore all these new applications in this research.

Nanoparticles of magnetite ($FeO.Fe_2O_3$) and maghemite γFe_2O_3, which are the most studied magnetic nanoparticles due to their ease of synthesis and chemical modification, and their non-toxicity, have been used in work. Magnetite nanoparticles (henceforth also referred to as magnetic nanoparticles) in the range of 6 nm – 20 nm can be visualized as miniature magnets. Due to their small size, the thermal energy at room

temperature causes their dipole orientations to fluctuate (for e.g. at room temperature, the dipole vector of an 8 nm magnetite nanoparticle changes direction after every 10^{-8} s). This leads to zero effective magnetization of these nanoparticles at room temperature as determined by averaging the dipole orientations over times, longer than their typical fluctuations. However, in the presence of a magnetic field, the dipoles overcome these thermal fluctuations and align with the external field. This process is reversible and the dipole orientations are randomized once the field is removed. Hence, these particles behave like magnets only in the presence of a magnetic field. This switching property of magnetic nanoparticles can be used in creating "smart field responsive materials" which will display the desired properties on demand, i.e., only when the stimulus (magnetic field in our case) is switched on.

Figure 1-1 shows the effect of magnetization on interparticle interactions. Magnetization, which is the measure of average magnetic moment developed by a magnetic nanoparticle in the direction of the applied field, scales with the strength of the applied field. At higher field strength the interparticle interaction comes into play. The magnetized nanoparticles should form chains in the direction of the applied field to lower the magneto-potential energy of the system. This is however not observed in an ensemble of magnetite nanoparticles. The dipolar interactions between individual magnetic nanoparticles in a suspension are negligible compared to the thermal energy. The thermal energy disrupts any structure formed under an applied field. However, we can induce aggregation of these nanoparticles in a controlled fashion to form structures (or clusters). Individual nanoparticles held together in a cluster can act in unison to overcome thermal energy and start aggregating in a magnetic field.

Our interest in inducing structure formations in magnetic nanoparticle system is multifold. Magnetic structures of different shapes should behave differently in a magnetic field and should aggregate to yield new structures. This will give us dual control in constructing complex multilevel magnetic structures. At the first level we can control the shape and size of the structures. At the second level the aggregation of the structures in a magnetic field will result in higher order architecture. The field-induced assembly of the magnetic structures should be reversible. A methodology was developed

to retain the aggregation configuration of the magnetic structures even in the absence of the field. During the process of aggregation and assembly we can also incorporate different materials in the magnetic structures to create novel, hybrid, higher order assemblies.
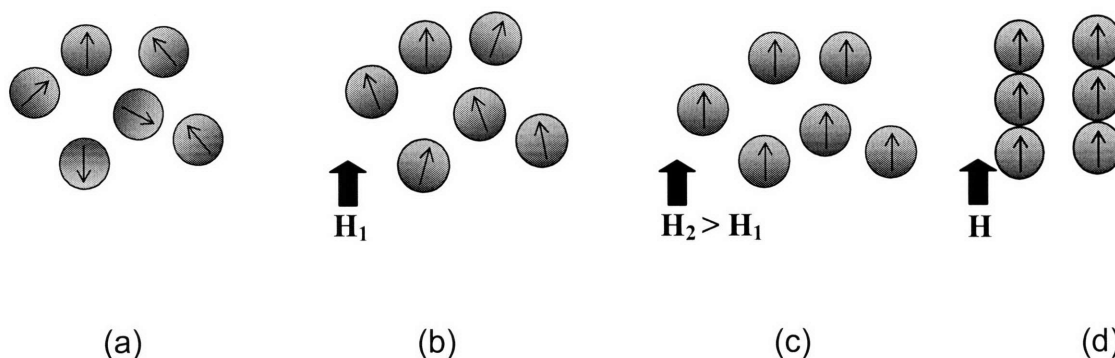
Figure 1-1. Schematic of magnetite nanoparticles (a) under zero external magnetic field. The dipoles point in random directions due to thermal fluctuations. (b) When a small external field (H_1) is applied, the dipoles develop a magnetic moment in the direction of the field. (c) At higher fields (H_2), the dipoles are saturated and point in the direction of the field. (d) When the dipolar interaction between the particles is strong enough to overcome the thermal energy, they should aggregate into chain like structures. This is however not observed in a system of magnetite nanoparticles due to weak interparticle dipolar interaction.

We have considered both template-directed assembly and *in situ* aggregation of nanoparticles into ordered three-dimensional structures. In the template based assembly we used polystyrene (PS) beads as scaffolds, and deposited magnetic nanoparticles on the surfaces to create core-shell structures. The magnetic PS beads assembled into chains under applied magnetic fields that could be linked permanently to form magnetic rods. The chemistry used to link the beads governed the rod rigidity. Titania was used to link the beads to create rigid rods while linking with poly (ethylene) glycol resulted in flexible chains. Hollow magnetic structures were obtained by removing the core. The dynamic and quasi-static behavior of the core-shell beads and of the linked chains under an applied magnetic field was modeled. Preliminary studies were also performed to create more exotic magneto-responsive structures such as rings and icosahedra. Self assembly of mixture of surfactants was utilized to generate rings and icosahedra shaped charged

templates. The aggregation behavior of a ring shaped cluster in the presence of a magnetic field was also analyzed theoretically.

In the *in situ* approach, nanoparticles were cross linked in solution phase in a controlled fashion to create macrostrucutres. Radiation crosslinking served as an efficient route to create different sized clusters. In this approach the nanoparticle was first coated with the radiation cross-linkable polymer. The degree of clustering was governed by the dosage amount and magnetic gels were synthesized using this approach. The magneto-responsive gel can be used as a "smart actuator" or as an "artificial muscle" [13, 14].

The effect of nanoparticle size on the magnetic response of the structures was studied. Theory suggested that the size based magnetic effect of the nanoparticles can be exploited in energy absorption areas. This was verified experimentally. The phenomenon was exploited for practical applications by embedding high energy adsorbing magnetic nanoparticles in polymeric fibers via. electrospinning.

1.2   Physics of Magnetic Nanoparticles

The structures composed of single domain ferro- or ferrimagnetic nanoparticles have attracted considerable interest due to their significance in technological applications as well as for the fundamental physics [15-17]. The term ferromagnetic refers to the solid in which the magnetic moment of the individual atoms in oriented in a fixed direction. However, when the size of the solid is on the nanometer scale (when it is a nanoparticle), the thermal energy at the room temperature is sufficient to randomize the direction of the net moment. The dipole orientation of the magnetic nanoparticle fluctuates at room temperature which leads to its zero magnetization.

Magnetic fluids, which are reviewed in detail in the next section, are stable colloidal dispersions of magnetite and maghemite nanoparticles. Under an external magnetic field, the magnetic nanoparticle is magnetized in the direction of the field and develops a magnetic moment $\bar{m}$ by

$$\vec{m} = \mu_o \vec{M} V \tag{1}$$

where μ_o is the permeability of free space, $\vec{M}$ is the magnetization which is the intrinsic property of the material and depends on the magnitude of the applied magnetic field and V is the particle volume. At high applied magnetic field, the magnetic dipole is completely aligned with the direction of the magnetic field (Figure 1-1). The corresponding magnetization developed is known as saturation magnetization $\vec{M}_s$. This property of the magnetic nanoparticles to behave like nano-magnets in the presence of a field and like non-magnetic materials in the absence of the field is known as superparamagnetism (M → 0 as H → 0).
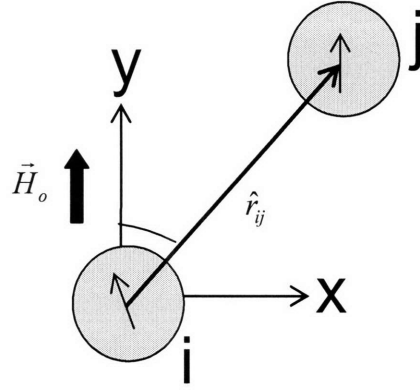
Figure 1-2. Schematic of two interacting dipoles.

The interaction energy between the magnetic nanoparticles in the presence of a magnetic field is given by [15]

$$U_{ij}^{dip} = \frac{1}{4\pi\mu_o} \frac{\vec{m}_i.\vec{m}_j - 3(\hat{r}.\vec{m}_i)(\hat{r}.\vec{m}_j)}{r^3} \tag{2}$$

where $\hat{r}$ is the unit vector in the direction of the line joining the center of the two dipoles (Figure 1-2) and r is the distance between the two dipoles. When the interaction between the magnetic nanoparticles is strong they should form chain like structures to minimize

the interaction energy. Parameter λ characterizes the ratio of maximum interaction energy between two magnetic dipoles (r=2a) to that of thermal energy [18]

$$\lambda = \frac{\pi \mu_o a^3 M^2}{19 k_B T} \qquad (3)$$

where k_B is the boltzmann constant and T is the temperature. When λ >>1, the dipolar interaction between particles is strong enough to overcome the Brownian motion and chaining is observed in the direction of the applied field. This is seen in magnetorheological (MR) fluids which are a suspension of micro-meter sized iron particles. Both M and a are high enough in this case and particles undergo reversible aggregation in under an applied magnetic field. λ is <<1 for magnetic nanoparticle dispersion due to their small size and magnetization, and any structure formation is disrupted by thermal energy. λ can be increased either by increasing M or by increasing a. M can only be increased to the saturation value of the magnetic nanoparticles M_s, by increasing H. a can be increased up to 20 nm with the current synthesis methods. With these limitations it is not possible to observe any appreciable structure formation in magnetic fluids. In this thesis we have explored different methods to form clusters of magnetic nanoparticles in a controlled fashion. This increases the effective value of a thereby making λ >>1.

1.3 Background: Magnetic Nanoparticles

1.3.1 Structure

Magnetic fluids, also known as ferrofluids, are colloidal dispersions of magnetic nanoparticles that do not settle in gravitational or moderate magnetic fields due to their small size and do not aggregate because of their surface coatings. The structure of a magnetic fluid is shown schematically in Figure 1-2. The nanoparticles can be either ferromagnetic materials such as iron or cobalt, or ferrimagnetic materials, the most common of which is magnetite (Fe_3O_4) [19]. This compound is a spinel iron oxide species with a 2:1 molar ratio of Fe ions in their III and II oxidation states [20].
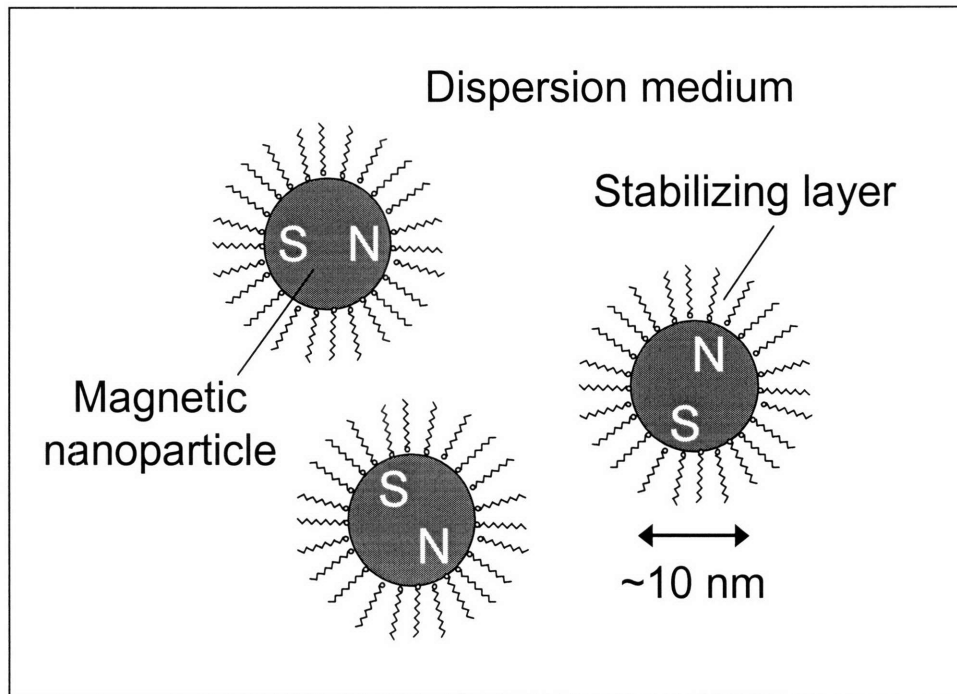
Figure 1-3. General structure of a magnetic fluid. Magnetic fluids consist of magnetic nanoparticles dispersed in a liquid medium, with a stabilizing layer around the particles to prevent flocculation. Each particle has a magnetic dipole but the suspension as a whole has zero net magnetization due to dipole fluctuations.

Magnetite is not prone to oxidation, which is an advantage over magnetic fluids based on cobalt or iron nanoparticles, which tend to lose their magnetic properties over time [21]. The typical particle size is ~10 nm, which is sufficiently small to prevent sedimentation of the particles, as Brownian motion will dominate the gravitational force and the magnetic force from a typical handheld magnet for a particle of this size [19].

Without a stabilizing layer, the ~10 nm particles in a magnetic nanoparticle would rapidly flocculate due to the van der Waals attractive force that exists between particles in a dispersion medium, and then settle. The van der Waals force is more important than interparticle magnetic attraction at short range for a moderately magnetic material like magnetite [22]. The role of the stabilizing layer is to prevent flocculation by exerting a repulsive force between particles at short range. The nature of the stabilizing layer depends on the dispersion medium. If the dispersion medium is a hydrocarbon, steric stabilization from an attached surfactant or polymer is typically used [23]. In an aqueous

magnetic fluid, where water is the dispersion medium, steric stabilization, electrostatic stabilization, or a combination of both can be used to prevent the particles from agglomerating. Aqueous magnetic fluids with no physical stabilizing layer have been produced, but require careful control of the ionic strength and pH to maintain sufficient surface charge on the bare particles for electrostatic stabilization [24]. Stabilizing agents for electrostatic stabilization must possess functional groups that are ionized at the pH of the magnetic fluid, while stabilizing agents for steric stabilization must be sufficiently well solvated by the dispersion medium to induce repulsive interactions when the stabilizing layers of two particles overlap. In addition, all stabilizing polymers or surfactants require a means of attachment to the nanoparticles. In some cases, the stabilizer is attached physically with a moiety that is insoluble in the dispersion medium. For example, block copolymers that contain a soluble block for steric stabilization and an insoluble block for physical attachment have been used successfully to stabilize magnetic fluids [21, 25]. A far more common method of stabilizer attachment to the particles is through the incorporation of a functional group that forms an electrostatic or covalent bond to the particle surface. For magnetite-based magnetic fluids, the most common functional group for attachment is carboxylic acid, which is known to form a strong *d*-orbital chelation to iron atoms on the magnetite surface [26], as shown in Figure 1-3. This attachment mechanism was used in the earliest magnetic fluids [27, 28], which consisted of fatty acid-stabilized magnetite nanoparticles in kerosene, where the carboxyl head group of the fatty acid attached to the magnetite surface and the alkyl tail provided steric stabilization.
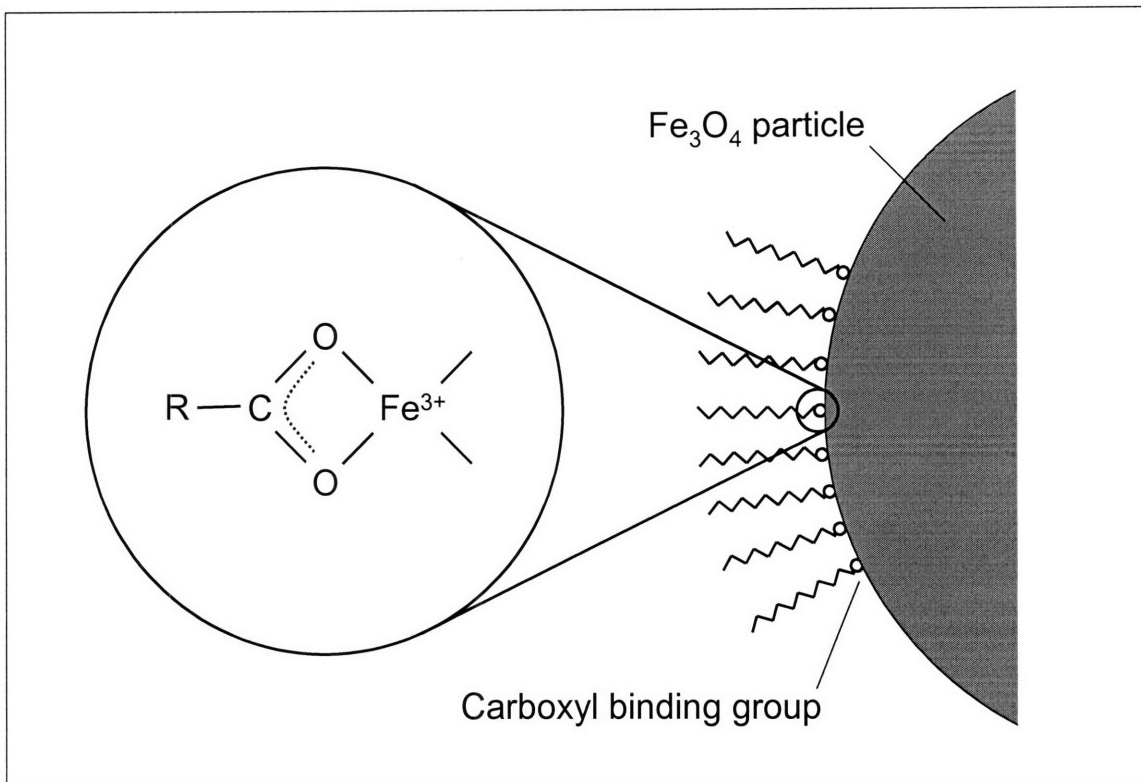
Figure 1-4. Attachment of carboxyl groups to the surface of a magnetite particle. The carboxyl group forms a chelate bidentate structure with surface iron atoms.

Another important property of magnetic nanoparticles is that they are sufficiently small to be single domain particles. The domain size of magnetite is ~25 nm [29], which indicates that 10 nm particles are composed of a single crystal of magnetite, each having a permanent magnetic dipole similar to that of the bulk material. In a magnetic fluid, these dipoles are randomized due to either Brownian relaxation (particle rotation) or Néel relaxation (spontaneous fluctuation of the dipole direction within the particle). The dominant mechanism depends on the size of the particle [19]. Magnetic nanoparticles exhibit superparamagnetism, in that they have approximately zero net magnetization in the absence of an applied field, but become strongly magnetized in an applied field due to alignment of the particle dipoles with the field.

1.3.2 Magnetic Nanoparticle Synthesis

1.3.2.1 General Concepts

The synthesis of magnetic nanoparticles requires two steps: formation of the nanoparticles and coating the nanoparticles with the stabilizing layer. Usually, the synthesis is performed in the eventual dispersion medium, but in some cases the nanoparticles are synthesized in one solvent and then transferred to another [28]. In addition, the synthesis of the nanoparticles is usually conducted in the presence of a stabilizing polymer or surfactant to prevent agglomeration during synthesis. This section reviews the three most common methods of stable magnetic nanoparticle production, although it should be noted that other techniques such as spark erosion [30] and plasma generation [31] have been used to produce magnetic nanoparticles.

1.3.2.2 Size Reduction

The oldest and most basic method of magnetic nanoparticle synthesis is through size reduction. In this technique, bulk magnetic materials are ground in a ball mill with the dispersion medium and the stabilizing surfactant. The surfactant must be present during grinding to produce stable nanoparticles. Size reduction was first described by Papell [27], who ground a 30 μm magnetite powder in heptane with oleic acid to produce a magnetic fluid with a final particle diameter of approximately 10 nm. The primary benefit of size reduction is that it is simple and flexible, in that any type of particle can be produced if a bulk powder is available. However, size reduction is a time-consuming and energy intensive process, requiring approximately 1000 hours of grinding at 45 rpm in order to reduce the particles to the required dimension [32].

1.3.2.3 Organometallic Decomposition

Magnetic nanoparticles can also be prepared by thermal decomposition of organometallic compounds in an organic solvent [21, 33-36]. In this technique, an organometallic compound and stabilizing surfactant are dissolved in a solvent and heated to an elevated temperature (approximately 200-300 °C, depending on the compound), at which point the organometallic species decomposes and the insoluble metal precipitates.

The surfactant binds to the particles just after nucleation, limiting the growth and forming nanoparticles. A variety of magnetic nanoparticle suspensions have been produced by this method, including cobalt particles from dicobalt octacarbonyl, [21, 33] iron particles from iron pentacarbonyl [35], and magnetite particles from iron acetylacetonoate [36] or iron pentacarbonyl followed by oxidation [34]. Magnetic nanoparticles produced from organometallic decomposition tend to be nearly monodisperse, which is likely a result of the elevated temperature used in the synthesis. This method of particle synthesis cannot be performed in water due to the high temperatures and insolubility of the organometallic compounds; however, aqueous magnetic nanoparticle dispersions can be produced by subsequently transferring the particles to water with a new stabilizing surfactant.

1.3.2.4 Chemical Coprecipitation

A less energy intensive technique that is well suited for making aqueous magnetic fluids is the chemical coprecipitation of metal salts, which was first achieved by Reimers and Khallafalla [28]. This technique is limited to the production of ferrite particles, such as magnetite (Fe_3O_4) [28], maghemite (γ-Fe_2O_3) [24], or cobalt ferrite ($CoFe_2O_4$) [37], and is probably the most common method for preparing magnetic fluids due to its simplicity and relatively low cost. The discussion here is limited to magnetite nanoparticle formation, as it is the basis of the magnetic fluids used in this study and of most magnetic fluids in the literature.

Magnetite is formed by basic precipitation of an aqueous solution of iron (III) chloride and iron (II) chloride in a 2:1 molar ratio, forming a spinel structure of Fe^{3+} and Fe^{2+} ions that results in a net magnetic dipole [20]. Magnetite nanoparticles are formed when this reaction is conducted in the presence of a dissolved stabilizing surfactant or polymer that binds to the particles just after nucleation, limiting the growth of the particles to ~10 nm. The overall stoichiometry of this reaction is shown in Equation 1-1, for the case where ammonium hydroxide is used as the precipitating agent.

$$2\ FeCl_3\ +\ FeCl_2\ +\ 8\ NH_4OH\ \rightarrow\ Fe_3O_4\ +\ 8\ NH_4Cl\ +\ 4\ H_2O \tag{1-1}$$

28
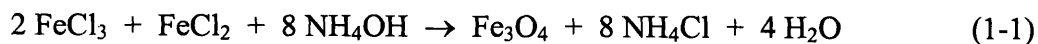
The base is usually added in excess so that the pH of the reaction medium is strongly basic (pH of 12-14). The size, composition, and magnetization of the nanoparticles are affected by the reagent concentrations, stabilizer concentration, temperature, and pH during synthesis [38-42]. The optimal reaction temperature for the formation of magnetite is generally thought to be approximately 80 °C [38, 41], although magnetite formation at room temperature has also been reported [43].

1.3.3 Applications of Magnetic Nanoparticles

1.3.3.1 Industrial Applications

Dispersion of magnetic nanoparticles also known as magnetic fluids have found commercial use in a variety of industrial applications. Three industrial applications in which magnetic fluids have found the most commercial success are sealing, damping, and heat transfer [44]. Magnetic fluids are commonly used as rotary shaft seals in hard drives because they provide a means of preventing gas leakage while avoiding rubber parts. In this application, rings of magnetic fluid are held in place around the shaft with external magnets that form a high pressure gas barrier [23]. Likewise, a film of magnetic fluid held in place with an external magnet is used in place of an oil film in stepper motors to damp vibrations and oscillations as the motor moves [44]. The damping properties of magnetic fluids are also used in loudspeakers [45], where they also act as an improved coolant fluid due to their high thermal conductivity and their development of magnetically-driven convection cells in the presence of a magnetic field [19]. The magnetic fluids used in these industrial applications are usually organic-based [45]. A relatively new application is the use of cobalt-based magnetic fluids to increase microwave absorption in the heating of nonpolar systems [33].

1.3.3.2 Biomedical Applications

Aqueous based magnetic nanoparticles have the potential to be used in a range of biomedical applications, in which the nanoparticles generally require a coating that provides colloidal stability in the body and is biocompatible. Magnetic nanoparticles with biocompatible stabilizing polymers have been developed as magnetic resonance imaging (MRI) contrast agents that have improved imaging properties in the body

compared to conventional ferric salt solutions [46, 47]. Magnetic nanoparticles have also been used in drug delivery applications, which requires the absorption or covalent attachment of drugs to the nanoparticles [48, 49]. Anti-cancer drugs absorbed on the stabilizing layer of magnetite nanoparticles have been directed *in vivo* to a tumor by applying an external magnetic field to concentrate the magnetic fluid in the affected area [48]. Magnetite particles with attached monoclonal antibodies have also been developed that are able to simultaneously deliver the antibody and generate heat by applying an alternating magnetic field to the particles [49].

1.3.3.3 Biological Separations

Magnetic fluids (or suspensions of submicron magnetic particles) have been applied to many different biological systems to separate cells [50] and proteins [51-56]. In most biological separation applications, the magnetic nanoparticles are used as tagging-agents for the biological species, which usually have a negligible magnetic moment. Cell separation with magnetic particles has been reviewed extensively by Safarik and Safarikova [50]. Most techniques for cell separation involve functionalizing the magnetic nanoparticles with ligands that bind reversibly to cells. When added to a fermentation broth, for example, the magnetic particles bind specifically to the target cells, which can then be removed by magnetic separation. In most cases, 1-5 μm polymer beads with imbedded nanoparticles, such as the commercial product Dynabeads, are used [50], which are not technically magnetic fluids due to the large particle size. In some cases, magnetic nanoparticles have been used in cell separations. For example, a magnetic fluid with functionalized maghemite nanoparticles has been used to separate erythrocyte cells [57]. The cells are many orders of magnitude larger than the nanoparticles and are therefore covered by many nanoparticles. Proteins, which are significantly smaller than the nanoparticles, can be separated with magnetic fluids on the basis of charge interactions [51, 52] or specificity of ligands attached to the nanoparticles [53-55]. Recently, magnetic nanoparticle based on phospholipid-coated and polymer-coated magnetite nanoparticles have been produced that are capable of protein loadings as high as 1200 mg/cm^3 of particles [51, 58]. The magnetic separation of biological

30

products remains an extremely active area of research due to the high value of these compounds.

1.3.3.4 Environmental Separations

Several techniques involving magnetic particles for environmental separations have been proposed and demonstrated at the research level . Usually, these processes use micron-sized particles composed of magnetite (or composites of magnetite and other materials) that are used as magnetic tagging agents by coating them with a selective adsorbent for targeted solutes, such as radionuclides [59], heavy metal ions [60], or water-soluble organic dyes [61, 62]. Other techniques include using highly porous magnetic beads that are effective in removing metal ions from water [63] and using charged magnetic particles that aggregate with bacteria and solids to purify wastewater [56]. An environmental separation with true magnetic fluid (i.e. suspensions of individually dispersed magnetic nanoparticles) was first explored by Moeser et al. [64].

1.3.3.5 Magnetophoretic Separations with Magnetic Fluids

In magnetophoretic separations, a magnetic fluid is used to exert body forces on nonmagnetic particles in order to separate them on the basis of size or density. This approach is different from the biological and environmental separations discussed in the previous sections, in which the magnetic particles serve as tagging agents. This process, also known as magnetoflotation, has been used to separate coal particles of different densities by suspending the particles in a magnetic fluid and applying a vertical magnet field gradient [65] . The field gradient causes the particles to experience a body force that acts opposite to gravity, changing the effective density of the fluid. By changing the magnetic field gradient, the effective fluid density can be set between the density of two types of particles, causing one to float and the other to sink. Recently, this concept has been extended to cell separations. By suspending nonmagnetic cells in a magnetic fluid, the cells can be driven against a magnetic field gradient; transport is opposed by the drag force on the cells, allowing sorting based on the cell size [66, 67].

31

1.4 Background: Aggregation

1.4.1 Template Based Synthesis

Template based strategies have been extensively used for extending the length scale of structural organization in materials. The underlying principle of template synthesis is similar to that of making structures through the use of replication e.g. die casting or mold casting. Membranes pores have long been used as templates to create micro- and nanomaterials. Bean [68] was the first to fill the pores of a membrane with silver to create silver nanowires. Poissin electrodeposited metals in etched mica membranes to grow microstructures [69]. Immersing the membrane in a solution containing desired monomer or salt and subsequent reduction or polymerization resulted in metallic or polymeric microtubules [70-73]. Bicontinuous polymeric gels have been used as templates for *in situ* mineralization of magnetite and polymerization of titanium alkoxide [74, 75]. Velv and co-workers have infiltrated latex colloidal crystal templates with gold sols. Subsequent removal of the template at elevated temperatures resulted in stable replicas [76, 77]. Mann and coworkers used macroporous dextran as a template for the production of metallic sponges [78]. Oil in water emulsions and micelles of block copolymers have also been used as scaffolds to create mesoporous structures/hollow capsules of materials [79-82]. One major limitation in the aforementioned techniques is the lack of ordering at local scale. It is possible to replicate macrostrucutres using this approach. It is like pouring cement into a mold to get the desired structure. At microscale the cement particles are still randomly oriented [83]. One technique to obtain certain degree of local scale ordering is using " Layer-by-Layer" (LbL) assembly. This approach was first developed for flat surfaces and involves sequential absorption of oppositely charged polyelectrolytes [84]. This method can also incorporate any charged moieties like biomolecules, nanoparticles and polymers. This process was extended to coat curved surfaces like spherical polymeric beads to create core-shell strucutres [85-95]. Subsequent dissolution of the spherical template resulted in hollow capsules [85-87]. We adapted this method of using Polystyrene beads coupled with LbL to prepare hierarchical magnetic materials.

1.4.2 Radiation Crosslinking

Modifications in polymeric structure of the plastic materials can also be brought about by exposure to ionizing radiation from either radioactive sources, or highly accelerated electrons [96, 97]. Radiation crosslinking yields high purity materials free of residual impurities such as crosslinking agents, catalyst or byproducts. The basic principle of radiation crosslinking is that all forms of ionizing radiation interact with matter by transferring energy to the electrons orbiting the atomic nuclei of target materials. These electrons may then be either released from the atoms, yielding positively charged ions and free electrons, or moved to a higher-energy atomic orbital, yielding an excited atom or molecule (free radical). These ions, electrons, and the excited species are the precursors of any chemical changes observed in irradiated material [38]. Ionizing radiation is, in a sense, a double-edged sword. It can both crosslink macromolecules and degrade them. In the absence of water, and in the presence atmospheric oxygen, the latter effect predominates and constitutes a method for reducing the molecular weight of ultra-high molecular weight e.g. Poly(ethylene) oxide (PEO) to levels appropriate to different commercial applications. In the presence of water, and preferably in the absence of oxygen, ionizing radiations produces hydroxyl radicals and hydrogen radicals. The former then attack the PEO chains randomly, creating radical carbon atoms on these chains, pairs of which couple to form the junctions [98]. The hydrogen radicals mostly combine in pairs forming hydrogen gas. The dosage of ionic radiation controls the amount of crosslinking. We have used to this technique to create clusters of magnetic nanoparticles *in situ*. Aqueous solution of PEO coated magnetic nanoparticles were prepared and rate of aggregation was studied as function of dosage rate.

1.5 Research Overview

The overall goals of this research were: i) to develop a scheme to aggregate magnetic nanoparticles in a controlled fashion to create 3-D magneto-responsive structures, ii) to characterize the magnetic response of these structures under an applied magnetic field, and iii) to demonstrate some novel applications of these structures.

Chapter 2 details the preparation of the rigid rod like structures (chains) with magnetic nanoparticles. The response of the magnetic chains in the magnetic field was quantified. Chapter 3 contains a detailed study of the comparison of the magnetic behavior of the prepared core-shell structures with the commercially available beads in which the nanoparticles are distributed in the bead matrix. The synthesis of flexible magnetic chains and their subsequent manipulation is discussed in Chapter 4. Chapter 5 deals with the use of surfactant as templates and radiation crosslinking to induce clustering in nanoparticle suspensions. Chapter 6 entails the magnetic characterization of the nanoparticles as a function of the nanoparticle size. The theory to employ magnetic relaxation of the nanoparticle for energy adsorption is outlined and verified experimentally. Chapter 7 outlines a practical method developed to encapsulate magnetic nanoparticles in polymeric matrix by using electospinning. The synthesis of "smart" energy absorbing magneto-responsive nanofibers using electrospinning and their response to an applied magnetic field is discussed in this Chapter.

1.6 References

1.   Philippe Knauth, J.S., *Nanostrucutred Materials, Selected Synthesis Methods, Properties and Applications*, ed. H.L. Tuller. 2002: Kluwer Academic Publishers.

2.   Frolov, G.I., *Film carriers for super-high-density magnetic storage.* Technical Physics, 2001. **46**(12): p. 1537-1544.

3.   Hasmonay, E., E. Dubois, S. Neveu, J.C. Bacri, and R. Perzynski, *Alternating magneto-birefringence of ionic ferrofluids in crossed fields.* European Physical Journal B, 2001. **21**(1): p. 19-29.

4.   Hasmonay, E., J. Depeyrot, M.H. Sousa, F.A. Tourinho, J.C. Bacri, R. Perzynski, Y.L. Raikher, and I. Rosenman, *Magnetic and optical properties of ionic ferrofluids based on nickel ferrite nanoparticles.* Journal Of Applied Physics, 2000. **88**(11): p. 6628-6635.

5.   Lucien Malenfant, P.R., H. Acar, P.J. Bonitatebus, W.T. Dixon, and A.M. Kulkarni, *Nanoparticles coated with biocompatible polymers as MRI contrast agent.* 2006, (General Electric Company, USA). Application: US US. p. 33 pp.

6. Evgenov, N.V., Z. Medarova, G. Dai, S. Bonner-Weir, and A. Moore, *In vivo imaging of islet transplantation.* Nature Medicine (New York, NY, United States), 2006. **12**(1): p. 144-148.

7. Ito, A., M. Shinkai, H. Honda, and T. Kobayashi, *Medical application of functionalized magnetic nanoparticles.* Journal of Bioscience and Bioengineering, 2005. **100**(1): p. 1-11.

8. Kalambur, V.S., B. Han, B.E. Hammer, T.W. Shield, and J.C. Bischof, *In vitro characterization of movement, heating and visualization of magnetic nanoparticles for biomedical applications.* Nanotechnology, 2005. **16**(8): p. 1221-1233.

9. Sun, C., O. Veiseh, N. Kohler, J. Gunn, D. Lee, R. Sze, A. Hallahan, and M. Zhang, *Intracellular uptake of folate receptor targeted superparamagnetic nanoparticles for enhanced tumor detection by MRI.* NSTI Nanotech 2005, NSTI Nanotechnology Conference and Trade Show, Anaheim, CA, United States, May 8-12, 2005, 2005. **1**: p. 74-77.

10. Kopelman, R., Y.-E.L. Koo, M. Philbert, B.A. Moffat, G. Ramachandra Reddy, P. McConville, D.E. Hall, T.L. Chenevert, M.S. Bhojani, S.M. Buck, A. Rehemtulla, and B.D. Ross, *Multifunctional nanoparticle platforms for in vivo MRI enhancement and photodynamic therapy of a rat brain cancer.* Journal of Magnetism and Magnetic Materials, 2005. **293**(1): p. 404-410.

11. Teunissen, W., F.M.F. de Groot, J. Geus, O. Stephan, M. Tence, and C. Colliex, *The structure of carbon encapsulated NiFe nanoparticles.* Journal Of Catalysis, 2001. **204**(1): p. 169-174.

12. Teunissen, W. and J.W. Geus, *Catalyst supports based on encapsulated magnetic metal particles*, in *Science And Technology In Catalysis 1998.* 1999. p. 185-190.

13. Varga, Z., G. Filipcsei, and M. Zrinyi, *Magnetic field sensitive functional elastomers with tuneable elastic modulus.* Polymer, 2006. **47**(1): p. 227-233.

14. Varga, Z., G. Filipcsei, A. Szilagyi, and M. Zrinyi, *Electric and magnetic field-structured smart composites.* Macromolecular Symposia, 2005. **227**: p. 123-133.

15. Dormann, J.L., A. Ezzir, R. Cherkakoui, M. Nogues, F. Lucari, F. dOrazio, M. Godinho, E. Tronc, J.P. Jolivet, and D. Fiorani, *Static and dynamical properties of gamma-Fe2O3 nanoparticles.* Journal De Physique Iv, 1997. **7**(C1): p. 509-512.

16. Puntes, V.F., K.M. Krishnan, and A.P. Alivisatos, *Colloidal nanocrystal shape and size control: The case of cobalt.* Science, 2001. **291**(5511): p. 2115-2117.

17. Sun, S.H., C.B. Murray, D. Weller, L. Folks, and A. Moser, *Monodisperse FePt nanoparticles and ferromagnetic FePt nanocrystal superlattices.* Science, 2000. **287**(5460): p. 1989-1992.

18. Gast, A.P. and C.F. Zukoski, *Electrorheological Fluids As Colloidal Suspensions.* Advances In Colloid And Interface Science, 1989. **30**(3-4): p. 153-202.

19. Rosensweig, R.E., *Ferrohydrodynamics.* 1985, Mineola, NY: Dover Publications, Inc.

20. Gokon, N., A. Shimada, H. Kaneko, Y. Tamaura, K. Ito, and T. Ohara, *Magnetic coagulation and reaction rate for the aqueous ferrite formation reaction.* Journal of Magnetism and Magnetic Materials, 2002. **238**(1): p. 47-55.

21. Pathmamanoharan, C. and A.P. Philipse, *Preparation and properties of monodisperse magnetic cobalt colloids grafted with polyisobutene.* Journal of Colloid and Interface Science, 1998. **205**(2): p. 340-353.

22. Shen, L.F., A. Stachowiak, S.E.K. Fateen, P.E. Laibinis, and T.A. Hatton, *Structure of alkanoic acid stabilized magnetic fluids. A small- angle neutron and light scattering analysis.* Langmuir, 2001. **17**(2): p. 288-299.

23. Rosensweig, R.E., *Magnetic Fluids: Phenomena and Process Applications.* Chemical Engineering Progress, 1989. **85**(4): p. 53-61.

24. Massart, R., R. Dubois, V. Cabuil, and E. Hasmonay, *Preparation and Properties of Monodisperse Magnetic Fluids.* Journal of Magnetism and Magnetic Materials, 1995. **149**: p. 1-5.

25. Elkafrawy, S., S.R. Hoon, P.R. Bissell, and C. Price, *Polymeric Stabilization of Colloidal Magnetite Magnetic Fluids.* IEEE Transactions on Magnetics, 1990. **26**(5): p. 1846-1848.

26. Mikhailik, O.M., V.I. Povstugar, S.S. Mikhailova, A.M. Lyakhovich, O.M. Fedorenko, G.T. Kurbatova, N.I. Shklovskaya, and A.A. Chuiko, *Surface*

Structure of Finely Dispersed Iron Powders. I. Formation of Stabilizing Coating. Colloids and Surfaces, 1991. **52**: p. 315-324.

27. Papell, S.S., *Low Viscosity Magnetic Fluid Obtained by the Colloidal Suspension of Magnetic Particles.* 1965: United States.

28. Reimers, G.W. and S.E. Khalafalla, *Preparing Magnetic Fluids by a Peptizing Method.* 1972, Twin Cities Metallurgy Research Center
      U.S. Department of the Interior: Minneapolis.

29. Lee, J., T. Isobe, and M. Senna, *Preparation of Ultrafine Fe3O4 Particles by Precipitation in the Presence of PVA at High pH.* Journal of Colloid and Interface Science, 1996. **177**: p. 490-494.

30. Berkowitz, A.E. and J.L. Walter, *Ferrofluids Prepared by Spark Erosion.* Journal of Magnetism and Magnetic Materials, 1983. **30**: p. 75-78.

31. Bica, I. and I. Muscutariu, *Physical Methods in Obtaining the Ultrafine Powders for Magnetic Fluids Preparation.* Materials Science and Engineering, 1996. **B40**: p. 5-9.

32. Berkowitz, A.E., J.A. Lahut, and C.E. VanBuren, *Properties of Magnetic Fluid Particles.* IEEE Transactions on Magnetics, 1980. **16**(2): p. 184-190.

33. Holzwarth, A., J.F. Lou, T.A. Hatton, and P.E. Laibinis, *Enhanced microwave heating of nonpolar solvents by dispersed magnetic nanoparticles.* Industrial & Engineering Chemistry Research, 1998. **37**(7): p. 2701-2706.

34. Kumar, R.V., Y. Koltypin, Y.S. Cohen, Y. Cohen, D. Aurbach, O. Palchik, I. Felner, and A. Gedanken, *Preparation of amorphous magnetite nanoparticles embedded in polyvinyl alcohol using ultrasound radiation.* Journal of Materials Chemistry, 2000. **10**(5): p. 1125-1129.

35. Park, S.J., S. Kim, S. Lee, Z.G. Khim, K. Char, and T. Hyeon, *Synthesis and magnetic studies of uniform iron nanorods and nanospheres.* Journal of the American Chemical Society, 2000. **122**(35): p. 8581-8582.

36. Sun, S.H. and H. Zeng, *Size-controlled synthesis of magnetite nanoparticles.* Journal of the American Chemical Society, 2002. **124**(28): p. 8204-8205.

37. Giri, A.K., K. Pellerin, W. Pongsaksawad, M. Sorescu, and S.A. Majetich, *Effect of light on the magnetic properties of cobalt ferrite nanoparticles.* Ieee Transactions on Magnetics, 2000. **36**(5): p. 3029-3031.

38. Bica, D., *Preparation of Magnetic Fluids for Various Applications.* Romanian Reports in Physics, 1995. **47**(3-5): p. 265-272.

39. Blums, E., H. Sandner, and S. Odenbach, *Nonstationary Mass-Transfer under Particle Magnetophoresis in Diluted Ferrocolloids.* Zeitschrift Fur Physik B-Condensed Matter, 1995. **96**(4): p. 563-566.

40. Feltin, N. and M.P. Pileni, *New Technique for Synthesizing Iron Ferrite Magnetic Nanosized Particles.* Langmuir, 1997. **13**: p. 3927-3933.

41. Shen, L., P.E. Laibinis, and T.A. Hatton, *Bilayer Surfactant Stabilized Magnetic Fluids: Synthesis and Interactions at Interfaces.* Langmuir, 1999. **15**(2): p. 447-453.

42. Shimoiizaka, J., *Method for Preparing a Water-based Magnetic Fluid.* 1978: United States.

43. Cabuil, V., N. Hochart, R. Perzynski, and P.J. Lutz, *Synthesis of Cyclohexane Magnetic Fluids Through Adsorption of End-functionalized Polymers on Magnetic Particles.* Progress in Colloid and Polymer Science, 1994. **97**: p. 71-74.

44. Raj, K., B. Moskowitz, and R. Casciari, *Advances in Ferrofluid Technology.* Journal of Magnetism and Magnetic Materials, 1995. **149**: p. 174-180.

45. Raj, K. and R. Moskowitz, *Commercial Applications of Ferrofluids.* Journal of Magnetism and Magnetic Materials, 1990. **85**: p. 233-245.

46. Douglas, T., J.W.M. Bulte, D.P.E. Dickson, R.B. Frankel, Q.A. Pankhurst, B.M. Moskowitz, and S. Mann, *Inorganic-Protein Interactions in the Synthesis of a Ferrimagnetic Nanocomposite.* Hybrid Organic-Inorganic Composites, 1995. **585**: p. 19-28.

47. Kawaguchi, T., A. Yoshino, M. Hasegawa, T. Hanaichi, S. Maruno, and N. Adachi, *Dextran-magnetite complex: temperature dependence of its NMR relaxivity.* Journal of Materials Science-Materials in Medicine, 2002. **13**(1): p. 113-117.

48. Lubbe, A.S., C. Bergemann, J. Brock, and D.G. McClure, *Physiological aspects in magnetic drug-targeting.* Journal of Magnetism and Magnetic Materials, 1999. **194**(1-3): p. 149-155.

49. Suzuki, M., M. Shinkai, M. Kamihira, and T. Kobayashi, *Preparation and Characteristics of Magnetite-Labeled Antibody with the Use of Poly(Ethylene Glycol) Derivatives.* Biotechnology and Applied Biochemistry, 1995. **21**: p. 335-345.

50. Safarik, I. and M. Safarikova, *Use of magnetic techniques for the isolation of cells.* Journal of Chromatography B, 1999. **722**(1-2): p. 33-53.

51. Bucak, S., D.J. Jones, P.E. Laibinis, and T.A. Hatton, *Protein separations using colloidal magnetic nanoparticles.* Biotechnology Progress, 2003. **19**(2): p. 477-484.

52. DeCuyper, M., B. DeMeulenaer, P. VanderMeeren, and J. Vanderdeelen, *Catalytic durability of magnetoproteoliposomes captured by high-gradient magnetic forces in a miniature fixed-bed reactor.* Biotechnology and Bioengineering, 1996. **49**(6): p. 654-658.

53. Hubbuch, J.J. and O.R.T. Thomas, *High-gradient magnetic affinity separation of trypsin from porcine pancreatin.* Biotechnology and Bioengineering, 2002. **79**(3): p. 301-313.

54. Khng, H.P., D. Cunliffe, S. Davies, N.A. Turner, and E.N. Vulfson, *The synthesis of sub-micron magnetic particles and their use for preparative purification of proteins.* Biotechnology and Bioengineering, 1998. **60**(4): p. 419-424.

55. Tong, X.D., B. Xue, and Y. Sun, *A novel magnetic affinity support for protein adsorption and purification.* Biotechnology Progress, 2001. **17**(1): p. 134-139.

56. Ditsch, A., D.I.C. Wang, and T.A. Hatton, *Magnetic fluids for ion-exchange purification of recombinant proteins.* Abstracts Of Papers Of The American Chemical Society, 2004. **227**: p. U211-U211.

57. Halbreich, A., J. Roger, J.N. Pons, D. Geldwerth, M.F. Da Silva, M. Roudier, and J.C. Bacri, *Biomedical applications of maghemite ferrofluid.* Biochimie, 1998. **80**(5-6): p. 379-390.

58. Ditsch, A., J. Yin, P.E. Laibinis, D.I.C. Wang, and T.A. Hatton, *Ion-Exchange Purification of Proteins Using Magnetic Nanoclusters*. Biotechnol. Prog., 2006.

59. Buchholz, B.A., L. Nunez, and G.F. Vandegrift, *Radiolysis and Hydrolysis of Magnetically Assisted Chemical Separation Particles*. Separation Science and Technology, 1996. **31**(14): p. 1933-1952.

60. Kaminski, M.D. and L. Nunez, *Extractant-coated magnetic particles for cobalt and nickel recovery from acidic solution*. Journal of Magnetism and Magnetic Materials, 1999. **194**(1-3): p. 31-36.

61. Safarik, I., *Removal of Organic Polycyclic Compounds from Water Solutions with a Magnetic Chitosan Based Sorbent Bearing Copper Phthalocyanine Dye*. Water Research, 1995. **29**(1): p. 101-105.

62. Safarik, I. and M. Safarikova, *Copper phthalocyanine dye immobilized on magnetite particles: An efficient adsorbent for rapid removal of polycyclic aromatic compounds from water solutions and suspensions*. Separation Science and Technology, 1997. **32**(14): p. 2385-2392.

63. Leun, D. and A.K. Sengupta, *Preparation and characterization of magnetically active polymeric particles (MAPPs) for complex environmental separations*. Environmental Science & Technology, 2000. **34**(15): p. 3276-3282.

64. Moeser, G.D., K.A. Roach, W.H. Green, P.E. Laibinis, and T.A. Hatton, *Water-based magnetic fluids as extractants for synthetic organic compounds*. Industrial & Engineering Chemistry Research, 2002. **41**(19): p. 4739-4749.

65. Fofana, M. and M.S. Klima, *Use of a magnetic fluid based process for coal separations*. Minerals and Metallurgical Processing, 1997. **14**(1): p. 35-40.

66. Sharpe, S., *Magnetophoretic Cell Clarification*, in *Department of Chemical Engineering*. 2004, Massachusetts Institute of Technology: Cambridge, MA.

67. Fateen, S.E.K., *Magnetophoretic Focusing of Submicron Particles Dispersed in a Polymer-Stabilized Magnetic Fluid*, in *Department of Chemical Engineering*. 2002, Massachusetts Institute of Technology: Cambridge, MA.

68. Bean, C.P. 1969: U.S.

69. Possin, G.E., *Method for forming very small diameter wires*. Rev. Sci. Instrum., 1970. **41**: p. 772-774.

70. Parthasarathy, R.V. and C.R. Martin, *Synthesis Of Polymeric Microcapsule Arrays And Their Use For Enzyme Immobilization.* Nature, 1994. **369**(6478): p. 298-301.

71. Cai, Z.H., J.T. Lei, W.B. Liang, V. Menon, and C.R. Martin, *Molecular And Supermolecular Origins Of Enhanced Electronic Conductivity In Template-Synthesized Polyheterocyclic Fibrils.1. Supermolecular Effects.* Chemistry Of Materials, 1991. **3**(5): p. 960-967.

72. Liang, W.B., J.T. Lei, and C.R. Martin, *Effect Of Synthesis Temperature On The Structure, Doping Level And Charge-Transport Properties Of Polypyrrole.* Synthetic Metals, 1992. **52**(2): p. 227-239.

73. Parthasarathy, R.V. and C.R. Martin, *Template-Synthesized Polyaniline Microtubules.* Chemistry Of Materials, 1994. **6**(10): p. 1627-1632.

74. Caruso, R.A., M. Giersig, F. Willig, and M. Antonietti, *Polymer gel template for porous TiO2 production.* Berichte Der Bunsen-Gesellschaft-Physical Chemistry Chemical Physics, 1998. **102**(11): p. 1540-1543.

75. Breulmann, M., H. Colfen, H.P. Hentze, M. Antonietti, D. Walsh, and S. Mann, *Elastic magnets: Template-controlled mineralization of iron oxide colloids in a sponge-like gel matrix.* Advanced Materials, 1998. **10**(3): p. 237-+.

76. Velev, O.D., P.M. Tessier, A.M. Lenhoff, and E.W. Kaler, *Materials - A class of porous metallic nanostructures.* Nature, 1999. **401**(6753): p. 548-548.

77. Velev, O.D. and E.W. Kaler, *Structured porous materials via colloidal crystal templating: From inorganic oxides to metals.* Advanced Materials, 2000. **12**(7): p. 531-534.

78. Walsh, D., L. Arcelli, T. Ikoma, J. Tanaka, and S. Mann, *Dextran templating for the synthesis of metallic and metal oxide sponges.* Nature Materials, 2003. **2**(6): p. 386-U5.

79. Huo, Q.S., J.L. Feng, F. Schuth, and G.D. Stucky, *Preparation of hard mesoporous silica spheres.* Chemistry Of Materials, 1997. **9**(1): p. 14-&.

80. Schacht, S., Q. Huo, I.G. VoigtMartin, G.D. Stucky, and F. Schuth, *Oil-water interface templating of mesoporous macroscale structures.* Science, 1996. **273**(5276): p. 768-771.

81. Sun, Q.Y., P.J. Kooyman, J.G. Grossmann, P.H.H. Bomans, P.M. Frederik, P. Magusin, T.P.M. Beelen, R.A. van Santen, and N. Sommerdijk, *The formation of well-derined hollow silica spheres with multilamellar shell structure.* Advanced Materials, 2003. **15**(13): p. 1097-+.

82. Wong, M.S., E.S. Jeng, and J.Y. Ying, *Supramolecular templating of thermally stable crystalline mesoporous metal oxides using nanoparticulate precursors.* Nano Letters, 2001. **1**(11): p. 637-642.

83. Davis, S.A., M. Breulmann, K.H. Rhodes, B. Zhang, and S. Mann, *Template-directed assembly using nanoparticle building blocks: A nanotectonic approach to organized materials.* Chemistry Of Materials, 2001. **13**(10): p. 3218-3226.

84. Decher, G., *Fuzzy nanoassemblies: Toward layered polymeric multicomposites.* Science, 1997. **277**(5330): p. 1232-1237.

85. Caruso, F., R.A. Caruso, and H. Möhwald, *Nanoengineering of Inorganic and Hybrid Hollow Spheres by Colloidal Templating.* Science, 1998. **282**(5391): p. 1111-1114.

86. Caruso, F., R.A. Caruso, and H. Mohwald, *Nanoengineering of inorganic and hybrid hollow spheres by colloidal templating.* Science, 1998. **282**(5391): p. 1111-1114.

87. Caruso, F., M. Spasova, A. Susha, M. Giersig, and R.A. Caruso, *Magnetic nanocomposite particles and hollow spheres constructed by a sequential layering approach.* Chemistry of Materials, 2001. **13**(1): p. 109-116.

88. Sukhishvili, S.A., *Responsive polymer films and capsules via layer-by-layer assembly.* Current Opinion in Colloid & Interface Science, 2005. **10**(1,2): p. 37-44.

89. Shenoy, D., A. Antipov, and G. Sukhorukov, *Layer-by-layer nanoengineering with polyelectrolytes for delivery of bioactive materials.* Polymeric Gene Delivery, 2005: p. 399-416.

90. Kotov, N.A. and L.M. Liz-Marzan, *Organization of layer-by-layer assembled nanocomposites: Functional effects in photonics and biomaterials.* Nanoscale Materials, 2003: p. 273-301.

91. Schoenhoff, M., *Layered polyelectrolyte complexes: Physics of formation and molecular properties.* Journal of Physics: Condensed Matter, 2003. **15**(49): p. R1781-R1808.

92. Fendler, J.H., *Layer-by-layer self-assembled polyelectrolytes and nanoplatelets.* Multilayer Thin Films, 2003: p. 245-269.

93. Advincula, R.C., *Polyelectrolyte layer-by-layer self-assembled multilayers containing azobenzene dyes.* Handbook of Polyelectrolytes and Their Applications, 2002. **1**: p. 65-97.

94. Sukhorukov, G.B., *Multilayer hollow microspheres.* Microspheres, Microcapsules & Liposomes, 2002. **5**(Dendrimers, Assemblies, Nanocomposites): p. 111-147.

95. Zhang, X., T. Wu, J. Sun, and J. Shen, *Ways for fabricating stable layer-by-layer self-assemblies: combined ionic self-assembly and post chemical reaction.* Colloids and Surfaces, A: Physicochemical and Engineering Aspects, 2002. **198-200**: p. 439-442.

96. Cooper, W.J., R.D. Curry, and K.E., *Environmental Applications of Ionizing Radiation.* 1998: Wiley-Interscience.

97. Merrill, E.W., K.A. Dennison, and C. Sung, *Partitioning and Diffusion of Solutes in Hydrogels of Poly(Ethylene Oxide).* Biomaterials, 1993. **14**(15): p. 1117-1126.

98. Stringer, J.L. and N.A. Peppas, *Diffusion of small molecular weight drugs in radiation- crosslinked poly(ethylene oxide) hydrogels.* Journal of Controlled Release, 1996. **42**(2): p. 195-202.

Chapter 2

Rigid, Superparamagnetic Chains of Permanently-Linked Beads Coated with Magnetic Nanoparticles

2.1 Introduction

Single domain magnetic nanoparticles have unique size dependent properties that are not exhibited in the bulk material state. Their colloidal suspensions in a dispersion medium are generally quite stable, and the nanoparticles do not settle under gravitational and moderate magnetic fields due to their small size (~10 nm) and do not aggregate because of their surface coatings [1]. These magnetic fluids, as they are commonly known, are superparamagnetic in that the individual dipoles align under an applied magnetic field, exhibiting magnetizations similar to those of the bulk magnetic material, but, in contrast to bulk materials, these suspensions exhibit no remanence (i.e., residual magnetization) once the field is removed as the dipoles are quickly dispersed by Brownian diffusion and Nèel relaxation phemomena. The magnetic interaction between magnetic nanoparticles in a dilute solution, even when they are aligned under an externally-applied magnetic field, is usually negligible, on the order of that of thermal energy (k_BT) at room temperature [2-6] so that Brownian diffusion can disrupt any dipole-dipole interactions that could otherwise lead to the formation of chains of these nanoparticles. Thus, while these suspensions have been used as sealants, refrigerants, biosensors, etc. [7], they cannot be used in applications where large-scale structuring and ordering of the particles is required, such as in magnetorheology and DNA separations.

Magnetic colloids in which magnetic nanoparticles (usually iron oxide) are distributed in a polystyrene matrix or emulsion [8] (typically 400-800 nm with ~30 wt% magnetic material), on the other hand, are often used as model systems for the study of magnetorheological (MR) fluid behavior [9-12]. Because the magnetic nanoparticles are immobilized within the beads, they can act in concert to provide a significant magnetic moment to the composite colloidal particle. This large magnetic moment under an

applied magnetic field enables bead dipole-dipole interactions to overcome thermal motion, allowing the beads to self-assemble into stable chains. The properties of these chains have been the subject of many MR-related and other studies under various shear and field conditions. The beads reflect the intrinsic properties of the embedded nanoparticles in that they are superparamagnetic, owing to Nèel relaxation of the magnetic dipoles in the individual nanoparticles, and the beads do not retain their magnetizations once the magnetic field is removed. Thus, the dipole-dipole interactions sustaining the chain formation are lost on removal of the field, and the colloidal particles return to their freely dispersed state through Brownian motion, reversing the aggregation.

In some cases, it may be desirable to preserve the chain structure once the field is removed, and it has been shown that these magnetically-driven self-assembled structures can be linked by polymers or other linkages [13, 14] to form *flexible* chains of permanently linked superparamagnetic beads which may have unique applications in their own right, based upon their rheological properties in suspension under different shear and magnetic field conditions. Such chains have been used, for instance, as probes of MR fluid behavior, [13, 14] as micromechanical sensors [15] and in DNA and other bio-separation processes that use rigid obstacles (e.g., columns of aligned magnetic particles) to impede the convective transport of biological species [16].

We have developed an inexpensive and versatile technique to produce *rigid* magnetic chains with peapod-like morphology on a relatively large scale. The magnetic particles used to form these chains are polystyrene (PS) beads coated with polyelectrolyte layers and maghemite (γ-Fe$_2$O$_3$) nanoparticles [17]. Sol-gel chemistry is used to link the polarizable particles permanently, once they have been aligned within a microchannel by an external magnetic field, to yield rigid superparamagnetic chains as a new class of magnetoresponsive materials. The magnetic properties of the beads, and hence those of the chains, can be controlled by varying the magnetic shell thickness. The extra strength imparted by the bonding material (titania in this work) ensures that the permanently linked rigid magnetic chains will be much stronger than those formed from free particles in suspension under a magnetic field, and should be more robust in applications requiring high shear or energy absorption rates. Hollow chains can be formed either by dissolution

of the PS beads using solvents, or during calcination of the chains themselves once they are formed. In addition to bonding the linked chains permanently, the titania coating can, in principle, be exploited in a range of other applications that include photocatalysis, sensor technology, and antimicrobial resistance. These rigid magnetic rods can also have potential microfluidic applications, for example, as microstirrers, microvalves and micropumps [18, 19]. An important consideration in these cases is the dynamic response of the rigid superparamagnetic microchains to externally applied magnetic fields; we analyze these effects theoretically to provide simple analytical solutions for the characteristic response times in terms of particle morphology and magnetic properties, and applied field strength, with predictions that compare favorably with experimental results.

2.2 Experimental

2.2.1 Materials

Titanium (IV) isopropoxide (99 wt%, TIP), poly(vinylpyrrolidone) (PVP, MW 150,000), anhydrous ethanol, poly (diallydimethyl) ammonium chloride (PDAMAC, MW 150,000), polystyrene sulfonate (PSS, MW 70,000), sodium chloride (NaCl), iron(III) chloride hexahydrate ($FeCl_3.6H_2O$, 97 wt%), iron(II) chloride tetrahydrate ($FeCl_2.4H_2O$ 99 wt%), sodium hydroxide pellets (NaOH, 99.99 wt% in water) and nitric acid (HNO_3, 70% in water) were obtained from Aldrich (Milwaukee, WI). All chemicals were used as received.

Teflon spacers and neodymium-boron-iron magnets (200 mT) were purchased from McMaster Carr. Poly(dimethylsiloxane) kit (Sylgard 184) was obtained from Dow Corning Company, MI. Micro glass tubes were procured from VitroCom, NJ. Sulfonated PS beads (average diameter 790 ± 19 nm) were purchased from Spherotech, IL.

2.2.2 Synthesis of Permanently Linked Chains

Figure 1 outlines the procedure for making the rigid magnetic chains. Positively charged superparamagnetic PS beads were prepared using a layer-by-layer (LbL) strategy

as described by Caruso et al [20, 21]. The surface charge was modified by coating the negatively charged bead alternately with layers of cationic (PDAMAC) and anionic (PSS) polyelectrolytes, with the final layer being PDAMAC. The resulting positively charged PS beads were then coated with negatively charged maghemite nanoparticles (γ-Fe_2O_3) and again with PDAMAC to yield positively charged *magnetic* beads. These beads were resuspended in anhydrous ethanol, mixed with PVP and TIP, and injected into a microchannel in which they were aligned upon the application of an external magnetic field. The titania resulting from the hydrolysis of TIP nucleated preferentially on the surface of the beads. This cemented the beads together and ensured that they retained the chain configuration even after removal of the magnetic field, thereby yielding permanently linked rigid magnetically susceptible chains.
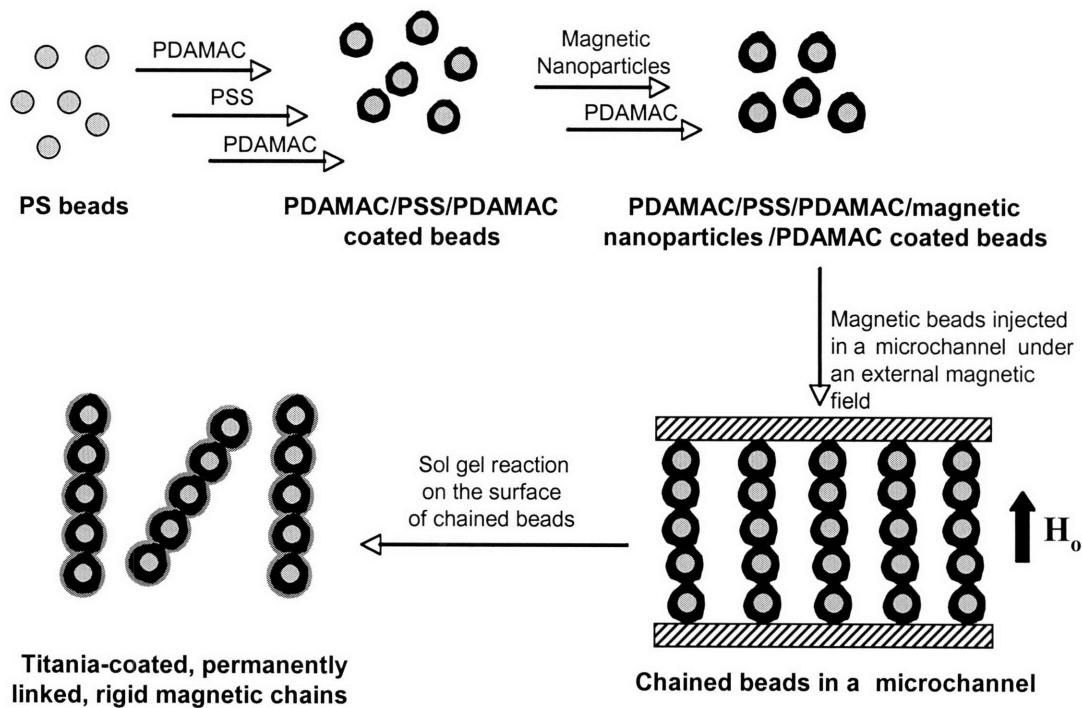
Figure 2-1. Production of permanently linked rigid magnetic chains. Polystyrene beads coated with polyelectrolytes and magnetic nanoparticles using the layer-by-layer approach are aligned in a microchannel under an applied magnetic field and cemented together through hydrolysis of sol-gel precursors in the polyelectrolye layer.

Positively charged PS beads: Commercially available negatively charged sulfonated PS beads (790 nm) were made positively charged using a layer-by-layer polyelectrolyte adsorption technique [20, 21]. In a typical process, 0.5 mL of a 0.5 wt% solution of PS beads was suspended in an aqueous solution of 0.5 mL of 1 mg/mL PDAMAC (0.5 M NaCl). After 30 min of adsorption, the beads were separated by centrifugation at 7000g for 10 min and resuspended in water. This process was repeated three times. The beads were then coated with a negatively charged polyelectrolyte by suspending them in a 1 mg/mL PSS (0.5 M NaCl) solution using the process outlined above. These negatively charged PS beads were finally coated with a second layer of PDAMAC to obtain positively charged particles.

Synthesis of magnetic nanoparticles: Citrate-coated magnetic nanoparticles with an average diameter of 10 nm (as estimated by TEM) were synthesized using Massart's method [22]. In brief, a 2:1 molar mixture of $FeCl3.6H2O$ and $FeCl2.4H2O$ was precipitated in the presence of 0.75M NaOH at 100°C. The black precipitate was decanted magnetically and after washing with 1M $HNO3$ was dispersed in deionized water and heated to 90°C, following which sodium citrate was added. The resulting stable magnetic fluid was reprecipitated by addition of excess acetone, separated magnetically, and redispersed in deionized water. This stable dispersion was centrifuged at 18000 rpm for 3hr to remove excess citrate ions. The resulting precipitate after centrifugation was finally suspended in deionized water to yield stable magnetic fluid.

Adsorption of magnetic nanoparticles on PS beads: The aqueous solution of magnetic nanoparticles (150 μL, concentration 0.005 wt% in water) was added to the positively charged PDAMAC/PSS/PDAMAC coated PS beads (1 mL, concentration 0.25 wt% in water). After continuous shaking for 30 min, maghemite-coated PS beads were recovered by centrifugation at 7000g for 10 min. They were again coated with PDAMAC using the procedure outlined above to yield positively charged magnetic beads. These beads were then centrifuged and washed with anhydrous ethanol four times and finally resuspended in anhydrous ethanol.

2.2.3 Microchannels

Three different types of microchannel were used to confine the chains during the synthesis of the rigid rods. In the first instance, the microchannel was prepared using two glass microslides separated by a teflon spacer (25 μm x 50 mm x 25 mm). In principle, the chain length can be controlled by varying the thickness of the spacer. The chains were recovered by disassembling the microchannel and washing the glass slides; it was necessary to assemble new microchannels for each batch.

In the second approach, PDMS microchannels were cast from a silicon master. The PDMS prepolymer and the curing agent were mixed in a ratio of 10:1 and were degassed under a vacuum of 15 mm of Hg for 45 mins. The mix was poured onto the silicon master and cured at 65 °C for 4 hrs. This resulted in a replica of the channel on the PDMS surface. The channel on the PDMS substrate and a glass slide were O_2 plasma treated and bonded permanently to yield a closed microchannel with a height of 50 μm and a width of 2 mm. Needles were punched in the PDMS to serve as inlet and outlet connections, as shown in Figure 2(a). The reactant mixture was injected through the inlet port. A thin layer of epoxy was applied on the top surface of the channel to prevent evaporation from the reaction mixture.

Commercially available glass microcells with dimensions ranging from 20 μm to 50 μm, and with an aspect ratio of 1:10, were used for the microchannels in the third approach. Ten to twenty microcells were collected together to form an assemblage of cells, each end of which was inserted into a tygon tube and epoxy-sealed around the periphery to provide a common inlet and outlet for all the microcells. This assembly was then epoxy-sealed on a glass slide for ease of handling (Figure 2b,c).
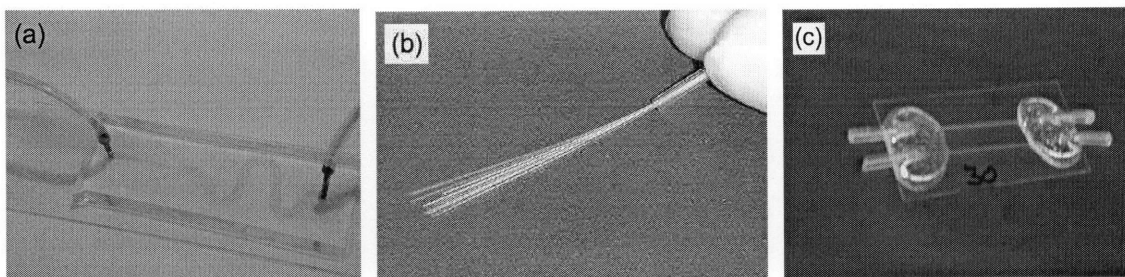
Figure 2-2. (a) A PDMS microchannel with inlet and outlet ports. The channel is 2 mm wide and 50 μm in height. The serpentine nature of the channel accommodates larger channel volume on a single glass slide. The colored dye was added for better contrast to highlight the channel geometry. **(b)** A bundle of glass microcells collected in a tube and **(c)** glued on to a glass slide with epoxy. This enables scaling out and makes the large scale production of rigid chains feasible.

2.2.4 Linking of magnetic beads

In a typical reaction, a mixture of 0.5 mL (10 mg/mL) of PDAMAC-coated magnetic PS beads in anhydrous ethanol, 3 μL of TIP and 5 mg of PVP were injected into a microchannel. Two neodymium-boron-iron magnets of 200 mT each were placed on opposite faces of the microchannel to provide a uniform magnetic field across the channel. The reaction proceeded for 24 h under the applied magnetic field in an ethanol-saturated chamber to prevent evaporation of ethanol from the microchannel reaction mixture. The chains were recovered by washing with ethanol in the case of glass slides or by flowing 2 ml of fresh ethanol into the channel for PDMS and glass microcells. In the latter case a fresh reactant mixture was injected into the microchannel after the recovery of the chains, and the process was repeated.

2.2.5 Hollow Chains

When desired the permanently linked magnetic chains were calcined at 500 °C during which the PS beads and PE layers burned off to yield magnetic chains that consisted of hollow spherical cores linked together by titania coating. For calcinations, samples were first dried in a refractive crucible in a furnace, heated to 500 °C at a rate of 5 °C /min, held at 500 °C for 8 h, and then cooled to room temperature at a rate of 5 °C /min.

In a second approach, the composite hollow magnetic shells were obtained by suspending the magnetic beads in tetrahydrofuran for 8 hrs to dissolve the PS core leaving the PE layers still intact. These hollow magnetic shells were then aligned in a microchannel and linked together with titania to yield permanently linked composite hollow magnetic chains.

2.2.6 Characterization

Transmission Electron Microscopy (TEM, JEOL 200CX, 200kV) and Scanning Electron Microscopy (SEM, JEOL-6060SEM) were used to visualize the beads and chains. TEM samples were prepared by drying a drop of suspension on a carbon substrate grid while for SEM the sample was dried on a carbon tape grid. Zeta potentials of the samples were measured in water (MilliQ, conductivity 18 MΩ) using a Brookhaven ZetaPals zeta potential meter. The concentration of water on the bead surface was measured using Karl Fischer Titration (Mettler Toledo DL31). A 0.5 wt% bead suspension in anhydrous ethanol was centrifuged and the concentration of water in the supernatant and in the centrifuged beads was measured to determine the partition coefficient. The magnetization of the sample was obtained using a vibrating sample magnetometer (ADE 880 VSM). The dynamic response of the chains to an applied field was measured by placing the microchannel containing the rigid chains in the center of a Helmoltz coil. The response was observed with an optical microscope (Zeiss, Axiovert 200) using 20X/1.0 objective. The chain response was captured with a digital camera (Hitachi, KPM1A) with a speed of 30 frames/sec using Scion Image (NIH public domain software) which was also used for image analysis.

2.3   Results and Discussion

2.3.1 Magnetic Beads

Magnetically-responsive beads were synthesized using the layer-by-layer technique in which the polystyrene beads were coated sequentially with positively and negatively charged polyelectrolytes, and magnetic nanoparticles. The effective sequential coating of the beads was monitored by the reversal of surface charge as each

polyelectrolyte layer was added, as determined by zeta (ζ) potential measurements, while complete coverage of the PS beads with magnetic nanoparticles was confirmed using SEM. The thickness of the maghemite coating, estimated by comparing the SEM images of bare and completely coated beads (Figure 3) to be 25 nm, was comparable with the maghemite thickness calculated (27 nm) based on the relative amounts of PS beads and magnetic nanoparticles added.
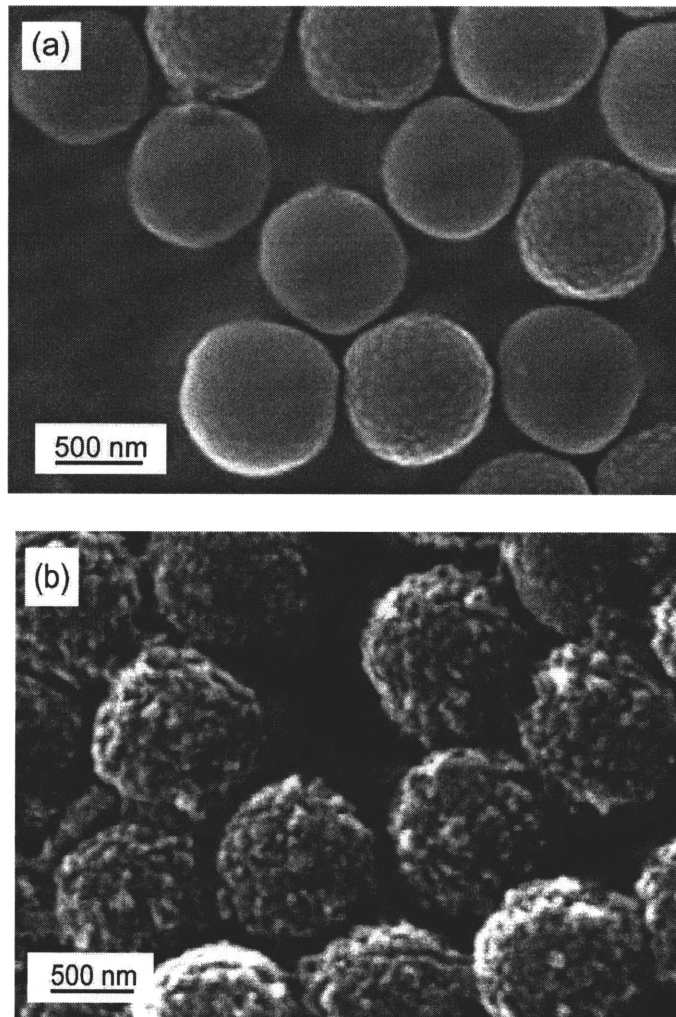
Figure 2-3. SEM micrograph of (a) plain PS beads and (b) magnetic nanoparticle-coated beads. The samples were sputter coated with gold for better contrast. The thickness of the magnetic coating was estimated to be 25 nm based on the difference in the diameters of the coated and the uncoated beads.

The magnetization of the positively charged magnetite beads, as determined using VSM, is shown in Figure 4 as a function of applied field strength. The lack of any remanence indicates that the particles are superparamagnetic in nature. This

superparamagnetic property of the beads, which are well-dispersed as individual particles in the absence of an applied magnetic field, enables their reversible aggregation as chains under an applied magnetic field. The slope of the magnetization curve M/H at H → 0 gives the value of the magnetic susceptibility (χ) of the bead which was estimated to be 3.3 for the magnetic material coating the beads. The saturation magnetization of the beads was found to be 238 A/m which is lower than the accepted value of 357 A/m for bulk maghemite. Since the average particle size is smaller than 10 nm this could be due to the surface spin canting that exists for small magnetic nanoparticles [23].
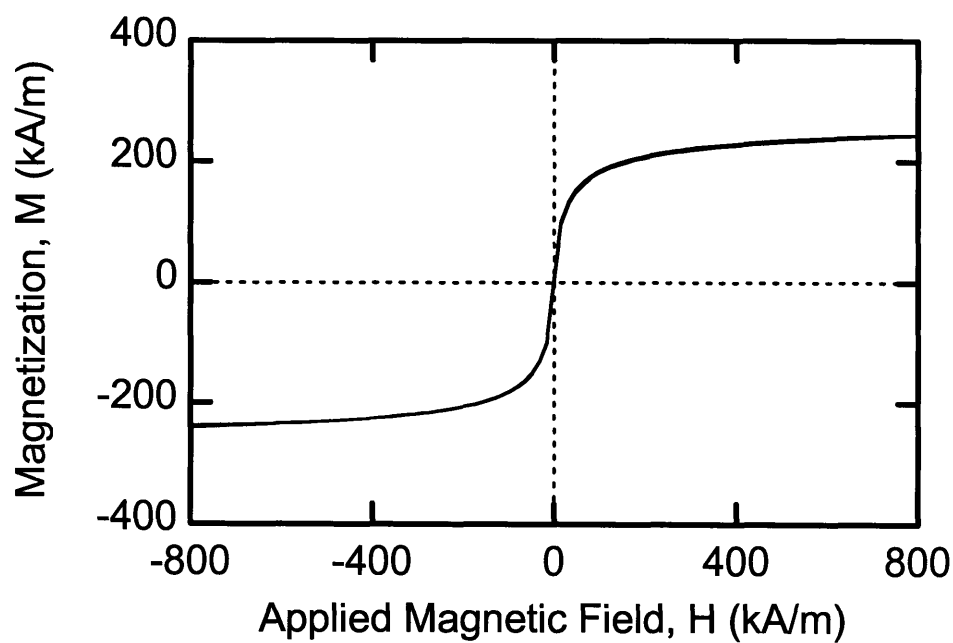
Figure 2-4. The magnetization curve for the magnetic beads shows no hysteresis; the forward and backward magnetization curves overlap completely and are indistiguishable. The beads have zero magnetization at zero applied field indicating that they are superparamagnetic in nature.

2.3.2 Microchannels

The microchannels prepared from glass slides separated with teflon spacers yielded a polydisperse chain length distribution, probably because the channel height was not uniform across the channel. Also, the total number of rigid chains that could be produced using these microchannels was very low and it is not feasible to scale up this process. These problems were overcome using PDMS channels, which have uniform

height and can be used on a semi-continuous basis. A drawback of the PDMS channel was that ethanol wicked away from the reactant mixture causing both the PDMS to swell when the reaction was run for a long time, and a localized drying in the channel with subsequent adhesion of the chains to the glass surface. To avoid this, the reaction had to be terminated after 4 hrs. Some chains were observed, but the incorporation of beads in the chains was incomplete. The chain length distribution was, however, comparatively monodisperse (Figure 5). Recovery of chains by flowing excess ethanol through the microchannel was difficult, as some breakage of these chains occurred at the outlet port junction where the needle was flush with the glass, which required the chains to bend around the corner. Another disadvantage of this process is the tedious procedure used to construct the microchannel itself.

None of the above-mentioned problems was observed when glass microcells were used as microchannels. No evaporation losses occurred, as glass is impermeable to ethanol, and relatively monodisperse chain length distributions were obtained (Figure 6). Chain breakage was reduced considerably since the direction of the ethanol flow during the recovery was in the plane of the channel. The glass microcells could be assembled and scaled out easily thereby making the relatively large-scale production of these chains on a continuous basis feasible.
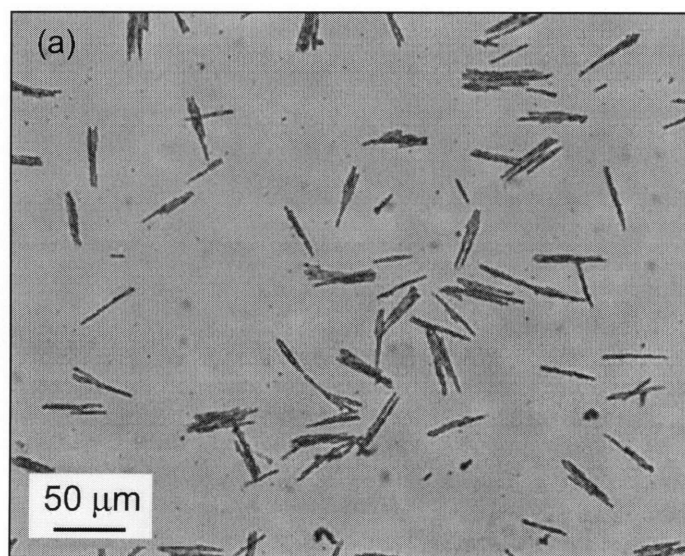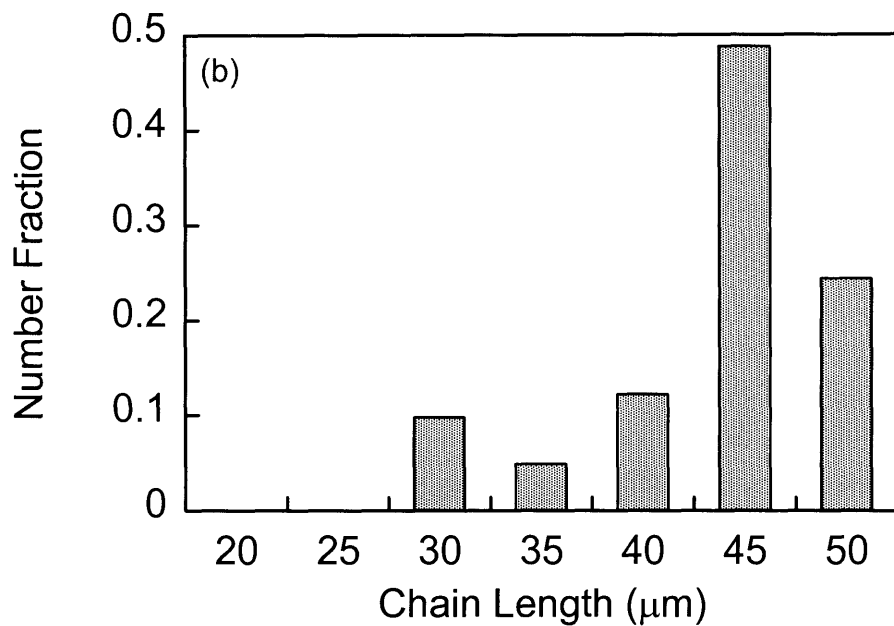
Figure 2-5. (a) Optical micrograph of chains synthesized in a PDMS microchannel. The reaction was terminated after 4 hr. (b) The chain length has a narrow distribution with an average length of 43.6 μm ± 5.9 μm.
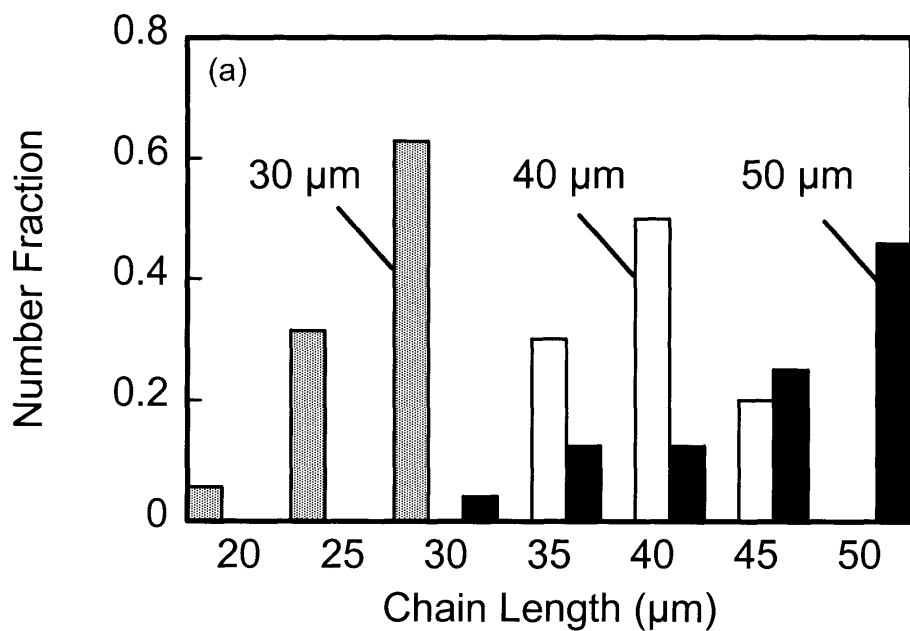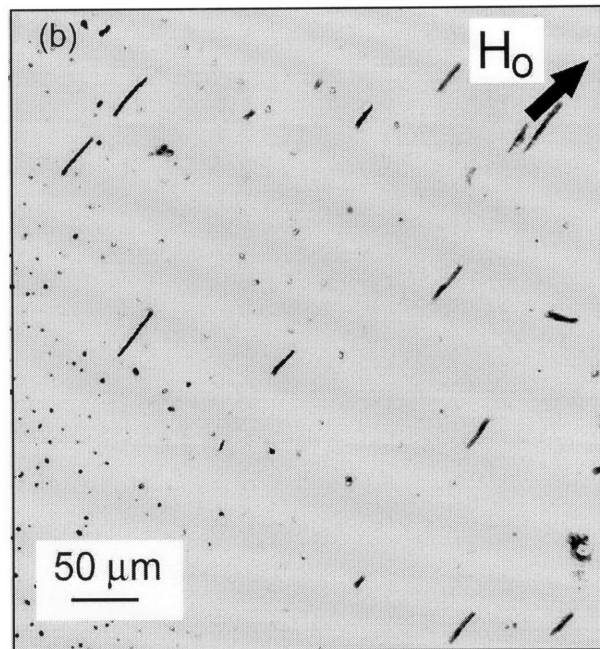
Figure 2-6. (a) The size distributions of chains synthesized in 30 μm x 300 μm, 40 μm x 400 μm and 50 μm x 500 μm glass microcells, with average lengths of 27 μm $\pm$ 3 μm, 40 μm $\pm$ 4.5 μm and 44.7 μm $\pm$ 6 μm respectively. (b) The optical micrograph shows the chains aligning with an external magnetic field.

2.3.3 Permanently Linked Chains

The outer PDAMAC layer on the magnetic PS beads was highly hygroscopic and retained some of its water of hydration even when suspended in anhydrous ethanol; the partition coefficient for water between the bead surface and the bulk ethanol was measured by Karl Fischer titration to be ~60. This localized concentration of water on the outer PDAMAC layer ensured preferential hydrolysis of TIP on the bead surface. A small degree of hydrolysis was observed in the bulk due to the low concentration of water in the solvent, but this did not affect the properties of the chains formed during this process. Titania is negatively charged at neutral pH [24], and the positive charge on the magnetic beads from the outermost PDAMAC layer ensured that the nucleated titania was captured efficiently by the particle surface. The charge on the bead surface reversed from positive to negative as the adsorption of titania continued. During this process of charge reversal, some of the beads acquired a negative charge, while others were still positively charged. The aggregation of such oppositely charged beads, which inhibited the formation of chains, was prevented by adding PVP to the suspension, which adsorbed on both titania

56

particles and the magnetic bead surfaces to impart a steric stabilization against bead aggregation [25]. At the end of the reaction, permanently linked rigid magnetic chains were formed which were stable and could be recovered and stored for months without degradation.

Transmission electron microscopy (JEOL 200CX, 200kV) indicated a titania coating thickness of 30 nm (Figure 7), that was close to the thickness (32 nm) calculated based on the concentrations of TIP and PS beads used in the experiments indicating that very little, if any, TIP was lost to hydrolysis in the bulk.
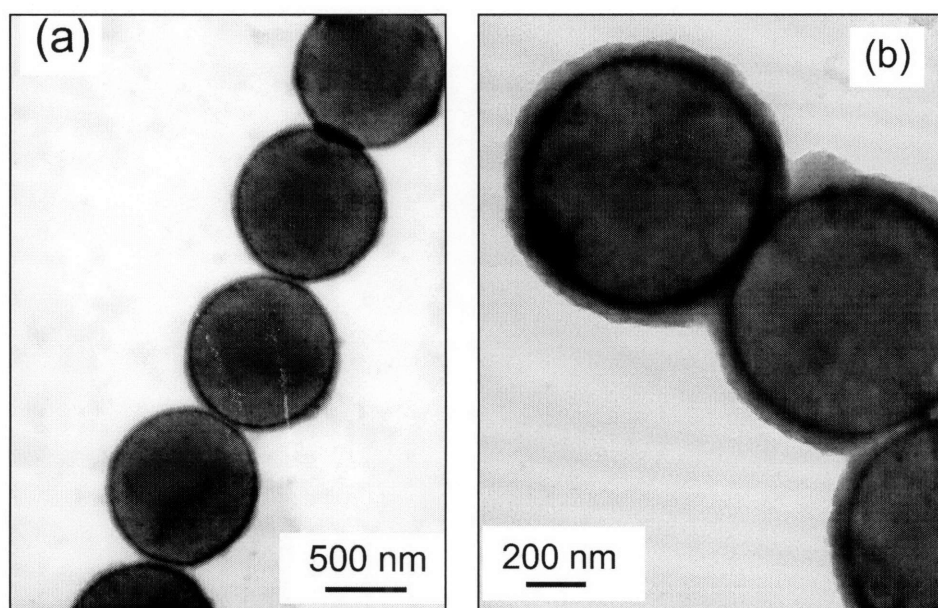
Figure 2-7. TEM micrographs of titania–coated magnetic chains. (a) Alignment of beads in the chain. (b) The magnetite and titania coating layers are clearly evident, allowing the thickness of the titania coating to be estimated as approximately 30 nm.

Column-like structures, where two or more chains of magnetic beads were fused together, were also observed (Figure 8) and attributed to the magnetic dipolar interaction between the individual chains in the presence of a magnetic field. If the adjacent chains are offset by half the particle diameter, the interaction is attractive in nature [26]; with no offset the interaction is repulsive.
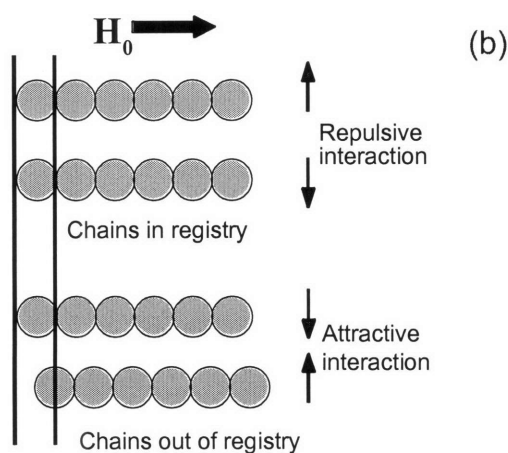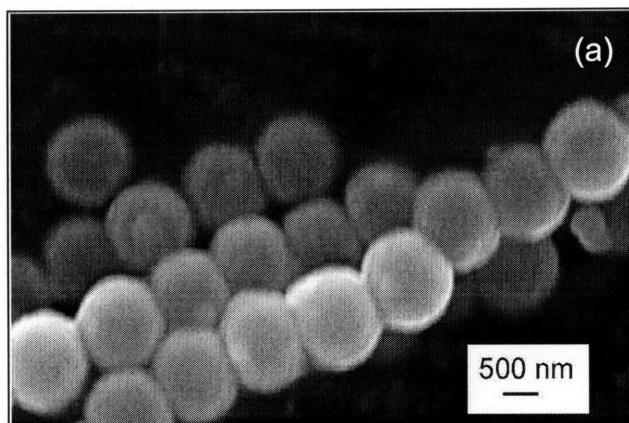
Figure 2-8. (a) SEM micrograph of interacting magnetic chains to form a partial doublet. (b) When two chains are aligned in a magnetic field, the overall interaction is repulsive in nature but when the chains are out of registry by half the diameter, it results in an attractive interaction.

2.3.4 Hollow Chains

Calcination of the permanently linked magnetic chains at 500 °C resulted in hollow chains as shown in Figure 9(a), and a conversion of the amorphous titania to its crystalline anatase form, as confirmed by X-ray diffraction (not shown). The anatase form of titania has a higher mechanical strength and a much wider range of application possibilities [27] than does the amorphous form of this oxide. The magnetization of the chain initially increased with calcination temperature (from 238 kA/m before calcination to 280 kA/m at 500 °C), attributed to an average increase in nanoparticle size due to aggregation during the calcination process [28] (Figure 10). The magnetization

eventually dropped to zero at higher temperatures (at and above the Curie temperature) due to thermal disordering of the magnetic domains in the fused nanoparticle shells.
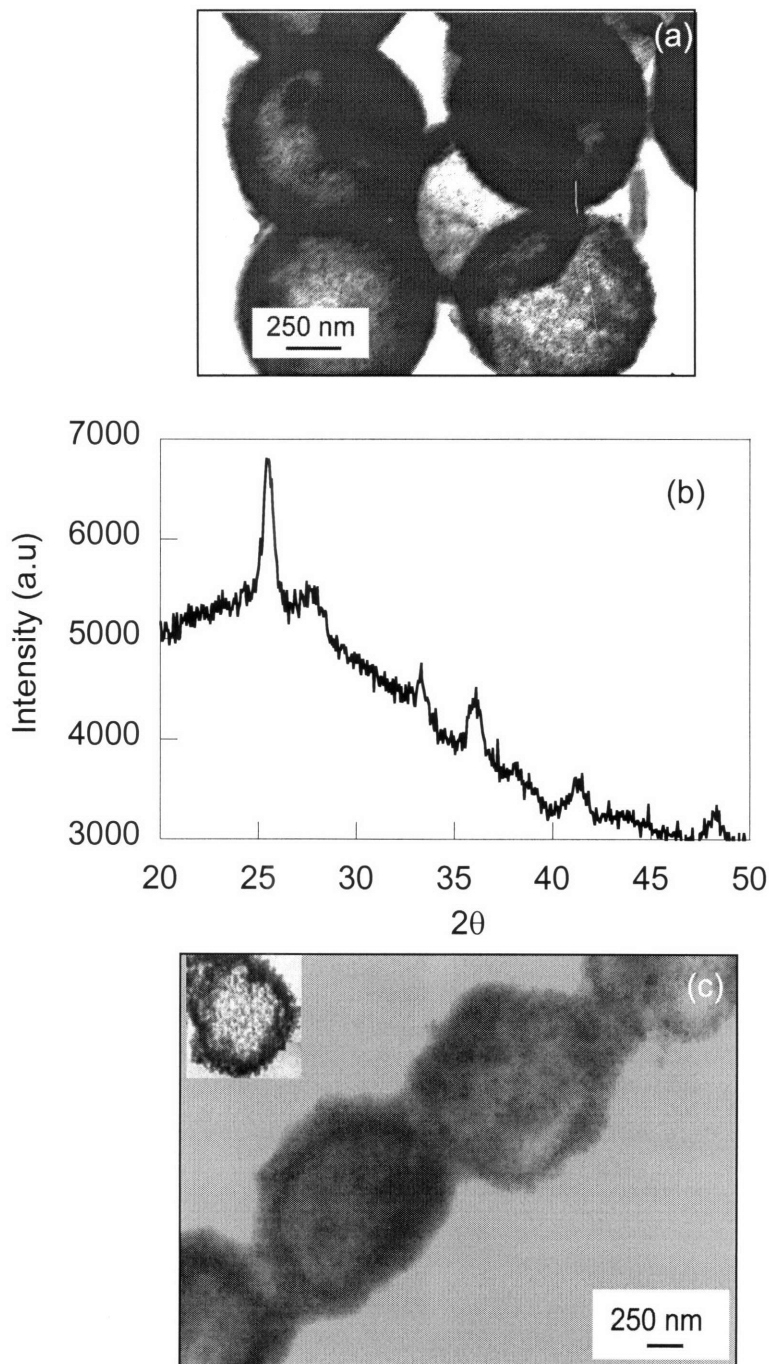
Figure 2-9. (a) TEM micrograph of hollow titania-linked magnetic chains prepared after calcination. The transparency of the beads in the micrograph provides evidence of their hollow structure. (b) XRD diffraction spectrum of the calcined chains confirms the presence of anatase. The peak at 25.369, 38.085, and 48.069 correspond to anatase form of titania. (c) Composite hollow beads, prepared after organic dissolution of the core

(inset micrograph) were used to prepare composite hollow chains. The presence of PE multilayers and a coating of amorphous titania gives the chain its opaque appearance.
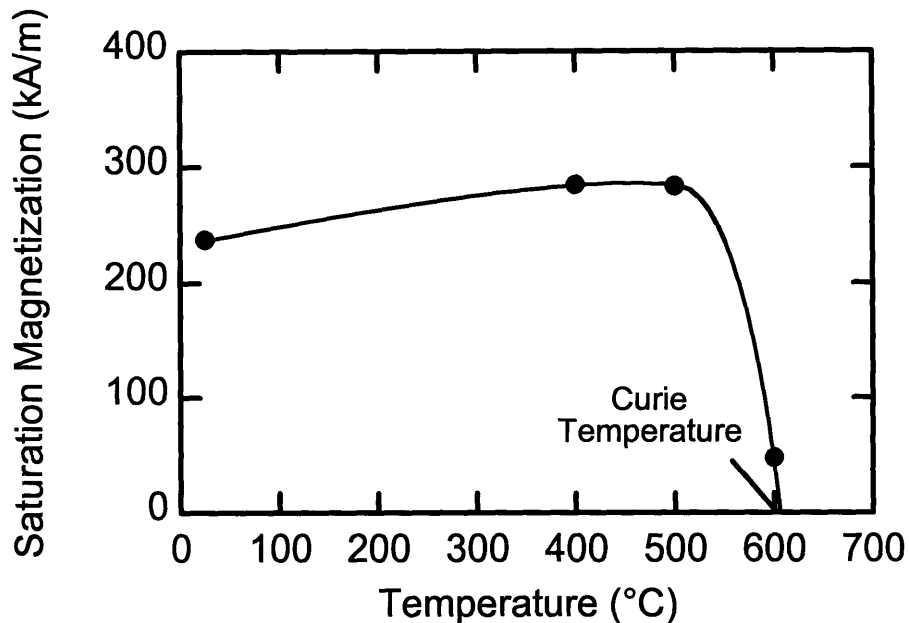
Figure 2-10. Magnetization of the chain as a function of calcination temperature. The magnetization of the calcined chains initially increases with the temperature due to net increase in nanoparticle size on sintering, but approaches zero near the Curie temperature.

The permanently linked composite hollow magnetic chains shown in Figure 9(b) were obtained by aligning and fusing together individual hollow shells in which the PS cores had been dissolved out by the solvent, tetrahydrofuran. These chains were partially distorted since the magnetic nanoparticles were supported only by the flexible PE layers. This type of structural configuration should impart elasticity to these chains, thereby improving the energy absorption capacity of these suspensions when shocked, which could be improved further by using polyelectrolytes with higher elasticity and strength. The saturation magnetization of these chains was the same as that of the original magnetic beads (238 kA/m).

2.4 Kinetic Response to an Applied Magnetic Field

The dynamic response of a magnetic chain to perturbations in applied magnetic fields, or to other forces that cause the rods to be deflected within a steadily applied magnetic field, may be exploited in a number of magnetically actuated micromixing, pumping and sensoric applications, and in microseparations and magnetorheological processes. The characteristic response times to externally applied forces can be estimated using methods similar to those employed to model the response of a magnetorheological (MR) fluid in a rotating magnetic field [29, 30]. We provide a short derivation below to arrive at an explicit analytical expression for the characteristic response time for single chains, and then extend this model to systems composed of clusters of two (doublet) or three (triplet) chains.

Consider a chain of N connected beads, each of radius a, enclosed in a microchannel (Figure 11(a)). Each bead can be approximated as a point dipole with a magnetic moment $\mathbf{m}$ determined by the amount of magnetic material in its shell and the local magnetic field to which it is subjected. When an external magnetic field of magnitude $\mathbf{H}_o$ is applied across the microchannel, a magnetic torque Γ_m acts on the magnetic chain, causing it rotate to try to align with this external magnetic field. The rotation is impeded by a counteracting viscous drag torque Γ_v as the chain moves through the solvent, resulting in a torque balance on the chain, $viz.$,

$$I\frac{d^2\theta}{dt^2} = \Gamma_m + \Gamma_v \tag{1}$$

where I is the moment of inertia around the point of rotation, θ is the angle between the chain and magnetic field, and t denotes time. The overall rotational response time to an applied magnetic field can be estimated once we identify appropriate expressions for the magnetic and drag torques.
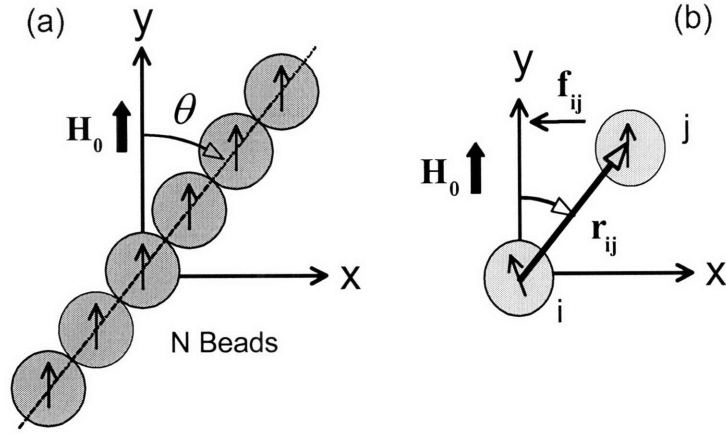
Figure 2-11. (a) A restoring torque acts between two dipoles to align the resulting moment of the beads parallel to the external magnetic field. (b) Schematic of a permanently linked chain (singlet) at an angle θ to the applied magnetic field.

The magnetic torque is generated when the system attempts to align the moment of each bead, **m**, with the external field (Figure 11(b)). The force responsible for the alignment of a pair of connected beads is given by [26]

$$\mathbf{f}_{ij} = \frac{3m^2}{4\pi\mu_0 r_{ij}^4}\left[\mathbf{e}_r\left(1 - 3\cos^2\theta_{ij}\right) - \mathbf{e}_\theta \sin\left(2\theta_{ij}\right)\right] \tag{2}$$

where μ_0 is the magnetic permeability of free space; m is the magnitude of the magnetic moment induced in each bead by the local magnetic field; θ_{ij} is the angle between the external magnetic field $\mathbf{H}_0$ and the vector $\mathbf{r}_{ij}$ (of magnitude r_{ij}) joining the centers of the two dipoles; $\mathbf{e}_r$ is the unit vector parallel to $\mathbf{r}_{ij}$; and $\mathbf{e}_\theta$ is the unit vector parallel to $\mathbf{e}_r \times \left(\mathbf{e}_r \times \mathbf{H}_0\right)$. The magnetic torque acting on the connected bead pair is

$$\Gamma_{m_{ij}} = \mathbf{f}_{ij} \times \mathbf{r}_{ij} \tag{3}$$

The total torque about the center of the chain of N connected beads can be obtained by summing over all connected bead pairs to yield

$$\Gamma_m = \frac{3m^2}{4\pi\mu_0}\sin\left(2\theta\right)\sum_{i=1}^{N/2}2r_i\sum_{\substack{j=-N/2\\j\neq i}}^{N/2}\frac{1}{r_{ij}^4} \qquad (4)$$

where r_i is the coordinate of the ith particle, and it is assumed that all beads have magnetic moments of the same magnitude, m. If only nearest neighbor interactions between magnetic beads are considered, then the magnetic torque on the chain can readily be evaluated to be [31]

$$\Gamma_m = \frac{3m^2L^2}{4\pi\mu_0 2(2a)^5}\sin(2\theta) \qquad (5)$$

where $L=2aN$ is the chain length.

The viscous torque on a chain of length L comprised of N beads rotating at an angular velocity $\omega = d\theta/dt$ was given by Doi and Edwards as [32],

$$\Gamma_v = \frac{-\pi\eta L^3}{3\ln(L/4a)}\omega \qquad (6)$$

where η is the viscosity of the medium through which the chain is rotating, and the minus sign indicates that the viscous torque acts in the direction opposite that of the rotation.

From scaling arguments [29], $I(d^2\theta/dt^2)\sim m_cL^2\omega^2$ where m_c is the mass of the chain and $\Gamma_v\sim\eta L^3\omega$. Thus, the viscous term will dominate when $\omega\ll\eta L/m_c\sim 10^6$ rad/s ($m_c\sim a^2L\rho$, $a\sim 10^{-6}$ m, $\rho\sim 10^3$ kg/m^3, and $L\sim 10^{-5}$ m). Generally $\omega\sim 10$ rad/s, and hence the inertial term can be neglected, and ω can be calculated from equations (4) and (5) for any given value of θ. Combining (4), (5) and (6) and rearranging, we get

$$\omega = \frac{d\theta}{dt} = \frac{9}{4(8\pi)^2}\frac{m^2\ln(L/4a)}{\mu_0\eta La^5}\sin(2\theta). \qquad (7)$$

Integration of this equation will give the time-dependent orientation of the chain relative to the applied magnetic field. Before we can perform this integration, however, we need to determine the magnitude of the bead magnetic moment m as a function of chain orientation relative to the magnetic field.

The induced magnetic dipole moment $\mathbf{m}$ of the bead is given by

$$\mathbf{m} = \mu_o V \mathbf{M} = \mu_o 4\pi a^2 s \chi \mathbf{H}_i \tag{8}$$

where $\mathbf{M}$ is its magnetization under a field $\mathbf{H}_i$, V is the volume of the magnetic material distributed as a thin shell of thickness s on the surface of the bead of radius a, and χ is the magnetic susceptibility of the magnetic materials. The total field $\mathbf{H}_i$ acting on the bead at position i is the sum of the external magnetic field and the local magnetic field at point i induced by the neighboring beads in the chain, i.e.,

$$\mathbf{H}_i = \mathbf{H}_0 + \sum_{j \neq i} \mathbf{H}_j \tag{9}$$

where the field induced by dipole j at position i is

$$\mathbf{H}_j = \frac{1}{4\pi\mu_0} \frac{3\mathbf{r}_{ij}(\mathbf{r}_{ij} \cdot \mathbf{m}_i) - \mathbf{m}_j}{r_{ij}^3} \tag{10}$$

If only nearest neighbor interactions are allowed between beads with center-to-center separation distances of $r_{ij} = 2a$, and if the magnetic moments are the same for all beads in the chain (i.e., $\mathbf{m}_i = \mathbf{m}_j = \mathbf{m}$), then the radial and angular components of $\mathbf{m}$ are readily evaluated to be [33]

$$m_r = \frac{\mu_o 4\pi a^2 s \chi H_o \cos\theta}{\left[1 - \dfrac{4a^2 s \zeta(3)\chi}{r^3}\right]} \quad \text{and} \quad m_\theta = \frac{\mu_o 4\pi a^2 s \chi H_o \sin\theta}{\left[1 + \dfrac{2a^2 s \zeta(3)\chi}{r^3}\right]} \tag{11}$$

64

respectively, where $\zeta(\bullet)$ is the Riemann zeta function ($\zeta(3) \sim 1.202$). These results show that as a direct consequence of the induced fields, the dipoles are not aligned completely in the direction of the applied field [33].

Noting that $m^2 = m_r^2 + m_\theta^2$ can now be evaluated explicitly as a function of θ, Equation (7) can be rewritten in dimensionless form as

$$\frac{d\theta}{d(t/\tau)} = \frac{\ln(N/2)}{(N/2)} \frac{\phi^2}{(1-2\phi)^2} \left(1 - \frac{3\phi(2-\phi)}{(1+\phi)^2} \sin^2\theta\right) \sin(2\theta) \qquad (12)$$

where $\tau = \dfrac{4\zeta^2(3)\eta}{9\mu_0 H_0^2}$ is a characteristic time constant, and $\phi = \dfrac{\zeta(3)\chi s}{4a}$ is an effective

magnetic susceptibility for the magnetic nanoparticle-covered beads. This equation can be integrated to give the angle θ implicitly as a function of time, for a given initial angle θ_0,

$$\frac{t}{\tau} = \frac{(N/2)}{4\ln(N/2)} \left(\frac{1+\phi}{\phi}\right)^2 \left\{\ln\left(\frac{\tan\theta}{\tan\theta_0}\right)^2 + \frac{3\phi(2-\phi)}{(1+\phi)^2} \ln\left(2\left[\frac{\csc^2\theta - \dfrac{3\phi(2-\phi)}{(1+\phi)^2}}{\csc^2\theta_0 - \dfrac{3\phi(2-\phi)}{(1+\phi)^2}}\right]\right)\right\} \qquad (13)$$

If the initial angle θ_0 is $\pi/2$, i.e., if the rod is initially in the plane perpendicular to the direction of the applied magnetic field, the magnetic dipoles are aligned with the magnetic field, and the there is no magnetic torque on the rod. Thus the rod will not move and the predicted response time is infinite. Similarly, the torque on the rod will tend to zero as it approaches complete alignment with the field, i.e., when the final angle θ_f approaches 0, and it takes infinite time to approach complete alignment. In reality, however, θ_0 and θ_f are never identically equal to these values because the rod will fluctuate about these equilibrium angles owing to thermal motion, and because the beads themselves may be slightly out of alignment in the rod (see Figure 7(a)), such that even at $\theta = 0$ or $\pi/2$, there is a finite torque on the rod under an applied magnetic field. If we

assume that the effective mean displacements from the initial (θ_0) and final (θ_f) orientations due either to thermal fluctuations at time $t = 0$ or to bead misalignment, or both, are small but non-zero then Equation (13) can be simplified to give the total response time, t_f, for the rod. Thus, setting $\theta_0 = \pi/2 \pm <\theta>_0$ and $\theta_f = \pm <\theta>_0$, we obtain

$$\frac{t_f}{\tau} = \frac{(N/2)}{\ln(N/2)} \frac{3(2-\phi)}{4\phi} \left\{ \ln\left(2\left[\frac{1+\phi}{1-2\phi}\right]^2 \right) + \left(\frac{4(1+\phi)^2}{3\phi(2-\phi)} - 2 \right) \ln <\theta>_0 \right\} \tag{14}$$

where we have used the fact that $<\theta>_0$ is small to linearize the trigonometric functions, and have recognized that $\left| \frac{3\phi(2-\phi)}{(1+\phi)^2} \right| <\theta>_0^2 \leq 3 <\theta>_0^2 \ll 1$. Thus, the normalized response time can be evaluated explicitly knowing the chain length and the effective magnetic susceptibility of the coated beads, for given initial and final effective displacements of $<\theta>_0$ relative to their nominal values of $\pi/2$ and 0, respectively. When the initial alignment of the rod is not perpendicular to the applied magnetic field, then a finite value of θ_0 can be specified, and the effective response time can be calculated directly using Equation (15).

When two chains are fused together (doublets), an analytical solution for the moment calculation is not possible and the system of equations above needs to be solved numerically. To do so, the center of each bead in the doublet is determined explicitly in the x-y coordinate system (Figure 12) such that the center i^{th} bead of chain 1 is fixed at the origin, and the coordinates of all the other beads in chain 1 and chain 2 are defined with respect to it. The x and y coordinates of chain 1 in a polar coordinate system are

$$x(i) = 2ai \sin(\theta); \quad y(i) = 2ai \cos(\theta) \qquad 0 \leq i \leq N/2 \tag{15}$$

By using standard trigonometric relations the x and y coordinates for chain 2 can be written as follows

66

$$x(j) = b_j \sin(\beta); \quad y(j) = b_j \cos(\beta);$$

$$b_j = (2a)^2 + (2aj)^2 - 2j(2a)^2 \cos(2\pi/3); \qquad (16)$$

$$\beta_j = \cos^{-1}\left(\frac{(2a)^2 + b_j^2 - (2aj)^2}{4ab_j}\right) + \theta - \pi/3; \qquad 0 \le j \le N/2$$
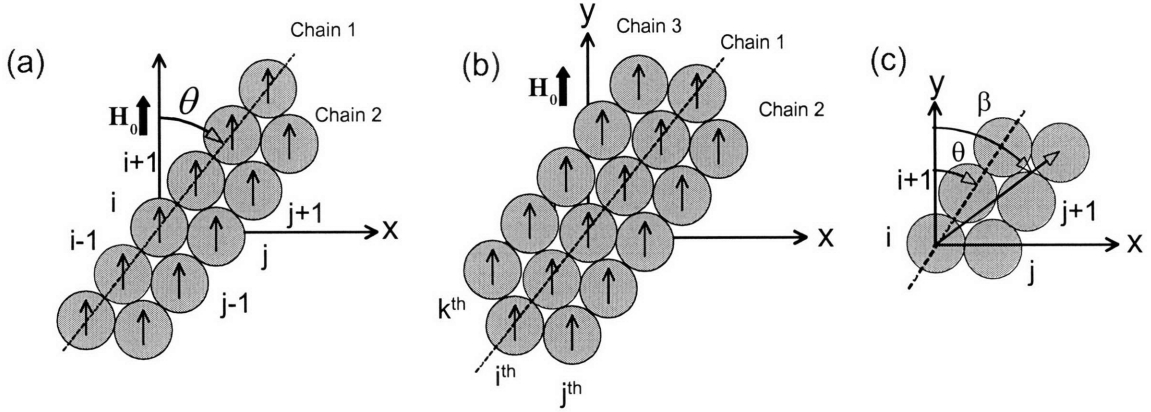
Figure 2-12. Schematic of (a) doublet and (b) triplet chains, and (c) the geometry used for specifying relative positions of beads in such chains.

It should be noted that in a doublet, each bead has four nearest neighbors and this is taken into account when the nearest neighbor interactions are calculated. The above equations can be extended to the triplet clusters due to the symmetry across chain 1(Figure 12b). Again we allow for nearest neighbor interactions only, noting that beads in chain 1 have 6 nearest neighbors while those in chains 2 and 3 have 4 nearest neighbors. For the calculation of viscous drag, the shapes of doublets and triplets are approximated as solid ellipsoids with long semi axis d, short semi axis e and volume V, for which the viscous drag torque is [34]

$$\Gamma_v = \frac{4(d/e)^2 \eta \, V\omega}{2\ln(d/e) - 1} \qquad (17)$$

With these equations and coordinates, Equations (8), (9) and (10) were solved numerically to determine the magnetic moments of the beads in the chain. Equations (4)

and (17) can be solved numerically to provide the angle of the rod relative to the applied magnetic field as a function of time.

The time-dependent orientation of a 45 μm chain in response to an externally-applied magnetic field is shown in a series of snapshots in Figure 13(a). Such results were used to evaluate the angular displacement and angular velocities of the chain as a function of time, as well as the total response time for the chain to align with the applied magnetic field. The predicted angular velocity for different chain configurations (singlets, doublets and triplets) shown as a function of θ in Figure 13(b) attains a maximum at θ close to 45°, where $\sin(2\theta) = 1$; there is a slight but relatively unimportant displacement from 45° in the maximum because the orientation of the magnetic dipoles is slightly different from the direction of the applied magnetic field. The magnetic dipoles are, in fact, aligned with the magnetic field only when $\theta = 0$ and $\theta = \pi/2$, and at these orientations the chain experiences no magnetic torque whatsoever. Note that the doublets and triplets respond more quickly to the applied magnetic field than do the singlets, reflecting the effect on the magnetic torque of the larger total magnetic material content per unit chain length in the bundled chains relative to the single chains. The increase in viscous drag on the bundled chains, which scales with bundle projected area, cannot counteract totally the increase in the magnetic forces acting on the chains, which scale with volume.

The predicted variation in the orientation of the chain, i.e., in θ, with time following the application of the magnetic field is shown in Figure 13(c) for various values of the effective magnetic susceptibility, ϕ. Experimental values for selected chains of three different lengths are in very good agreement with the *a priori* predictions for our core-shell beads, which have an effective magnetic susceptibility of approximately 0.06. These results reflect the angular dependence of the rotation rate given in Figure 13(b) – the initial changes with time are small, but then increase rapidly at intermediate chain orientation angles before slowing down again as the chain begins to align with magnetic field, i.e., θ approaches zero. Clearly, and as expected, the magnetic susceptibility has a strong effect on the response to the magnetic field, with a significant displacement of the curves to smaller times with increasing ϕ. These time response

curves were based on the assumption that $<\theta>_0 = 0.02$ rad; for other values of the initial angular displacement the curves will be shifted to the left (larger $<\theta>_0$) or right (smaller $<\theta>_0$), but the overall shapes of the curves will be preserved, albeit with some slight distortions depending on the value of ϕ.

The importance of the effective magnetic susceptibility, ϕ, chain length, N, and initial angular displacement, $<\theta>_0$, on the normalized total response time is shown in Figure 13(d). The solid lines represent the response times for $<\theta>_0 = 0.02$ rad, while the broken lines bracketing the curve for $N = 50$ show the sensitivity of the response time calculations to $<\theta>_0$. As anticipated, the response time decreases with increasing ϕ, and increases as the rod length increases. An important observation is that the response time is not particularly sensitive to small variations in the initial angular displacement about some nominal value, and the predictions probably fall well within the experimental tolerances.

(b)

Angular Velocity, ω (rad/s) vs Angular Displacement, θ (deg)

Triplet

Doublet

Singlet

(c)

Angular Displacement, θ (deg) vs Normalized Time, $\dfrac{\ln(N/2)}{(N/2)}\left(\dfrac{t}{\tau}\right)$

0.4 0.3 ϕ 0.2 0.1 0.06

20 µm 30 µm 45 µm

$\langle\theta\rangle_0 = 0.02$ rad
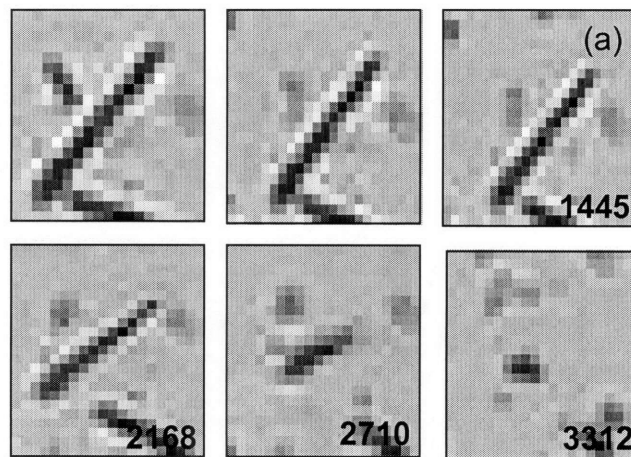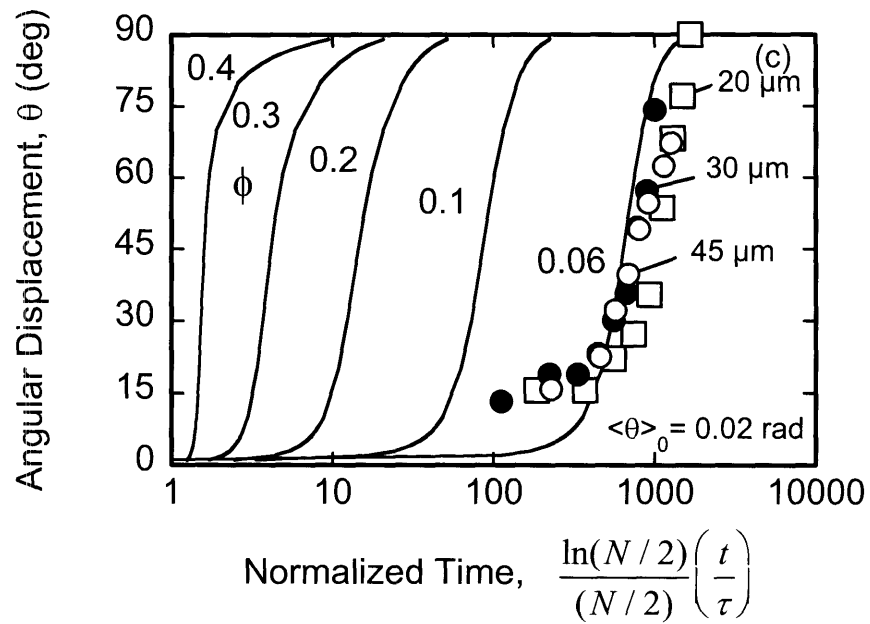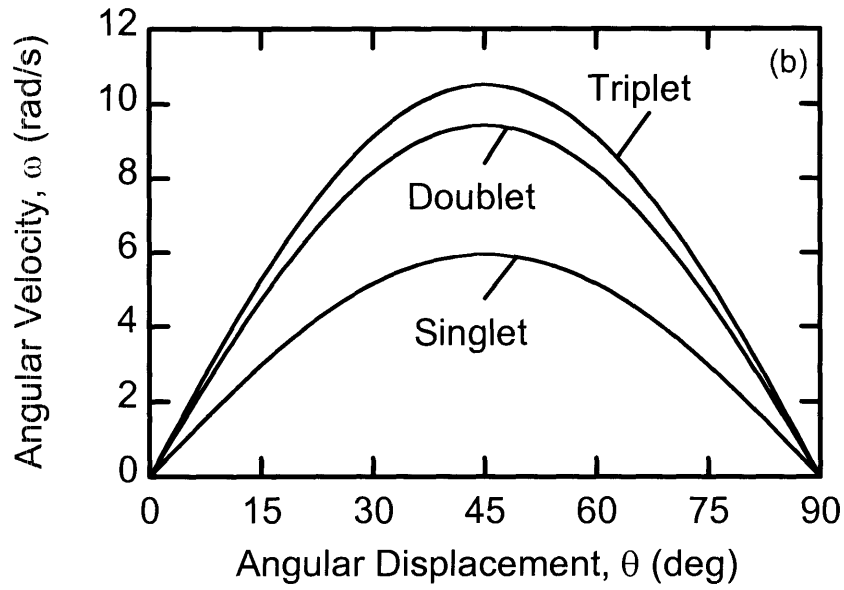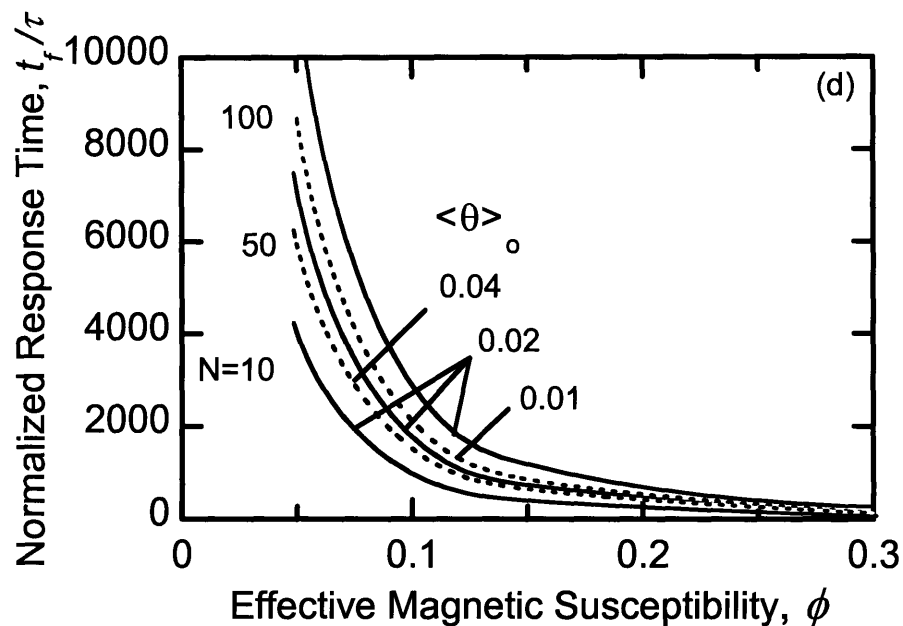
Figure 2-13. (a) Snapshots of a chain (45 μm) as it responds to an externally applied magnetic field normal to the plane of the paper. The numbers on the snapshots indicate time in milliseconds. (b) Angular velocity predictions for a 50 μm chain as a function of θ. The angular velocity increases with the chain clustering and achieves a maximum at close to $\theta = 45°$. (c) Time-dependent orientation of magnetic chains showing importance of shell structure and dimensions on the chain response to a magnetic field. Note that the effects of length, magnetic field and solvent are incorporated in the normalized time variable. Experimental results for selected chains of three different lengths with $\phi = 0.06$ are in good agreement with predictions. (d) The normalized response time for chains of varying length as a function of effective magnetic susceptibility, ϕ, for different initial displacements $<\theta>_0$.

The response times for 25 μm ($N = 28$) and 50 μm ($N = 56$) chains determined from experimental results for singlets, doublets, and triplets are shown in Figure 14, where they are compared with theoretical predictions. The appropriate values of $<\theta>_o$ used in the predictions were those that provided a match between the predicted and experimental response times at $H_0 = 0.005T$ (e.g. $<\theta>_o$ was taken to be 0.018 rads for a 50 μm singlet chain). The predicted and experimental variations of the response times for different chains agree well, as shown as a function of H_0 on a logarithmic scale for chain lengths of 25 μm and 50 μm. As predicted, the dynamic response of a chain of fixed length scales with $1/H_0^2$. The difference in the response times between the singlet and the doublet and that between the doublet and the triplet decreases with the number of chains

71

because the proportional increase in the magnetic torque is higher than the proportional increase in the viscous drag. Depending on the length and the diameter of the rigid chains and the externally applied magnetic field, the response time of the chain ranges from on the order of milliseconds to seconds.
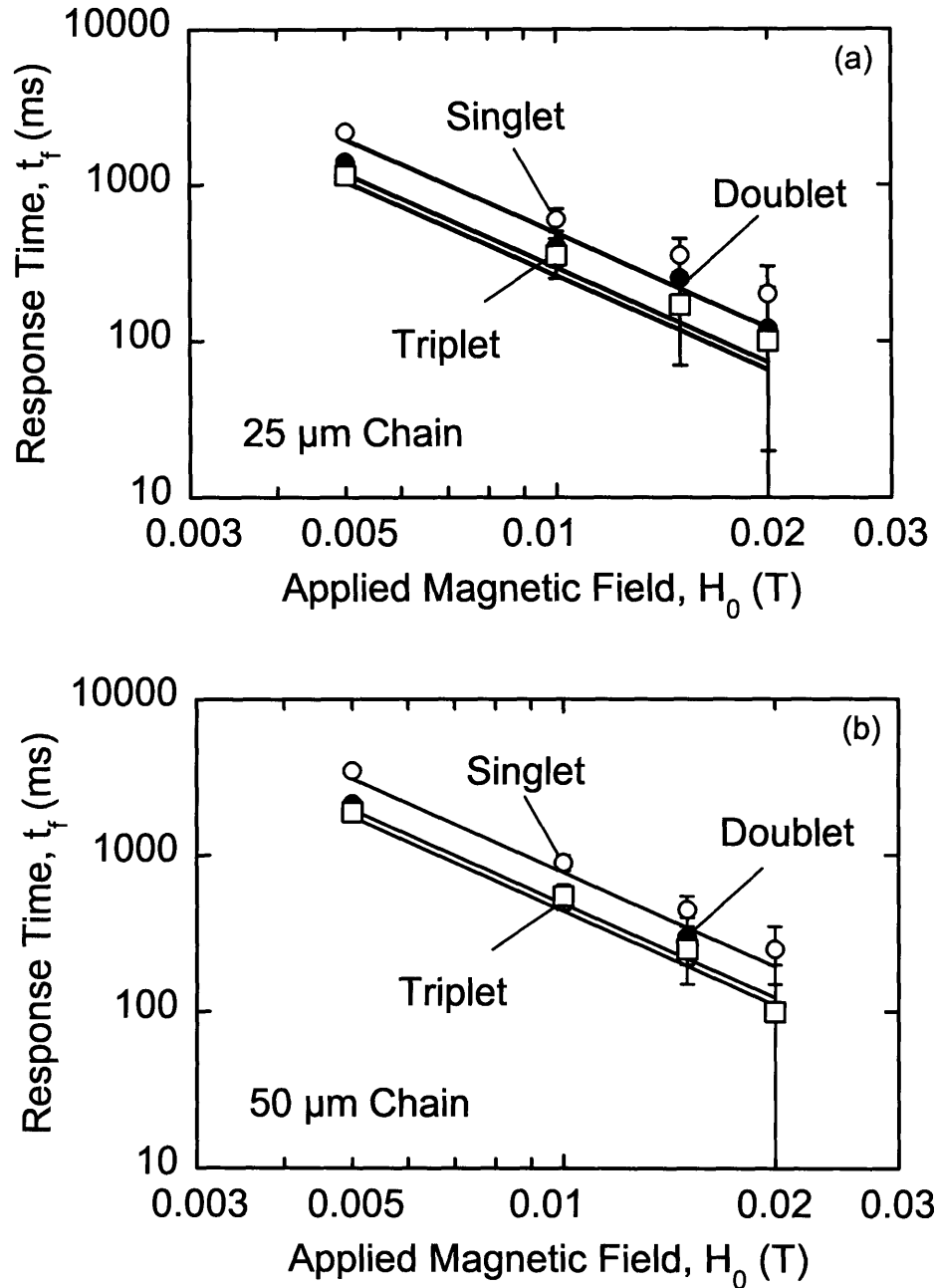
Figure 2-14. The response times for (a) $25\,\mu m$ and (b) 50 μm singlet, doublet and triplet chains compare favorably with theoretical predictions, and scale with $1/H_0^2$.

2.5 Conclusions

An inexpensive and versatile approach has been developed for the synthesis of monodisperse magnetoresponsive rods of desired diameter, length and magnetic susceptibility based on the confined alignment of magnetic beads in microchannels of selected channel height, followed by localized hydrolysis of sol-gel precursors within the shells of the beads. A variety of sol-gel precursors and magnetic nanoparticles can be used to create the desired morphologies. The diameter and length of the chains can be controlled by changing the polystyrene bead diameter and the height of the microchannel, respectively. The magnetization of the beads can be enhanced by depositing additional magnetite layers on the particle surfaces, following the established layer-by-layer technique. Glass microcells provided the best option for the microchannels as they can be assembled readily into bundles and allow easy recovery of the final product. Predictions of the dynamic response of the system agreed well with experimental observations and indicated that, depending on the applications of interest, the response time can be tuned readily either by changing the magnetic field or by varying the chain length, bead diameter and nanoparticle coating thickness. Potential applications of these rods are similar to those described by Biswal et al. [33], who have shown that permanently linked flexible magnetic chains can improve micromixing in microchannels under a rotating magnetic field. They can also be used as micropumps in a microchannel under a rotating magnetic field.

Acknowledgements

2.6 References

1.   Rosenweig, R.E., *Ferrohydrodynamics*. 1985, New York: Cambridge University Press.

2.   Chantrell, R.W., A. Bradbury, J. Popplewell, and S.W. Charles, *Agglomerate Formation in a Magnetic Fluid.* Journal of Applied Physics, 1982. **53**(3): p. 2742-2744.

3.   Chantrell, R.W., A. Bradbury, J. Popplewell, and S.W. Charles, *Particle Cluster Configuration in Magnetic Fluids.* Journal of Physics D-Applied Physics, 1980. **13**(7): p. L119-L122.

4.   Huke, B. and M. Lucke, *Magnetization of ferrofluids with dipolar interactions: A Born-Mayer expansion.* Physical Review E, 2000. **62**(5): p. 6875-6890.

5.   Morozov, K.I. and A.V. Lebedev, *The Effect Of Magneto-Dipole Interactions On The Magnetization Curves Of Ferrocolloids.* Journal Of Magnetism And Magnetic Materials, 1990. **85**(1-3): p. 51-53.

6.   Pshenichnikov, A.F., *Equilibrium Magnetization of Concentrated Ferrocolloids.* Journal of Magnetism and Magnetic Materials, 1995. **145**(3): p. 319-326.

7.   Dormann, J.L., Fiorani, D., *Magnetic properties of fine particles.* 1992, Amsterdam: North-Holland.

8.   Schmitt, V., F. Leal-Calderon, and J. Bibette, *Preparation of monodisperse particles and emulsions by controlled shear.* Colloid Chemistry Ii, 2003. **227**: p. 195-215.

9.   Cutillas, S. and J. Liu, *Particle dynamics of structure formation and disintegration in a model magnetorheological fluid.* International Journal of Modern Physics B, 2002. **16**(17-18): p. 2314-2320.

10.   Furst, E.M. and A.P. Gast, *Micromechanics of dipolar chains using optical tweezers.* Physical Review Letters, 1999. **82**(20): p. 4130-4133.

11.   Gulley, G.L. and R. Tao, *Structures of a magnetorheological fluid.* International Journal of Modern Physics B, 2001. **15**(6-7): p. 851-858.

12.   Jin, K.J. and W.J. Wen, *The evolution of bending chains in magnetorheological fluid at external field.* Physics Letters A, 2001. **286**(5): p. 347-352.

13.   Biswal, S.L. and A.P. Gast, *Mechanics of semiflexible chains formed by poly(ethylene glycol)-linked paramagnetic particles.* Physical Review E, 2003. **68**(2).

14. Goubault, C., F. Leal-Calderon, J.L. Viovy, and J. Bibette, *Self-assembled magnetic nanowires made irreversible by polymer bridging.* Langmuir, 2005. **21**(9): p. 3725-3729.

15. Goubault, C., P. Jop, M. Fermigier, J. Baudry, E. Bertrand, and J. Bibette, *Flexible magnetic filaments as micromechanical sensors.* Physical Review Letters, 2003. **91**(26).

16. Doyle, P.S., J. Bibette, A. Bancaud, and J.L. Viovy, *Self-assembled magnetic matrices for DNA separation chips.* Science, 2002. **295**(5563): p. 2237-2237.

17. Bizdoaca, E.L., M. Spasova, M. Farle, M. Hilgendorff, L.M. Liz-Marzan, and F. Caruso, *Self-assembly and magnetism in core-shell microspheres.* Journal of Vacuum Science & Technology A, 2003. **21**(4): p. 1515-1518.

18. Biswal, S.L. and A.P. Gast, *Micromixing with linked chains of paramagnetic particles.* Analytical Chemistry, 2004. **76**(21): p. 6448-6455.

19. Terray, A., J. Oakey, and D.W.M. Marr, *Microfluidic control using colloidal devices.* Science, 2002. **296**(5574): p. 1841-1844.

20. Caruso, F., R.A. Caruso, and H. Möhwald, *Nanoengineering of Inorganic and Hybrid Hollow Spheres by Colloidal Templating.* Science, 1998. **282**(5391): p. 1111-1114.

21. Caruso, F., A.S. Susha, M. Giersig, and H. Mohwald, *Magnetic core-shell particles: Preparation of magnetite multilayers on polymer latex microspheres.* Advanced Materials, 1999. **11**(11): p. 950-+.

22. Massart, R., E. Dubois, V. Cabuil, and E. Hasmonay, *Preparation and Properties of Monodisperse Magnetic Fluids.* Journal of Magnetism and Magnetic Materials, 1995. **149**(1-2): p. 1-5.

23. Morales, M.P., S. Veintemillas-Verdaguer, M.I. Montero, C.J. Serna, A. Roig, L. Casas, B. Martinez, and F. Sandiumenge, *Surface and internal spin canting in gamma-Fe2O3 nanoparticles.* Chemistry of Materials, 1999. **11**(11): p. 3058-3064.

24. Barringer, E.A. and H.K. Bowen, *High-Purity, Monodisperse Tio2 Powders by Hydrolysis of Titanium Tetraethoxide.2. Aqueous Interfacial Electrochemistry and Dispersion Stability.* Langmuir, 1985. **1**(4): p. 420-428.

25.   Smith, J.N., J. Meadows, and P.A. Williams, *Adsorption of polyvinylpyrrolidone onto polystyrene latices and the effect on colloid stability.* Langmuir, 1996. **12**(16): p. 3773-3778.

26.   Tao, R., *Super-strong magnetorheological fluids.* Journal of Physics-Condensed Matter, 2001. **13**(50): p. R979-R999.

27.   Balcioglu, I.A. and I. Arslan, *Application of photocatalytic oxidation treatment to pretreated and raw effluents from the Kraft bleaching process and textile industry.* Environmental Pollution, 1998. **103**(2-3): p. 261-268.

28.   Sun, S.H., H. Zeng, D.B. Robinson, S. Raoux, P.M. Rice, S.X. Wang, and G.X. Li, *Monodisperse MFe2O4 (M = Fe, Co, Mn) nanoparticles.* Journal of the American Chemical Society, 2004. **126**(1): p. 273-279.

29.   Sandre, O., J. Browaeys, R. Perzynski, J.C. Bacri, V. Cabuil, and R.E. Rosensweig, *Assembly of microscopic highly magnetic droplets: Magnetic alignment versus viscous drag.* Physical Review E, 1999. **59**(2): p. 1736-1746.

30.   Wilhelm, C., J. Browaeys, A. Ponton, and J.C. Bacri, *Rotational magnetic particles microrheology: The Maxwellian case.* Physical Review E, 2003. **67**(1).

31.   Melle, S., G.G. Fuller, and M.A. Rubio, *Structure and dynamics of magnetorheological fluids in rotating magnetic fields.* Physical Review E, 2000. **61**(4): p. 4111-4117.

32.   Doi, M., Edwards, S.F., *The Theory of Polymer Dynamics.* 1987: Oxford University Press.

33.   Biswal, S.L. and A.P. Gast, *Rotational dynamics of semiflexible paramagnetic particle chains.* Physical Review E, 2004. **69**(4).

34.   Perrin, J., J. Phys. Radium., 1934. **7**(497): p. 1934.

Chapter 3

Orientational Dependence of Apparent Magnetic Susceptibilities of Superparamagnetic Nanoparticles in Planar Structured Arrays:
Effect on Magnetic Moments of Nanoparticle-Coated Core-Shell Magnetic Beads

3.1 Introduction

The current strong interest in magneto-responsive colloidal systems arises from their potential applications in, *inter alia*, magnetic resonance imaging [1-4], targeted drug delivery [5-9], hyperthermia treatment [10-14] and other biomedical areas, as well as in chemical, environmental and biological separation processes [15-19] These magnetic colloids are usually either stabilized dispersions of individual magnetic nanoparticles and clusters of these nanoparticles in a solvent phase, or they are suspensions of micron-sized polymer beads with the nanoparticles embedded within them. These latter magnetic colloids also exhibit magnetorheological (MR) behavior upon application of a magnetic field by forming chains in the direction of the magnetic field, thereby causing the MR fluid to change from a liquid-like to a solid-like state with a commensurate dramatic increase in yield stress [20-23]. In all cases, the governing parameter that determines the response of the colloidal particles to the magnetic field is the particle magnetic moment induced by the magnetic field [20, 24, 25].

It is generally assumed that the larger magnetic beads behave as point dipoles when subjected to an externally-applied magnetic field, and that their magnetization is governed primarily by the total amount of magnetic material encapsulated in the beads [20, 24, 26, 27], usually 25 - 40 wt % iron oxide (either γ-Fe_2O_3 or Fe_3O_4) in the form of nanoparticles with an average size of about 8 nm. The spatial distribution of the magnetic nanoparticles within a bead is assumed not to be critical. This is true for systems in which the distance between magnetic nanoparticles distributed in the matrix is sufficiently large that any inter-particle interactions can be neglected, but is not necessarily the case when

core-shell magnetic colloids are used, in which the nanoparticles are adsorbed as layers on the bead surface using, e.g., the technique of Caruso et al. [28, 29] as shown in Figure 3-1. The magnetic nanoparticles in the core-shell structure are in close proximity to each other and, in addition to the applied magnetic field, these particles can also experience the magnetic fields of the neighboring nanoparticle dipoles. These particles themselves have, on average, magnetizations induced by the combination of the applied magnetic fields and those associated with the individual surrounding nanoparticle dipoles, and can thus affect the net magnetization of the collection of particles.
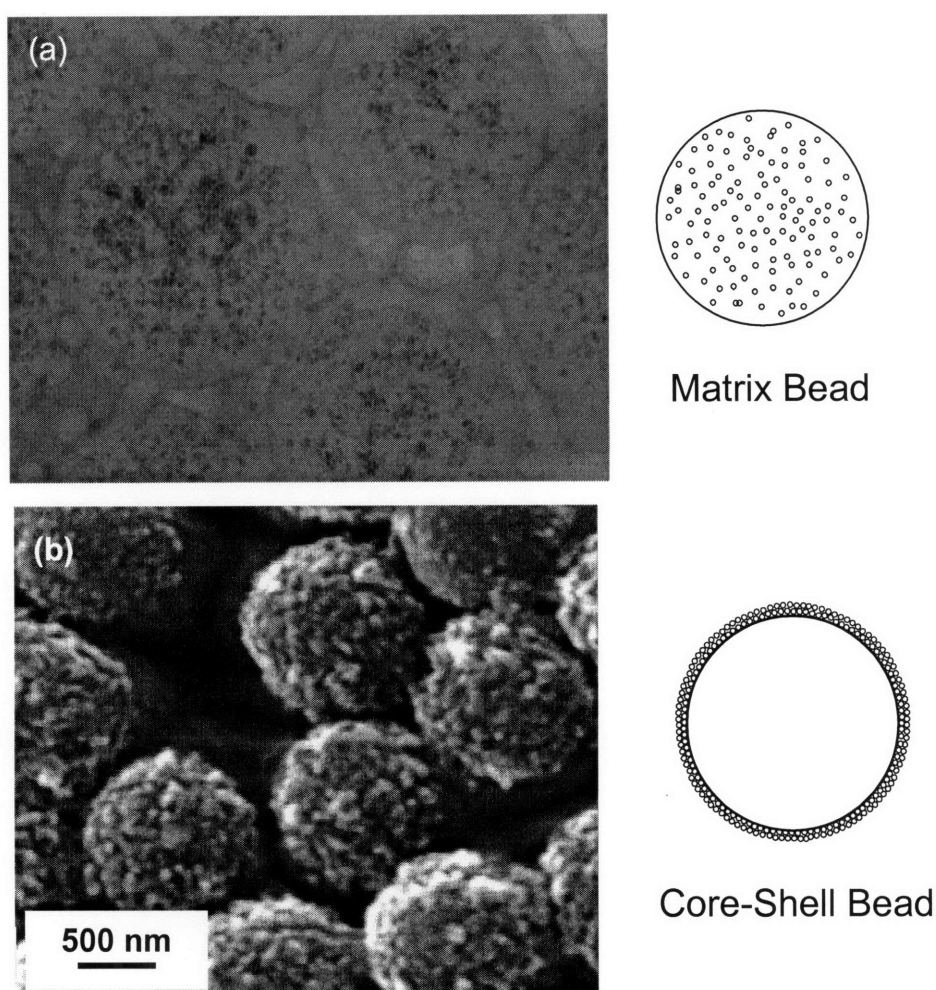
Figure 3-1. (a) TEM micrograph and schematic of matrix type magnetic colloids, and (b) TEM micrograph and schematic of nanoparticle-coated polystyrene beads.

Planar arrays of interacting magnetic nanoparticles have been analyzed [30-34] under conditions for which the local moment distribution of the nanoparticles is governed

by short-range exchange interactions and long range dipolar interactions. For systems composed of 10 nm magnetite nanoparticles, as in this work, the exchange energy can be taken to be small and so we only consider the effects of dipolar interactions on the net magnetic moment. The goal of this paper is to examine the magnetic moment developed by core-shell type magnetic beads under externally-applied magnetic fields and show that in some cases this magnetic moment can be greater than that for equivalent matrix-type configurations, by up to about 30% for iron oxide nanoparticles. This implies that the interaction energies between colloids, which depend on the square of their magnetic moments, can be significantly larger for core-shell magnetic colloids than for matrix-type beads. In constructing the model, we recognize that the orientations of the particle arrays relative to the external magnetic field are defined by the azimuthal angle. Thus, we model the particle arrays as being planar at each point, evaluate the effects of the induced magnetizations on the effective magnetic moments of the particles in the planar arrays at different orientations of this array, and then integrate the effective moments over the particle surface, allowing for their azimuthal dependence, to arrive at a result for the magnetic moment of the entire bead itself.

It is not possible to probe experimentally the azimuthal dependence of the magnetic moments of nanoparticles in the shell of the shell-core model. In contrast, it is relatively simple to probe orientational effects on the magnetization of layers of nanoparticles deposited on planar substrates. We present magnetization studies performed on such arrays of magnetic nanoparticles to verify the model predictions of the effect of orientation on the effective magnetic properties of these arrays.

3.2 Theory

The average magnetic moment per particle for a collection of superparamagnetic nanoparticles under an applied magnetic field $\bar{H}_i = H_i \hat{H}_i$ can be represented well by the equation [35]

$$\bar{m}_i = \frac{\mu_0 V \chi}{1 + \beta H_i} \bar{H}_i = \begin{cases} \mu_0 V \chi \bar{H}_i & \text{for } H_i \ll \beta \\ \mu_0 V (\chi / \beta) \hat{H}_i & \text{for } H_i \gg \beta \end{cases} \tag{1}$$

79

where $H_i = \left(\bar{H}_i \cdot \bar{H}_i \right)^{1/2}$ is the magnitude of the magnetic field, and $\hat{H}_i$ is the unit vector in the direction of the magnetic field. The permeability of free space is given by μ_0, V is the effective volume of the magnetic core, and χ is its magnetic susceptibility, which is a constant given by the slope of the magnetization (M) curve at low magnetic fields i.e., $\chi = \left(dM / dH \right)_{H \to 0}$. The magnitude of the magnetic field at which the magnetization is half its saturation value is $1/\beta$. The dimensionless quantity $\mu_0 V \chi$ is the effective magnetic moment per unit magnetic field strength at low field strength, while $\mu_0 V \chi / \beta$ is the saturation magnetization at high field strengths.

The effective magnetic moment of an assembly of N superparamagnetic nanoparticles is the sum of the moments of the individual nanoparticles in the assembly, i.e.,

$$\bar{m}_{total} = \sum_{i=1}^{N} \bar{m}_i = \kappa \sum_{i=1}^{N} \bar{H}_i \tag{2}$$

For non-interacting particles, such as those distributed uniformly within a polymer bead, all particles will experience the same magnetic field, i.e., the externally applied field $\bar{H}_0$, and hence

$$\bar{m}_{total}^{non-int} = N\bar{m}_0 \tag{3}$$

When the particles are in close proximity, as in the shells of the core-shell superparamagnetic beads considered here, the magnetic field associated with the magnetic moments of the individual dipoles themselves must also be accounted for in determining their effective magnetic moments. Thus, when the assembly of particles is in an externally applied field $\bar{H}_0$ the net magnetic field acting on a nanoparticle i is

$$\bar{H}_i = \bar{H}_0 + \sum_{j \neq i} \bar{H}_{ij} \tag{4}$$

where $\bar{H}_{ij}$ is the field of the jth particle acting on the ith particle, and is given by [36]

$$\bar{H}_{ij} = \frac{1}{4\pi\mu_0} \frac{3\hat{r}_{ij}\left(\hat{r}_{ij}\cdot\bar{m}_j\right)-\bar{m}_j}{r_{ij}^3} \qquad (5)$$

Here, $\hat{r}_{ij}$ is the unit vector joining the centers of the two particles, which are separated by a distance r_{ij}. Thus, the average magnetic moment for a magnetic nanoparticle in a collection of such particles is

$$\bar{m}_i = \frac{\mu_0 V\chi}{(1+\beta H_i)}\left(\bar{H}_0 + \sum_{j\neq i}\frac{1}{4\pi\mu_0}\frac{3\hat{r}_{ij}\left(\hat{r}_{ij}\cdot\bar{m}_j\right)-\bar{m}_j}{r_{ij}^3}\right). \qquad (6)$$

At low field strengths, when $\beta H_i = 1$, this equation can be solved for the magnetic moments explicitly, as shown below. Under conditions where βH_i cannot be neglected relative to unity, the equations are non-linear, and cannot be solved to give closed form solutions for the moments of the particles as a function of field strength; for this purpose we use a perturbation theory analysis to linearise the problem, as developed in a later section.

3.2.1 Magnetic Moments Under Small Applied Magnetic Fields

When the applied magnetic field $\bar{H}_0$ is sufficiently small that $\beta H_0 = 1$, then Equation (1) can be written in non-dimensional form as

$$\bar{\mu}_i = \frac{\bar{m}_i}{\mu_0 V\chi H_0} = \hat{H}_0 + \phi\sum_{j\neq i}\frac{3\hat{r}_{ij}\left(\hat{r}_{ij}\cdot\bar{\mu}_j\right)-\bar{\mu}_j}{\eta_{ij}^3} \qquad (7)$$

where $\mu_0 V\chi H_0$ is the magnetic moment of an isolated magnetic nanoparticle under the same applied field, directed along the unit vector $\hat{H}_0 = \bar{H}_0/H_0$, and $\eta_{ij} = r_{ij}/2a$ is the normalized interparticle distance ($\eta_{ij} = 1$ for nearest neighbor particles

81

if they are touching). The normalized magnetic susceptibility $\phi = \frac{1}{24}\left(V/V_p\right)\chi$ allows for differences in the actual volume of the nanoparticle, V_p, and the volume of the magnetic core, V, as captured by $V/V_p = \left(1-\delta/a\right)^3$, where δ is the combined thickness of the nonmagnetic surface layer on the iron oxide particle and the thickness of the surfactant or polymer stabilizing layer on the nanoparticle surface.

This equation holds when all particles are in the same environment, as, for instance, when the particles are packed regularly in a planar monolayer oriented at an angle α relative to the applied magnetic field. For multiple layers, equations can be written for the magnetic moments of nanoparticles in each layer, and the resulting coupled set of independent linear equations solved simultaneously for the moments in each layer. When the magnetic nanoparticles are arranged as a monolayer, or as multiple layers, adsorbed to the surface of a large bead, and if the size of the bead is considerably greater than that of the individual magnetic nanoparticles, i.e., $a = R$, then locally we can consider the particle array to lie in a plane tangent to the bead surface at that point. Thus, we can determine the effective magnetic moments of the particles at any azimuthal angle α (see Figure 3-2) by treating the system locally as a planar array of nanoparticles, and then, by integrating these local moments over the surface of the bead, we can obtain the overall magnetic moment of the core-shell bead itself.

The enhancement in the magnetic moment for the core-shell bead owing to the interactions between particles relative to when the nanoparticles do not interact is then

$$\bar{\mu}_{bead(K)} = \frac{\bar{m}_{bead}}{NKH_0} = \sum_{k=1}^{K}\int_0^{2\pi}\int_0^{\pi/2}\bar{\mu}_{k_K}(\alpha,\theta)\cos\alpha\,d\alpha\,d\theta = \hat{H}_0\sum_{k=1}^{K}\int_0^{\pi/2}\mu_{k_K\hat{H}_0}(\alpha)\cos\alpha\,d\alpha \quad (8)$$

where $\bar{\mu}_{k_K}(\alpha,\theta)$ is the normalized magnetic moment for a nanoparticle in layer k of a K-layer array located at an azimuthal angle α and rotational angle θ on the surface of the bead. Owing to symmetry, only the component $\mu_{k_K\hat{H}_0} = \left(\hat{H}_0\cdot\bar{\mu}_{k_K}\right)$ in the direction of the applied magnetic field is non-zero.
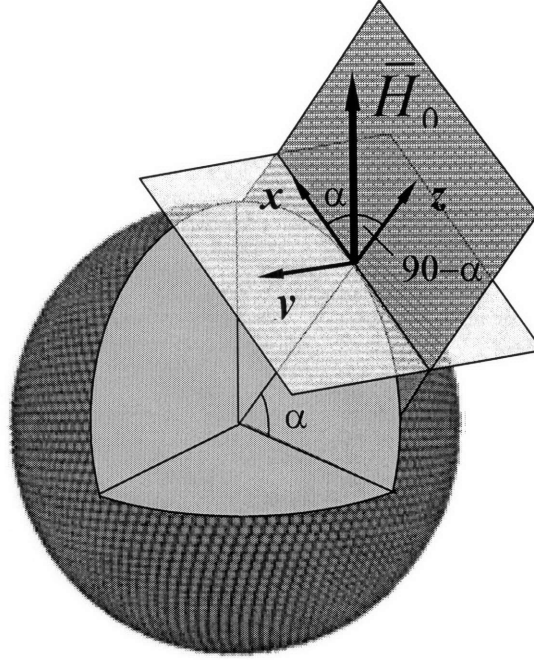
Figure 3-2. Pictorial representation of a core-shell bead. The particles at an azimuthal angle α are assumed to lie in the tangent plane to the surface, with the x and z axes in the plane normal to the tangent plane, and coplanar with the applied magnetic field. The y axis is in the tangent plane, and normal to the applied magnetic field.

To evaluate $\bar{\mu}_{k_K}(\alpha)$ (for convenience, and because of symmetry, we drop the explicit dependence of this quantity on rotational angle θ), we consider a planar array of particles in the tangent plane located at an azimuthal angle α on the surface of the bead, and establish the local (x, y, z) coordinates such that the (x, y) plane is in the tangent plane, with the y axis normal to the applied magnetic field, and the z axis normal to the tangent plane, as shown in Figure 3-2. Under these conditions, $\hat{H}_0$ is in the (x, z) plane, forming an angle α relative to the x-axis, the y component of $\bar{\mu}_{k_K}(\alpha)$ is zero, and the component of $\bar{\mu}_{k_K}(\alpha)$ in the direction of the applied magnetic field is

$$\mu_{k_K \hat{H}_0}(\alpha) = \mu_{x k_K} \cos\alpha + \mu_{z k_K} \sin\alpha .$$

In the sections that follow, we derive the appropriate expressions for monolayer, bilayer and trilayer coverage, and generalize these results to multilayer systems. The predicted magnetic moments of the particles are compared for the different systems, both

for the individual layers as functions of α, and for the core-shell beads as a whole. Experimental measurements of the magnetic response of planar nanoparticle-coated films under different orientations relative to the magnetic field are used to validate the theoretical predictions.

3.2.1.1 Monolayer Coverage

For a monolayer, the solution to equation (7) is

$$\mu_{x1_1} = \frac{\cos\alpha}{1-3\phi}; \quad \mu_{z1_1} = \frac{\sin\alpha}{1+6\phi} \tag{9}$$

if only nearest neighbors are considered, where $\eta_{ij} = 1$ for all i and j. If we also account for interactions with second nearest neighbors, then it can be shown that

$$\mu_{x1_1} = \frac{\cos\alpha}{1-3.95\phi}; \quad \mu_{z1_1} = \frac{\sin\alpha}{1+7.95\phi} \tag{10}$$

which indicates that, depending on the value of ϕ, the second nearest neighbor interactions cannot generally be neglected. Third nearest neighbor interactions have only a small effect (< 5 percent for magnetite nanoparticles) on the moments, and hence in what follows we restrict our analysis to include only first and second nearest neighbor interactions.

The net moment in the direction of the applied field of a particle in a monolayer at position α is

$$\mu_{1_1\hat{H}_0}(\alpha) = \frac{\cos^2\alpha}{1-3.95\phi} + \frac{\sin^2\alpha}{1+7.95\phi} = b_{x1_1}\cos^2\alpha + b_{z1_1}\sin^2\alpha \tag{11}$$

Because of the dipole-dipole interactions between the particles, the average magnetic moment does not necessarily align with the applied magnetic field direction. The angle θ between the applied magnetic field and the net nanoparticle moment as a function of the position on the bead surface is determined by the equation

$$\theta = \alpha - \tan^{-1}\left(\frac{1-3.95\phi}{1+7.95\phi}\tan\alpha\right). \tag{12}$$

This angle attains a maximum value at $\alpha_{max} = \sin^{-1}\sqrt{\dfrac{1+7.95\phi}{2(1+2\phi)}}$. Note that at the equator

and at the pole the nanoparticle magnetic moments are aligned perfectly with the applied field.

The magnetic moment for the bead is obtained using Equation (8):

$$\mu_{bead(1)} = \mu_{bead,1_1} = \int_0^{\pi/2}\left(b_{x1_1}\cos^2\alpha + b_{z1_1}\sin^2\alpha\right)\cos\alpha\, d\alpha = \tfrac{1}{3}\left(2b_{x1_1} + b_{z1_1}\right) \tag{13}$$

3.2.1.2 Bilayer Coverage

For a bilayer system, the individual x components of the magnetic moments for the two layers are related by

$$\begin{aligned}
\left(1-3.95\phi\right)\mu_{x1_2} + 1.31\phi\mu_{x2_2} &= \cos\alpha \\
1.31\phi\mu_{x1_2} + \left(1-3.95\phi\right)\mu_{x2_2} &= \cos\alpha
\end{aligned} \tag{14}$$

for the x components, where the subscript xk_K denotes the x component of the moment for the kth layer in a K-layer system. The z components can similarly be shown to be related by

$$\begin{aligned}
\left(1+7.95\phi\right)\mu_{z1_2} - 2.62\phi\mu_{z2_2} &= \sin\alpha \\
-2.62\phi\mu_{z1_2} + \left(1+7.95\phi\right)\mu_{z2_2} &= \sin\alpha
\end{aligned} \tag{15}$$

These sets of two equations each can be solved simultaneously to yield

$$\mu_{x1_2} = \mu_{x2_2} = \frac{\cos\alpha}{1-2.64\phi}; \qquad \mu_{z1_2} = \mu_{z2_2} = \frac{\sin\alpha}{1+5.34\phi} \tag{16}$$

from which we can show

$$\mu_{1_2,\hat{H}_0}(\alpha) = \mu_{2_2,\hat{H}_0}(\alpha) = \frac{\cos^2\alpha}{1-2.64\phi} + \frac{\sin^2\alpha}{1+5.34\phi} = b_{x1_2}\cos^2\alpha + b_{z1_2}\sin^2\alpha \qquad (17)$$

The net contribution of each layer to the overall magnetic moment of the core-shell bead is then

$$\mu_{bead,1_2} = \mu_{bead,2_2} = \tfrac{1}{3}\left(2b_{x1_2} + b_{z1_2}\right) \qquad (18)$$

This result is similar to that for the monolayer, except that the numerical coefficients for ϕ are different, reflecting interactions between particles in the different layers, in addition to the intra-layer interactions. Note that the moments are the same for particles in both layers, because of the symmetry of the interactions between the two layers.

For the bead as a whole, we have

$$\mu_{bead(2)} = \mu_{bead,1_2} + \mu_{bead,2_2} = \tfrac{2}{3}\left(2b_{x1_2} + b_{z1_2}\right) \qquad (19)$$

3.2.1.3 Trilayer Coverage

For a trilayer system, the equations obtained for the x and z components for each of the three layers are

$$(1-3.95\phi)\mu_{x1_3} + 1.31\phi\mu_{x2_3} + 0.863\phi\mu_{x3_3} = \cos\alpha$$
$$1.31\phi\mu_{x1_3} + (1-3.95\phi)\mu_{x2_3} + 1.31\phi\mu_{x3_3} = \cos\alpha \qquad (20)$$
$$0.863\phi\mu_{x1_3} + 1.31\phi\mu_{x2_3} + (1-3.95\phi)\mu_{x3_3} = \cos\alpha$$

and

$$(1+7.95\phi)\mu_{z1_3} - 2.62\phi\mu_{z2_3} - 1.30\phi\mu_{z3_3} = \sin\alpha$$
$$-2.62\phi\mu_{z1_3} + (1+7.95\phi)\mu_{z2_3} - 2.62\phi\mu_{z3_3} = \sin\alpha \qquad (21)$$
$$-1.30\phi\mu_{z1_3} - 2.62\phi\mu_{z2_3} + (1+7.95\phi)\mu_{z3_3} = \sin\alpha$$

respectively, with solutions

$$\mu_{x1_3} = \mu_{x3_3} = \frac{(1-5.26\phi)\cos\alpha}{8.76\phi^2 - 7.04\phi + 1} = b_{x1_3}\cos\alpha; \qquad \mu_{x2_3} = \frac{(1-6.57\phi)\cos\alpha}{8.76\phi^2 - 7.04\phi + 1} = b_{x2_3}\cos\alpha$$

$$(22)$$

$$\mu_{z1_3} = \mu_{z3_3} = \frac{(1+10.56\phi)\sin\alpha}{39.19\phi^2 + 14.6\phi + 1} = b_{z1_3}\sin\alpha; \qquad \mu_{z2_3} = \frac{(1+11.88\phi)\sin\alpha}{39.19\phi^2 + 14.6\phi + 1} = b_{z2_3}\sin\alpha$$

$$(23)$$

The resulting total moments for the individual layers on the bead are

$$\mu_{bead,1_3} = \mu_{bead,3_3} = \tfrac{1}{3}\left(2b_{x1_3} + b_{z1_3}\right) \qquad \mu_{bead,2_3} = \tfrac{1}{3}\left(2b_{x2_3} + b_{z2_3}\right), \qquad (24)$$

and the total moment for the trilayer coated bead is

$$\mu_{bead(3)} = \tfrac{2}{3}\left(2b_{x1_3} + b_{z1_3}\right) + \tfrac{1}{3}\left(2b_{x2_3} + b_{z2_3}\right) \qquad (25)$$

3.2.1.4 Multilayer Coverage

The average magnetic moments for particles in an array of K layers can be developed in the same way as above. The solution to the resulting system of linear, independent equations can be written in matrix form as

$$\mu_x = \mathbf{K}_x^{-1}\mathbf{I}_K\cos\alpha = \mathbf{b}_x\cos\alpha; \qquad \mu_z = \mathbf{K}_z^{-1}\mathbf{I}_K\sin\alpha = \mathbf{b}_z\sin\alpha \qquad (26)$$

where μ_x and μ_z are K-dimensional vectors with components μ_{xk_K} and μ_{zk_K}, respectively, and $\mathbf{I}_K$ is the K-dimensional unitary vector. The matrices are

$$\mathbf{K}_x = \begin{bmatrix} 1-3.95\phi & 1.31 & 0.86 & 0 & 0 & \cdots & 0 & 0 & 0 & 0 & 0 \\ 1.31 & 1-3.95\phi & 1.31 & 0.86 & 0 & \cdots & 0 & 0 & 0 & 0 & 0 \\ 0.86 & 1.31 & 1-3.95\phi & 1.31 & 0.86 & \cdots & 0 & 0 & 0 & 0 & 0 \\ \vdots & \vdots & \vdots & \vdots & \vdots & \vdots & \vdots & \vdots & \vdots & \vdots & \vdots \\ 0 & 0 & 0 & 0 & 0 & \cdots & 0.86 & 1.31 & 1-3.95\phi & 1.31 & 0.86 \\ 0 & 0 & 0 & 0 & 0 & \cdots & 0 & 0.86 & 1.31 & 1-3.95\phi & 1.31 \\ 0 & 0 & 0 & 0 & 0 & \cdots & 0 & 0 & 0.86 & 1.31 & 1-3.95\phi \end{bmatrix}$$

$$(27)$$

and

$$\mathbf{K}_z = \begin{bmatrix} 1+7.95\phi & -2.62 & -1.30 & 0 & 0 & \dots & 0 & 0 & 0 & 0 & 0 \\ -2.62 & 1+7.95\phi & -2.62 & -1.30 & 0 & \dots & 0 & 0 & 0 & 0 & 0 \\ -1.30 & -2.62 & 1+7.95\phi & -2.62 & -1.30 & \dots & 0 & 0 & 0 & 0 & 0 \\ \vdots & \vdots & \vdots & \vdots & \vdots & \vdots & \vdots & \vdots & \vdots & \vdots & \vdots \\ 0 & 0 & 0 & 0 & 0 & \cdots & -1.30 & -2.62 & 1+7.95\phi & -2.62 & -1.30 \\ 0 & 0 & 0 & 0 & 0 & \cdots & 0 & -1.30 & -2.62 & 1+7.95\phi & -2.62 \\ 0 & 0 & 0 & 0 & 0 & \cdots & 0 & 0 & -1.30 & -2.62 & 1+7.95\phi \end{bmatrix}$$

(28)

respectively. Note that these matrices are pentadiagonal as a particle in an intermediate layer interacts with particles in the two layers above and the two layers below the layer in which that particle resides (only first and second nearest neighbors are considered).

The integrated moments over the bead surface for each layer, and the total moment for the multilayer shell-coated bead are then obtained from

$$\mu_{bead,\hat{H}_0} = \tfrac{1}{3}\left(2\mathbf{b}_x + \mathbf{b}_z\right)$$

(29)

and

$$\mu_{bead(K)} = \mathbf{I}_K^T \mu_{bead,\hat{H}_0}$$

(30)

respectively, where $\mathbf{I}_K^T$ denotes the transpose of the unitary vector.

3.2.2 Magnetic Moments Under Larger Magnetic Fields

Under higher magnetic fields, where the linearity assumption no longer holds, the magnetic moment can be normalized more conveniently by the moment under saturation conditions ($\mu_0 V \chi / \beta$) to yield the dimensionless equation

$$\bar{\sigma}_i = \frac{\beta \bar{m}_i}{\mu_0 V \chi} = \frac{\beta H_0}{1+\beta H_i}\bar{\Psi}_i$$

(31)

88

where

$$\bar{\Psi}_i = \frac{\bar{H}_i}{H_0} = \hat{H}_0 + \frac{\phi}{\beta H_0}\sum_{j\neq i}\frac{3\hat{r}_{ij}\left(\hat{r}_{ij}\cdot\bar{\Psi}_j\right)-\bar{\Psi}_j}{\eta_{ij}^3\left(\Psi_j+\dfrac{1}{\beta H_0}\right)} \tag{32}$$

The quantity $\varepsilon = \phi / \beta H_0 = 1$ at sufficiently high field strengths, and can be used as a perturbation parameter in a perturbation expansion of the field strength according to

$$\bar{\Psi}_i = \bar{\Psi}_i^0 + \varepsilon\bar{\Psi}_i^1 + \varepsilon^2\bar{\Psi}_i^2 + \cdots\cdots \tag{33}$$

Retaining only terms up to first order, we can show that the magnitude of $\bar{\Psi}_i$ can be approximated by

$$\Psi_j = \left(\bar{\Psi}_j\cdot\bar{\Psi}_j\right)^{1/2} \simeq \Psi_j^0\left(1+\varepsilon\frac{\bar{\Psi}_j^0\cdot\bar{\Psi}_j^1}{\left(\Psi_j^0\right)^2}\right) \tag{34}$$

and equation (32) can be expanded to give, to first order,

$$\bar{\Psi}_j^0 + \varepsilon\bar{\Psi}_j^1 = \hat{H}_0 + \varepsilon\sum_{j\neq i}\frac{3\hat{r}_{ij}\left(\hat{r}_{ij}\cdot\bar{\Psi}_j^0\right)-\bar{\Psi}_j^0}{\eta_{ij}^3\left(\Psi_j^0+\dfrac{1}{\beta H_0}\right)} \tag{35}$$

Thus, we have

$$\bar{\Psi}_j^0 = \hat{H}_0 \tag{36}$$

and, since $\Psi_j^0 = \left(\hat{H}_0\cdot\hat{H}_0\right)^{1/2} = 1$,

$$\bar{\Psi}_j^1 = \frac{\beta H_0}{1+\beta H_0}\sum_{j\neq i}\frac{3\hat{r}_{ij}\left(\hat{r}_{ij}\cdot\hat{H}_0\right)-\hat{H}_0}{\eta_{ij}^3} \tag{37}$$

Thus, to first order in ε, we have

$$\bar{\sigma}_i = \frac{\beta H_0 \bar{\Psi}_i}{(1+\beta H_0 \Psi_i)} = \frac{\beta H_0 \left(\hat{H}_0 + \frac{\phi}{(1+\beta H_0)} \sum_{j \neq i} \frac{3\hat{r}_{ij}\left(\hat{r}_{ij}\cdot\hat{H}_0\right)-\hat{H}_0}{\eta_{ij}^3} \right)}{1+\beta H_0 \left(1 + \frac{\phi}{(1+\beta H_0)} \sum_{j \neq i} \frac{3\left(\hat{r}_{ij}\cdot\hat{H}_0\right)^2-1}{\eta_{ij}^3} \right)}$$

(38)

The net moment in the direction of the applied field is, then,

$$\sigma_{i,\hat{H}_0} = \left(\bar{\sigma}_i \cdot \hat{H}_0\right) = \frac{\beta H_0 \left(1 + \frac{\phi}{(1+\beta H_0)} \sum_{j \neq i} \frac{3\left(\hat{r}_{ij}\cdot\hat{H}_0\right)^2-1}{\eta_{ij}^3} \right)}{1+\beta H_0 \left(1 + \frac{\phi}{(1+\beta H_0)} \sum_{j \neq i} \frac{3\left(\hat{r}_{ij}\cdot\hat{H}_0\right)^2-1}{\eta_{ij}^3} \right)}$$

(39)

If we consider only first and second nearest neighbors in a monolayer, we can readily show that

$$\sigma_{i,\hat{H}_0}(\alpha = 90°) = \frac{\beta m_{i,\hat{H}_0}(\alpha = 90°)}{\mu_0 V \chi} = \frac{\beta H_0 \left(1 - \frac{6\phi}{(1+\beta H_0)} \right)}{1+\beta H_0 \left(1 - \frac{6\phi}{(1+\beta H_0)} \right)}$$

(40)

and

$$\sigma_{i,\hat{H}_0}(\alpha = 0°) = \frac{\beta m_{i,\hat{H}_0}(\alpha = 0°)}{\mu_0 V \chi} = \frac{\beta H_0 \left(1 + \frac{3\phi}{(1+\beta H_0)} \right)}{1+\beta H_0 \left(1 + \frac{3\phi}{(1+\beta H_0)} \right)}$$

(41)

90

3.3 Experimental Section

Monodisperse magnetic nanoparticles were synthesized using seed mediated growth technique as developed by Sun *et. al.* [37].

3.3.1 Materials

Iron(III) acetylacetonate (97%), Benzyl ether (99%), 1-2 hexadecanediol (97%), ethanol, oleic acid (90%) and oleylamine (70%) were purchased from Sigma Aldrich and used as received.

3.3.2 Magnetic Nanoparticle Synthesis

Two millimoles of Iron (III) acetylacetonate, 10 mmol of 1-2 hexadecanediol, 6 mmol of oleic acid, 6 mmol of oleylamine and 20 ml of benzyl ether were mixed in a 3 neck flask and were stirred continuously under a blanket of nitrogen. The temperature was ramped up slowly to 200 °C (2.5 °C /min) and the mixture was kept at this temperature for 2 hrs. Finally, the mixture was refluxed at 300 °C for 1 hr. The resulting black mixture was cooled to room temperature and ethanol was added, followed by centrifugation at 7000g to separate out the magnetic nanoparticles. The centrifuged product was resuspended in hexane and used for seed-mediated growth.

3.3.3 Seed-Mediated Growth of Larger Nanoparticles

Two millimoles of Iron(III) acetylacetonate, 10 mmol of 1-2 hexadecanediol, 2mmol of oleic acid, 2 mmol of oleylamine , 20 ml of benzyl ether and 80 mg of seeds in 4 ml of hexane were mixed in a 3 neck flask and stirred continuously under a blanket of nitrogen. The mixture was kept at 100 °C for 30 mins and at 200 °C for 1h. Finally, the mixture was refluxed at 300 °C for 30 mins. The magnetite was recovered using the procedure outlined above. The resulting magnetic nanoparticles were used as seeds for subsequent synthesis and growth of particles. In this manner stable 12 nm nanoparticles were synthesized.

3.3.4 Angle-Dependent Magnetization Experiments on Planar Nanoparticle Films

Five microliters of 12 nm magnetite nanoparticles at dilute concentrations (0.1; 0.02; 0.01 and 0.005 wt%) were deposited on a silicon substrate and dried under air. The magnetization curves for each sample were measured at orientations of the sample plane relative to the direction of the applied external magnetic field of 0°, 45°, and 90° using a vibrating sampling magnetometer (ADE Model EV5).

3.4 Results and Discussion

We exploit below the results of our theoretical analysis to evaluate systematically the effect of the orientation of an externally-applied magnetic field on the apparent magnetic susceptibility of superparamagnetic nanoparticles in structured arrays. The causes of the apparent orientational dependence of the magnetic susceptibility are the unbalanced contributions to the local magnetic field experienced by any given particle in the array by the fields associated with the dipoles of neighboring particles.

The $\hat{H}_0$-component of the effective magnetic moments of individual particles as a function of the orientation of the array relative to the applied field is shown in Figure 3-3 for mono-, bi- and tri-layer coated beads; the parameters used in these simulations are those for the magnetite nanoparticles used in this work. The magnitude of the magnetic moment (or apparent magnetic susceptibility) is highest for the field applied in the plane of the arrays, i.e., at the equator of the core-shell bead where $\alpha = 0°$, where the fields associated with the individual magnetic dipoles reinforce the applied field, enhancing the alignment of the dipoles with the applied field. At the poles of the bead, on the other hand, where $\alpha = 90°$, the full parallel alignment of the dipoles is unfavorable and the fields from neighboring particle dipoles counteract the applied field so that the net aligning field experienced by the particles is reduced relative to that for non-interacting particles. The effects are most significant for monolayers at the equator, where the apparent magnetic susceptibility is about 66 percent larger than the true susceptibility of non-interacting particle suspensions; at the poles the magnetic

susceptibility is reduced by about 45 percent. Also, since the fields in adjoining layers in multi-layer systems tend to cancel each other to some extent, the maximum increase in apparent magnetic susceptibility for a bilayer is only slightly greater than half that for the monolayer case. For the trilayer, the apparent susceptibilities are smaller yet again, with the two outer layers exhibiting a larger apparent susceptibility than the middle layer. In this case, the middle layer interacts with the top and bottom layers, with fields acting in opposite directions, which results in a lower induced magnetic field acting on the nanoparticles and hence a lower change in apparent magnetic moment. The top and bottom layers, on the other hand, are subjected to asymmetric induced fields and thus exhibit larger apparent magnetic moments than do the particles in the middle layer. At the poles of the bead the relative importance of particle interactions does not change, except now it is a reduction rather than an increase in apparent susceptibility that is predicted for these systems. There is a crossover point near 60° at which the magnetic susceptibilities change order i.e., the monolayer apparent susceptibility becomes less than that of the bilayer or trilayer cases.
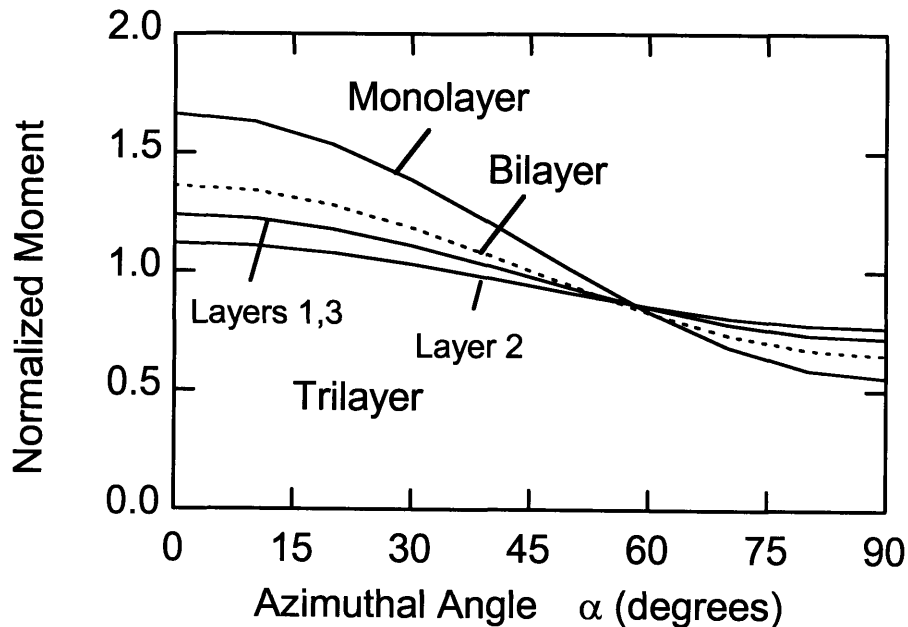
Figure 3-3. The effective magnetic moments of nanoparticles in a core-shell structure depend on their orientation with respect to the applied magnetic field, as determined by their azimuthal position on the bead surface. Monolayers exhibit a stronger response to the applied field than do multilayers owing to the compensating effects of the particle

dipole magnetic fields in adjacent layers. Note that for trilayers, the effective magnetic moments of particles depend on whether they are in the middle layer or in the two outer layers. The moments are normalized with respect to their values in the absence of interparticle interactions.

The effect of interparticle interactions on the average orientation of the individual particle dipoles relative to the direction of the applied magnetic field is shown in Figure 3-4 for the mono-, bi- and trilayers. At the equator and the poles of the core-shell bead, the nanoparticle dipoles align with the applied magnetic field, but at all other angles there is a significant deviation from such alignment, which is a maximum at azimuthal angles close to 60°.
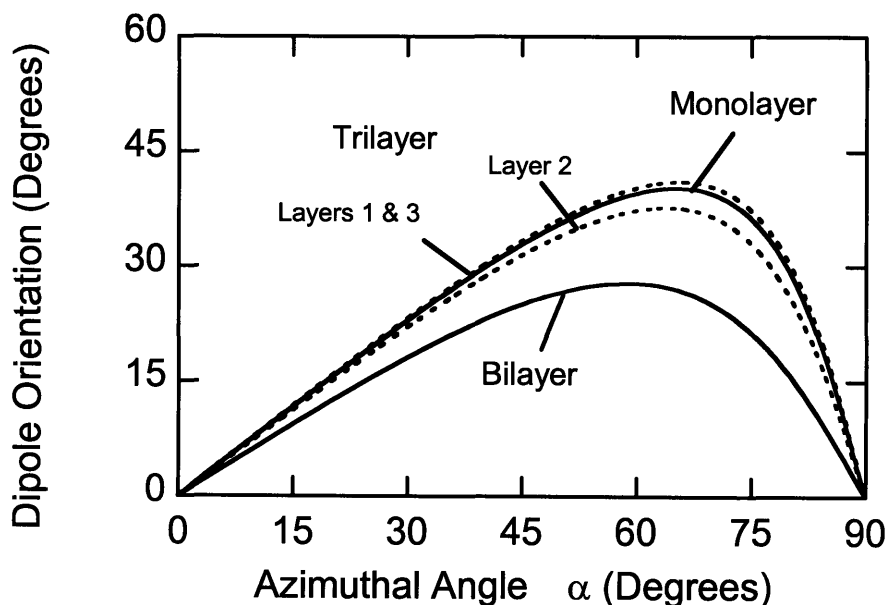
Figure 3-4. The average dipole orientation relative to the externally-applied magnetic field for nanoparticles arrayed as layers on a bead surface depends on both their azimuthal position on the bead surface and on their location within the multilayers.

Figure 3-5 shows that the magnetic moment of a multilayer core-shell bead approaches that of a non-interacting dispersion of nanoparticles, i.e., that of the bulk material, as the number of layers increases. Under these conditions, the interactions of a particle in a given layer with particles in adjacent layers on either side of that layer cancel each other, so that the particle collection behaves as an isotropic bulk material. It is only the layers of particles near the surfaces, for which the inter-layer interactions are

unbalanced, that give rise to the orientation effect observed here – with an increasing number of layers, the fraction of particles participating in 'unbalanced' interlayer interactions becomes smaller and hence the orientation effects are also diminished.
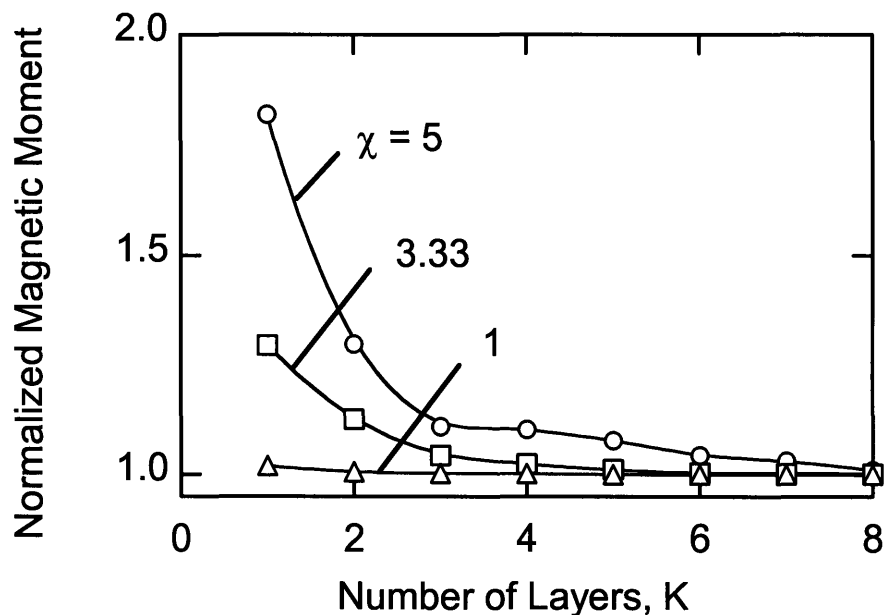
Figure 3-5. The integrated magnetic moments of core-shell beads as determined by the number of layers arrayed on their surfaces, showing the importance of the magnetic properties of the particles themselves, as reflected in the parameter ϕ. The moments are normalized with respect to their values in the absence of interparticle interactions.

The effect on the average particle magnetic moment of changes in χ, for citrate-coated magnetite particles, and δ, for surfactant stabilized nanoparticles, relative their base-case values, is shown in Figure 3-6. With increasing values of χ, the fields associated with the dipoles of individual particles increase, and the induced fields as the dipoles are aligned with the externally-applied magnetic field become more significant for a given field strength H_0. There is a trade-off, however, since the theoretical predictions are valid only at low field strengths far from saturation, where the identity $M = \chi H$ is valid, and with increasing χ, the results are restricted to ever-lower external applied fields. At low external field strength the induced field due to interparticle interactions is comparable to the external field and this is reflected in the higher value of the component of the net magnetic moment in the direction of the applied field. The

interparticle interactions decay rapidly with the separation distance between the particles ($\sim 1/\delta^3$) as shown in Figure 3-6 (b). For $\delta > 2$ nm the interparticle interactions are negligible.
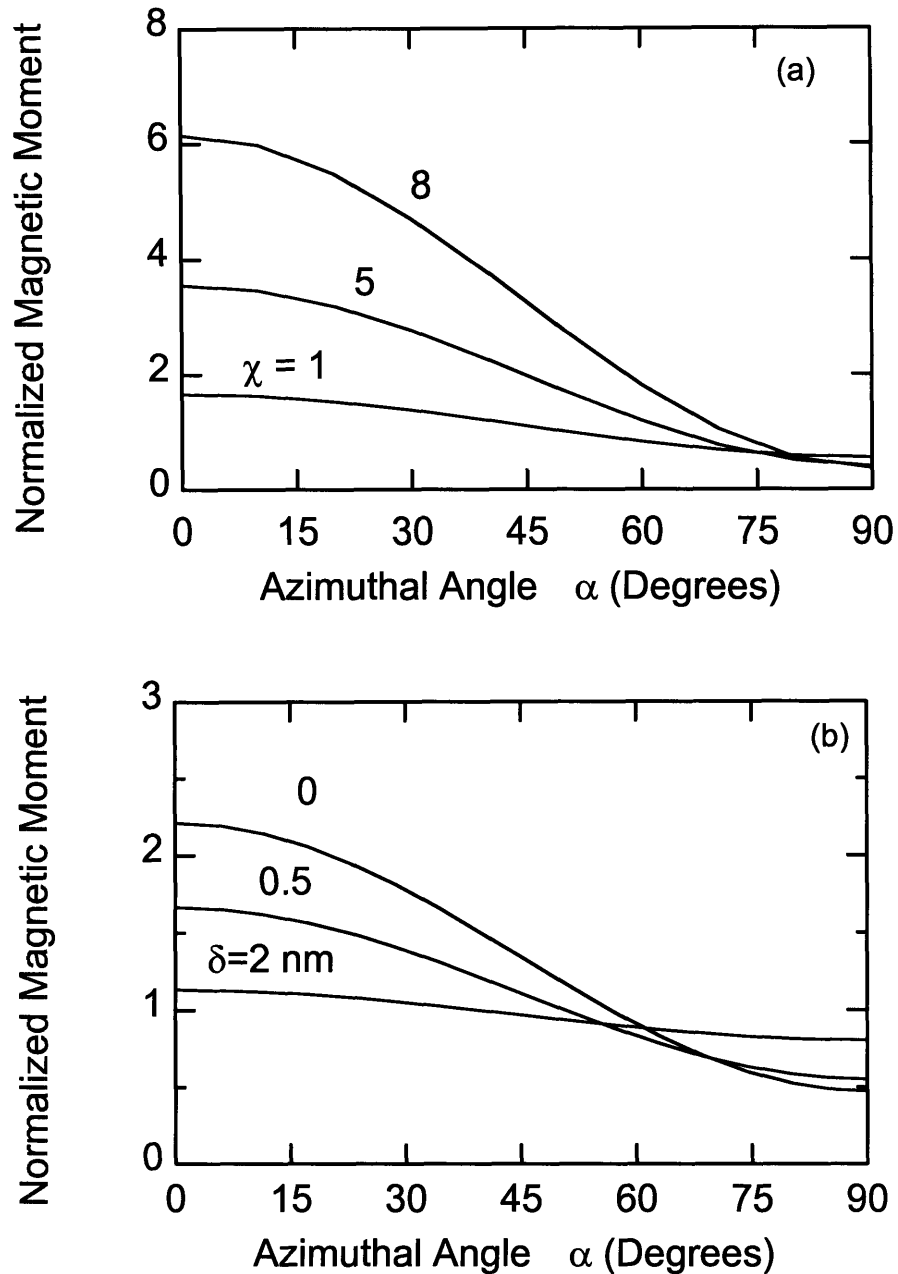
Figure 3-6. Effect of magnetic nanoparticle properties on the normalized magnetic moments of particle monolayers at different azimuthal positions on the bead surface. (a) The larger the intrinsic bulk magnetic susceptibility the greater the effects on the magnetic moments ($\delta = 0$ nm). (b) With increasing surfactant layer thickness, the

particles are further apart and the interparticle interactions are weaker (χ = 3.33 for magnetite, d_p = 8 nm).

At higher magnetic field strengths, the linearity between magnetization and applied magnetic field no longer holds, and we use the perturbation analysis results to explore the effect of the orientation of the nanoparticle layer relative to the applied field on its magnetic response. The predicted magnetization, $\sigma_{i\hat{H}_0}$, for a monolayer is shown in Figure 3-7 as a function of normalized applied field βH_0 for the two extremes of orientation, 0° and 90°, and for different values of the effective magnetic susceptibility, ϕ; the predicted curves are shown only for conditions where $\phi / \beta H_0 \leq 0.1$, in accord with the retention of only the first order term in the perturbation expansion, i.e., the error in the predictions is less than one percent. Clearly, the effect seen at low field strengths, where the normalized response at 0° is greater than that at 90°, as predicted by equation (11) continues into the higher field strength region, described by Equation (39). The differences between the normalized magnetizations for the two orientations decrease until at very high field strengths, the curves for any given value of ϕ approach each other. The effect of ϕ is quite dramatic, in that with increasing ϕ the difference between the two orientations increases significantly; the magnetization for an array in the plane of the field (i.e., α = 0°) increases with increasing ϕ, since the induced dipoles add to the external applied field, while it decreases when the array is perpendicular to field, when the dipoles counteract the applied field.

Three important points emerge from these calculations. First, it has been shown that a monolayer coated core-shell bead has the largest net interparticle interactions, resulting in a higher magnetic moment as compared to the bulk material. Second, with a higher number of magnetic layers, the effect of these interactions dwindles, and above about eight layers we can assume that the particles on the bead behave as bulk material. Finally, the dependence of the moment of the nanoparticle within the shell of a nanoparticle coated bead on its position on the bead surface provides insight into the importance of orientational effects in the magnetic response of multilayered nanoparticle coatings. It is difficult to verify these observations experimentally, however, because it is

challenging to prepare uniformly coated multilayer core-shell magnetic beads, and it is not possible to probe the surface of a bead directly to measure the moments of individual nanoparticles within the layers. However, we can study experimentally the effect of orientation and the number of nanoparticle layers on the effective magnetic properties of
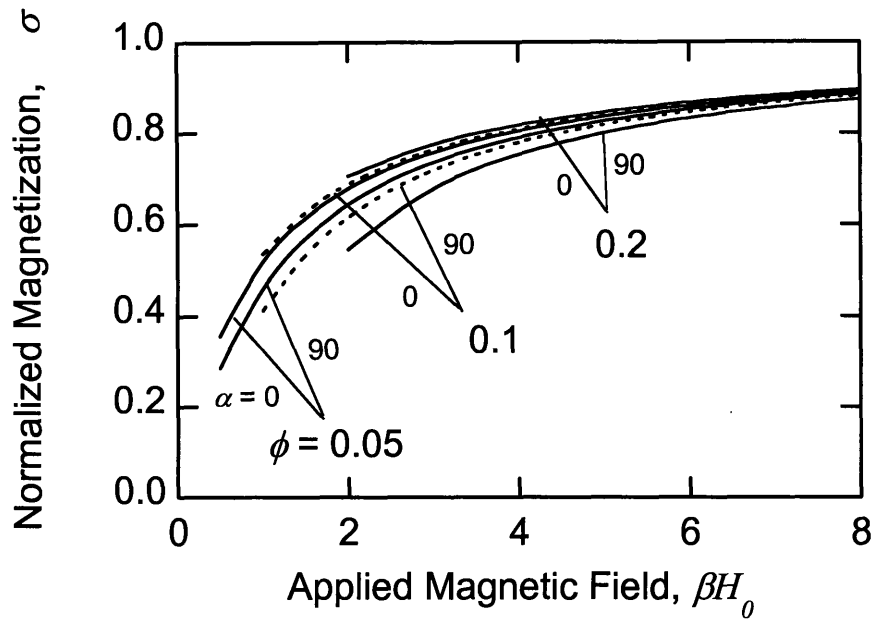
Figure 3-7. The magnetic moments normalized with respect to the saturated magnetization show a strong dependence on orientation of the planar array relative to the magnetic field. With increasing bulk susceptibility, the magnetization increases for particle arrays aligned with the magnetic field (0°), but decrease when the particle layers are normal to the applied field (90°). Only results for which $\phi / \beta H_0 \leq 0.1$ are shown; thus the perturbation predictions are accurate to within one percent.

planar nanoparticle assemblies, which can be prepared by depositing a nanoparticle suspension drop on a planar substrate and evaporating the suspending solvent, as described below.

The number of nanoparticle layers deposited on a planar substrate can be controlled by the concentration of the nanoparticles in the suspension used to prepare the sample, assuming that the area occupied by the droplet is unchanged during the deposition process and is unaffected by the nanoparticle concent   The orientation, α, relative to the applied field direction of the nanoparticle layers on a curved surface (as

98

on beads) on the magnetic moment can be determined by comparing the χ values from the magnetization studies performed on planar samples at different angles (i.e. the angle between the external magnetic field and the sample plane) [34, 36, 38].

The magnetic nanoparticles used in the preparation of the deposited layers were prepared as described in the Experimental section; the TEM micrograph given in Figure 3-8 shows that the particles were reasonably monodispersed and spherical, and of size 12 nm.
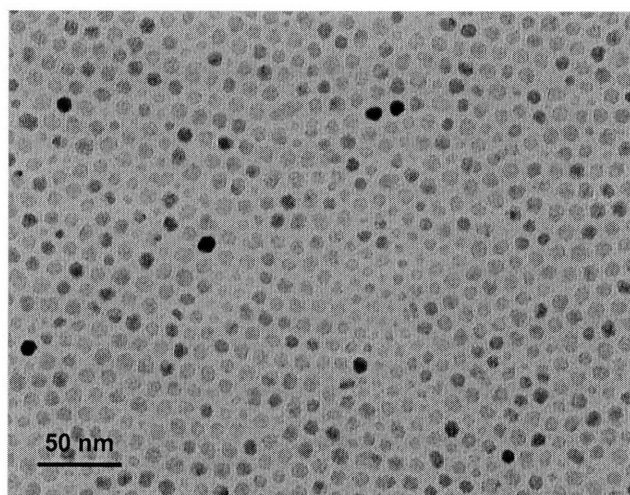
Figure 3-8. TEM micrograph of the 12 nm nanoparticles showing them to be monodisperse and regularly shaped.

Magnetization curves obtained for a nanoparticle multi-layer on a planar substrate oriented at three different angles relative to the applied field ($\alpha = 0°$, 45°, and 90°) are shown in Figure 3-9(a); similar curves were obtained for all samples, in which the effective number of layers varied from 1 to 20. In no cases did we observe hysteresis or remanence in the samples, indicating that the particles retained their superparamagnetic properties even when deposited in packed layers. It is clear that the effective magnetic susceptibility, given by the slopes of the curves under low field conditions, as shown in Figure 3-9(b), is dependent on the orientation of the sample relative to the applied field. The magnetization curves, with the magnetic moments normalized with respect to the saturation magnetization, are shown in Figure 3-9(c), and are in good agreement with the

values predicted using the perturbation model and reasonable values of ϕ and β for magnetite, again showing the importance of the orientation of planar arrays on their response to an applied magnetic field.
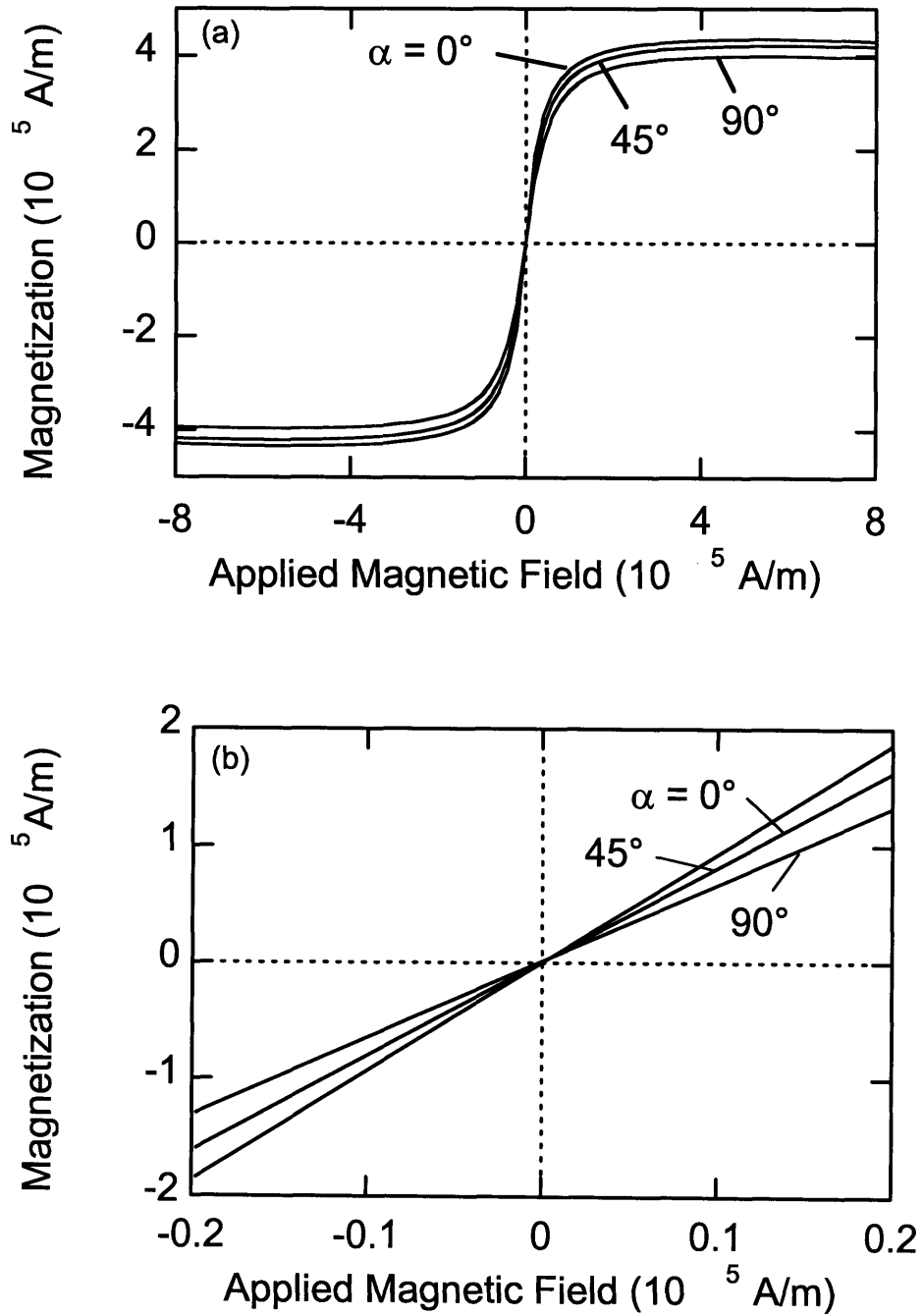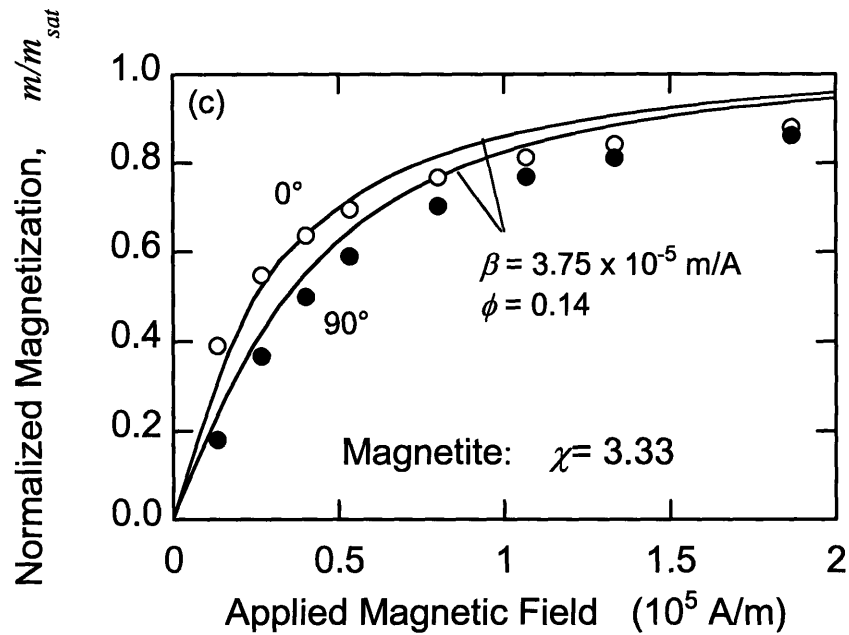
Figure 3-9. Experimental magnetization curves for planar arrays at different orientations relative to the applied magnetic field, as determined by vibrating sample magnetometry. (a) Complete magnetization curves showing the superparamagnetic properties of the particles as reflected in the absence of remanance, and that the saturation magnetization depends on the orientation. (b) The magnetization at low field strengths showing that the magnetic susceptibility, proportional to the slope, depends on the orientation of the array. (c) Comparison of normalized experimental and predicted magnetization curves.

The effect of orientation on the normalized magnetic moments is shown in Figure 3-10(a) where the experimental results are compared favorably with model predictions for the orientational dependence of a multilayer system. An unexpected observation in these experiments was the orientation dependence of the saturation magnetization, i.e., the magnetization curves for the same sample have different asymptotic values at high field strengths, which is not predicted by the particle interaction models presented in this paper. The saturation magnetization is shown in Figure 3-10(b) to vary by about ten percent on changing orientation from 0 to 90°, but not significantly on nanoparticle concentration (i.e., number of layers). Additional experiments and theoretical analyses indicated that such effects are not due to particle anisotropy or irregular surface coatings, and that they are completely reproducible.
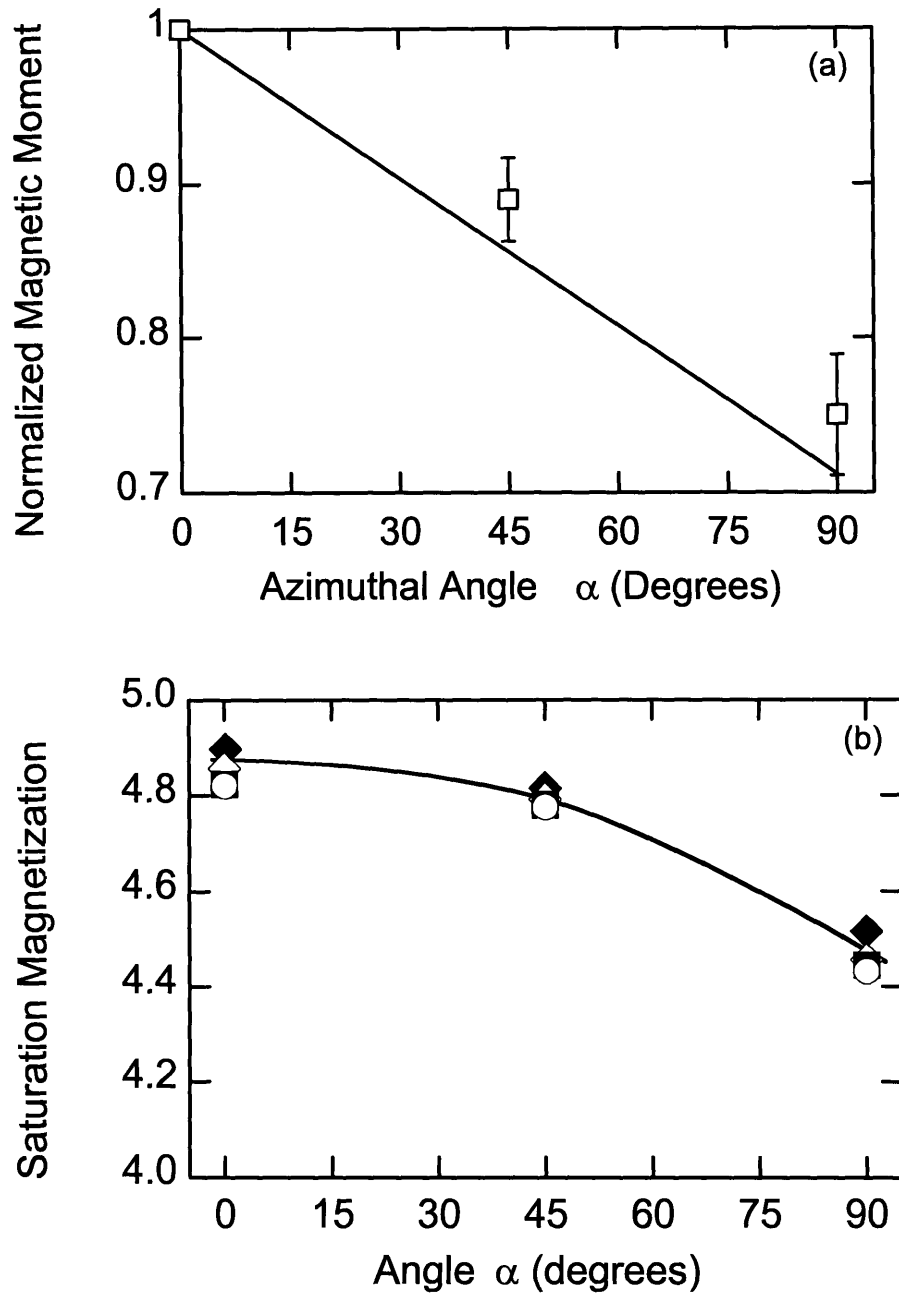
Figure 3-10. The effect of orientation on (a) the normalized magnetic moment and (b) the saturation magnetization.

When normalized by their respective saturation magnetizations, however, these curves show the same trends with orientation as predicted by the theoretical perturbation

analysis and shown in Figure 3-9(c). Thus, the observed effects of orientation on the magnetization curves are real, even when the effect of the anomalous variation of the saturation is accounted for in the normalization of the curves.

The fractional changes in magnetic moment when the layers are orientated at $45°$ and $90°$, relative to the moment at an orientation of $0°$, i.e., $\Delta\mu/\mu_0 = (\mu_\alpha - \mu_0)/\mu_0$, are shown in Figure 3-11 as a function of the nominal number of layers deposited on the substrate. For a small number of layers the experimental and predicted results agree well, but the deviations between the two become more significant as the number of layers increases. These deviations can be attributed to non-uniformities in the layers deposited on the substrate surface.
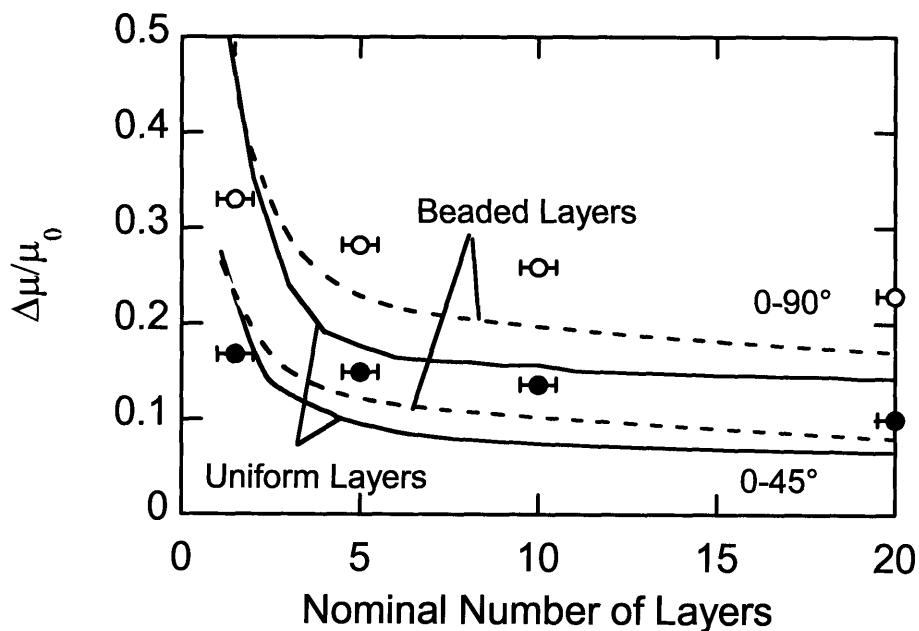
Figure 3-11. The relative changes in magnetic moment with changes in orientation of the nanoparticle arrays of varying number of layers. The solid lines are the predicted effects for a uniforma layers, while the broken lines are adjusted to allow for the fact that the layers are not uniform, but beaded.

The Atomic Force Microscopy (AFM) results shown in Figure 3-12 indicate that the multilayer-coated surfaces are not uniform in thickness, but consist of small islands of nanoparticle clusters surrounded by regions in which the effective number of layers is considerably smaller than the nominal number calculated based on the assumption of

103

uniform layers. The size of these clusters also depends on the surface concentration of particles, being smaller for lower surface concentrations, i.e., for lower nominal numbers of layers. We can account for these effects approximately by noting that it is primarily the outer layers that contribute to the deviations from bulk-like behavior, while the inner layers exhibit bulk-type behavior, which is isotropic. Thus, we can assume that the net changes in magnetic moment can be ascribed primarily to effects associated with the particles in the outer layer or two, and not to the particles in the inner layers. The fraction of the total nanoparticle population that reports to the surface layers on a beaded surface can be significantly greater than when the surface is coated uniformly. To account for this increased surface effect, we revised the estimate of the moments using the equation

$$\frac{\Delta\mu}{\mu_0} = \frac{\left[f_s\mu_{\alpha,s} + (1-f_s)\mu_{\alpha,b}\right] - \left[f_s\mu_{0,s} + (1-f_s)\mu_{0,b}\right]}{f_s\mu_{0,s} + (1-f_s)\mu_{0,b}} = \frac{f_s\left(\mu_{\alpha,s} - \mu_{0,s}\right)}{f_s\mu_{0,s} + (1-f_s)\mu_{0,b}} \tag{42}$$

where f_s is the volume fraction of the nanoparticles in the surface layers, and $\mu_{\alpha,s}$ and $\mu_{\alpha,b}$ are the moments of the surface and bulk nanoparticles, respectively, at an orientation angle of α. Note that we assume that the bulk moments are not dependent on the orientation, and allow only for variations in the moments of the surface layers with orientation. The fraction f_s can be estimated if it is assumed that the islands are hemispherical in shape with diameter d, and the surface layer has a thickness given by the nanoparticle diameter, a_p, as shown schematically in Figure 3-12(b). Then, we have, for $a_p << d$,

$$f_s \approx \frac{6a_p}{d} \tag{43}$$

104
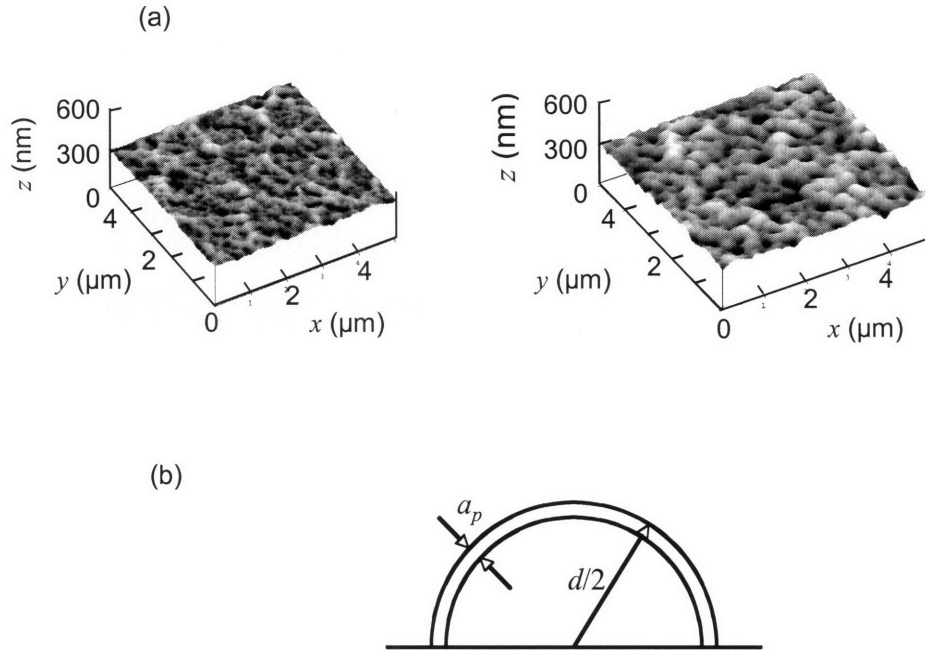
Figure 3-12. AFM pictures showing that the nanoparticle arrays on planar substrates are not uniformly distributed, but consist of islands of clustered particles ranging in size from 100 to 500 nm. Larger islands are formed when more particles are deposited on the substrate, i.e., for larger nominal numbers of layers.

For typical values of $d \sim 300$ to 500 nm, corresponding to the nominal numbers of layers from 2 to 20, we obtain $f_s \sim 0.2$ to 0.1. We use the values for μ_s and μ_b calculated for each system with particular number of layers to estimate the correction factors to allow for the beaded layers, with the results shown using the broken lines in Figure 3-11. Clearly, orientational effects can be described well by our modeling approach even when there are significant non-uniformities in the layers.

3.5 Conclusions

We have shown both theoretically and experimentally that the magnetization curves of structured layers of superparamagnetic nanoparticles can depend on the orientation of the layers relative to the applied magnetic field. The primary reason for this effect is that the magnetic fields of the dipole alignments induced in neighboring

particles by the field acting on them can act either in concert with the applied magnetic field, as when the field direction and the array are co-directional, or can oppose it, as when the array is normal to the applied field. These results have implications for the effective magnetic properties of magnetic nanoparticle-coated beads, where the layers adopt all orientations relative to the applied field, the equatorial particles being aligned with the field and the particles at the poles of the bead being arrayed perpendicular to the external field. For magnetite particle monolayers, for instance, about a 30 % increase in effective magnetic susceptibility is predicted relative to the case when the particles do not interact. As the number of layers increases, however, these effects are diminished, which we attribute to the reduction in the asymmetry of the interactions between particles in adjoining layers when in the 'bulk' state relative to when they are in the outer layers of the particle arrays.

Acknowledgments

3.6   References

1.   Chouly, C., L. Bordenave, R. Bareille, V. Guerin, A. Baquey, D. Pouliquen, C. Baquey, and P. Jallet, *In vitro study of the hemocompatibility of superparamagnetic contrast agent for magnetic resonance imaging.* Clinical materials, 1994. **15**(4): p. 293-301.

2.   Kim, E.H., H.S. Lee, B.K. Kwak, and B.-K. Kim, *Synthesis of ferrofluid with magnetic nanoparticles by sonochemical method for MRI contrast agent.* Journal of Magnetism and Magnetic Materials, 2005. **289**: p. 328-330.

3.   Kopelman, R., Y.-E.L. Koo, M. Philbert, B.A. Moffat, G. Ramachandra Reddy, P. McConville, D.E. Hall, T.L. Chenevert, M.S. Bhojani, S.M. Buck, A. Rehemtulla, and B.D. Ross, *Multifunctional nanoparticle platforms for in vivo MRI*

enhancement and photodynamic therapy of a rat brain cancer. Journal of Magnetism and Magnetic Materials, 2005. **293**(1): p. 404-410.

4.   Nitin, N., L.E.W. LaConte, O. Zurkiya, X. Hu, and G. Bao, *Functionalization and peptide-based delivery of magnetic nanoparticles as an intracellular MRI contrast agent.* JBIC, Journal of Biological Inorganic Chemistry, 2004. **9**(6): p. 706-712.

5.   Dobson, J., *Gene therapy progress and prospects: magnetic nanoparticle-based gene delivery.* Gene Therapy, 2006. **13**(4): p. 283-287.

6.   Dutz, S., R. Hergt, J. Muerbe, J. Toepfer, R. Mueller, M. Zeisberger, W. Andrae, and M.E. Bellemann, *Magnetic nanoparticles for biomedical heating applications.* Zeitschrift fuer Physikalische Chemie (Muenchen, Germany), 2006. **220**(2): p. 145-151.

7.   Ma, Y., S. Manolache, F. Denes, D. Vail, D. Thamm, and I. Kurzman, *Immobilization of doxorubicin on surfaces of plasma synthesized C/Fe and C/Fe/N magnetic nanoparticles for targeted drug delivery.* Surface Engineering, Proceedings of the International Surface Engineering Congress, 3rd, Orlando, FL, United States, Aug. 2-4, 2004, 2005: p. 63-71.

8.   Mykhaylyk, O.M., N.O. Dudchenko, and A.K. Dudchenko, *Pharmacokinetics of the doxorubicin magnetic nanoconjugate in mice. Effects of the nonuniform stationary magnetic field.* Ukrains'kii Biokhimichnii Zhurnal, 2005. **77**(5): p. 80-92.

9.   Yao, P., A.-j. Zhao, C.-s. Kang, X.-b. Yuan, J. Chang, and P.-y. Pu, *Construction of multi-functional delivery system: transferrin mediated tat and drug-loaded magnetic nanoparticles.* Nanoscience, 2005. **1**(1): p. 18-26.

10.   Haik, Y., V. Mohite, and C.J. Chen, *Magnetic nanoparticles for self controlled hyperthermia treatment of tumors.* NSTI Nanotech 2005, NSTI Nanotechnology Conference and Trade Show, Anaheim, CA, United States, May 8-12, 2005, 2005. **1**: p. 300-303.

11.   Ito, A., H. Honda, and T. Kobayashi, *Cancer immunotherapy based on intracellular hyperthermia using magnetite nanoparticles: a novel concept of*

\"heat-controlled necrosis\" with heat shock protein expression. Cancer Immunology Immunotherapy, 2005. **55**(3): p. 320-328.

12. Matsuki, H., *New trends in hyperthermia technology.* Magune, 2006. **1**(2): p. 70-76.

13. Rabin, Y., *Is intracellular hyperthermia superior to extracellular hyperthermia in the thermal sense?* International journal of hyperthermia: the official journal of European Society for Hyperthermic Oncology, North American Hyperthermia Group, 2002. **18**(3): p. 194-202.

14. Yan, S.-y., D.-s. Zhang, N. Gu, J. Zheng, Z.-y. Wang, Y.-q. Du, H.-y. Ni, M. Ma, L.-q. Jin, and M.-l. Wan, *The biocompatibility study of magnetic nanoparticles containing F2O3 used in tumor hyperthermia.* Dongnan Daxue Xuebao, Yixueban, 2005. **24**(1): p. 8-12.

15. Bucak, S., D.A. Jones, P.E. Laibinis, and T.A. Hatton, *Protein Separations Using Colloidal Magnetic Nanoparticles.* Biotechnology Progress, 2003. **19**(2): p. 477-484.

16. Ditsch, A., S. Lindenmann, P.E. Laibinis, D.I.C. Wang, and T.A. Hatton, *High-Gradient Magnetic Separation of Magnetic Nanoclusters.* Industrial & Engineering Chemistry Research, 2005. **44**(17): p. 6824-6836.

17. Moeser, G.D., W.H. Green, P.E. Laibinis, P. Linse, and T.A. Hatton, *Structure of Polymer-Stabilized Magnetic Fluids: Small-Angle Neutron Scattering and Mean-Field Lattice Modeling.* Langmuir, 2004. **20**(13): p. 5223-5234.

18. Owen, C.S., *Magnetic cell sorting using colloidal protein-magnetite.* Journal of immunogenetics, 1989. **16**(2): p. 117-23.

19. Ghebremeskel, A.N. and A. Bose, *A continuous, hybrid field-gradient device for magnetic colloid-based separations.* Journal of Magnetism and Magnetic Materials, 2003. **261**(1-2): p. 66-72.

20. Furst, E.M. and A.P. Gast, *Micromechanics of dipolar chains using optical tweezers.* Physical Review Letters, 1999. **82**(20): p. 4130-4133.

21. Melle, S., G.G. Fuller, and M.A. Rubio, *Structure and dynamics of magnetorheological fluids in rotating magnetic fields.* Physical Review E, 2000. **61**(4): p. 4111-4117.

22. Nakano, M.K., K., *Electro-Rheological Fluids, Magneto-Rheological Suspensions and Their Applications.* 1998, Singapore: World Scientifica.

23. Tao, R., *Super-strong magnetorheological fluids.* Journal of Physics-Condensed Matter, 2001. **13**(50): p. R979-R999.

24. Biswal, S.L. and A.P. Gast, *Rotational dynamics of semiflexible paramagnetic particle chains.* Physical Review E, 2004. **69**(4).

25. Gulley, G.L. and R. Tao, *Structures of a magnetorheological fluid.* International Journal of Modern Physics B, 2001. **15**(6-7): p. 851-858.

26. Goubault, C., P. Jop, M. Fermigier, J. Baudry, E. Bertrand, and J. Bibette, *Flexible magnetic filaments as micromechanical sensors.* Physical Review Letters, 2003. **91**(26).

27. Goubault, C., F. Leal-Calderon, J.L. Viovy, and J. Bibette, *Self-assembled magnetic nanowires made irreversible by polymer bridging.* Langmuir, 2005. **21**(9): p. 3725-3729.

28. Caruso, F., R.A. Caruso, and H. Möhwald, *Nanoengineering of Inorganic and Hybrid Hollow Spheres by Colloidal Templating.* Science, 1998. **282**(5391): p. 1111-1114.

29. Singh, H., P.E. Laibinis, and T.A. Hatton, *Rigid, superparamagnetic chains of permanently linked beads coated with magnetic nanoparticles. Synthesis and rotational dynamics under applied magnetic fields.* Langmuir, 2005. **21**(24): p. 11500-11509.

30. Xu, C., Y.Q. Ma, and P.M. Hui, *Equilibrium magnetic moment configurations in magnetic nanoparticle films: Effects of anisotropy, dipolar interaction, and Zeeman energy.* Journal of Applied Physics, 2005. **98**(8): p. 084303/1-084303/8.

31. Iglesias, O. and A. Labarta, *Magnetic relaxation in a model of interacting nanoparticles in terms of microscopic energy barriers.* Physica Status Solidi A: Applied Research, 2004. **201**(15): p. 3329-3332.

32. Ghazali, A. and J.-C. Levy, *Two-dimensional arrangements of magnetic nanoparticles.* Physical Review B: Condensed Matter and Materials Physics, 2003. **67**(6): p. 064409/1-064409/5.

33. Tamura, I. and T. Mizushima, *Explanation for magnetic properties of interacting iron oxide nanocrystals.* Journal of Magnetism and Magnetic Materials, 2002. **250**(1-3): p. 241-248.

34. Vasquez-Mansilla, M., R.D. Zysler, C. Arciprete, M.I. Dimitrijewits, C. Saragovi, and J.M. Greneche, *Magnetic interaction evidence in a-Fe2O3 nanoparticles by magnetization and Mossbauer measurements.* Journal of Magnetism and Magnetic Materials, 1999. **204**(1-2): p. 29-35.

35. Gonzalez, L.A., in *Chemical Engineering.* 2005, MIT: Cambridge.

36. Rosenweig, R.E., *Ferrohydrodynamics.* 1985, New York: Cambridge University Press.

37. Sun, S.H., H. Zeng, D.B. Robinson, S. Raoux, P.M. Rice, S.X. Wang, and G.X. Li, *Monodisperse MFe2O4 (M = Fe, Co, Mn) nanoparticles.* Journal of the American Chemical Society, 2004. **126**(1): p. 273-279.

38. Huke, B. and M. Lucke, *Magnetization of ferrofluids with dipolar interactions: A Born-Mayer expansion.* Physical Review E, 2000. **62**(5): p. 6875-6890.

Chapter 4

Synthesis of Flexible Magnetic Nanowires of Permanently-Linked Core-Shell Magnetic Beads Tethered to a Glass Surface Patterned by Microcontact Printing

4.1 Introduction

Magnetic colloids often undergo reversible aggregation in the presence of a magnetic field. Once the magnetic field is removed, however, thermal energy disrupts the structures and the magnetic colloids return to their original freely dispersed state. By linking the magnetic beads together permanently once they are arranged in the magnetic field, it is possible to preserve their chain structure even after the field is removed. Depending on the chemistry used to link the beads, these chains can be either flexible [1, 2] or rigid [3].

To date, there has been limited research into the formation of permanently linked magnetic chains, also known as magnetic nanowires [4]. Goubalt et al. [4] have exploited depletion forces due to the presence of high molecular weight polymers to create the desired flexible nanowires by bridging the polymer between the magnetic colloids. The environmental sensitivity of the depletion effect can, however, make the chains very sensitive to exposure to different medium conditions. Gast et al. [1] have synthesized flexible chains of superparamagnetic beads linked permanently by a flexible polymer using either amine coated beads linked by gluteraldehyde, or streptavidin-coated beads linked with a poly(ethylene) glycol linker bifunctionalized with biotin. These linked chains can be used as micromagnetic actuators and micromechanical sensors [2], micropumps and micromixers [5], and, in DNA and other bio-separations, as obstacles to impede the convective transport of biological species [6, 7]. Once these permanently linked chains have been formed, they can be fixed on channel surfaces to prevent their drag-induced convective migration in microfluidic flow processes. To this end, Lyles et.

al. [8] showed that magnetic colloids patterned on a glass surface can serve as templates for chain growth from the patterned spots. Their multi-step approach relied on an intial seeding of the system with magnetic colloids to adsorb them on functionalized spots patterned on the surface by microcontact printing, followed by a second step in which additional magnetic colloids were introduced to the microchannel and the chains were grown from the surface-attached colloids and linked by reaction.

We have developed a flexible, inexpensive, versatile, and efficient one-step method to produce stable, tethered, flexible chains of magnetic colloids that is simpler to implement than the multi-step approach suggested by Lyles et al. [8], and that uses inexpensive chemical reagents for the covalent coupling of the beads. This approach can, in principle, be used with any magnetic colloidal particles, including those used by others [1, 2, 4, 8] in which the magnetic materials are distributed as nanoparticles uniformly throughout the polymer beads. Here, however, we have elected to use core-shell particles consisting of polystyrene beads coated with polyelectrolyte (PE) layers and maghemite (γ-Fe$_2$O$_3$) nanoparticles [9], because the magnetic and surface properties can be manipulated readily by selecting the types, quantities and ratios of the various surface coatings used. We were also able to grow the chains directly in a Poly(dimethylsiloxane) channel using this technique. In this Chapter, we provide details of the synthesis procedures developed for the tethering of flexible chains either to glass surfaces or directly inside PDMS microchannels, and report on some aspects of the equilibrium responses of these chains to varying magnetic fields. The response of the chains to a rotating magnetic field can be exploited for micropumping. This is entailed in the final part of the Chapter.

Figure 4-1 illustrates the procedures for both the synthesis of the core-shell magnetic colloids and the one-step assembly, linking and tethering of magnetic chains of these beads to form the magnetic nanowires within a glass or PDMS microchannel. The glass surface of the glass microchannel was patterned with an amine functionality by microcontact printing [10, 11] to enable selective localization of primary beads on the microchannel surface and their subsequent covalent attachment through an amidation reaction between the patterned amine functionality and the carboxylated bead surfaces.

The PDMS microchannel was uniformly coated with amine functionality. The non-adsorbed core-shell magnetic beads remaining in suspension formed well-defined chains across the channel, anchored to the surface-adsorbed beads, on application of a magnetic field. The adjacent beads in any given chain were linked together by a diamine compound using amidation chemistry to yield tethered, flexible magnetic nanowires.
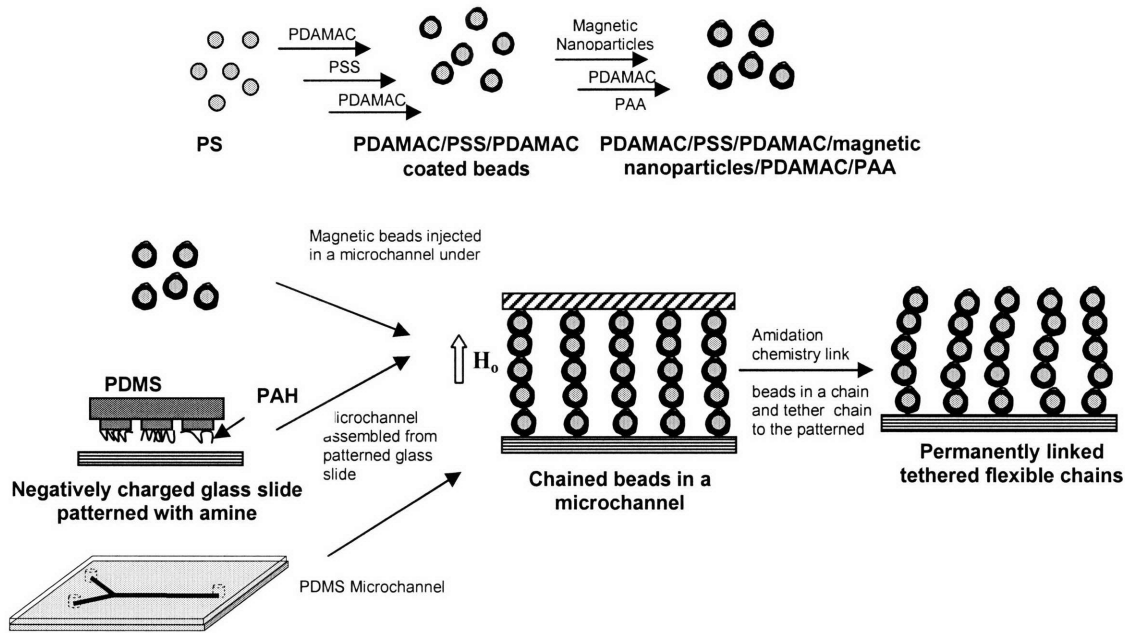
Figure 4-1. Process for producing permanently linked flexible tethered magnetic chains. (a) Preparation of carboxylated core-shell magnetic beads using the layer-by-layer technique [3, 9] (b) Directed assembly and chemical linking of magnetic colloids on a patterned glass surface in a microchannel to form tethered magnetic chains of controlled height, flexibility and diameter.

4.2 Experimental Section

4.2.1 Carboxylated Magnetic Beads

Core-shell magnetic beads were prepared as discussed in an earlier communication [3] using a method similar to that developed by Caruso et al. [12]. In brief, the charge on the initially negatively charged sulfonated polystyrene (PS) beads (Spherotech, average diameter 790 ± 19 nm) was manipulated by successively coating the beads with positively charged poly (diallydimethyl) ammonium chloride (PDAMAC, MW 150,000, Aldrich) and negatively charged polystyrene sulfonate (PSS, MW 70,000, Aldrich) polyelectrolyte layers. In a typical PE coating process, 0.5 mL of a 0.5 wt%

solution of PS beads was suspended in an aqueous solution of 0.5 mL of PE (1 mg/mL). After 30 min of adsorption, the beads were separated by centrifugation at 7000g for 10 min and re-suspended in water. This process was repeated three times. After three PE coatings to generate a PDAMAC/PSS/PDAMAC multilayer, the positively charged beads were coated with negatively charged citrate-coated magnetic nanoparticles prepared using Massart's method [13]; the complete coating of the beads is evident from the Scanning Electron Microscope (JEOL-6060 SEM) images shown in Figure 4-2. The resulting magnetic beads were again coated with PDAMAC and finally with polyacrylic acid (PAA, MW 100,000, Aldrich). During the coating of the magnetic beads with PAA, the pH of the PAA solution was adjusted to 7.0 to ensure that the PAA was negatively charged. This process resulted in the formation of magnetic beads functionalized with carboxylic acid groups. Reversal of the surface charge on the PS beads during the sequential layer-by-layer assembly of PE layers was confirmed by Zeta potential measurements (Brookhaven, Zetapals). These beads, which have been characterized in detail elsewhere [3], were superparamagnetic and chained reversibly in the presence of an external magnetic field.
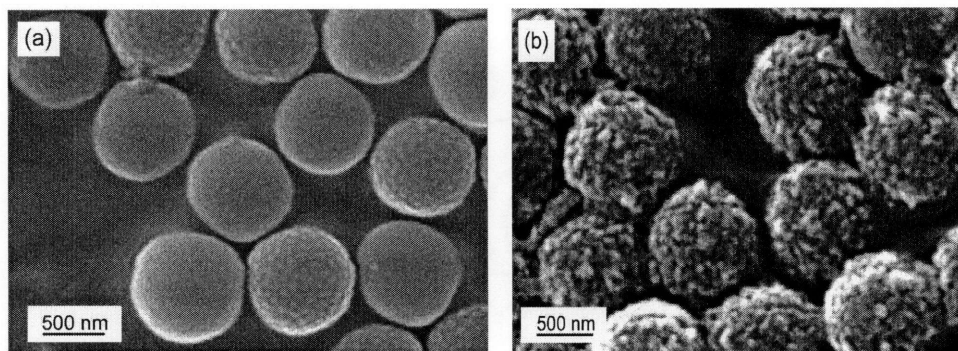
Figure 4-2. SEM micrographs of (a) plain PS beads and (b) magnetic nanoparticle-coated beads. The samples were sputter coated with gold for better contrast. The thickness of the magnetic coating was estimated to be 25 nm based on the differences in the diameters of the coated and the uncoated beads.

4.2.2 Patterning

A glass slide coated with PE multilayers was patterned with amine functionality in a regular array of equally-spaced spots of defined size. To initiate the deposition of PE

multilayers [14], the glass slide was cleaned in a plasma chamber under oxygen (Harrick Scientific PDG-32) and was alternately dipped in PDAMAC and PSS solutions (5 mg/mL, 0.1 M NaCl) for 20 min. After each coating of PDAMAC or PSS, the glass slide was rinsed with MilliQ water for 1 min. In this manner, five PE bilayers were coated on the glass slide with PSS as the final coating.

Poly(dimethylsiloxane) (PDMS, Dow Corning) stamps with periodic arrays of dots [15] were utilized to pattern the amine functionality on the PE-coated glass slides. The stamp was cleaned with soap water solution and dried under nitrogen. It was then exposed to 0.5 wt%, pH 10, poly(allylamine) (PAL, MW 65,000, Aldrich) solution for 10 min. After this inking process the stamp was dried under nitrogen and placed on the multilayer-coated glass slide for 30 min. A microchannel was constructed using patterned and plain glass slides separated by a teflon spacer of desired thickness (12 μm, 25 μm, 50 μm or 75 μm) selected according to the required the channel height.

PDMS microchannels with a height of 75 μm and a width of 2 mm were prepared as explained in Chapter 2 (Section 2.2.3). The channel was filled with PDAMAC solution (5 mg/mL, 0.1 M NaCl) followed by rinsing with MilliQ water after 20 min. This was repeated with PSS (5 mg/mL, 0.1 M NaCl) solution and finally with PAL solution (0.5 wt%, pH 7) to get a uniform coating of amine groups .

4.2.3 Linking

0.2 mL of 0.1 wt% of carboxylated beads with 0.005M of 1-[3-(dimethylamino)propyl]-3-ethylcarbodiimide hydrochloride (EDC, Aldrich) and 0.005 M of diamine crosslinker was injected into microchannel (Glass or PDMS Microchannel). Either 2,2'-(ethylenedioxy)bis(ethylamine) (EBE, MW 148.21, Aldrich) or Polyethylene glycol (PEG) diamine (XTJ 502, MW 2000, Huntsman) was used as the diamine linker. The microchannel was then placed in a uniform magnetic field created by two neodymium-boron-iron magnets (200 mT). The reaction was quenched after 2 h by injecting 10 μL of 2-mercaptoethanol (Aldrich). The product formed in the microchannel was viewed under an optical microscope (Zeiss, Axiovert 200) using a 20X/1.0 objective, and images were captured at a speed of 30 frames/s using a digital camera (Hitachi,

KPM1A) with Scion Image processing software (NIH public domain). Rotating magnetic field created by applying sinusoidal current $I = I_o sin(\omega t)$ and $I = I_o sin(\omega t + \pi/2)$ which have a phase lag of $\pi/2$ on two orthogonal pairs of magnetic coils. This resulted in a homogeneous magetic field in the horizontal direction. The magnetic coils were prepared by wounding 2000 turns of 20 gauge copper wire on a cast iron core. The ac sinusoidal current was generated using a multifrequency synthesizer (HP 8904A). The current was magnified using an amplifier. Magnetic field up to 200 mT was generated using this set up.

4.2.4 Micropumping

10 μl of 10 μm PS beads (Spherotech) were injected in the PDMS microchannel with the tethered chains. The microchannel was placed in the rotating field set up. We waited for 2 hr for the system to reach equilibrium before the field was turned on.

4.3 Results

Following the injection of the carboxylated beads, EDC, and linker molecules into the microchannel, the formation of permanently linked chains was controlled by the sequence of bead adsorption on the patterned spots, chaining of remaining suspended beads, and covalent linking of the chained beads to each other and to the surface. The positively-charged patterned dots were covered with negatively-charged beads due to electrostatic interaction, the number of adsorbed beads on each spot being determined by the relative sizes of the dots and the projected areas of the beads. When a transverse magnetic field was applied to the suspension, chains of beads were formed, emanating from these adsorbed particles. The carboxylic acid groups on adjacent beads in a chain were linked together by a diamine linker molecule via amidation, while the carboxylated beads adsorbed to the surface of the glass slide were similarly attached covalently to the glass side by amidation reaction with the amines on the patterned area. This led to permanently linked flexible superparamagnetic chains tethered to the glass surface. The time scale for adsorption and chaining was on the order of milliseconds [16], while that of the linking reaction was an hour or more. Some permanently linked untethered chains were also formed during this process but they could be washed off easily.

The length of the nanowire was controlled by the spacer thickness while the diameter and spacing of the chains or chain clusters were determined by the spot patterns established during the microcontact printing. The optical micrographs in Figure 4-3 show clearly the spacing of the patterned spots on the glass surface, and the effect of tethered chain length (or microchannel height; 25 μm in Figures 4-3(a) and (b) and 75 μm in Figures 4-3(c) and (d)) on the relative orientations of the chains in the absence and presence of an applied magnetic field. The short chains, once formed, tended to retain their vertical orientation even after the magnetic field was removed, and are seen end-on as a pattern of dots in Figure 4- 3(a). These chains responded to a new magnetic field by aligning in the direction of the applied field, as shown in Figure 4-3(b). The longer chains exhibited different behavior in that, in the absence of a magnetic field, they tended to bend downwards under their own weight to form the loops seen in Figure 4-3(c), which generally unfurled on the application of a new magnetic field (Figure 4-3(d)). Not all the chains unfolded, however, because some of the looped chains were tethered at both ends; although this behavior was observed primarily when the spacer thickness was greater than 50 μm, some of the chains in the shallower channels also formed loops (Figure 4-3(b)), probably because of non-idealities and fluctuations in the chain orientation during growth.
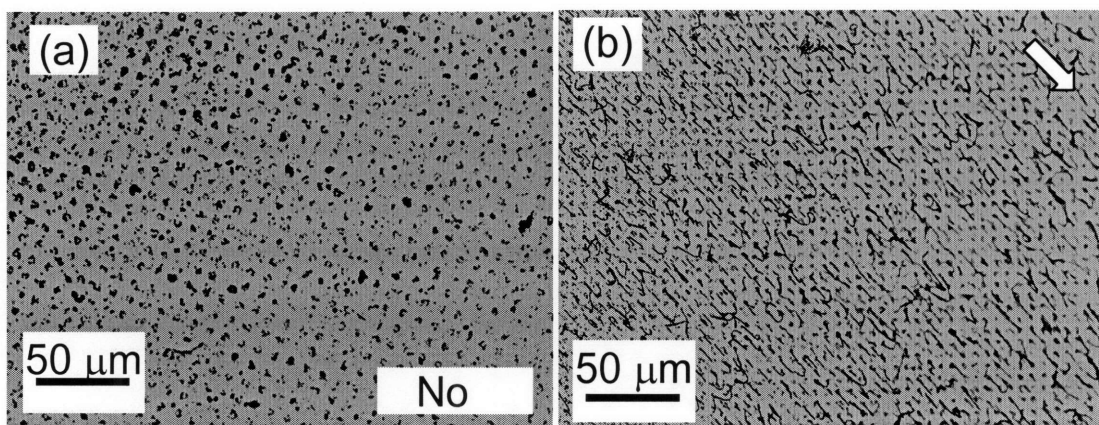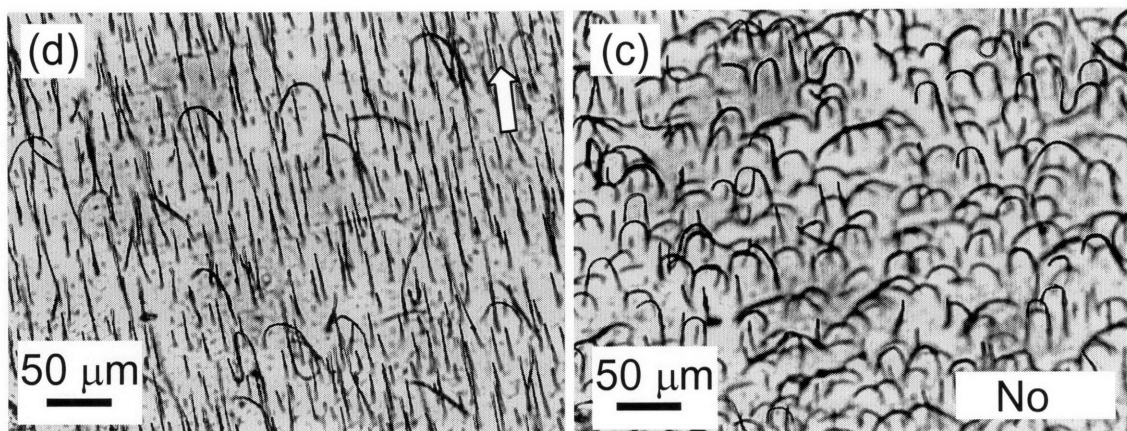
Figure 4-3. Optical micrographs of PEG linked chains, or magnetic nanowires, tethered to the amine patterned glass surface. The chains respond to an externally applied magnetic field with field direction indicated by the arrows. (a) In the absence of a magnetic field the short (25 μm), relatively inflexible nanowires orient vertically and are observed end-on, while (b) they align uniformly with the applied magnetic field. (c) With no applied field the longer, more flexible chains (75 μm) bend over under their own weight to form loops. (d) Unless tethered at both ends, the loops formed by the long chains unfold and align with the applied magnetic field.

The strong presence of loops for the longer chains can be attributed to disruption of their alignment with the magnetic field during growth by perturbations due to thermal fluctuations. With sufficiently strong misalignments the gravitational force can overcome the magnetic field and pull the growing end towards the glass surface; the resulting U loop configuration formed is also a stable equilibrium state [2] for long chains and they continue to align in that fashion rather than reverting to the straight chain configuration. If the looped end encounters a patterned amine group it will react with and tether the chain to the glass surface, forming a permanent U loop. While all the longer nanowires appeared to bend under their own weight, and many of them later unfurled to align with an applied magnetic field, some of the chains are clearly tethered at both ends and the U loops thus formed also respond to the magnetic field. The configurations taken on by the loops under different applied field directions are shown in Figure 4-4. Since the two ends of the U loops are fixed in their orientations, they affect the chain configurations quite remarkably, and the shapes taken on by the loops, whether simple arcs or more complex S-shaped structures, depend on the direction of the applied magnetic. For instance, in the top panels in Figure 4-4, the orientation of the loop at the anchor point does not necessarily line up with the magnetic field direction, suggesting

that the chains are quite stiff locally and that some directional orientation is imposed on them by the local chain structure rather than by the magnetic field. The loop shown in the lower panels of Figure 4-4 behaves as expected, its orientation following the direction of the magnetic field fairly well although there is a kinking of the chain near the anchor points, which may be due to the local stiffness of the structure there.
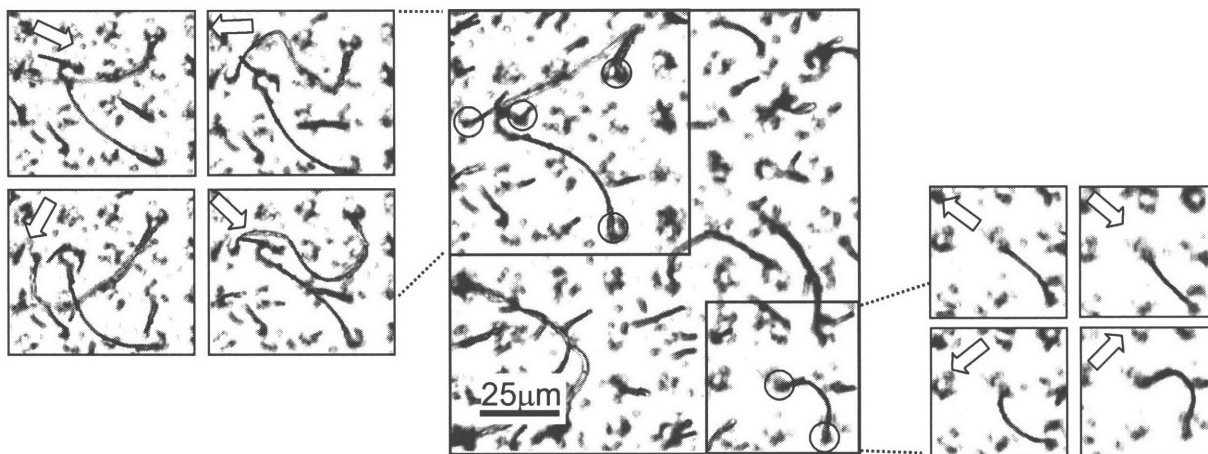
Figure 4-4. Optical micrographs showing the response of flexible chains tethered at both ends (U bends) to an external magnetic field. The circles indicate tethering points and the arrows indicate the direction of the external magnetic field.

The length of the diamine linker molecule governs the chain flexibility [1]. For example, chains linked with PEG diamine (MW 2000) were found to be quite flexible as they formed different structures when the field was applied in different directions. As shown in Figure 4-5, depending on the initial conditions, the chain configuration can be straight, hairpin, or S-shaped. The magnetic force tending to align the nanowire is counteracted by the viscous drag and elastic restoring forces acting on the moving chain as it responds to the applied magnetic field. The balance of these forces gives rise to the different structures observed, which are trapped in local minimum energy configurations.
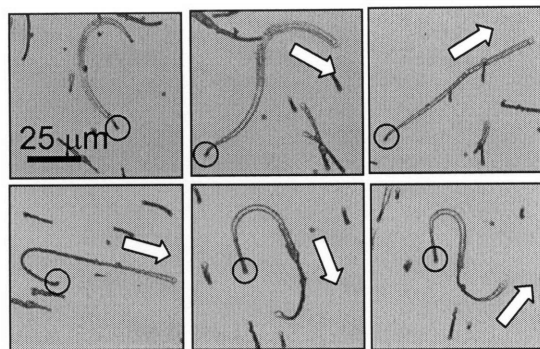
Figure 4-5. Optical micrographs showing the response of a PEG linked flexible chain to an applied magnetic field. The initial orientation of the chain and direction of the applied field govern the final configuration of the chain. The circles indicate the point of tethering.

In contrast, the chains linked with EDE, a small molecule with a molecular weight of 148, are stiffer, and, as shown in Figure 4-6, no loops or bends were formed during the directional response of these chains to the magnetic field.
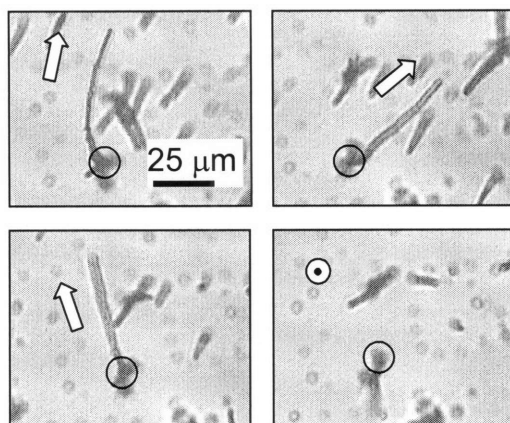
Figure 4-6. Optical micrographs showing the response of an EDE linked chain to an applied magnetic field. The circles indicate the point of tethering. The chains are comparatively rigid relative to their PEG counterparts in Figure 4-4.

The PDMS stamp used for printing the amine functionality on the glass slides consisted of a regular array of dots with diameters ranging from 1.25 μm to 9 μm while the center-to-center distance between two dots was kept constant at 18 μm. The dot size governed the number of chains that grew from each dot and hence the degree of clustering of the chains. For 1.25 μm-sized patterned dots, single magnetic chains were observed while clusters of chains resulted when larger dots were stamped on the glass slides, on which multiple beads could be adsorbed and serve as nuclei for multiple chain

formations. Figure 4-7 shows that chains grown from 1.25 μm dots are essentially single strands, while those cultivated on 8 μm dots are thicker and consist of multistranded ropes of these magnetic bead chains. No single-stranded chains were observed to grow from the larger dots indicating that the attractive interactions between the chains growing from the same dot induce clustering of these chains. The interaction energy between two magnetic chains decays rapidly with interchain distance and results in chain attraction if they are out of registry and repulsion if they are perfectly aligned [17]. For our beads, the cut off distance is on the order of the bead diameter, i.e., ~ 500 nm, which governs the minimum distance of approach between two rigid chains before they will attract each other, and hence sets the maximum desirable grafting density of the chains on the surface. In reality when the magnetic beads assemble in this way, the free ends of the chains sway due to Brownian motion, and they are not perfectly aligned with neighboring chains, which results in a mutual attractive interaction. Also, the interaction between the curved chains is much stronger [18] than that between straight chains and decays less rapidly with distance. Thus, chains growing from the same dot are prone to clustering.

The dynamic response of these chains to spatial and temporal changes in magnetic fields is expected to provide unique opportunities for the enhancement of some microfluidic fluid processing operations, and is currently under active study in our laboratories and elsewhere. Preliminary results show that, when subjected to rotating magnetic fields, these tethered chains can be used as micropumps and mixers for the movement and blending of liquid streams and for the manipulation of microparticle distributions in microchannels.
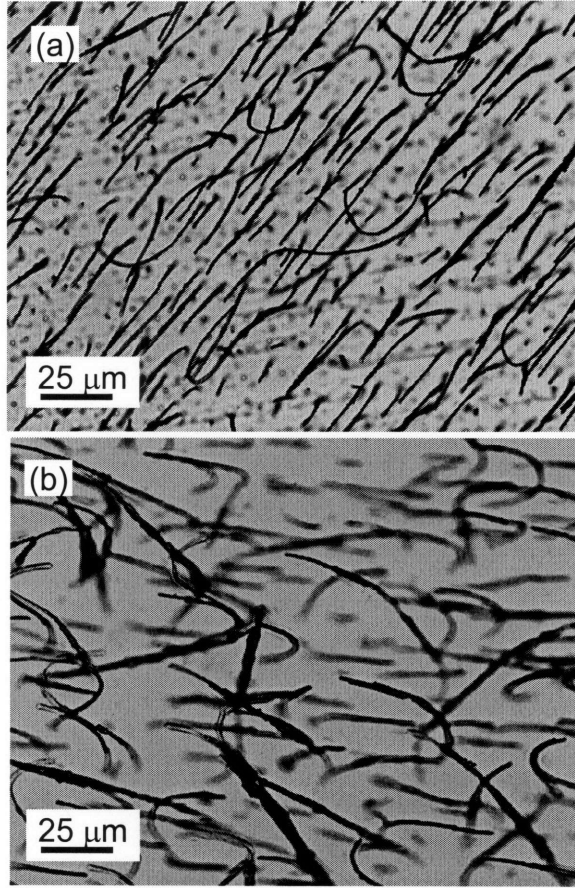
Figure 4-7. Optical micrographs of the chains growing from patterned (a) 1.25 μm dots and (b) 8 μm dots. Individual chains for the most part grow from 1.25 μm dots, while those growing from 8 μm dots are clustered.

The response of the chain to the rotating magnetic field is shown in Figure 4-8. The chains are rotate synchronously with the rotating magnetic field up to a critical frequency above which they become asynchronous. The frequency at which the chains transition from synchronous rotation to asynchronous rotation depends on the chain length. This critical frequency f_c can be calculated using the model developed in Chapter 2 to capture the kinetics of the chain to the applied magnetic field (Section 2.4). Using equation (7) and (8) in Chapter 2 we get

$$\sin(2\theta) = \frac{16\eta L a \omega}{9\mu_o s^2 \chi^2 H^2 \ln(L/4a)} \tag{1}$$

In the regime when sin(2θ) < 1, the chain will be in phase with the rotating field. For 25 μm and 50 μm chain the critical frequency was found to be ~ 0.2 Hz and ~ 0.14 Hz respectively for H = 0.01 T. The chains in Figure 4-8 are ~ 25 μm in length and hence they rotate synchronously with the 0.1 Hz rotating magnetic field.
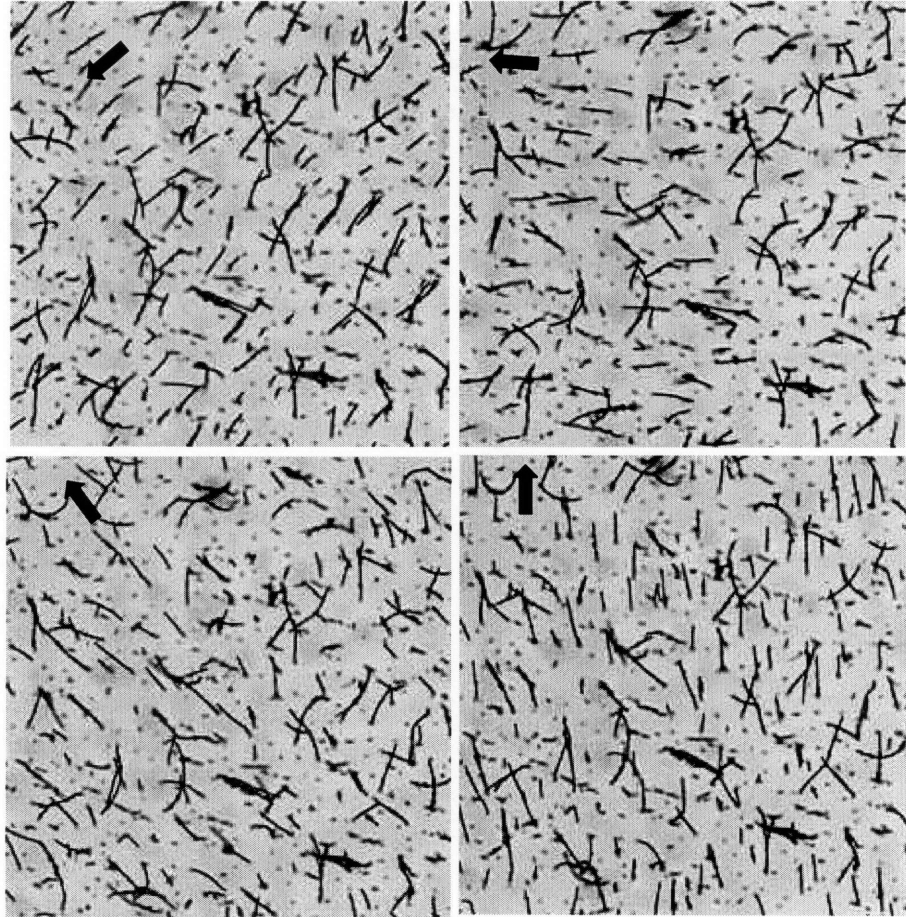
Figure 4-8. Optical micrographs of the response of the PEG 2000 tethered chains to a rotating magnetic field. The average chain length is 25 μm and the corresponding f_c is 0.2 Hz. The chains are in phase with the applied rotating field which has a frequency of 0.1 Hz. The arrow indicates the instantaneous direction of the magnetic field.

There was no control on the tethering density of the chains when they were grown in a PDMS microchannel since the bottom surface of the channel is uniformly coated with amine groups. The distance between the chains was governed by the concentration of the beads. When the magnetic beads are present in excess the distance between the two chains approaches ~ 500 nm which is governed by the dipolar action between the chains (as discussed above).

Figure 4-9 illustrates the results from the micro pumping experiments. The motion of the 10 μm particles was captured by the microscope camera. The average length of the chain tethered in PDMS microchannel was 50 μm. The frequency of the applied was kept at 0.2 hz which was close to f_c for the corresponding length. The strength of the applied field was 0.01 T. The Reynolds number at the given length scale is on the order of 10^{-4}. At such low Reynolds number the flow should be reversible and hence no pumping action should be observed but the snapshots at different time clearly indicated that the beads were pumped forward by the rotating tethered chains. At frequency closed to f_c the chains exhibit "jerky" asynchronous motion. The "jerky" motion of chains ensured that the elastic energy is released only in one direction which resulted in the preferential movement of the beads in that direction. The motion of the beads was not smooth and they moved for ward in a pulsating fashion. The results presented here are very preliminary and more work is required in this regard.
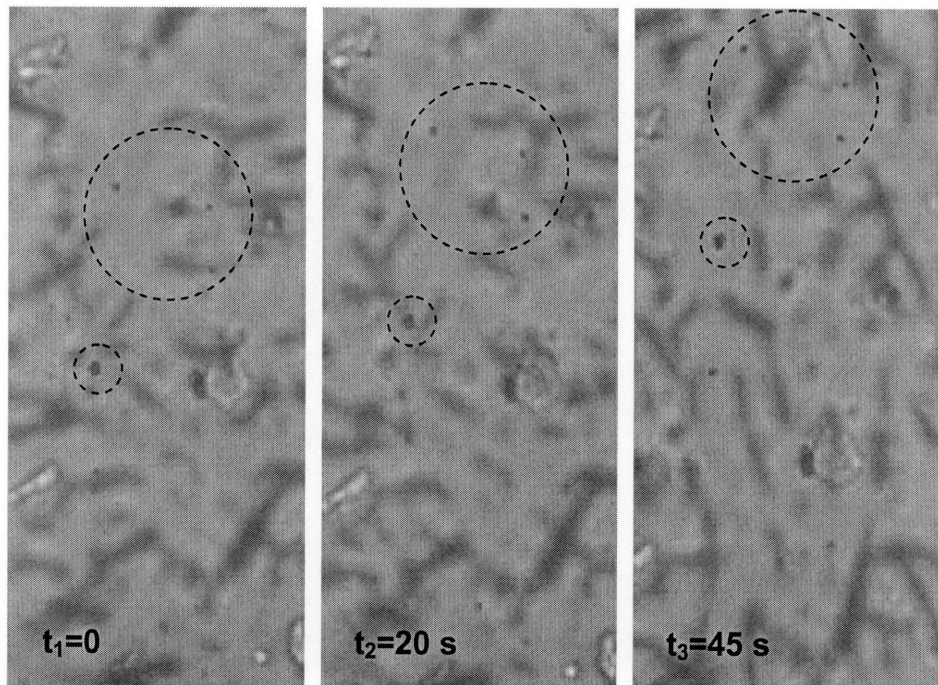
Figure 4-9. Optical micrographs illustrating the micropumping action of the chains tethered in a microchannel. The dashed circles track the beads at different times ($t_3 > t_2 > t_1$) which indicates that the beads are moving forward. The faint outline of the tethered chains can be seen in the background.

4.4   Conclusions

We have developed an inexpensive and efficient one-step method to create permanently linked chains of sub-micron magnetic beads having varying flexibility, and have successfully tethered them to a patterned glass surface using simple amidation chemistry. The flexibility of the resulting nanowires was governed by the molecular weight of the linker molecule and their length by the height of the microchannel in which they were synthesized. The chain diameter is determined both by the bead size, and by the number of beads adhering to each dot in the microstamped, patterned array. The tethered chains respond to a rotating magnetic field and can be used as micropumps.

Acknowledgments

4.5   References

1.   Biswal, S.L. and A.P. Gast, *Mechanics of semiflexible chains formed by poly(ethylene glycol)-linked paramagnetic particles.* Physical Review E, 2003. **68**(2).

2.   Goubault, C., P. Jop, M. Fermigier, J. Baudry, E. Bertrand, and J. Bibette, *Flexible magnetic filaments as micromechanical sensors.* Physical Review Letters, 2003. **91**(26).

3.   Singh, H., P.E. Laibinis, and T.A. Hatton, *Rigid, superparamagnetic chains of permanently linked beads coated with magnetic nanoparticles. Synthesis and rotational dynamics under applied magnetic fields.* Langmuir, 2005. **21**(24): p. 11500-11509.

4.   Goubault, C., F. Leal-Calderon, J.L. Viovy, and J. Bibette, *Self-assembled magnetic nanowires made irreversible by polymer bridging.* Langmuir, 2005. **21**(9): p. 3725-3729.

5.   Biswal, S.L. and A.P. Gast, *Micromixing with linked chains of paramagnetic particles.* Analytical Chemistry, 2004. **76**(21): p. 6448-6455.

6.   Ditsch, A., S. Lindenmann, P.E. Laibinis, D.I.C. Wang, and T.A. Hatton, *High-Gradient Magnetic Separation of Magnetic Nanoclusters.* Industrial & Engineering Chemistry Research, 2005. **44**(17): p. 6824-6836.

7.   Doyle, P.S., J. Bibette, A. Bancaud, and J.L. Viovy, *Self-assembled magnetic matrices for DNA separation chips.* Science, 2002. **295**(5563): p. 2237-2237.

8.   Lyles, B.F., M.S. Terrot, P.T. Hammond, and A.P. Gast, *Directed patterned adsorption of magnetic beads on polyelectrolyte multilayers on glass.* Langmuir, 2004. **20**(8): p. 3028-3031.

9.   Caruso, F., A.S. Susha, M. Giersig, and H. Mohwald, *Magnetic core-shell particles: Preparation of magnetite multilayers on polymer latex microspheres.* Advanced Materials, 1999. **11**(11): p. 950-+.

10.   Kumar, A. and G.M. Whitesides, *Features of Gold Having Micrometer to Centimeter Dimensions Can Be Formed through a Combination of Stamping with an Elastomeric Stamp and an Alkanethiol Ink Followed by Chemical Etching.* Applied Physics Letters, 1993. **63**(14): p. 2002-2004.

11.   Mrksich, M. and G.M. Whitesides, *Patterning Self-Assembled Monolayers Using Microcontact Printing - a New Technology for Biosensors.* Trends in Biotechnology, 1995. **13**(6): p. 228-235.

12.   Caruso, F., R.A. Caruso, and H. Möhwald, *Nanoengineering of Inorganic and Hybrid Hollow Spheres by Colloidal Templating.* Science, 1998. **282**(5391): p. 1111-1114.

13.   Massart, R., E. Dubois, V. Cabuil, and E. Hasmonay, *Preparation and Properties of Monodisperse Magnetic Fluids.* Journal of Magnetism and Magnetic Materials, 1995. **149**(1-2): p. 1-5.

14.   Decher, G., *Fuzzy nanoassemblies: Toward layered polymeric multicomposites.* Science, 1997. **277**(5330): p. 1232-1237.

15.   Lee, I., H.P. Zheng, M.F. Rubner, and P.T. Hammond, *Controlled cluster size in patterned particle arrays via directed adsorption on confined surfaces.* Advanced Materials, 2002. **14**(8): p. 572-577.

16. Martin, J.E., K.M. Hill, and C.P. Tigges, *Magnetic-field-induced optical transmittance in colloidal suspensions.* Physical Review E, 1999. **59**(5): p. 5676-5692.

17. Aizenberg, J., P.V. Braun, and P. Wiltzius, *Patterned colloidal deposition controlled by electrostatic and capillary forces.* Physical Review Letters, 2000. **84**(13): p. 2997-3000.

18. Tao, R., *Super-strong magnetorheological fluids.* Journal of Physics-Condensed Matter, 2001. **13**(50): p. R979-R999.

Chapter 5

Other Aggregation Techniques

5.1   Introduction

In Chapter 2 and 4 we used electrostatically stabilized magnetic nanoparticles to coat charged polystyrene (PS) beads to create novel core-shell magnetic beads. Spherical PS beads were used as templates because they were easily available commercially. However the use of electrostatic interaction to adsorb nanoparticles on a surface is a very general technique and can be extended to a charged template of any shape [1, 2]. Self assembly of non-spherical magnetic structures under an applied magnetic field has not been explored because of the difficulty in synthesizing these structures. Template based techniques can be used but the challenge is to make non-sperical charged templates.

It is well known that in aqueous solutions, above the critical micelle concentration (CMC), surfactants assemble into micelles, spherical or cylindrical nanostructures. Further increases in surfactant concentration result in the self-organization of micelles into periodic hexagonal, cubic, or lamellar mesophases [3]. The surfactant structures have been used as template to create porous ceramic materials [4-6] but have not been used to adsorb nanoparticles. In the first part of this chapter we will discuss other templates that were explored to induce controlled clustering in nanoparticle suspensions. In the first section of this chapter we will discuss some work done to create ring shaped and icosahedra shaped magnetic clusters. The disk and icosahedra shaped charged templates were created from mixtures of surfactants.

In the second part of this chapter, we will discuss some work done on creating magnetic clusters *in situ* without using any templates. The focus here was to synthesize magnetic nanoparticles stabilized with different polymers. The polymer on the nanoparticles was then directly crosslinked using ionizing radiation to create nanoparticle clusters. We used a graft copolymer of Poly(acrylic) acid and Poly(ethylene) oxide to stabilize magnetic nanoparticles in aqueous solution because of the ease of crosslinking

PEO with ionizing radiation [7, 8]. The advantage of Radiation crosslinking is that yields high purity materials free of residual impurities such as crosslinking agents, catalyst or byproducts. The basic principle of radiation crosslinking is that all forms of ionizing radiation interact with matter by transferring energy to the electrons orbiting the atomic nuclei of target materials. These electrons may then be either released from the atoms, yielding positively charged ions and free electrons, or moved to a higher-energy atomic orbital, yielding an excited atom or molecule (free radical). These ions, electrons, and the excited species are the precursors of any chemical changes observed in irradiated material [9].

5.2   Surfactant as Templates

We have used the method of Dubois et al. [10, 11] to synthesize charged surfactant templates which could be used for the adsorption of the nanoparticles. They have shown that organic rigid nanodisks of controlled size with positively charged edges can be created by a balanced mixture of cationic and anionic surfactants, when the cationic surfactant is in excess. The counter ion for the anionic surfactant should be hydroxide while that of the anionic surfactant should be the hydronium ion. The overall size of the disks can be continuously adjusted from micrometer to nanometer size by controlling the ratio of the surfactant. Similarly when the anionic surfactant is in excess, negatively charged icosahedras are formed. However the icosahedras had positively charged edges. Coating these templates with magnetic nanoparticles should result in ring and cage shaped magnetic clusters (Figure 5-1).

5.2.1 Experimental Section – Surfactant Templates

5.2.1.1 Materials

Cetyltrimethylammonium hydroxide (CTAOH) (0.5 M in water) was purchased from Acros Organics (NJ). Myristic acid (MA) (99.5%), iron(III) chloride hexahydrate (97%), iron(II) chloride tetrahydrate (99%), ammonium hydroxide (28 wt% in water), sodium hydroxide pellets (NaOH, 99.99 wt% in water), nitric acid (HNO_3, 70% in water) and polylysine (FITC grade) were obtained from Sigma-Aldrich (Milwaukee, WI).

129
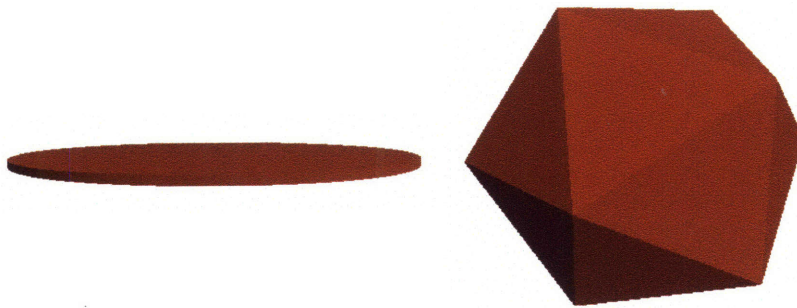
Figure 5-1. Cartoon of disk and icosahedra shaped templates. Both the structures have positively charge edges.

5.2.1.2 Preparation of Disks and Icosahedras

The anionic mole fraction r and volume fraction of the surfactants are the two controlling parameters. r is defined as

$$r = [C_{13}COO^-]/([CTA^+]+[C_{13}COO^-]) \tag{1}$$

When $r < 0.5$ disks are formed and when $r > 0.5$ icosahedras are formed. The size of the disk and icosahedra formed can controlled by varying r in the given range. CTAOH and MA were mixed at a volume fraction of 2 wt% in degassed water. The entire process was performed under a nitrogen hood to avoid contamination with carbon dioixde. Disks were synthesized with $r = 0.39$ and $r = 0.454$ which corresponded to disk diameters of 30 nm and 2600 nm respectively. 1 μm icosahedras were synthesized with $r = 0.63$. The mixture of surfactant was stirred for 72 hrs. The milky solution was then heated to 60 $^{\circ}$C and cooled down with continuous shaking. The solution transformed into a clear solution on cooling, indicating the formation of disks or icosahedras.

5.2.1.3 Nanoparticles Syntheis

Citrate-coated magnetic nanoparticles with an average diameter of 10 nm (as estimated by TEM) were synthesized using Massart's method [12]. In brief, a 2:1 molar

mixture of $FeCl_3.6H_2O$ and $FeCl_2.4H_2O$ was precipitated in the presence of 0.75M NaOH at 100°C. The black precipitate was decanted magnetically and after washing with 1M HNO_3 was dispersed in deionized water and heated to 90°C, following which sodium citrate was added. The resulting stable magnetic fluid was reprecipitated by addition of excess acetone, separated magnetically, and redispersed in deionized water. This stable dispersion was centrifuged at 18000 rpm for 3hr to remove excess citrate ions. The resulting precipitate after centrifugation was finally suspended in deionized water to yield stable magnetic fluid.

5.2.1.4 Nanoparticle Adsorption on the Templates

3 ml of 0.1 wt% surfactant solution with *r = 0.45, r = 0.40* and *r = 0.63* was mixed with 0.014, 0.275 and 0.01 ml of 0.5 wt% of magnetic fluid respectively. The mixture was continuously shaken for 20 mins.

5.2.2 Characterization

Transmission electron microscopy (TEM) experiments were performed on a JEOL 2010 (200 kV) instrument. Samples were prepared by evaporating dilute suspensions on a carbon-coated film. The median size and polydispersity of the magnetite particles was determined by measuring 150 particles.

Dynamic light scattering (DLS) experiments were performed with a Brookhaven BI-200SM light scattering system at a measurement angle of 90°. The autocorrelation function was fit with an exponential fitting software program to extract the diffusion coefficient, and the Stokes-Einstein equation was used to convert the diffusion coefficient to the hydrodynamic diameter. Intensity-average size distributions provided by the light scattering software were converted to number average for further analysis.

The zeta potential of particle suspensions was measured on a Brookhaven ZetaPals Zeta Potential Analyzer. Particle suspensions were diluted to 0.005 wt% Fe_3O_4 with 1 mM NaCl prior to measurement. Approximately 2 mL of the sample was loaded into the electrode cell. The electrophoretic mobility (μ_e) of the particles was measured

131

over fifteen electrode cycles. The Smoluchowski equation was used to convert the electrophoretic mobility to the zeta potential (ζ):

$$\zeta = \frac{\eta}{\varepsilon} \mu_e \qquad (5\text{-}1)$$

where η and ε are the viscosity and dielectric constant of the dispersion medium. The quoted zeta potential was an average of five measurements.

Confocal microscopy was used to detect the magnetic aggregates. FITC grade polylysine was used to fluorescently label the sample. For each 100 μl aliquot of the disk or icosahedra solution, 2.6 μl of 0.01 wt% of polylysine was added. Polylysine being positively charged tagged on the negatively charged nanoparticles which adsorbed on the templates. The fluorescently labeled solution was added to the multi-well culture plate for visualization under the microscope.

The replica cryo-TEM samples were prepared through the quick freeze-deep etch (QFDE) method. First, a 1.5 μL drop of aggregate solution was deposited on the top of a metal plate, and the drop was frozen by inserting the metal plate rapidly into propane, which was cooled to about -186 °C by liquid nitrogen. Second, the frozen drop was transferred to a sealed chamber, where it was equilibrated and evaporated for 36 min under a vacuum of 10^{-7} Torr. This served to evaporate the propane and to sublime some of the water, thereby producing a bas-relief of any aggregates that were present near the drop surface. In the third step, the frozen drop was coated first with a thin platinum film of thickness 2-3 nm; and then with a 20-30 nm carbon film. Finally, the frozen drop was removed from the chamber and kept at room temperature for a few minutes. After the remaining ice had melted, the metal plate was plunged into water and the replica film floated to the water surface. The film was then placed on the grid and readied for TEM examination. The prepared samples were examined using a JEOL 2010 (200 kV) electron microscope.

In vitrified cryo-TEM a few (2-3) microliters of an aqueous suspension stored at 25 ° C in a controlled environment vitrification system (CEVS, University of Minnesota;

the temperature within the CEVS box is controlled precisely, and the relative humidity is kept at >90%) were withdrawn in a pipet, deposited on a specially prepared lacey carbon electron microscope grid, and blotted to remove excess liquid. This processing took place within the CEVS unit, preventing water evaporation and temperature changes in the sample. The grid bearing the sample was plunged into a liquid ethane reservoir cooled by liquid nitrogen to a temperature close to its freezing point. The rapid heat transfer away from the grid vitrified the sample. The specimen was transferred under liquid nitrogen to the cooled tip of a cryotransfer stage (CT3500J, Oxford Instruments) which was then inserted under positive dry nitrogen pressure into the JEOL 1200 TEM and imaged at slight underfocus (1-3 μm). The sample temperature was maintained at -165 °C at all times during imaging, to prevent the amorphous-to-crystalline phase transformation in ice.

5.2.3 Results and Discussion

Dynamic light scattering was performed on solutions of pure nanoparticles, pure disks and on the mixture of nanoparticles and disks. Figure 5-2 shows the intensity average plot of the measurements. In the DLS spectra of the mixture of disks and magnetic nanoparticles, the peak corresponding to pure magnetic nanoparticles disappeared and that the new peaks are further to the right of pure disks. This indicates that the particles are adsorbed on the disk. The number average size of the nanoparticle was 12 nm, disk was 376 nm and that of the nanoparticle and disk mixture was ~ 390 nm (Figure 5-3). The increase in number average size further confirmed the hypothesis that the nanoparticles get adsorbed on the templates.

133
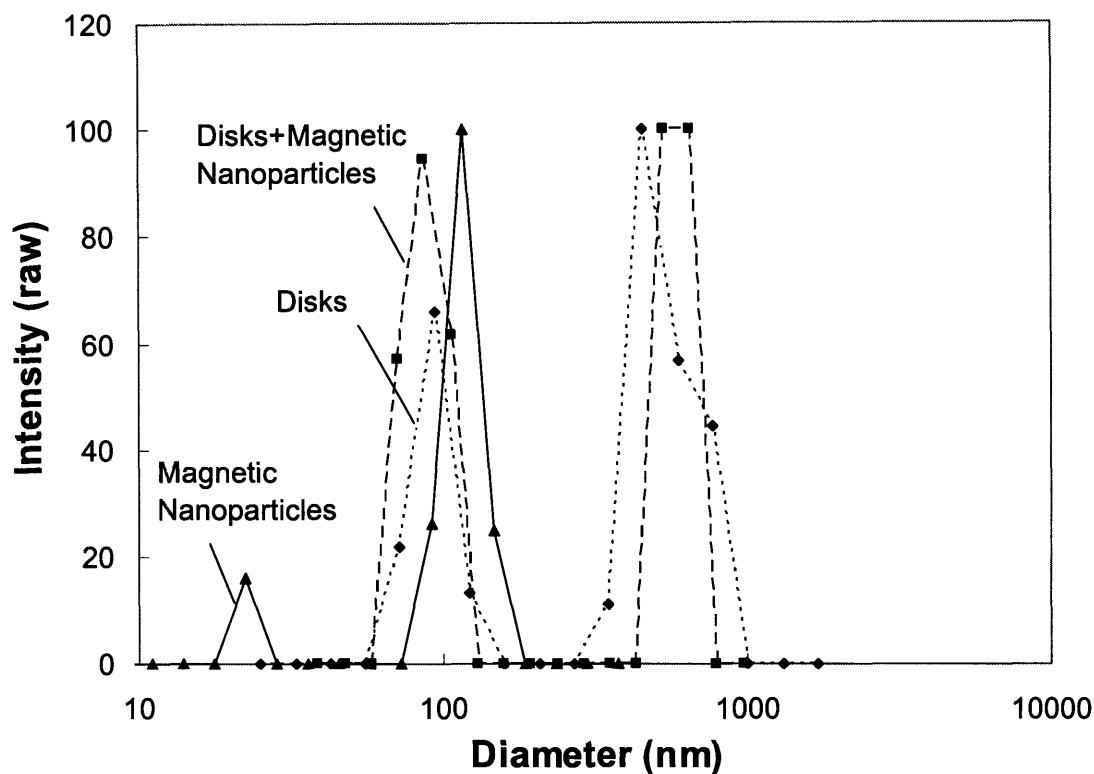
Figure 5-2. Dynamic Light Spectra of pure magnetic nanoparticles, pure disks and the mixture of disks and nanoparticles. Signature spectra of magnetic nanoparticles disappear in the presence of the disk template, indicating their adsorption on the disk.

Zeta potential was used to measure the surface charge on the particle and the disk. Disks were positively charged with a zeta potential of 65 mV and magnetite nanoparticles were negatively charged with a zeta potential of -34 mV. The mixture of disks and nanoparticles was visualized using confocal microscopy. FITC labeled polylysine was used as a fluorescent label. Several disk shaped objects were observed but it was difficult to focus on them because they were under constant Brownian motion. Hence it was not possible to reconstruct the 3D view of the object. The sectional view captured at a focal plane is shown in Figure 5-4a. The micrograph indicates the adsorption of the nanoparticles on to the disks but did not confirm that the nanoparticles were only adsorbing on the edges. Cryo-TEM was performed on the disk nanoparticle samples to verify this. Figure 5-4b shows the Cryo-TEM micrographs. The micrograph shows that

the particles adsorbed randomly on the disk surface. The charge difference between the surface and edges of the disk is not sufficient to enable selective adsorption of the nanoparticles on the edges only.
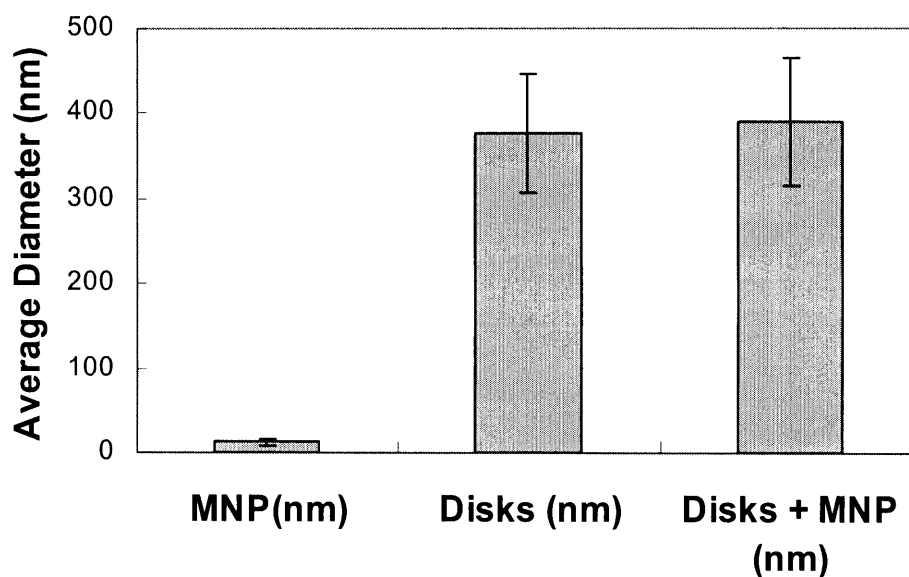
Figure 5-3. The number average size of pure magnetic nanoparticles, pure disks and the mixture of disks and nanoparticles. The number average size of the mixture of disks and nanoparticles compared to that of the pure disk is higher by 14 nm which is approximately the size of magnetic nanoparticle (~ 12 nm).

Confocal (Figure 5-5a), Cryo-TEM (Figure 5-5b) and Freeze fracture (Figure 5-5c,d) experiments were performed with icosahedra-nanoparticle mixtures. Micrographs show random adsorption of nanoparticles on different facets of the icosahedra. Electrostatic affinity value between the edges and the faces of the icosahedra is not large enough to obtain selective adsorption of the particles on the edges only.
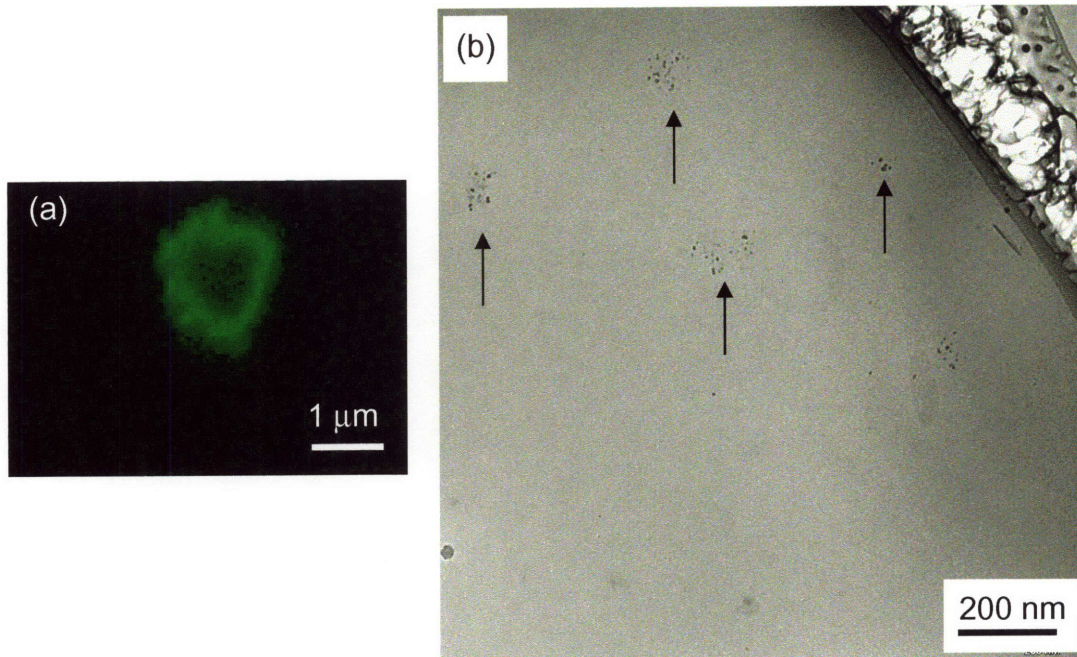
Figure 5-4. (a) Confocal micrograph at a given focal plane of the disk coated with magnetic nanoparticles. (b) Cryo-TEM micrograph of the disk nanoparticle mixture. The particle adsorb randomly on the disk surface and edges.

Our unsuccessful attempt to obtain magnetic rings and magnetic cage like structures lead to the formation of disk and icosahedra shaped clusters. Icosahedra shaped magnetic boxes can be used as a delivery vehicle for drugs, genes etc [13-16]. Recently Dendukadi et al. [17] have devised a scheme to generate different shaped micron size colloids like, disks, rings, pyramids etc. by photo-crosslinking poly(ethylene glycol) using the technique of continuous flow lithography [17]. The templates can also be made negatively charged by photo-crosslinking a mixture of poly(ethylene glycol) diacrylate and acrylic acid. These are very stable templates and we can use the Layer-by-Layer method as discussed in Chapter 2 to coat the negatively charged templates with magnetic nanoparticles. Magnetic rings represent an interesting class of material for fundamental studies [18-20]. The next section focuses on the modeling the behavior of the magnetic rings in the presence of a magnetic field. We predict how a single magnetic ring would respond to an external magnetic field. We extend this modeling to a system of interacting rings where we calculate that the magnetic rings will form links under an applied magnetic field. We then discuss the experiments performed to verify this behavior of
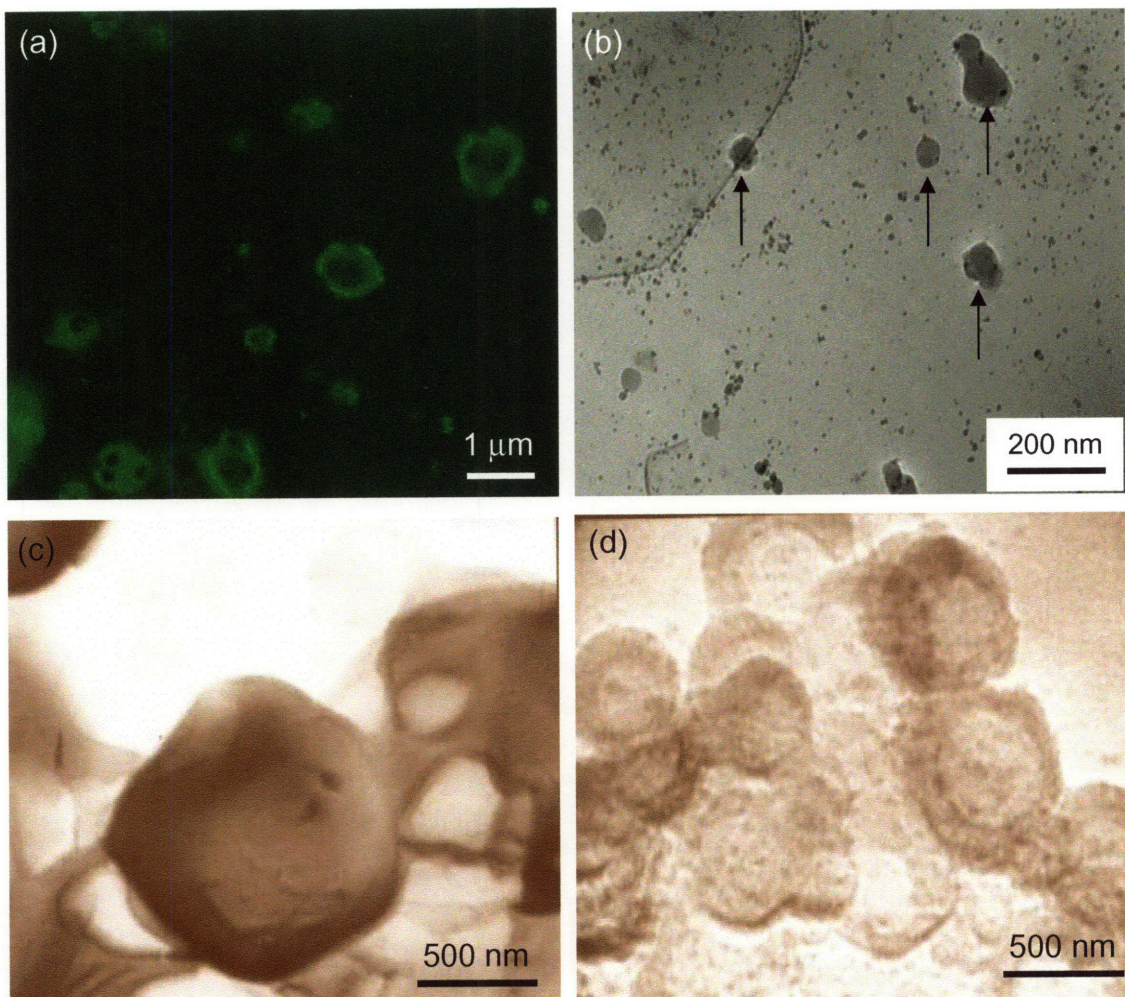
Figure 5-5. (a) Confocal image of icosahedra nanoparticle mixture at a given focal plane. The particle adsorbed on all the faces of the icosahedra resulting in uniform fluorescence from around the edges. (b) Cryo-TEM micrograph also shows random adsorption of the nanoparticles on the faces of the icosahedras. (c) Freeze fracture micrograph of pure icosahedra mixture illustrates smooth walls which turn grainy (d) due to the adsorption of the nanoparticles.

the magnetic rings. We also extended this study to the self–assembly of magnetic disks under an applied magnetic field. Negatively charged ring and disk shaped templates were generously donated by Dhananjay Dendukuri from Doyle & Hatton group at MIT and were made magnetic for this study.

5.2.4 Modeling of the Behavior of the Magnetic Rings

In this section we have calculated the magnetic interaction energy between two magnetic rings. The rings are composed of magnetic nanoparticles as illustrated in Figure 5-6. The purpose of the calculation was to predict how the magnetic rings would self assemble in the presence of an external magnetic field. This is analogous to the behavior of the magnetic colloids which aggregate reversibly in the presence of an external magnetic field to form chain like structures in the direction of the external magnetic field [21-24]. The magnetic rings can either stack or link together as shown in Figure 5-7 under the application of the magnetic field.
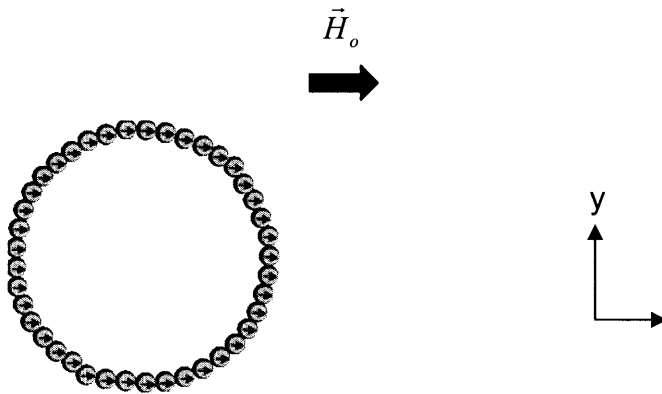
Figure 5-6. Schematic of a Magnetic Ring.
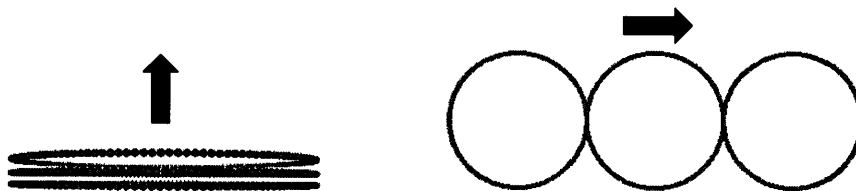
Figure 5-7. Representation of a) Stacked magnetic rings b) Linked magnetic rings. The arrow indicates the direction of the applied field.

The interaction energy U_{ij}^{dip} between two magnetic dipoles i and j, separated by distance r_{ij} (Figure 5-8) is given by

138

$$U_{ij}^{dip} = \frac{1}{4\pi\mu_o} \frac{\vec{m}_i.\vec{m}_j - 3(\hat{r}.\vec{m}_i)(\hat{r}.\vec{m}_j)}{r_{ij}^{3}} \qquad (1)$$

where μ_0 is the magnetic permeability of free space and $\hat{r}$ is the unit vector in the direction of r.
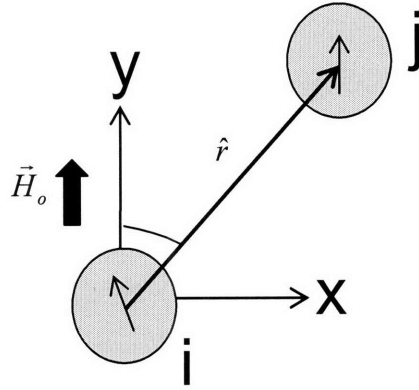
Figure 5-8. Interaction between two magnetic dipoles.

The induced magnetic dipole moment $\vec{m}$ of the bead is given by

$$\vec{m} = \mu_o V\vec{M} \qquad (2)$$

where $\vec{M}$ is its magnetization under a field $\vec{H}$, V is the volume of the magnetic material. The total field $\vec{H}_i$ acting on the bead at position i is the sum of the external magnetic field $\vec{H}_o$ and the local magnetic field at point i induced by the neighboring nanoparticles in the ring

$$\vec{H}_i = H_o + \sum_{j \neq i} H_j \qquad (3)$$

where the field induced by dipole j at position i is

$$H_j = \frac{1}{4\pi\mu_o} \frac{3(\hat{r}.\vec{m}_i) - \vec{m}_j}{r_{ij}^{\,3}} \qquad (4)$$

$|M| \to |M_s|$ where M_s is the saturation magnetization of the nanoparticles, when the external applied field, $\vec{H}_o$ is sufficiently high to saturate the magnetic dipole of the nanoparticles. Under this condition we can neglect the induced field so that $\vec{H}_i = \vec{H}_o$. We can estimate this value of M_s from the magnetization curve of the nanoparticle (Figure 5-9).

Consider a ring of radius R made up of N magnetic nanoparticles. The magnetic moment the saturated nanoparticle will be in the direction of the external magnetic field and is given by

$$m = \mu_o V M_s \qquad (5)$$

The ith particle in the ring interacts with all the other $(N\text{-}1)$ particles in the ring.

$m_i \neq f(H)$
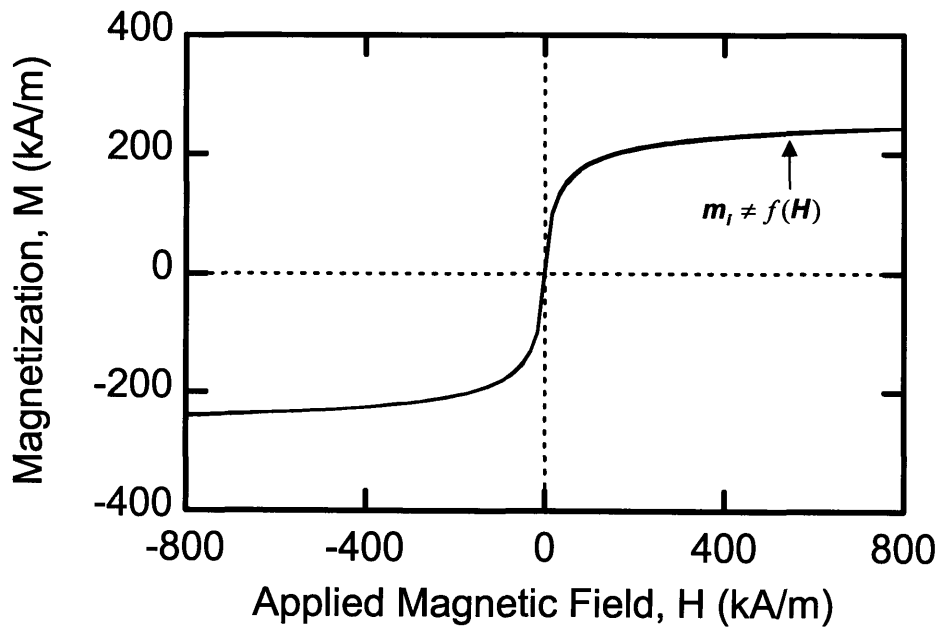
Figure 5-9. Typical magnetization curve of a magnetic nanoparticle. In this modeling we assumed that the external field was high enough to saturate the dipole.

Assuming pairwise interaction, the total dipolar interaction energy of a nanoparticle 'i' with all the other nanoparticles in the ring can be written as

$$U_i^{dip} = \sum_{j \neq i} U_{ij} \qquad (6)$$

Summing $\sum_{j \neq i} U_{ij}$ over for all the particles in the ring gave the total magnetic interaction energy U_{self}^{ring}

$$U_{self}^{ring} = \frac{1}{2} \sum_{i=1}^{N} U_i^{dip} \qquad (7)$$

The factor of ½ in equation (7) accounts for the double counting in a pairwise interaction scheme.

Consider a ring on a xy plane with field applied in the z direction (Figure 5-10). The magnetic dipole of the nanoparticle and permeability $(4\pi\mu_o)$ was set to unity for ease of calculation.
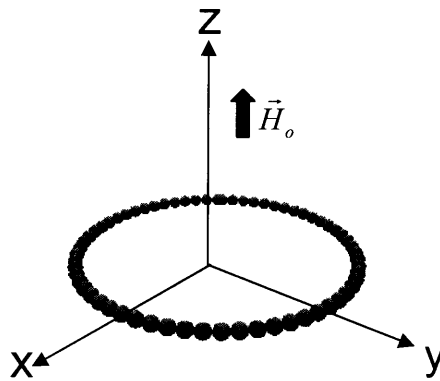
Figure 5-10. Schematic of a Magnetic ring on a xy plane with the external field in z direction.

In the presence of the magnetic field, the ring will attain the orientation at which U_{self}^{ring} is minimum. The minimum orientation was calculated by rotating the ring in all possible direction and calculating U_{self}^{ring} for each direction. The orientation of a ring in a 3D space was expressed by defining a unit vector normal to the plane of the ring. Using spherical co-ordinate system (Figure 5-11), the unit vector $\hat{n}$ can be written as

$$\hat{n} = \sin\theta\cos\Phi \ \hat{x} + \sin\theta\sin\Phi \ \hat{y} + \cos\theta \ \hat{z}$$
$$0 \le \theta \le \pi; \ 0 \le \Phi \le \pi$$

(8)

$\hat{x}, \hat{y}, \hat{z}$ are the unit vectors in x, y and z directions respectively.
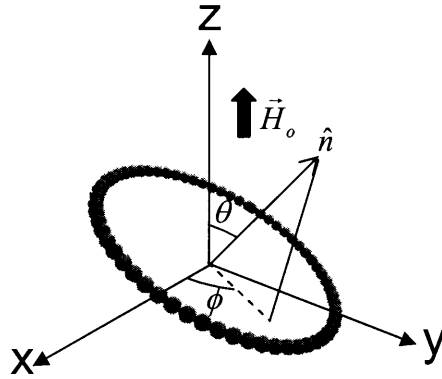
Figure 5-11. General orientation of a ring defined using spherical co-ordinate.

The next challenge was to parameterize a ring in any general orientation i.e. assigning xyz co-ordinates to the particles on the ring. The methodology of Gram-Schmidt orthogonalization was adopted (Figure 5-12). Given an arbitrary basis set of independent vectors, it is possible to construct the orthogonal basis. For example if $B = \{\underline{b}_1, \underline{b}_2, \underline{b}_3\}$ is a set of independent vectors, then we can construct an orthogonal basis $\{\underline{u}_1, \underline{u}_2, \underline{u}_3\}$ where

$$\underline{u}_1 = \underline{b}_1$$

$$\underline{u}_2 = \underline{b}_2 - \frac{\underline{b}_2 \cdot \underline{u}_1}{\left|\underline{u}_1\right|^2}\underline{u}_1 \qquad (13)$$

$$\underline{u}_3 = \underline{b}_3 - \frac{\underline{b}_3 \cdot \underline{u}_1}{\left|\underline{u}_1\right|^2}\underline{u}_1 - \frac{\underline{b}_3 \cdot \underline{u}_2}{\left|\underline{u}_2\right|^2}\underline{u}_2$$

So if $\hat{x}'$, $\hat{y}'$ are two mutually perpendicular unit vectors which are perpendicular to the unit normal vector $\hat{n}$, then any point on the circle can be parameterized in the polar co-ordinate system as follows:

$$\vec{r} = \vec{c} + R\cos(\alpha)\hat{x}' + R\sin(\alpha)\hat{y}'$$
$$\alpha = (j-1)\psi, \ 0 \le j \le N \qquad (14)$$

where, $\vec{c}$ is the co-ordinate of the centre. In our case since the circle is at the origin $\vec{c}$ is (0,0,0). Ψ is the angular distance between two nanoparticles and is given by

$$\psi = \cos^{-1}(1 - \frac{2a^2}{R^2}) \qquad (15)$$
$$0 \le \psi \le 2\pi$$
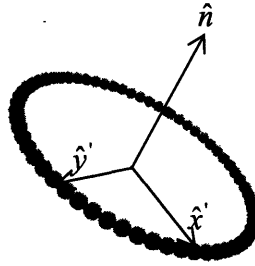
Figure 5-12. Orthogonalization of the ring orientated in a general direction using Gram-Schmidt Method.

The orthogonal set for each orientation was found by setting $\underline{b}_1 = \hat{n}$ and picking $\underline{b}_2$ and $\underline{b}_3$ from the set of unit vectors $(\hat{x}, \hat{y}, \hat{z})$. The $(\hat{x}, \hat{y}, \hat{z})$ indices of $\hat{n}$ were compared. The unit vectors corresponding the lowest two of the three were set as $\underline{b}_2$ and

$\underline{b}_3$. For example, if $(\hat{x}, \hat{y}, \hat{z})$ indices of $\hat{n}$ were given by (0.31, 0.60, 0.74) then the $\hat{x}$ and $\hat{y}$ indices are the lowest of the three. So $\hat{x} = \underline{b}_2$ and $\hat{y} = \underline{b}_3$. This ensured that the basis set $B = \{\underline{b}_1, \underline{b}_2, \underline{b}_3\}$ was composed of independent vectors.

Using equation (1), (6), (7) U_{self}^{ring} was estimated for all the possible orientations of the ring in the space. The results presented here are for $N=32$ and $a =12.5$ nm. Figure 5-13 describes the potential energy surface of the ring when the external field was in the x direction. The minimum energy of the ring was when either $\theta = 0$ or $\phi = \pi/2$. In either case, it meant that the minimum energy orientation of the ring was when the applied field was in the plane of the ring.
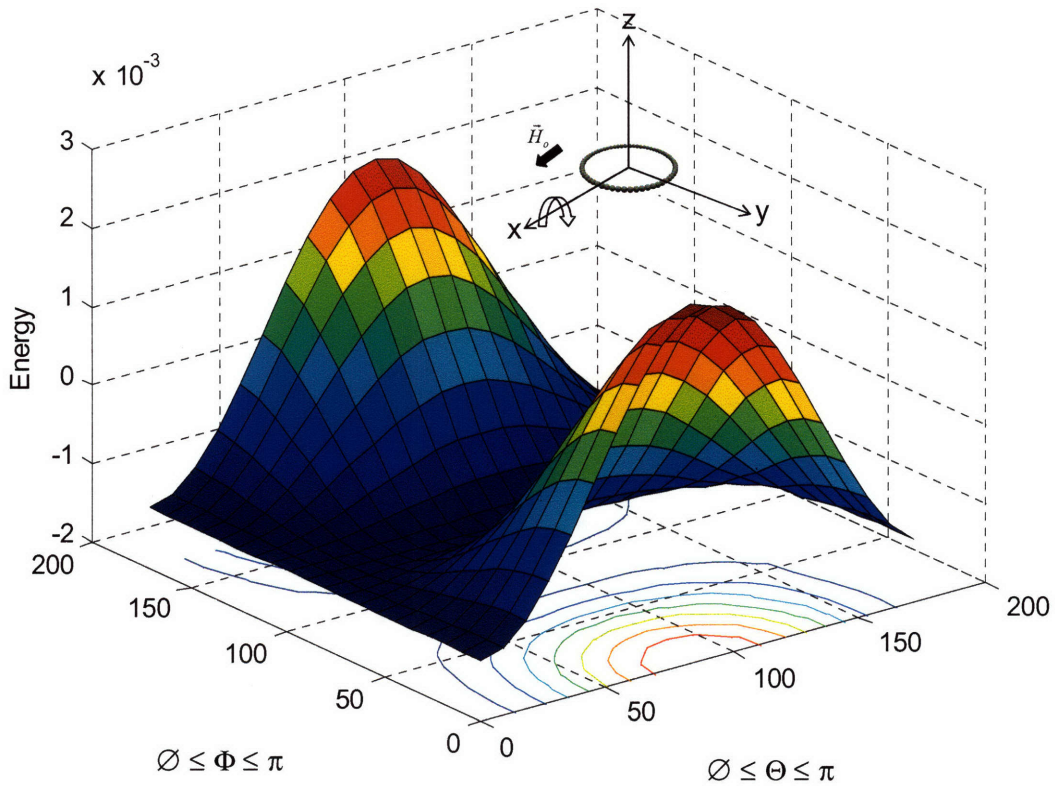
Figure 5-13. Potential energy surface of a magnetic ring when the field is applied in the x direction. The inset shows that U_{self}^{ring} is minimum for the orientation attained when the ring is rotated around the x axis.

144

Similarly when the external field was in *y* direction the minimum energy orientation corresponded to when $\theta = 0$ or $\phi=0$. This corresponded to the orientation when the applied field was in the plane of the ring (Figure 5-14).
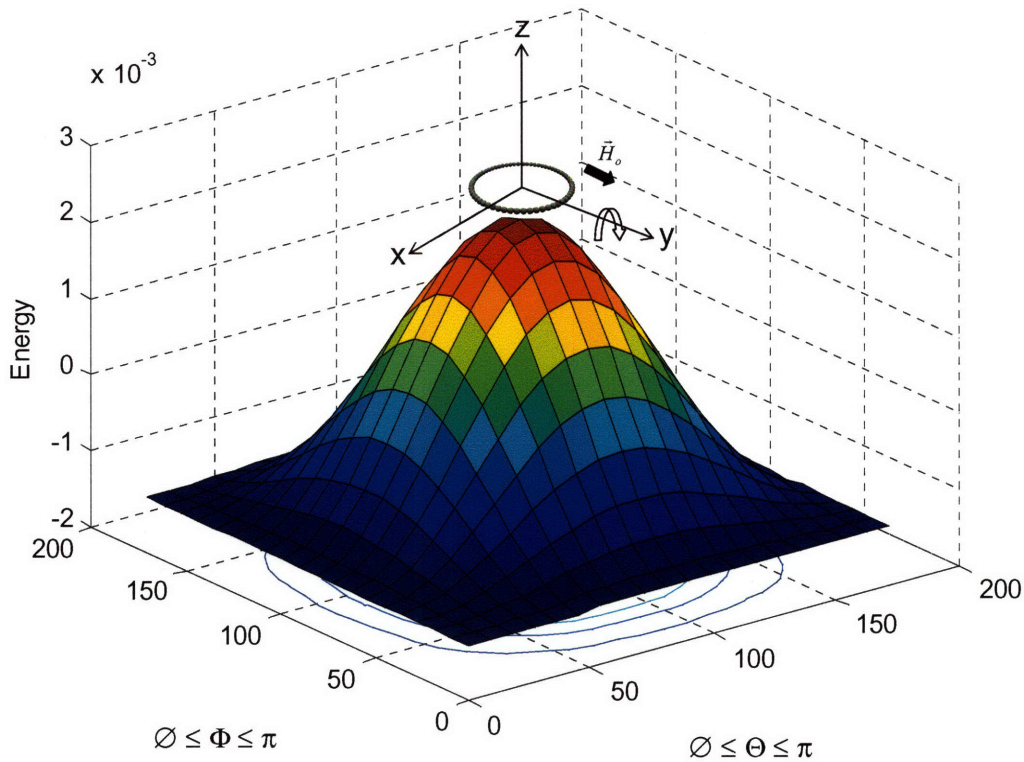
Figure 5-14. Potential energy surface of the magnetic ring with the applied field in the direction.

Similarly, minimum orientation case when the field was in *z* direction was when $\theta =\pi/2$ (Figure 5-15), which ensured that the applied field was always in the plane of the ring. Next we modeled the interaction potential between two rings to determine the most favorable orientation of the combined system. Figure 5-16 shows two rings with one at the origin and the second ring at distance *d* on the y axis.
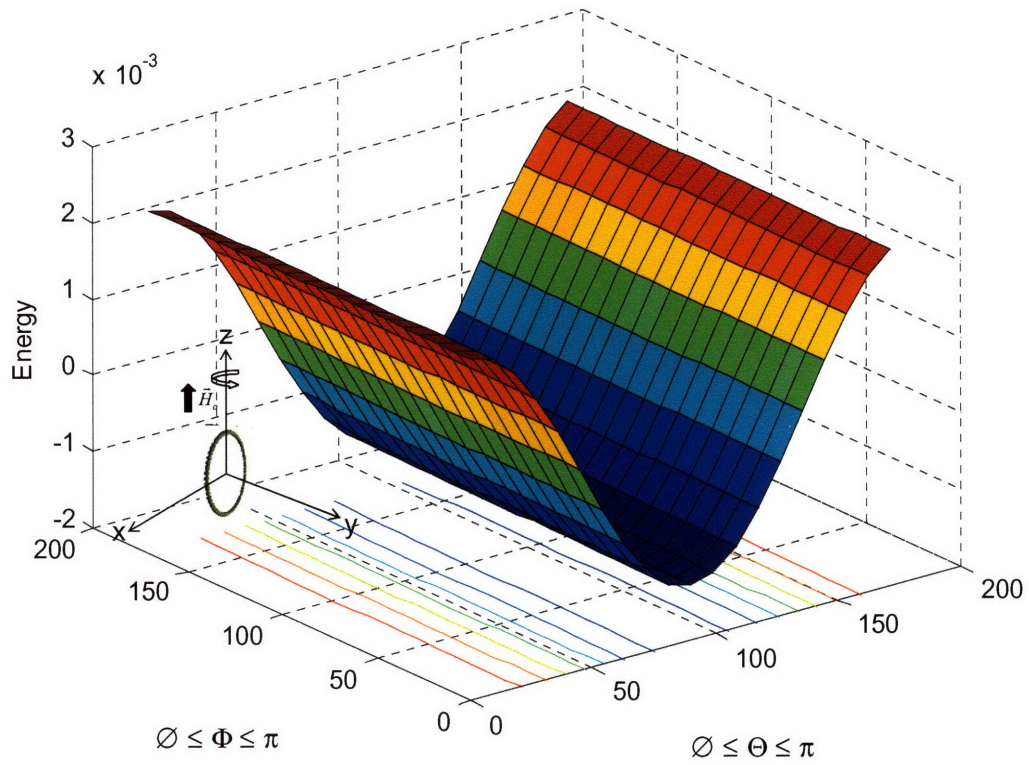
Figure 5-15. Potential energy surface of the magnetic ring with the applied field in the z direction.
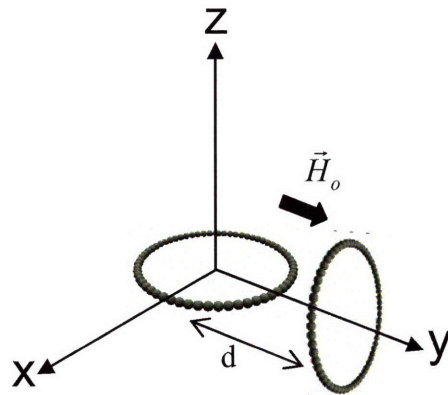
Figure 5-16. Schematic of interaction between two magnetic rings.

The total magnetic interaction energy between the two rings can be written as

146

$$U^{ring} = U_{self}^{ring} + U_{inter}^{ring} \tag{16}$$

where U_{self}^{ring} was same as calculated before for the single ring. U_{inter}^{ring} accounts for the interaction between the nanoparticles of the two rings. Equation (16) was evaluated numerically to find the mutual orientation between the two rings that will minimize U^{ring} The magnetic field was fixed in the y direction. During the calculation, ring 1 was fixed on the xy plane and ring 2 was spanned in all possible directions. Figure 5-17 illustrates the total potential energy surface estimated for the two ring system. U^{ring} was found to be minimum when $\theta = 0$ or π, which will be the case when the two rings are on the xy plane with the applied field in the plane of the rings. This means that in the presence of the external magnetic field the rings will aggregate in a fashion as shown in Figure 5-18.
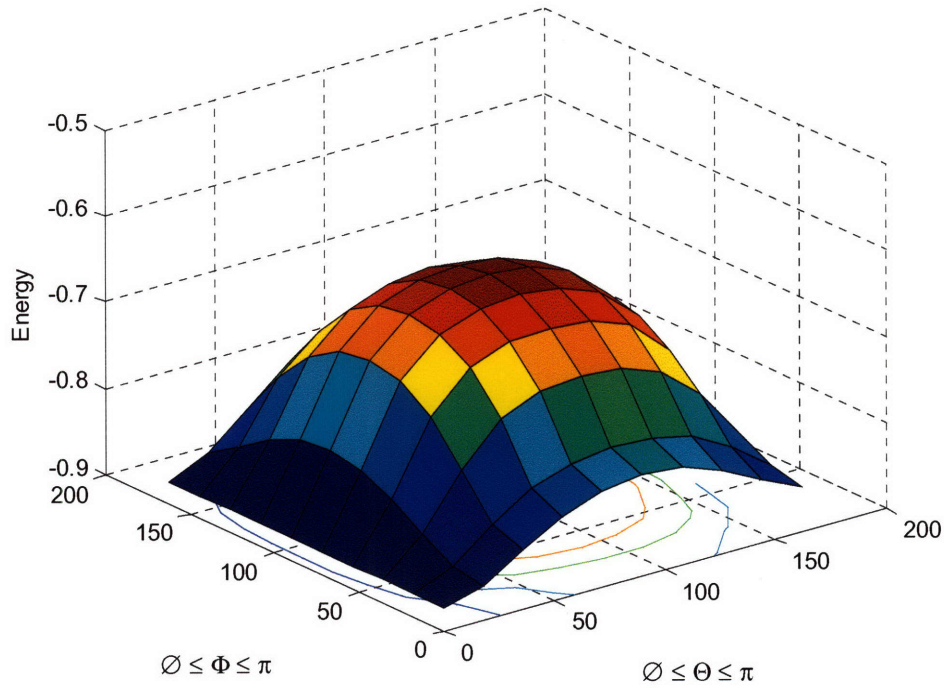
Figure 5-17. Potential energy surface of the system of two interacting rings.
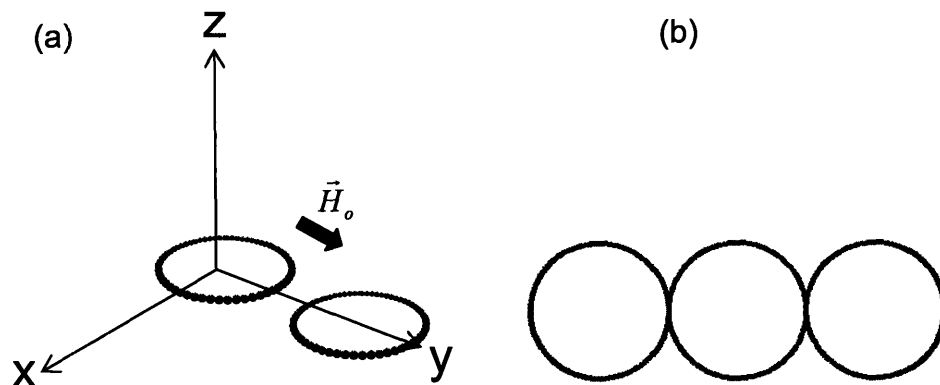
Figure 5-18. (a) Mutual orientation between the magnetic rings at which U^{ring} is minimum. (b) This means that the rings will link not stack in the presence of the magnetic field.

5.2.5 Experimental: Synthesis of Magnetic Rings and Disks

5.2.5.1 Materials

Poly(diallydimethyl) ammonium chloride (PDAMAC, MW 150,000), sodium chloride (NaCl), iron(III) chloride hexahydrate (FeCl$_3$.6H$_2$O, 97 wt%), iron(II) chloride tetrahydrate (FeCl$_2$.4H$_2$O 99 wt%), sodium hydroxide pellets (NaOH, 99.99 wt% in water) and nitric acid (HNO$_3$, 70% in water) were obtained from Aldrich (Milwaukee, WI). All chemicals were used as received. Negatively charged rings (25 μm O.D. x 20 μm I.D. and 12 μm height) and disks templates (60 μm Diameter x 15 μm height) and were synthesized by Dendukadi et al. and were used as received.

5.2.5.2 Methods

The negatively charged templates were made positively charged using a layer-by-layer polyelectrolyte adsorption technique [25]. In a typical process, 0.5 mL of the template solution with ~ 2000 templates was suspended in an aqueous solution of 0.5 mL of 1 mg/mL PDAMAC (0.1 M NaCl). After 30 min of adsorption, the templates were separated by centrifugation at 2500g for 10 min and resuspended in water. This process was repeated three times. The aqueous solution of negatively charged magnetic

nanoparticles (200μL, concentration 0.05 wt% in water) was then added to the positively charged PDAMAC coated templates (0.5 ml). Magnetic nanoparticles were synthesized according to the method outlined in Chapter 2 [26]. After continuous shaking for 30 min, magnetic nanoparticle coated templates were recovered by centrifugation at 2500g for 10 min. They were again coated with PDAMAC and magnetic nanoparticles using the procedure outlined above to yield magnetic disks and rings.

5.2.5.3 Characterization

The magnetic response of the rings and disks was viewed under an optical microscope (Zeiss, Axiovert 200) using a 20X/1.0 objective, and images were captured using a digital camera (Zeiss Axiocam, MRC) with Axiovision image processing software. A magnetic field was generated using hand held 0.2 T neodymium-boron-iron magnets (McMaster Carr).

5.2.5.4 Results and Discussion

Magnetically-responsive rings and disks were synthesized using the layer-by-layer technique in which the templates were coated sequentially with positively and negatively charged polyelectrolytes, and magnetic nanoparticles. Figure 5-19 shows the optical micrograph of the response of the magnetic rings to the applied field. An isolated magnetic ring flipped when the magnetic field was applied. The new orientation (Figure 5-19b) ensured that the applied field was in the plane of the paper. This is in line with the model predictions (Figure 5-15). When the two rings were close enough to interact magnetically, they linked together in the direction of the magnetic field. This equilibrium orientation agrees with the model predictions (Figure 5-17). The response of the magnetic disks to the applied field was similar to that of the rings (Figure 5-20). We can, thus, conclude that the magnetic structures with high aspect ratio will link together along the edge in the direction of the applied magnetic field. This is the minimum energy configuration with the direction of the applied field in the plane of the structure formed.
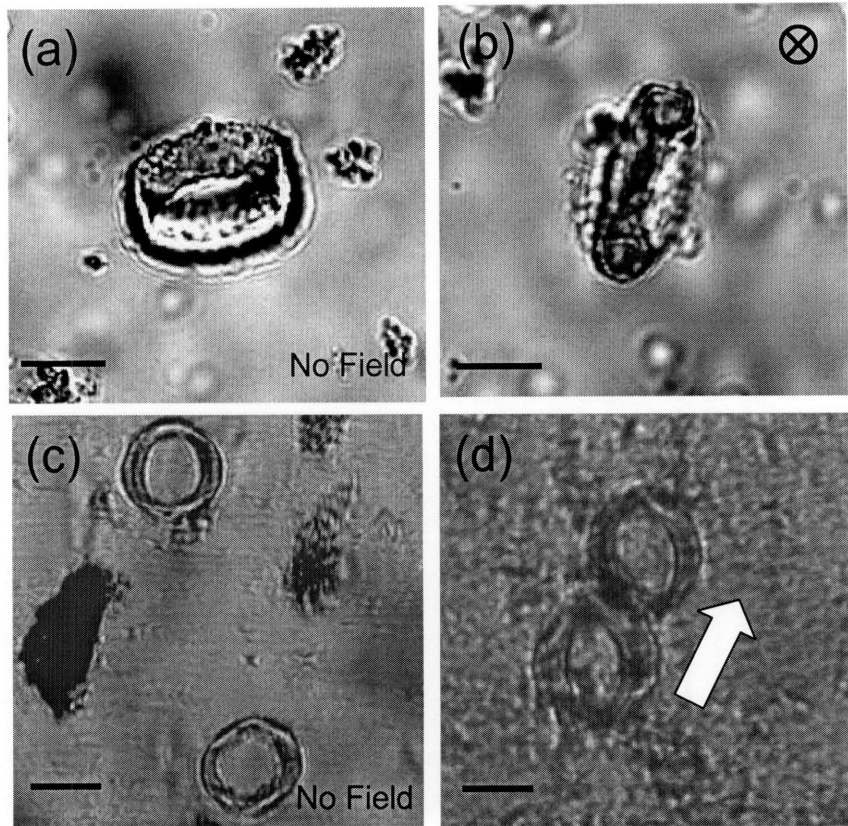
Figure 5-19. (a) Optical micrograph of a magnetic ring under a zero applied field. (b) When the magnetic field was applied in the direction perpendicular to the plane of the paper ($\otimes$), the ring stood up on its edge. The magnetic potential of the ring is minimized when the applied field is the plane of the ring. (c) Optical micrograph of the two magnetic rings in the absence of the magnetic field. (c) The magnetic rings linked together reversibly when the magnetic field was applied (arrow indicates the direction of the field). The scale bar on the optical micrograph represents 10 μm.
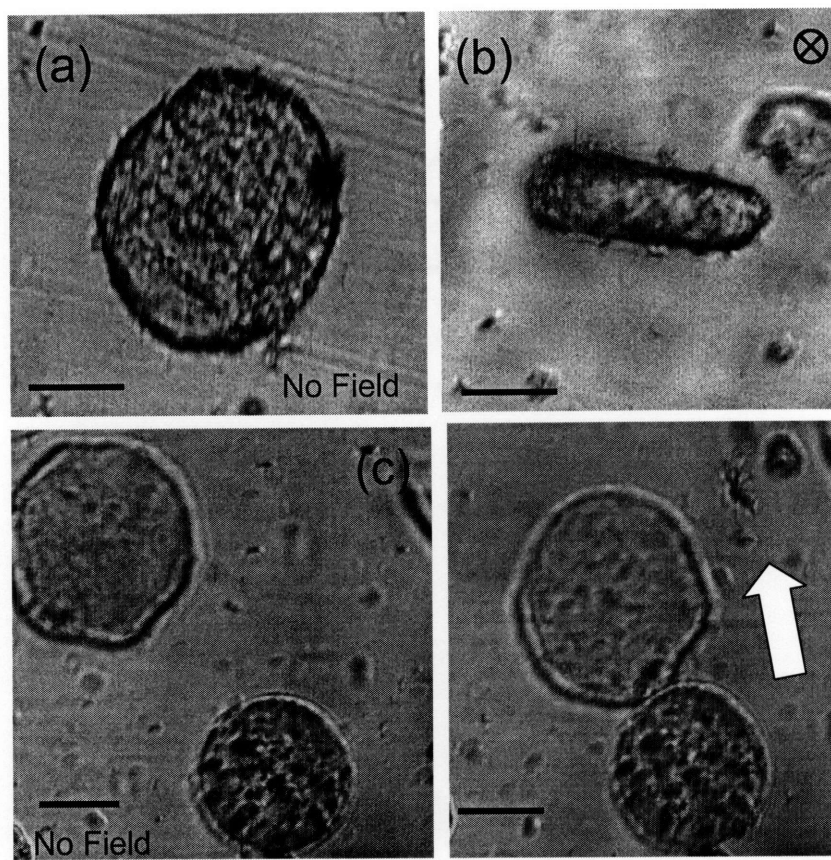
Figure 5-20. (a) Optical micrograph of a single magnetic disc under zero applied field. (b) The micrograph represents the response of the magnetic disk to a magnetic field applied in the direction perpendicular to the plane of the paper. (c) When the magnetic disks are in close vicinity to interact, (d) they linked together in the direction of the applied magnetic field.

5.2.6 Conclusions: Surfactant and Polymeric Templates

Surfactant templates can be used to create exotic magnetoresponsive structures like disks and icosahedras. However, the charge difference between the surface and the edges is not large enough to support selective adsorption on the edges to yield rings or cage like magnetic structures. Polymeric templates synthesized by Dendukadi et al. [17] were used to create magnetic rings and disks. Layer-by-Layer process was used to coat these non-spherical scaffolds with magnetic nanoparticles to generate magneto-responsive colloids. Coating ring shaped colloids with magnetic nanoparticles and observing their behavior under an applied magnetic field provided experimental proof to the model predictions.

5.3 Radiation Crosslinking

Until now we have discussed and studied template based generation of magnetic cluster. The magnetic nanoparticles in suspension adsorbed on the oppositely charged template to generate a magnetic clusters shaped liked the template. In this section we will describe will discuss the "templateless" coupling of magnetic nanoparticles. Unlike the presence of electrical charge which was important in the template based technique, the polymer coating stabilizing the magnetic nanoparticle in suspension is critical for this method.

Radiation crosslinking is the method of linking polymeric chains by exposing the aqueous solution of polymer to ionizing radiation [27]. The ionizing radiation generate free radicals on the polymer chains which couple together to generate a crosslinked network (Figure 5-19). This method has been extensively applied for crosslinking poly(ethylene oxide) (PEO) [7, 28] to synthesize hydrogels from high molecular weight PEO or to convert low molecular PEO into high molecular weight PEO. The degree of crosslinking can be controlled by the amount of radiation dosage. The advantages of radiation crosslinking are that the network formation is completed without a potentially toxic crosslinking agent and that there are no chemical functional groups in the crosslinked structure.
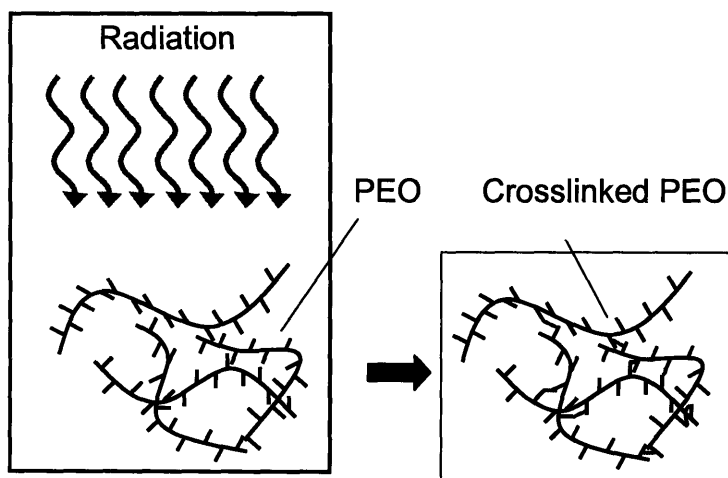
Figure 5-21. Illustration of crosslinkg of PEO chains with radiation crosslinking.

In the following sections we will discuss a methodology for using radiation crosslinking for generating aggregates in the magnetic fluids composed of magnetic naoparticles stabilized with PEO. Graft co-polymer of poly(acrylic acid) (PAA) and PEO stabilized magnetic nanoparticles were synthesized using the technique developed by Moeser et al [29]. Carboxylic acid groups along the PAA backbone are required to coordinate to the magnetic nanoparticle particle surface and the PEO side chains on the graft copolymer providing steric stabilization in aqueous solution. Electron beam (e beam) was used as a source of ionizing radiation.

5.3.1 Experimental

5.3.1.1 Materials

Polyacrylic acid (50 wt% in water, M_w = 5000), iron(III) chloride hexahydrate (97%), iron(II) chloride tetrahydrate (99%), and ammonium hydroxide (28 wt% in water) were obtained from Aldrich (Milwaukee, WI). Jeffamine XTJ-234 (CH_3-O-PEO/PPO-NH_2, EO:PO = 6.1:1, M_w = 3000) was obtained as gifts from Huntsman Corporation (Houston, TX). All chemicals were used as received.

The amino-terminated PEO polymer used in this work consisted of random copolymers of ethylene oxide (EO) and propylene oxide (PO) repeat units. XTJ-234 contained 6.1 EO units per PO unit, so its character is similar to that of a pure PEO chain and designate it as PEO-NH_2 for simplicity.

5.3.1.2 Polymer Synthesis

Graft copolymers were prepared by reacting polyacrylic acid (PAA) with amino-terminated PEO and PPO, as illustrated in Figure 5-20. 16 % of the carboxylic acid groups on the PAA were reacted with PEO-NH_2 chains
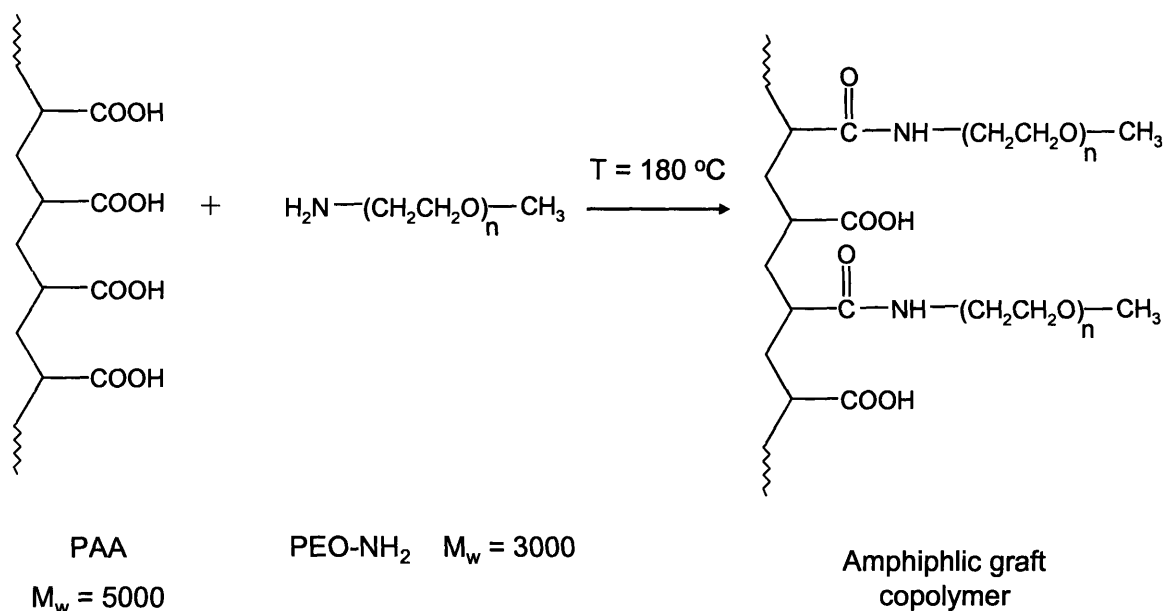
Figure 5-22. Amphiphilic graft copolymer synthesis. The graft copolymers are synthesized by attaching amino-terminated PEO to a PAA backbone via an amidation reaction. The majority of the COOH groups are left unreacted for subsequent attachment to the magnetite nanoparticles.

In a typical reaction, 5 g of PAA and 33 g of PEO-NH₂ was added to a reaction vessel. The mixture was heated to 180 °C and reacted for 2 h under a bubbling flow of nitrogen that provided mixing, prevented oxidation, and expelled water produced by the condensation reaction. The product was cooled to room temperature and dissolved in water to produce a 33 wt% solution.

5.3.1.3 Nanoparticle Synthesis

The magnetite nanoparticles were produced by chemical coprecipitation in a graft copolymer solution. In a typical procedure (Figure 5-21), an aqueous solution containing 2.35 g of iron(III) chloride hexahydrate, 0.86 g of iron(II) chloride tetrahydrate, and 3.75 g of the 33 wt% graft copolymer solution was prepared by dissolving the reagents in 37.5 mL of deoxygenated water. Deoxygenation was achieved by sparging with nitrogen under vigorous stirring for 30 min before reaction. The resulting Fe^{3+} and Fe^{2+} concentrations were 0.22 and 0.11 M, respectively, which provided the 2:1 ratio required to produce Fe_3O_4 stoichiometrically. To begin the reaction, the aqueous solution was

154

heated to 80 °C with continual nitrogen sparging and stirring. When the temperature reached 80 °C, the flow of nitrogen was stopped, and 5 mL of 28 wt% ammonium hydroxide were added to precipitate iron oxide in the form of magnetite. The mixture was then stirred for 30 min at 80 °C before cooling to room temperature. After cooling, the coated nanoparticles remained suspended in water indefinitely. This procedure produced 1 g of magnetite in 40 mL of water, which is equivalent to a 2.5 wt% suspension of magnetite.
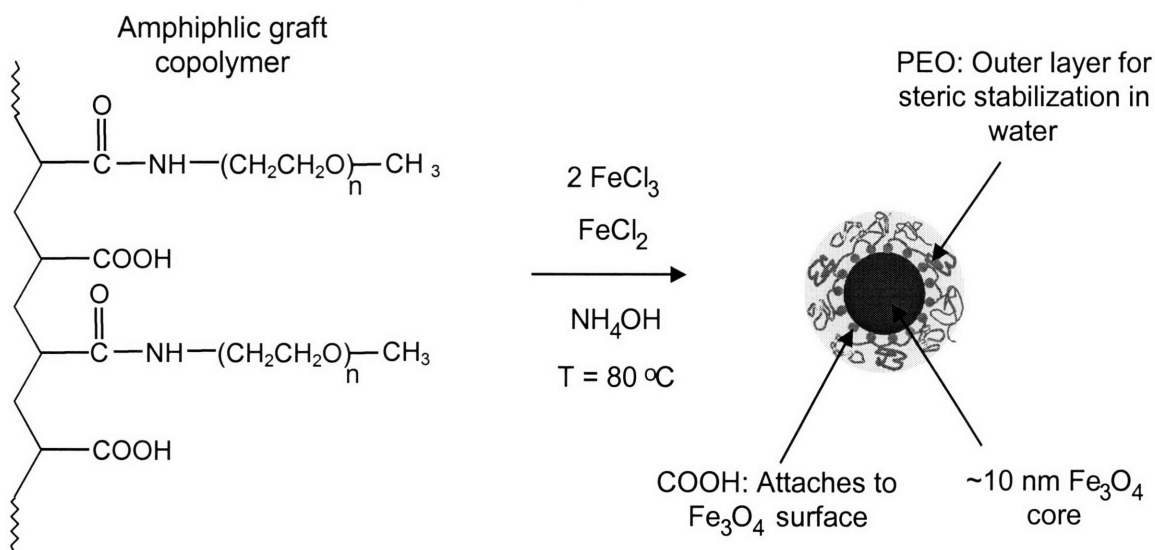
Figure 5-23. Aqueous magnetic fluid synthesis. The magnetic nanoparticles are produced by chemical coprecipitation of iron salts in an aqueous solution of the PEO-PAA graft copolymer. Soon after Fe_3O_4 nucleation begins, carboxylic acid groups on the polymer backbone bind to the particle surface, limiting particle growth and forming nanoparticles with a polymer coating.

The magnetic fluids were purified in a Centricon-Plus 100,000 molecular weight cutoff centrifugal ultrafiltration cell (Millipore). The suspensions were first diluted to 0.5 wt% Fe_3O_4 with distilled water and then concentrated to 2.5 wt% in the filter. The polymer-coated nanoparticles were retained in the filter while unattached polymer and ions were removed in the filtrate. This process of dilution and concentration in the filter was repeated four times to fully remove free polymer and ions, which we confirmed by evaporating the filtrate and measuring the mass of residual solid until none remained.

5.3.1.4 Radiation Crosslinking

5ml of 0.5 wt% of magnetic fluid was sparged with nitrogen for 30 mins to remove any traces of dissolved oxygen. It was then poured into a 2.5 cm culture plate and covered with Saran wrap. The samples were exposed to the electron beam for a given amount of time (High Voltage Research Laboratory, MIT). The exposure time governs the amount of dosage which was varied from 0.1 Mrad - 1 Mrad.

5.3.2 Results and Discussion

Average size of the magnetic nanoparticle was found to be 25 nm from the Dynamic light scattering measurements (Figure 5-22a). The average core size of the magnetic nanoparticle was found to be 10 nm from the TEM measurements (Figure 5-22b). This indicate that the polymeric shell has a thickness of ~ 7.5 nm.
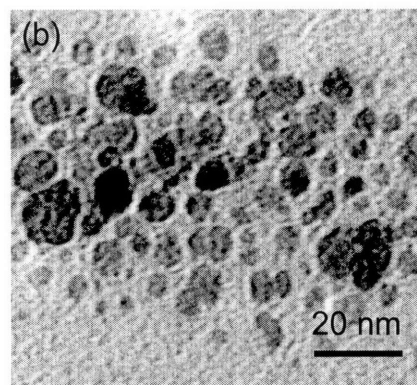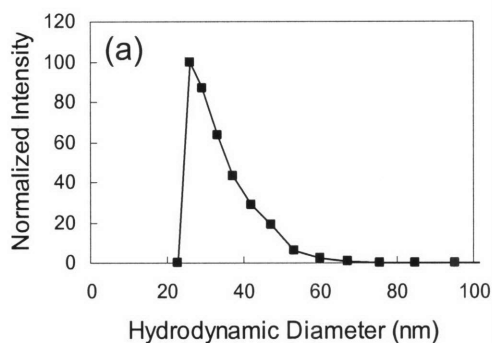
Figure 5-24. (a) Dynamic light scattering spectra of the magnetic nanoparticles. The average hydrodynamic radius of the nanoaprticle was ~ 25 nm. (b) TEM micrograph of the magnetic nanoparticles. The average magnetic core size was ~ 7.5 nm.

The size of the aggregate formed after radiation was also measured with DLS. Figure 5-23 shows the average hydrodynamic diameter as measured from DLS as a function of radiation dosage. The aggregate size increases with radiation dosage upto a threshold beyond which the crosslinking of polymer chains results in gelation of the suspension. The upper limit of aggregate size that can be made from this technique is ~ 60 nm which are still small enough to form any observable structures in a magnetic field. Nonetheless, this is a very simple method to make magnetic gels. Magnetic gels have

gained lots of interest for their potential applications as biosensors and actuators [30-33]. The magnetoelastic characteristics of these gels make them "smart materials" because they undergo a change in shape under a presence of a magnetic field [31]. The available methods to synthesize magnetic gels involve chemical crosslinking of the magnetic nanoparticles in the gel matrix. Chemical crosslinker used to crosslink the nanoparticles can contaminate the gel making them unfit for any biological applications. However radiation crosslinking technique developed in our work is an efficient way to create non-toxic magnetic gels. The only requirement for this method is the ability to make magnetic nanoparticles stabilized with the polymer of interest.
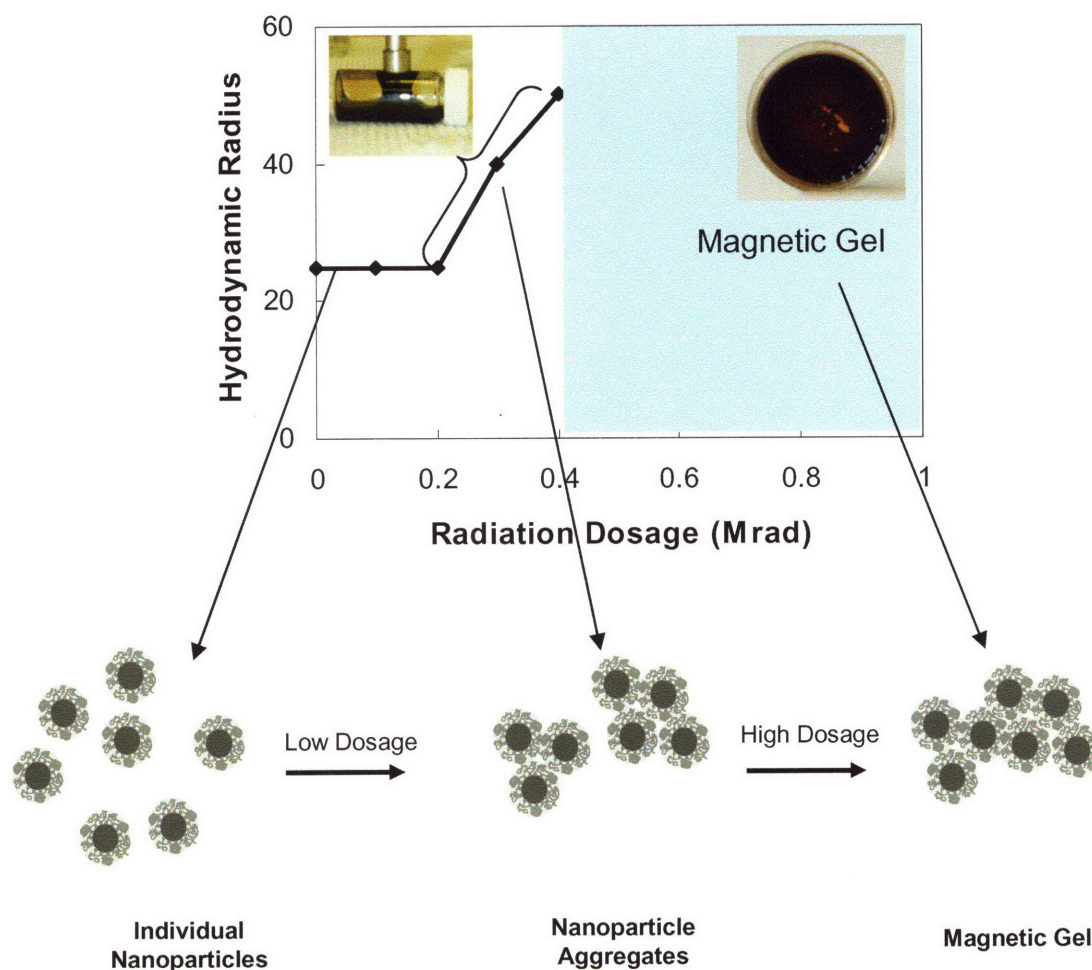
Figure 5-25. DLS plot of aggregation formed during radiation crosslinking as a function of radiation dosage.

5.3.3 Conclusions: Radiation Crosslinking

Radiation crosslinking is a very clean way to create either small size aggregates or macro aggregates like gels. It is not a very efficient way of making intermediate size aggregates (~200 nm-800 nm) which are of interest to us for this work. Nonetheless it is an efficient way of making ferrogels. The polymer in the gel synthesized in our work was PEO, which is a benign polymer. This can make these gels an attractive candidate for novel biological applications.

5.4   References

1.   Zhan, Y., E.A. Van Kirk, P. Xu, W.J. Murdoch, M. Radosz, and Y. Shen, *PH-responsive three layer onion-structured nanoparticles for Drug Delivery*. Abstracts of Papers, 231st ACS National Meeting, Atlanta, GA, United States, March 26-30, 2006, 2006: p. PMSE-092.

2.   Correa-Duarte, M.A. and L.M. Liz-Marzan, *Carbon nanotubes as templates for one-dimensional nanoparticle assemblies*. Journal of Materials Chemistry, 2006. **16**(1): p. 22-25.

3.   Israelachvili, J.N., *Intermolecular And Surface Forces*. 1992: Academic Press.

4.   Di Renzo, F., A. Galarneau, P. Trens, and F. Fajula, *Ordered mesoporous oxides: micelle-templated materials*. Handbook of Porous Solids, 2002. **3**: p. 1311-1395.

5.   Desplantier-Giscard, D., O. Collart, A. Galarneau, P. Van Der Voort, F. Di Renzo, and F. Fajula, *Mechanical strength of micelle-templated silicas (MTS)*. Studies in Surface Science and Catalysis, 2000. **129**(Nanoporous Materials II, Proceedings of the Conference on Access in Nanoporous Materials, 2000): p. 665-672.

6.   Beck, J.S., J.C. Vartuli, W.J. Roth, M.E. Leonowicz, C.T. Kresge, K.D. Schmitt, C.T.W. Chu, D.H. Olson, E.W. Sheppard, and et al., *A new family of mesoporous molecular sieves prepared with liquid crystal templates*. Journal of the American Chemical Society, 1992. **114**(27): p. 10834-43.

7.   Merrill, E.W., K.A. Dennison, and C. Sung, *Partitioning and Diffusion of Solutes in Hydrogels of Poly(Ethylene Oxide)*. Biomaterials, 1993. **14**(15): p. 1117-1126.

8. Geoffrey D. Moeser, K.A.R., William H. Green, Paul E. Laibinis, and T. Alan Hatton, *Water-Based Magnetic Fluids as Extractants for Synthetic Organic Compounds.* Ind. Eng. Chem. Res., August 17, 2002. **41 (19), 4739 -4749, 2002.**

9. Yada Akira, K.Y., Nishiguchi Hiroshi,Kitada Akira, Mori Yoshiyuki, *Modified polyvinyl alcohol,* in *Patent abstracts of Japan.* 1996: Japan.

10. Dubois, M., B. Deme, T. Gulik-Krzywicki, J.C. Dedieu, C. Vautrin, S. Desert, E. Perez, and T. Zemb, *Self-assembly of regular hollow icosahedra in salt-free catanionic solutions.* Nature, 2001. **411**(6838): p. 672-675.

11. Zemb, T., M. Dubois, B. Deme, and T. Gulik-Krzywicki, *Self-assembly of flat nanodiscs in salt-free catanionic surfactant solutions.* Science, 1999. **283**(5403): p. 816-819.

12. Massart, R., *Ferromagnetic fluid.* 1981.

13. Qian, J. and Y. Zhang, *Manufacture of hollow capsule from plant gum.* 2005, (Zhejiang Xinchang Spice Plastic Pills Co., Ltd., Peop. Rep. China). Application: CN. p. 5 pp.

14. Park, M.-K., S. Deng, and R.C. Advincula, *Sustained release control via photo-crosslinking of polyelectrolyte layer-by-layer hollow capsules.* Langmuir, 2005. **21**(12): p. 5272-5277.

15. Liu, Y.-j., Y.-h. Zhu, S.-q. Zhang, and X.-l. Yang, *Production and application of hollow capsules templated on melamine-formaldehyde microspheres.* Guocheng Gongcheng Xuebao, 2004. **4**(6): p. 513-518.

16. Mercier, P., M. Peyrot, F. Nguyen-Cauzac, F. Kalcz, Y. Lazorthes, F. Hauzanneau, and B. Sallerin, *Method and device for making hollow starch-based particles containing active substances.* 2002, (Kappa Biotech S.A., Fr.). Application: WO. p. 44 pp.

17. Dendukuri, D., D.C. Pregibon, J. Collins, T.A. Hatton, and P.S. Doyle, *Continuous-flow lithography for high-throughput microparticle synthesis.* Nature Materials, 2006. **5**(5): p. 365-369.

18. Vaz, C.A.F., C. Athanasiou, J.A.C. Bland, and G. Rowlands, *Energetics of magnetic ring and disk elements: Uniform versus vortex state.* Physical Review B: Condensed Matter and Materials Physics, 2006. **73**(5): p. 054411/1-054411/9.

19.   Imre, A., L. Zhou, A. Orlov, G. Csaba, G.H. Bernstein, W. Porod, and V. Metlushko, *Application of mesoscopic magnetic rings for logic devices*. IEEE-NANO 2004, Fourth IEEE Conference on Nanotechnology, Muenchen, Germany, Aug. 16-19, 2004, 2004: p. 124-126.

20.   Heyderman, L.J., M. Klaeui, B. Noehammer, C.A.F. Vaz, J.A.C. Bland, and C. David, *Fabrication of nanoscale magnetic ring structures and devices*. Microelectronic Engineering, 2004. **73-74**: p. 780-784.

21.   Furst, E.M. and A.P. Gast, *Micromechanics of magnetorheological suspensions*. Physical Review E, 2000. **61**(6): p. 6732-6739.

22.   Martin, J.E., K.M. Hill, and C.P. Tigges, *Magnetic-field-induced optical transmittance in colloidal suspensions*. Physical Review E, 1999. **59**(5): p. 5676-5692.

23.   Melle, S., G.G. Fuller, and M.A. Rubio, *Structure and dynamics of magnetorheological fluids in rotating magnetic fields*. Physical Review E, 2000. **61**(4): p. 4111-4117.

24.   Tao, R., *Super-strong magnetorheological fluids*. Journal of Physics-Condensed Matter, 2001. **13**(50): p. R979-R999.

25.   Decher, G., *Fuzzy nanoassemblies: Toward layered polymeric multicomposites*. Science, 1997. **277**(5330): p. 1232-1237.

26.   Massart, R., E. Dubois, V. Cabuil, and E. Hasmonay, *Preparation and Properties of Monodisperse Magnetic Fluids*. Journal of Magnetism and Magnetic Materials, 1995. **149**(1-2): p. 1-5.

27.   Peppas, N.A., *Hydrogels in Medicine and Pharmacy*. Fundamentals. Vol. 1. 1986, FL.: CRC Press, Inc.

28.   Grollmann, U. and W. Schnabel, *On The Kinetics Of Polymer Degradation In Solution.9. Pulse-Radiolysis Of Poly(Ethylene Oxide)*. Makromolekulare Chemie-Macromolecular Chemistry And Physics, 1980. **181**(6): p. 1215-1226.

29.   Moeser, G.D., K.A. Roach, W.H. Green, P.E. Laibinis, and T.A. Hatton, *Water-based magnetic fluids as extractants for synthetic organic compounds*. Industrial & Engineering Chemistry Research, 2002. **41**(19): p. 4739-4749.

30.   Varga, Z., J. Feher, G. Filipcsei, and M. Zrinyi, *Smart nanocomposite polymer gels*. Macromolecular Symposia, 2003. **200**: p. 93-100.

31.   Varga, Z., G. Filipcsei, and M. Zrinyi, *Magnetic field sensitive functional elastomers with tuneable elastic modulus*. Polymer, 2006. **47**(1): p. 227-233.

32.   Varga, Z., G. Filipcsei, A. Szilagyi, and M. Zrinyi, *Electric and magnetic field-structured smart composites*. Macromolecular Symposia, 2005. **227**: p. 123-133.

33.   Chatterjee, J., Y. Haik, and C.J. Chen, *pH-reversible magnetic gel with a biodegradable polymer*. Journal Of Applied Polymer Science, 2004. **91**(5): p. 3337-3341.

Chapter 6

Nanoparticle Size and Energy Absorption Applications

6.1　Introduction

The magnetic behavior of a magnetic nanoparticle under an applied field depends on its size. This, in turn, affects the behavior of magnetic structures composed of magnetic nanoparticles. The two most important properties that rely on nanoparticle size are magnetic moment and magnetic relaxation. The magnetic moment is a measure of the magnetization developed by a nanoparticle under an applied magnetic field and scales linearly with nanoparticle volume (Chapter 1, equation 1). Relaxation is a measure of the time a nanoparticle would take to come to equilibrium when the external field is perturbed. The magnetization of the magnetic nanoaprticle in suspension can relax by two different mechanisms after the applied field has been changed; Brownian relaxation and Néel relaxation. Brownian relaxation is due to the rotational diffusion of the whole particle in the dispersion [1]. Néel relaxation is caused by the reorientation of the magnetic vector within the particle [2] . The effective time constant is governed by the faster relaxation process. Néel relaxation time constant depends much stronger on the particle diameter than the Brownian relaxation. In our system the nanoparticles are adsorbed on the template, hence only Néel relaxation is operative.

Structures composed of different sized nanoparticles will respond differently to a spatially varying magnetic field. For example when an ensemble of fixed small nanoparticles is deflected in a magnetic field, the dipole of the nanoparticles will always be aligned with the external magnetic field because they relax essentially instantaneously. However for the slow relaxing particles (i.e. bigger particles) when the time scale of impact is shorter than the relaxation time of the nanoparticle, the dipoles are misaligned relative to the field, resulting an additional mechanism for energy adsorption that depends on deflection and is tunable through the magnitude of the applied magnetic field (Figure 6-1). The energy penalty associated with deflection of the dipole in a magnetic field can actually increase the rigidity modulus of the material containing the nanoparticles. This

can be exploited in making smart energy absorbing materials. These materials will be active only in the presence of the magnetic field and will behave normally otherwise.
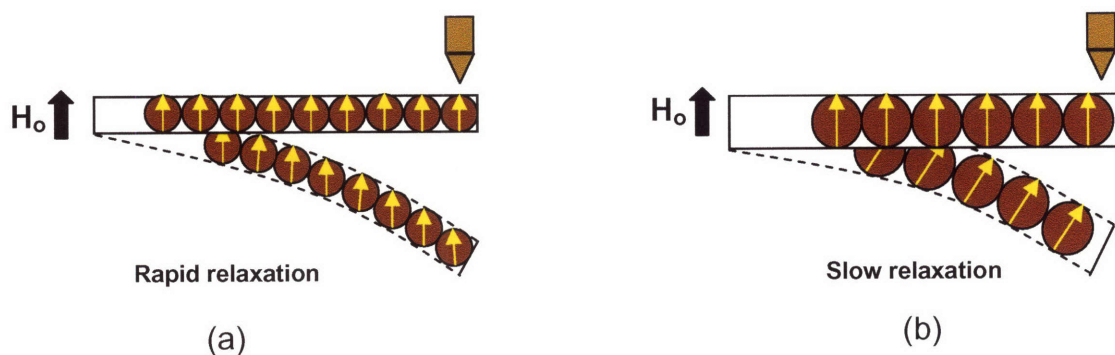
Figure 6-1. An illustration of an ensemble of (a) fast relaxing and (b) slow relaxing nanoparticles. The time scale of the deflection is higher than the relaxation time of the smaller particle and lower than the relaxation time of the bigger nanoparticles. The smaller nanoparticles (a) remain aligned with the external field under deflection. The bigger particles (b) however relax slowly and are misaligned against the field which requires additional energy.

In Chapters 2, 4, and 6, we used ~ 8 nm nanoparticles to create magneto-responsive core-shell and chain-like structures. Aqueous route synthesis of magnetic nanoparticles was used to synthesize magnetite nanoparticles which produced polydisperse nanoparticles with an average size of 8 nm. An organic route synthesis [3] was adopted to produce monodisperse magnetic nanoparticles of different sizes. A scheme was devised to transfer these nanoparticles from organic solvent to water for their subsequent use in layer by layer assembly process. The LbL process was however not successful due to the resulting instability of the nanoparticles in aqueous solution. We however, studied the relaxation properties of the nanoparticles with the size ranging from 6 nm to 16 nm and explore the use of larger sized particles in energy adsorption scenarios. The magnetization properties of the nanoparticles as a function of size were characterized in detail. Field cooling experiments were performed on the nanoparticles embedded in the polymeric matrix to confirm the existence of the Néel relaxation.

Impact test was performed on a matrix impregnated with nanoparticles in the presence and absence of a magnetic field to test the hypothesis that the relaxation

phenomenon can be used for energy adsorption. The amount of energy adsorbed by the nanoparticles depended on its magnetization. We used iron nanoparticles instead of magnetite nanoparticles for the impact test experiments because they have infinite Néel relaxation and magnetization which is much higher compared to magnetite. This enhanced the energy absorbing capability of the matrix impregnated with the iron nanoparticles and it was possible to measure it experimentally.

6.2 Experimental

6.2.1 Materials

Iron(III) acetylacetonate (97%), benzyl ether (99%), 1,2 hexadecanediol (97%), ethanol, oleic acid (90%), oleylamine (70%), Poly(maleic anhydride alt-1-tetradecene) ($M_n \sim 7300$), hexane and chloroform were purchased from Aldrich (Milwaukee, WI). Raw material to cast Polyurethane foam was procured from Smooth-it® (Easton, PA). 25 nm iron particles were procured from Reade Advanced Materials (Providence, RI). All chemicals were used as received.

6.2.2 Synthesis of Monodisperse Magnetite Nanoparticles

Monodisperse magnetite nanoparticles were produced using the scheme of Sun et al. [3]. An organometallic precursor is decomposed in the presence of a mixture of surfactants at high temperature resulting in monodisperse magnetite nanoparticles [3]. Seed mediated growth is then utilized to produce bigger size magnetite nanoparticles upto 16 nm in diameter, as described below.

Synthesis of seeds

2 mmol of Iron(III) acetylacetonate, 10 mmol of 1-2 hexadecanediol, 6mmol of oleic acid and 6 mmol of oleylamine and 20 ml of benzyl ether were mixed in a 3 neck flask and were stirred continuously under a blanket of nitrogen. The temperature was ramped up slowly upto 200 °C (2.5 °C /min) and the mixture was kept at this temperature for 2 hrs. Finally the mixture was refluxed at 300 °C for 1 hr. The resulting black mixture was cooled down to room temperature and ethanol was added followed by centrifugation

at 7000g to separate out magnetite. The centrifuged product was re-suspended in hexane and was used for seed mediated growth.

Synthesis of bigger nanoparticles

2 mmol of Iron(III) acetylacetonate, 10 mmol of 1-2 hexadecanediol, 2mmol of oleic acid and 2 mmol of oleylamine , 20 ml of benzyl ether and 80 mg of seeds in 4 ml of hexane were mixed in a 3 neck flask and stirred continuously under a blanket of nitrogen. The mixture was kept at 100 $^{\circ}$C for 30 mins and at 200 $^{\circ}$C for 1h. Finally the mixture was refluxed at 300 $^{\circ}$C for 30 mins. The magnetite was recovered using the procedure outlined above. The resulting magnetite nanoparticles can then be used as seeds for subsequent synthesis. In this manner stable nanoparticles up to 16 nm were synthesized in 3 cycles.

6.2.3 Phase Transfer of Magnetic Nanoparticles

Poly(maleic anhydride alt-1-tetradecene) solution in chloroform was mixed with a solution of monodisperse nanoparticles in chloroform (100 polymer units per nm^2) [4]. The mixture was stirred for 2 hrs at room temperature. The solution was sonicated for 20 min and the solvent was evaporated. The solid was dissolved in water and sonicated for 5 min. The aqueous nanoparticles were then adsorbed on the PS beads using the technique described previously (Chapter 2, Section.2.3.1).

6.2.4 Synthesis of Foam with Iron Nanoparticles

. The monomer and the curing agent to cast PU foam were mixed in a 1:1 ratio in a 100 ml beaker. The iron nanoparticles were stirred in the precursor mixture (30 wt%) to create a uniform dispersion of particles in the foam. The resulting composite was cured for 2 hrs. A cylindrical shape piece was cut out from the cured matrix and was used for the drop ball test.

6.2.5 Characterization

Transmission electron microscopy (TEM) experiments were performed on a JEOL 2010 (200 kV) instrument. Samples were prepared by evaporating dilute

suspensions on a carbon-coated film. Superconducting Quantum Interference Device (SQUID) experiments using a Quantum Design MPMS instrument were conducted to determine relaxation behavior and magnetization curve for native magnetite nanoaparticles. In the drop ball test a polycarbonate ball weighing 4 g was dropped onto a polyurethane/nanoparticle foam from a height of ~150 cm through a transparent acrylic tube guide, with a impact velocity of 5.4 m/s. A horseshoe type permanent magnet was used to generate 0.15 T of magnetic field across the foam. The trajectory of the ball was recorded by a high speed digital video camera (Phantom v 5.0, Vision Research Inc.) at 1900 frames per second.

6.3 Results and Discussion

6.3.1 Relaxation Behavior

The TEM micrographs of magnetite nanoparticles of different diameters synthesized at different stages by the organic route are shown in Figure 6-2. Using seed mediated growth we were able to make monodisperse nanoparticles from 6nm - 16 nm.

(a)

20 nm
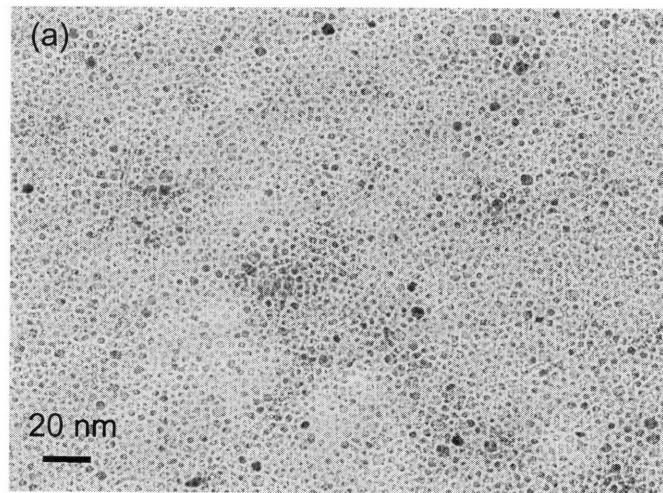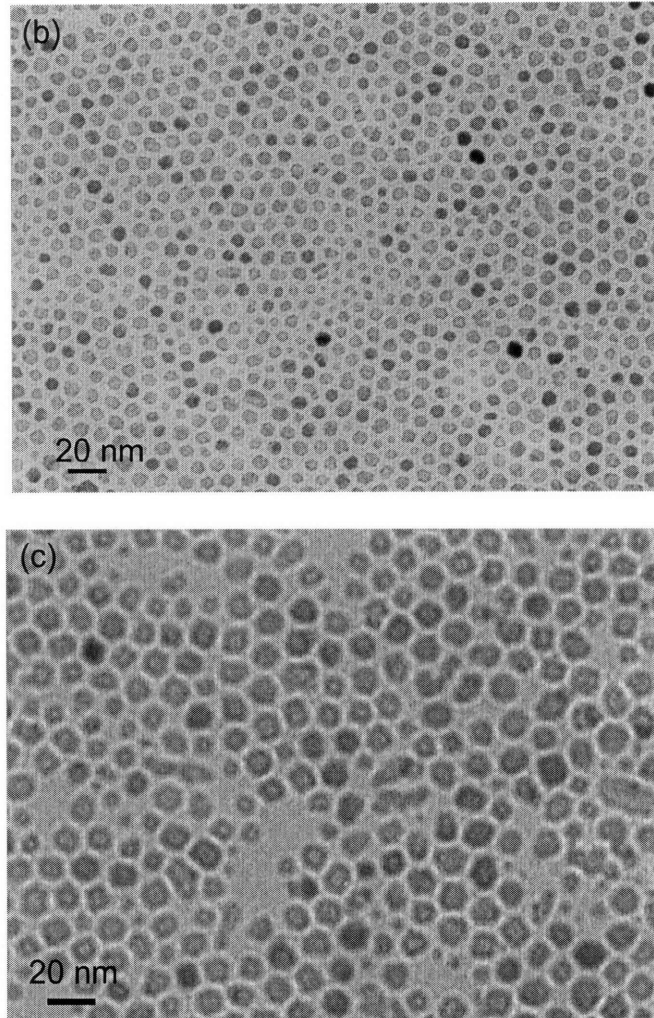
Figure 6-2. TEM images of magnetite nanoparticles at different stages of seed mediated growth. (a) 6 nm diameter (b) 12 nm diameter (c) 16 nm diameter nanoparticles.

The Néel relaxation time of a magnetic nanoparticle is given by the expression

$$\tau_N = \frac{1}{f_o}\left(\frac{KV}{k_B T}\right) \tag{1}$$

where f_o is frequency term which is $\sim 10^9$ for magnetite, K is the anisotropy constant of the material, V is the volume of the magnetic nanoparticle and k_B is the boltzmann constant and T is the temperature. Note that the Néel relaxation time scales with the exponential of the volume of the particle. At room temperature it is 10^{-8} s for 8 nm and 1ms for 16 nm magnetite nanoparticles [5]. Figure 2 compares the relaxation curves for 6

167

nm and 16 nm nanoparticle as synthesized by us. The nanoparticles were embedded in a polymeric matrix using the technique of Electrospinning. This will be discussed in detail in the next chapter [6]. The experiment was performed at 5K. The samples were exposed to a pulse of 1000 Oe (~ 0.1T) magnetic field which was then switched off. The resultant decay in magnetization was then measured as a function of time. The experiment was performed at a low temperature (5K) to enhance the relaxation time of the particles thereby making it easy to measure. The measurements (Figure 6-3) clearly indicate that the relaxation of the 16 nm nanoparticles is slower than the 6 nm particles and is a definite proof of size dependence of the Néel relaxation.
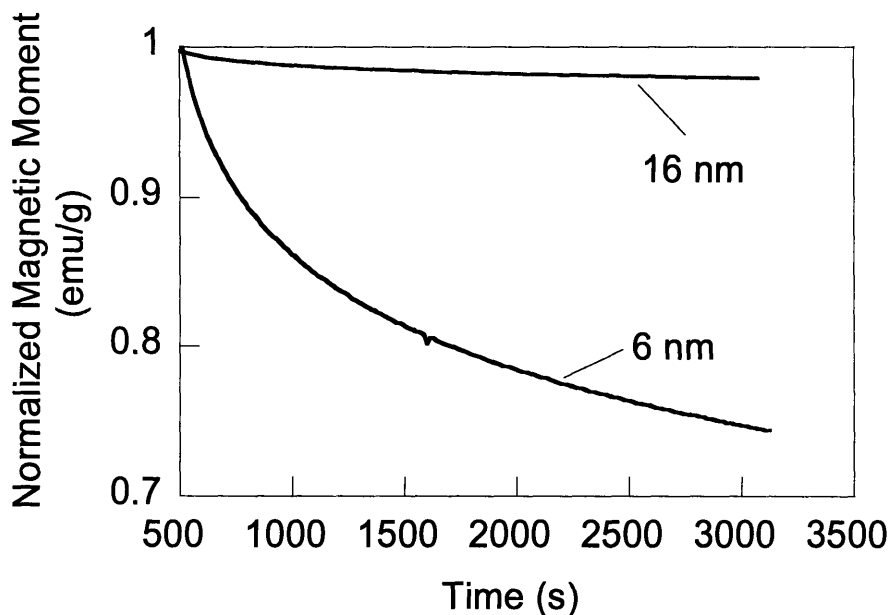
Figure 6-3. Magnetic relaxation curves for 6 nm and 16 nm nanoparticles at 5K. The relaxation of the 16 nm magnetite particles is significantly slower than the 6 nm particles.

Field cooling experiments were conducted to further confirm the size dependence behavior of the magnetic nanoparticles (Figure 6-4). First the sample of magnetic nanoparticle in the polymeric matrix was cooled to 5K. Then a small uniform external field was applied and the net magnetization was measured while heating the sample to 300 K at a constant rate. The samples were then cooled back to 5K at a constant rate and the magnetization was measured. Figure 6-4 depicts the cooling curves for 6 and 16 nm

nanoparticles. Before the heating cycle, when the particles are cooled to 5K the magnetic moment of the nanoparticles are randomly oriented and remain locked in the easy axes of magnetization. As the temperature is increased, the thermal energy is available to align with the external field direction. Eventually, the net moment reaches a maximum when the greatest population of moments aligns with the external field. This maximum temperature is called the blocking temperature (T_B). Above blocking temperature thermal energy is strong enough to randomize the moment. During the cooling cycle measurement, the curve diverges from the heating cycle values near the blocking temperature. This is because the individual moment of each nanoparticle will tend to align with the easy axes of magnetization that is closest to the applied field and remain locked in that direction at low temperature. The blocking temperature for 6 nm was 11 K and 6 nm was 62 K.
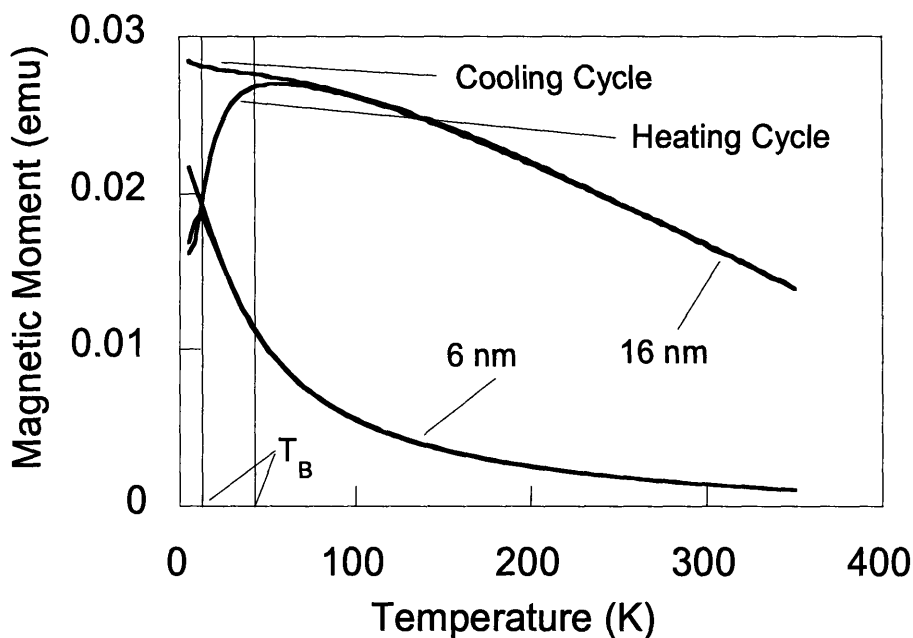
Figure 6-4. Field cooling curves for 6 nm and 16 nm magnetite nanoparticles. The blocking temperature difference between 6 nm and 16 nm particles is vastly different.

Above the blocking temperature, the nanoparticle exhibit superparamagnetism i.e. they have a zero magnetization at zero applied field. This was confirmed by performing the magnetization studies. Figure 6-5 shows the magnetization curve for 6 nm and 16 nm

particles. There was no remanence when the applied field was reduced to zero. At high fields, the dipoles are completely aligned with the external field and they achieve saturation. The smaller value of the saturation magnetization value for the 6 nm nanoparticles can be attributed to the surface spin canting of the small nanoparticles [7].
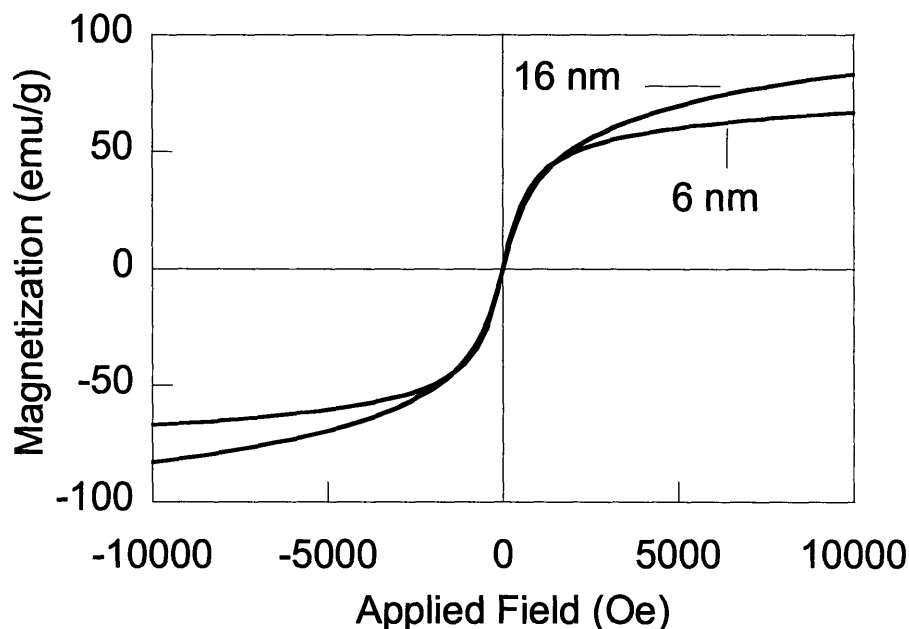
Figure 6-5. The magnetization curves of 6 nm and 16 nm particle at room temperature. Both nanoparticles are superparamagnetic at room temperature and have zero remanence when the applied field is zero.

6.3.2 Phase Transfer

The technique to transfer the monodisperse nanoparticles from organic to aqueous phase was similar to the method developed by Pellegrino et al. [4]. The hydrophobic part of the polymer interacted with the hydrophobic part of the oleic acid forming a bilayer [8] (Figure 6-6). The maleic anhydride part of the polymer hydrolyzed to carboxylic acid group in the presence of water. This provided both steric and electrostatic stabilization to the nanoparticles in aqueous solution. However the efforts to adsorb the nanoparticles on the positively charged PS beads to create core-shell structures were not successful. Destabilization of the magnetic nanoparticles was observed in the presence of the PS beads. This could be due to the stripping off the negatively charged bilayer when the

170

nanoparticle approached the positively charged bead, thereby making the nanoparticles unstable.

Organic Phase   Aqueous Phase

Phase
Transfer

Oleic acid/Oleyl amine coated
magnetic nanoparticles

Oleic acid/Oleyl amine coated
magnetic nanoparticles
stabilized with a bilayer of
Poly(maleic anhydride alt-1-
tetradecene)
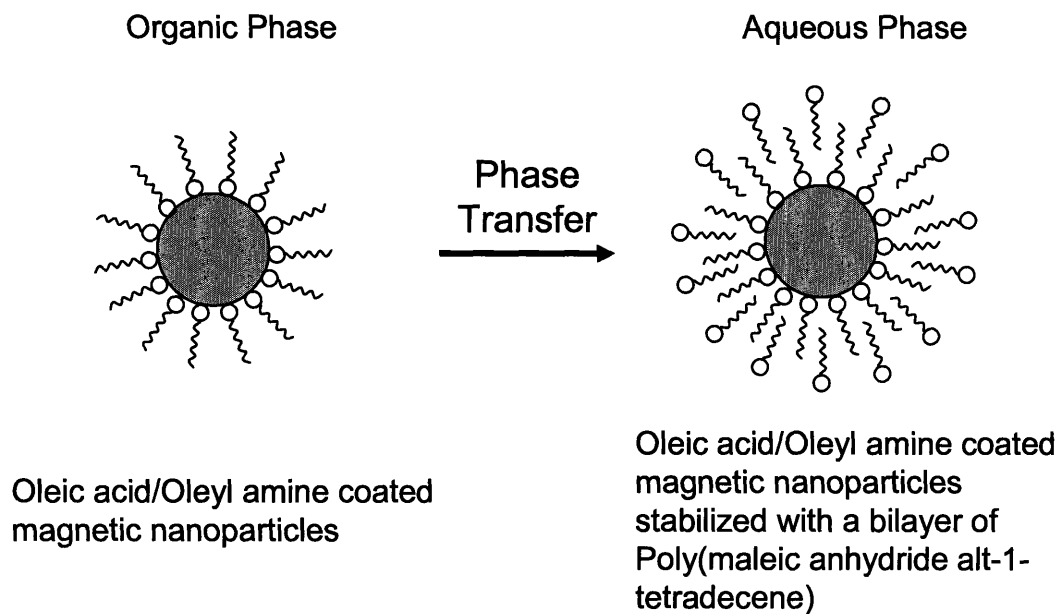
Figure 6-6. Schematic of the phase transfer of the nanoparticles from organic to aqueous phase using a bilayer type approach.

Recently our lab has developed a ligand exchange method to exchange the surfactants (Oleic acid/Oleyl amine) present on the surface of the nanoparticles with a hydrophilic polymer [9]. These nanoparticles were successfully adsorbed on a charged template (positively charged silica beads) without any problem of aggregation that was observed with bilayer type stabilized magnetite nanoparticles (Figure 6-6). Using this technique it should be possible to create core-shell structures of monodisperse magnetic nanoparticles and can be explored further in future.

6.3.3 Energy Absorption

The energy absorption capability of the slow relaxing nanoparticles was confirmed with a drop ball test. Figure 6-1 illustrates the underlying theory proposed by us. Figure 6-1a can also be visualized as a matrix impregnated with 6 nm nanoparticles and 1b as a polymeric matrix with 16 nm particles. In both the cases, the matrix is exposed to a strong enough magnetic field with the magnetic dipole aligned in the

171

direction of the field. When the fiber is deflected, the 6 nm particles will always be aligned with the external magnetic field because they relax instantaneously. However for the 16 nm particles when the time scale of impact is smaller than the relaxation time of the nanoparticle, the dipoles are misaligned against the field which has an energy penalty associated with it. This should increase the energy absorption capacity of the matrix. The interaction energy between a dipole with magnetic moment $\vec{m}$ and external magnetic field is given by

$$E_h = -(\vec{m}.\vec{H}_o) \qquad (2)$$

$$\vec{m} = \mu_o \vec{M} V \qquad (3)$$

where $\vec{H}_o$ is the external magnetic field, μ_o is the permeability of free space, $\vec{M}$ is the magnetization of the material and V is the volume of magnetic nanoparticle.

Given the loading density of the nanoparticles and the deflection of the matrix, the energy absorbed by the nanoparticles can be calculated using Equation (2) and (3). The amount of energy adsorbed is a function of the size (V) and the magnetization of the nanoparticles ($\vec{M}$). Magnetization value of the 16 nm magnetite nanoparticles was not sufficient to observe any measurable amount of energy absorbed. 25 nm iron nanoparticles were used instead. The magnetization and the volume of the 25 nm iron nanoparticles are 2 times and 4 times respectively, to that of 16 nm magnetite nanoparticles and this should yield measurable amount of energy absorption. Also the iron nanoparticles have infinite Néel relaxation time and the time scale of impact should not be critical (Figure 6-7).
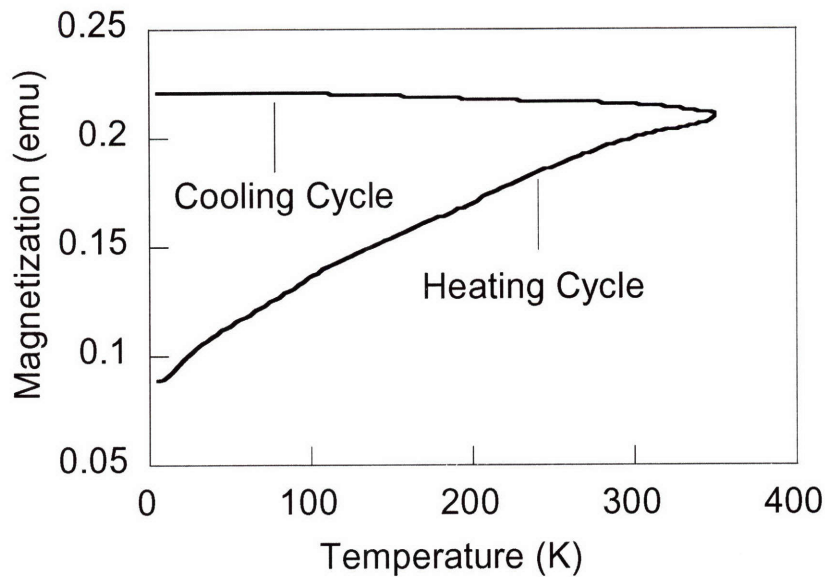
Figure 6-7. Field cooling experiment curve for 25 nm iron nanoparticles. The blocking temperature is 350 K. At room temperature, these nanoparticles will behave like magnetic dipoles permanently magnetized in the direction of the applied field.

The PU foam embedded with nanoparticles undergoes a large deflection under a small load. The amount of energy absorbed by the nanoparticle is proportional to the deflection. Hence the increment in the foam stiffness (due to energy absorption of the nanoparticles) in the presence of the field should be measurable. Figure 6-8 shows the trajectory of the ball as followed by the high speed camera. The indentation in the absence of the field is 20 % higher compared to that in the presence of the field.
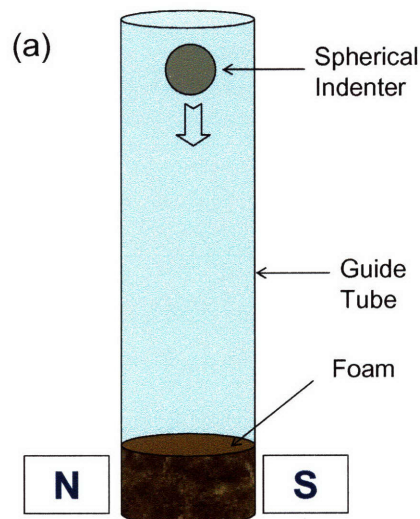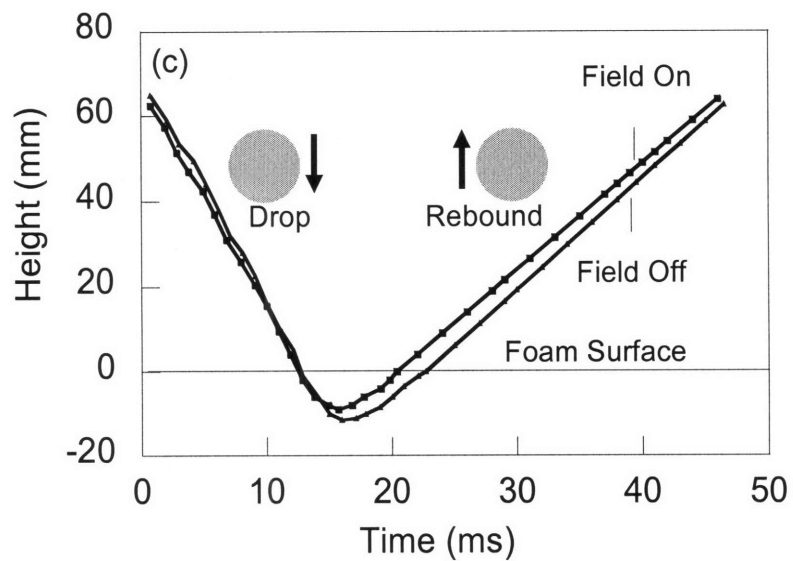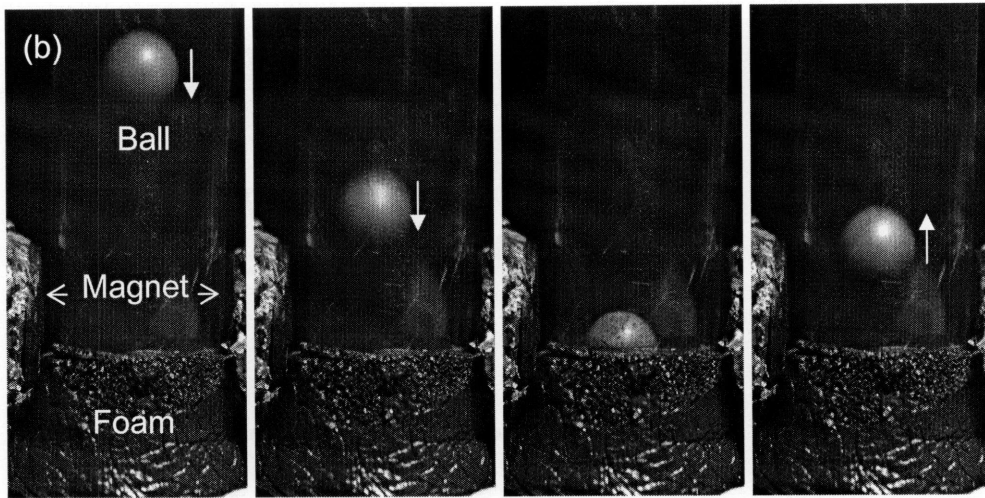
Figure 6-8. (a) Schematic of the drop ball impact test setup. (b) Impact test images at different times as captured with a high speed camera (c) trajectory of ball during the impact test.

The low indentation indicates the increase in the foam stiffness under the magnetic field. The extra energy required to bend the dipoles against the field leads to the stiffening of the foam.

6.3.4 Impact Test Modeling

We used Hertz contact theory to model the deflection of the foam and prove that the increase in the modulus of the foam in the presence of the field is indeed due to the magnetic effect of the nanoparticles. The magnitude of the energy taken up by the nanoparticles can be calculated if the strain field within the foam is known. The strain field can be converted into the deflection of the associated nanoparticles. Once the deflection is known the amount of energy required to bend the calculated from equation (2). We assumed the foam acts like an elastic flat plate and neglected the viscoplastic effects associated with the foam. We adapted the case of indentation of a semi infinite plane by a spherical indenter (Figure 9) [10, 11].
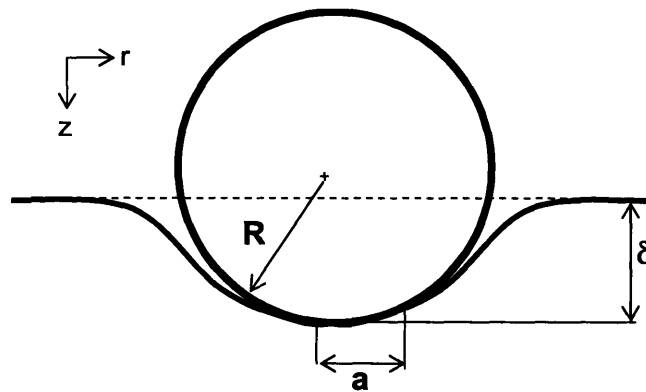
Figure 6-9. Schematic of indentation of a semi-infinite flat plane by a spherical indenter.

The normal and radial stress profile on the surface and in the interior of the sample was estimated. At the surface z = 0, normal (σ_z) and radial stresses (σ_r) are given by

$$\frac{\sigma_z}{p_m} = -\frac{3}{2}\left(1-\frac{r^2}{a^2}\right)^{1/2}; \quad r \le a$$

$$\sigma_z = 0; \quad r > a \tag{4}$$

$$\frac{\sigma_r}{p_m} = \frac{1-2v}{2}\frac{a^2}{r^2}\left[1-\left(1-\frac{r^2}{a^2}\right)^{3/2}\right]-\frac{3}{2}\left(1-\frac{r^2}{a^2}\right)^{1/2}; \quad r \le a$$

$$\frac{\sigma_r}{p_m} = \frac{1-2v}{2}\frac{a^2}{r^2}; \quad r > a \tag{5}$$

Within the specimen interior the stresses are given by

$$\frac{\sigma_r}{p_m} = \frac{3}{2}\left\{\begin{array}{l}\dfrac{1-2v}{3}\dfrac{a^2}{r^2}\left[1-\left(\dfrac{z}{u^{1/2}}\right)^3\right]+\left(\dfrac{z}{u^{1/2}}\right)^3\dfrac{a^2u}{u^2+a^2z^2}+\\[3mm]\dfrac{z}{u^{1/2}}\left[u\left(\dfrac{1-v}{a^2+u}\right)+(1+v)\dfrac{u^{1/2}}{a}\tan^{-1}\left(\dfrac{a}{u^{1/2}}\right)-2\right]\end{array}\right\} \tag{6}$$

$$\frac{\sigma_\theta}{p_m} = -\frac{3}{2}\left\{\begin{array}{l}\dfrac{1-2v}{3}\dfrac{a^2}{r^2}\left[1-\left(\dfrac{z}{u^{1/2}}\right)^3\right]+\\[3mm]\dfrac{z}{u^{1/2}}\left[2v+u\left(\dfrac{1-v}{a^2+u}\right)-(1+v)\dfrac{u^{1/2}}{a}\tan^{-1}\left(\dfrac{a}{u^{1/2}}\right)\right]\end{array}\right\} \tag{7}$$

$$\frac{\sigma_z}{p_m} = -\frac{3}{2}\left(\frac{z}{u^{1/2}}\right)^3\frac{a^2u}{u^2+a^2z^2} \tag{8}$$

$$\frac{\tau_{rz}}{p_m} = -\frac{3}{2}\left(\frac{a^2u^{1/2}}{a^2+u}\right)\frac{rz^2}{u^2+a^2z^2} \tag{9}$$

where:

$$u = \frac{1}{2}\left[(r^2+z^2-a^2)+\left[(r^2+z^2-a^2)^2+4a^2z^2\right]^{1/2}\right]$$

176

In the above equations v is the poison's ratio of the foam, σ_θ is the angular stress, τ_{rz} is the shear stress, p_m is the mean pressure below the sphere and a is the radius of contact. p_m can be written as

$$p_m = \frac{P}{\pi a^2} \tag{10}$$

where P is the load imparted by the projectile on the surface. According to the Hertz contact theory [12], circle of contact is related to the elastic properties of the specimen and load P by

$$a^3 = \frac{4kPR}{3S} \tag{11}$$

where k is the elastic mismatch factor and for a rigid indenter and it is given by

$$k = \frac{9(1-v^2)}{16} \tag{12}$$

P can be calculated by equating the potential energy of the ball to the strain energy stored in the specimen [10].

$$\frac{1}{2}mv_o^2 = \frac{2}{5}\delta^{5/2}R^{1/2}\frac{3S}{4k} \tag{13}$$

R is the radius of the sphere and δ is the maximum deflection of the top surface.

δ and a are related by

$$\delta = \frac{a^2}{R} \tag{14}$$

We can calculate P from equation (10), (11), (13) and (14) as

$$P = \left[\left(\frac{5}{4}\right)^3 \frac{9}{16}\frac{S^2}{k^2} m^3 v_o^6 R \right]^{1/5} \tag{15}$$

177

In the drop ball test we observed 20% less deflection in the presence of the field. We can translate this into an equivalent amount of elastic energy using equation 13. We assumed that the energy absorbed by the foam and the particle is additive i.e. $E_{impact} = E_{foam} + \Delta E_{particle}$ where E_{impact} is the impact energy from the ball, E_{foam} is the energy absorbed by the foam and $\Delta E_{particle}$ is the energy taken up by the magnetic particles. For $S = 9e4$, $v = 0.4$ (Vendor data), δ_{off} (deflection when the magnetic field was off) = 0.01 m, $\delta_{on} = 0.008$ m (deflection when the magnetic field was off), $\Delta E_{particle}$ was found to be 0.024 J. From stress equations we can calculate the strain ε_i, using Hook's law.

$$
\begin{aligned}
\varepsilon_r &= \frac{1}{S}\left[\sigma_r - v(\sigma_\theta + \sigma_z)\right] \\
\varepsilon_\theta &= \frac{1}{S}\left[\sigma_\theta - v(\sigma_r + \sigma_z)\right] \\
\varepsilon_z &= \frac{1}{S}\left[\sigma_z - v(\sigma_\theta + \sigma_r)\right]
\end{aligned}
\tag{16}
$$

The strains were then used to calculate the displacement for given (r, z) using the following equations

$$
\varepsilon_r = \frac{\partial u_r}{\partial \theta}; \ \varepsilon_\theta = \frac{u_r}{r} + \frac{1}{r}\frac{\partial u_\theta}{\partial \theta}; \varepsilon_z = \frac{\partial u_z}{\partial z}; \ \tau_{rz} = \frac{\partial u_r}{\partial z} + \frac{\partial u_z}{\partial r}
\tag{17}
$$

u_i is the displacement in the ith coordinate. $\frac{\partial u_\theta}{\partial \theta} = 0$ since our system is axis-symmetric.

It is possible to solve analytically for the displacement at the surface. The displacement in the interior of the foam was calculated by numerically solving equation 6 and 8. Figure 6-10 shows displacement profile calculated in r and z direction. The boundary conditions that u_r, $u_z = 0$ as r and z $\rightarrow \infty$ is satisfied.

178
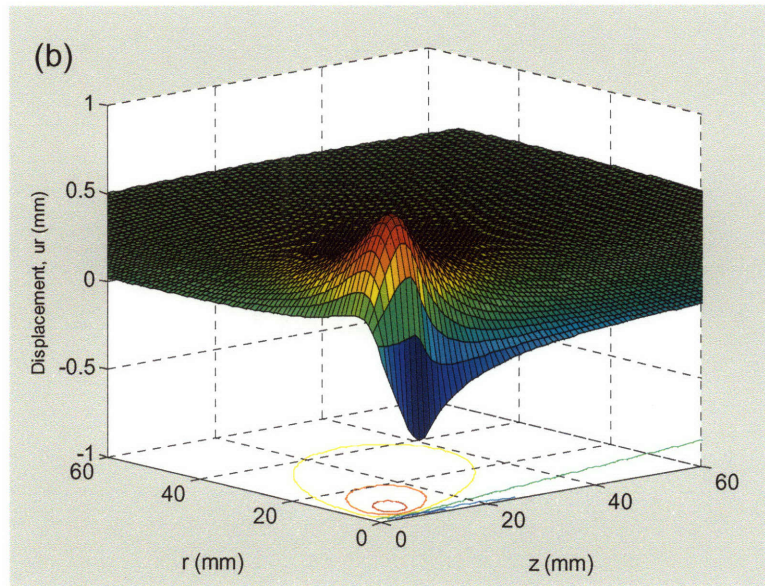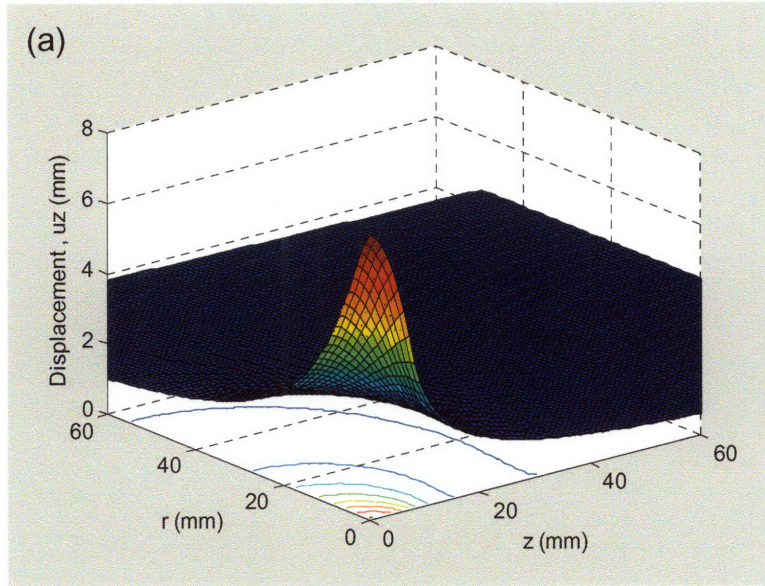
Figure 6-10. Surface plots of the model prediction of the displacement profile (a) $u_z(r,z)$ and (b) $u_r(r,z)$ of the foam.

The negative radial displacement indicates the corresponding points are pulled inward towards the center of contact. The calculated displacements were converted into the angular deflection at a given point (Figure 6-11).
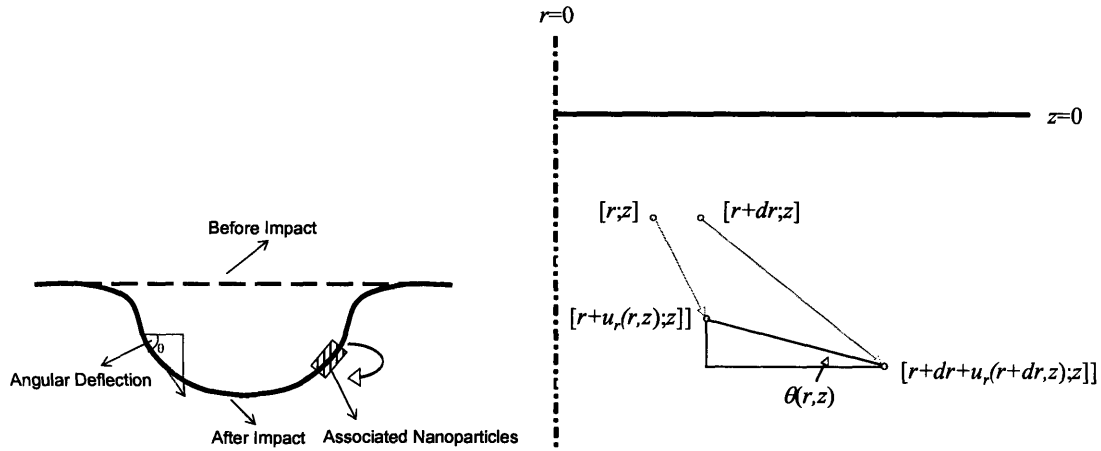
Figure 6-11. A schematic of the surface profile before and after the impact. The angular deflection can be calculated if the displacement in r (u_r) and z (u_z) direction is known.

The angular displacement of two points in the foam, originally at positions $[r,z]$ and $[r + dr, z]$ to their final positions

$[r + u_r(r,z); z + u_z(r,z)]$ and $[r + dr + u_r(r + dr,z); z + u_z(r + dr,z)]$, as shown Figure 9. Then, it follows that

$$\cos\theta(r,z) = \frac{r + dr + u_r(r + dr,z) - [r + u_r(r,z)]}{\sqrt{[r + dr + u_r(r + dr,z) - [r + u_r(r,z)]]^2 + [u_z(r + dr,z) - u_z(r,z)]^2}}$$

$$= \frac{1 + du_r / dr}{\sqrt{[1 + du_r / dr]^2 + [du_z / dr]^2}} \tag{18}$$

The net energy required to deflect an aligned dipole by an angle θ in a magnetic field is given by

$$E_h = mH_o(1 - \cos\theta) \tag{19}$$

Integrating E_h over the whole volume of the foam gave the net energy absorbed due to the deflection of the dipoles.

$$E_h = \int_0^{2\pi} \int_0^{\infty} \int_0^{\infty} n_0 mH[1 - \cos\theta(r,z)]r\,dr\,dz\,d\psi$$

$$= 2\pi n_0 mH \int_0^{\infty} \int_0^{\infty} [1 - \cos\theta(r,z)]r\,dr\,dz \qquad (20)$$

$$= 2\pi n_0 mH \int_0^{\infty} \int_0^{\infty} \left[1 - \frac{1 + du_r/dr}{\sqrt{[1 + du_r/dr]^2 + [du_z/dr]^2}} \right] r\,dr\,dz$$

where $\theta(r,z)$ is the angle a particle originally at position $[r,z]$ makes with the magnetic field when it has been displaced to its new position $[r + u_r(r,z); z + u_z(r,z)]$ and n_o is the number of particles per unit volume. The local change in the volume fraction of the nanoparticles is implicitly accounted for in the relative displacements of the different points within the foam.

The net energy required to deflect an aligned dipole by an angle θ in a magnetic field is given by

$$E_h = mH_o(1 - \cos\theta) \qquad (21)$$

Summing E_h over the whole volume of the foam gave the net energy absorbed due to the deflection of the dipoles. For the given loading (30 wt%) of the high magnetization iron nanoparticles in the matrix, the interparticle interactions are also important. λ (Chapter 1, Equation 3) was calculated to be ~ 5. Hence the change in interparticle interaction due to the deflection of the matrix was also considered and is given by

$$E_d = \frac{3m^2}{4\pi\mu_o t^3}(1 - \cos^2\theta) \qquad (22)$$

where t here is the interparticle distance in the matrix.

The summation of E_h and E_d over the whole volume of the foam was found to be ~ 0.019J, which was very close to what we observed experimentally (0.024 J). Table 1 shows the distribution of the energy absorbed by different mechanisms in the foam. The presence of magnetic field results in 33 % absorption of the energy by the nanoparticles. Out of this, 91% can be attributed to the Neél relaxation behavior. The change in inter particle interactions contributes to only 9% of the total energy taken up by the field activated nanoparticles.

Table 1: The distribution of energy absorption by different components of the foam

	% Energy Adsorbed
Foam	67%
E_h	30%
E_d	3%

The increase in elastic modulus of PU foam due to the coupling interaction between the magnetic field and the dipole moment of nanoparticles can be calculated using equation 14.

$$\frac{S_{on}}{S_{off}} = (\frac{\delta_{off}}{\delta_{on}})^{2.5} = 1.75 \tag{23}$$

where S_{on} and S_{off} are the modulus of foam in the presence and absence of the field. In this case, the modulus of polyurethane foam increased by 75% in the presence of the magnetic field. We can thus conclude that the Néel relaxation can be used enhance the energy absorption capacity of the matrix in which they are embedded.

The close agreement between the model prediction and the experimental value validated our model. The fraction of energy absorbed by the particles, E_p as a function of n_omH/S is shown in Figure 6-12, where n_o is the number of nanoparticles per unit volume of the foam. n_omH/S is the ratio of the magnetic energy associated with the unit volume of the foam to that of the elastic energy per unit volume of the foam. The variation of $\delta_{on}/ \delta_{off}$ with n_omH/S is also shown on the same plot. The fraction of the energy absorbed

by the magnetic nanoparticles scales inversely with the foam modulus. Softer foams (with lower S) deflect more than the harder foams (with higher S) for the given impact energy. The energy absorbed by the nanoparticles scales with the deflection volume. Hence the increment in foam stiffness will be higher for the softer foam.
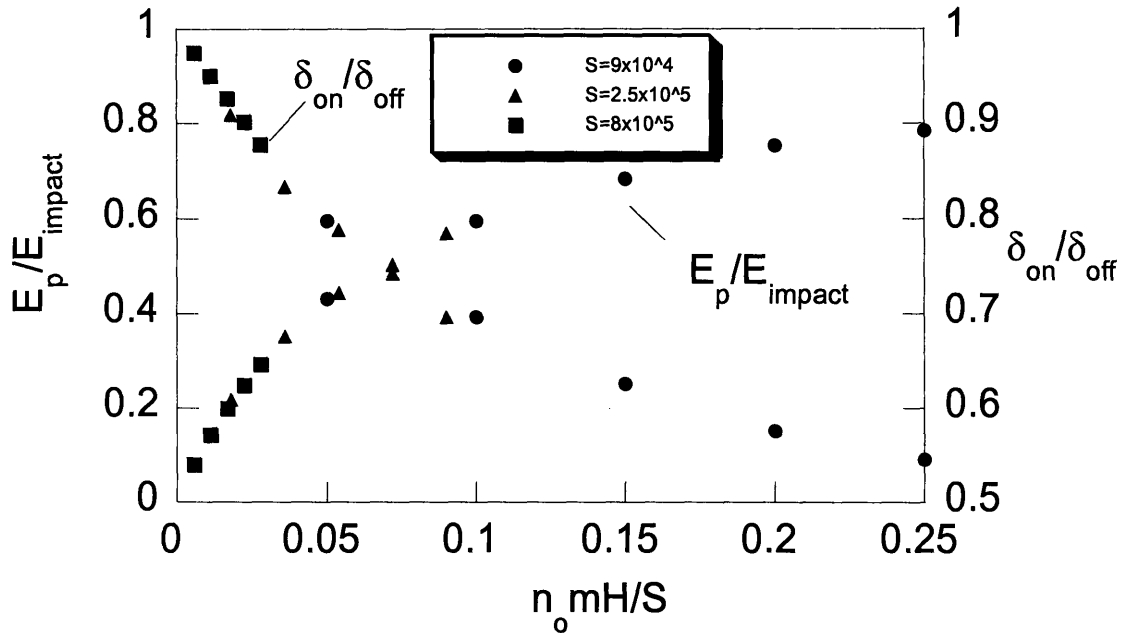
Figure 6-12. Graph of the energy absorbed by the magnetic nanoparticle as a function of impact energy for the foam with different modulus. The energy absorbed by the nanoparticle is highest at the lowest value of the foam modulus.

The ratio of δ_{on}/δ_{off}, where δ_{on} and δ_{off} is the deflection of the foam in the presence and in the absence of the field, was found to be constant for a given S. The energy absorbed by the nanoparticle is the difference between the energy absorbed by the foam when the field is on and when the field is off. Energy absorbed by the foam scales with $\delta^{5/2}$ (Equation 14). Therefore the energy absorbed by the nanoparticle should also scale with $\delta_{on}^{5/2}$ (Figure 6-13). In other words, $\delta^{5/2}$ captures the deflection profile in the foam which governs the energy absorbed by the nanoparticles.
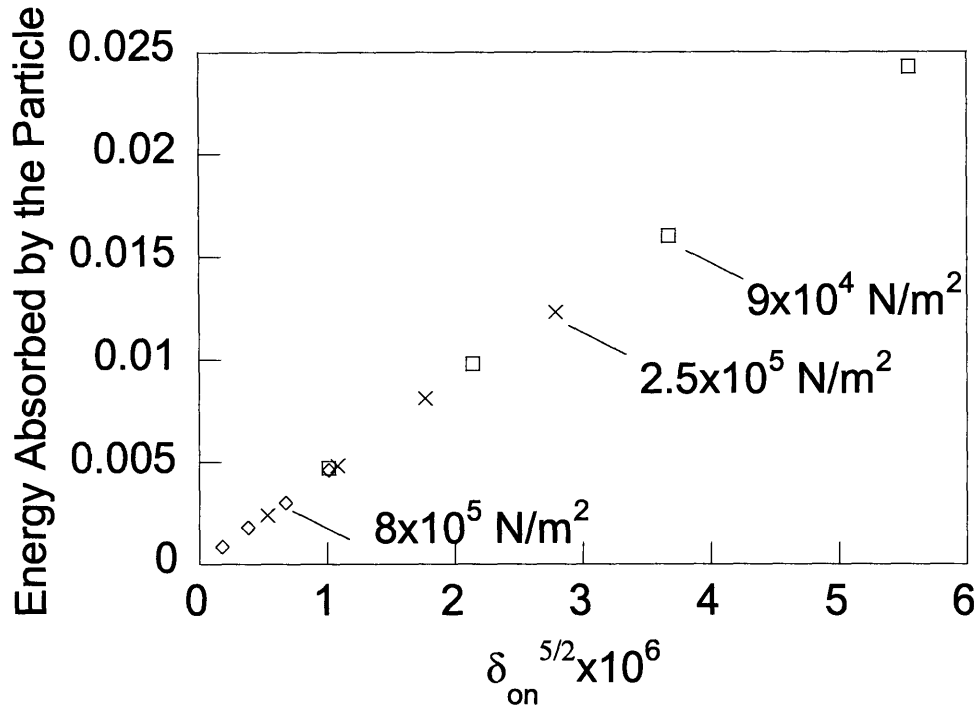
Figure 6-13. The energy absorbed by the magnetic nanoparticles for different modulus of the foam scales with $\delta_{on}^{5/2}$ as observed by the linear nature of the plot.

The deflection profile in the foam can also be changed by changing the shape of the indenter. The cone shape indenter imitates the sharp edge projectiles which are common in energy absorbing scenarios. The deflection profile imparted by the conical indenter is governed by the angle of the cone (Figure 6-14, Refer Appendix). Figure 12 compares the amount of energy absorbed by the foam for different conical indenters which have the same impact energy but different cone angles. The amount of energy absorbed the magnetic nanoparticle depends on the deflection profile and the volume of the foam affected by the indenter. At smaller cone angles, the deflection of the foam is higher but the volume of the foam deflected by the indenter is lower. Similarly at the higher cone angles the deflection of the foam is lower but the number of nanoparticles in the foam which are deflected against the magnetic field are higher (Figure 6-15). The energy absorbed by the foam is the maximum when the cone angle is 60°. The value of the energy absorbed by the nanoparticle when impacted with a 60° conical indenter is however lower than the equivalent spherical indenter by ~ 10%. The volume displace by

the spherical indenter is more than the conical indenter which leads to the lower energy associated with the deflection of the nanoparticle. The deflection profile of the foam at different cone angles and that of an equivalent sphere is shown in Figure 6-16.
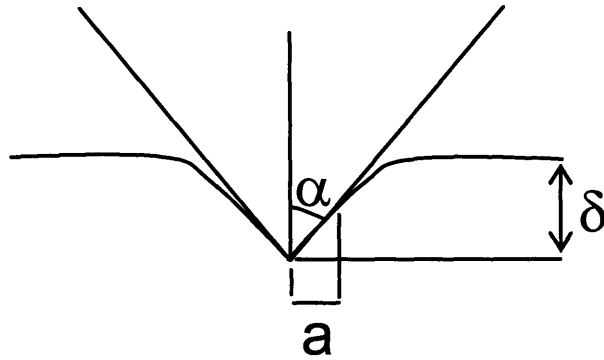
Figure 6-14. Schematic of indentation of the foam with a conical indentor.
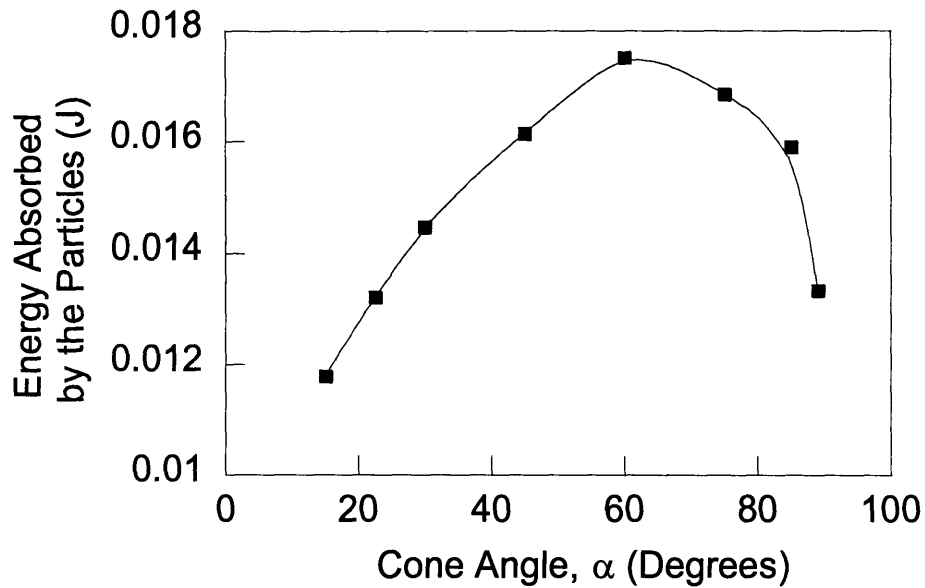
Figure 6-15. Graph of energy absorbed the magnetic nanoparticle as a function of cone angle.

185

(a)

$\alpha = 15°$

(b)

$\alpha = 30°$

(c)

$\alpha = 45°$
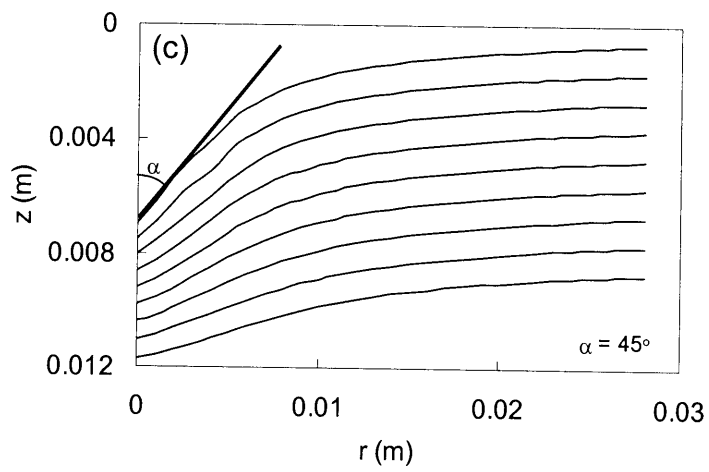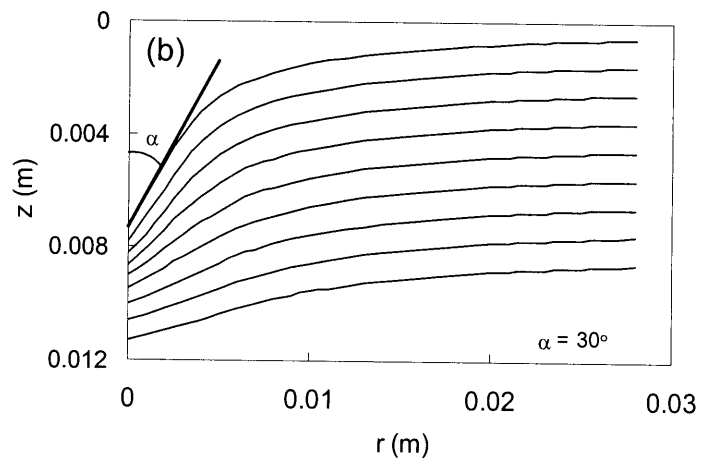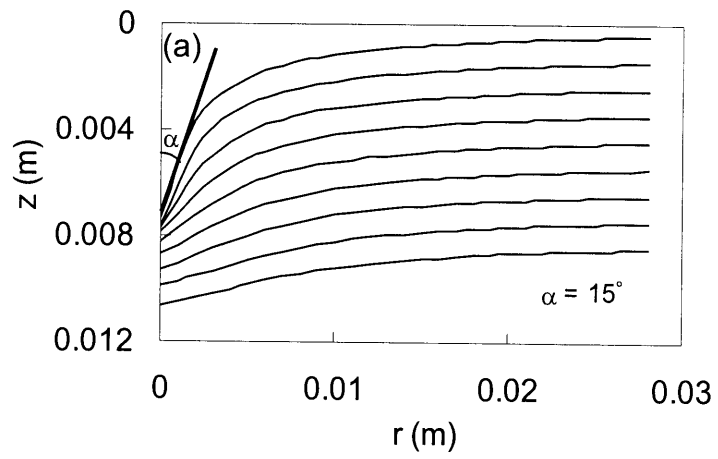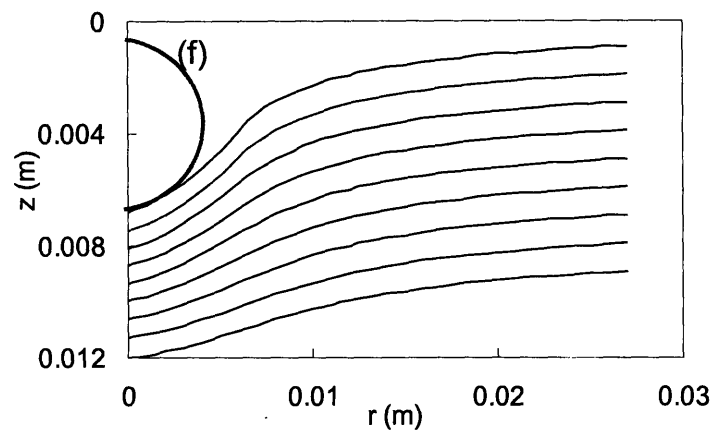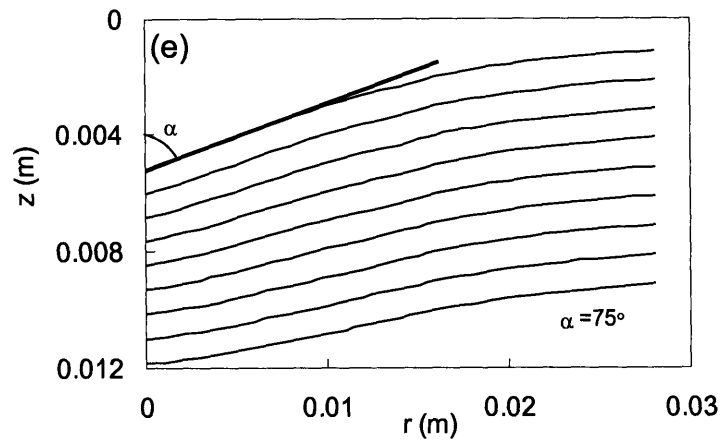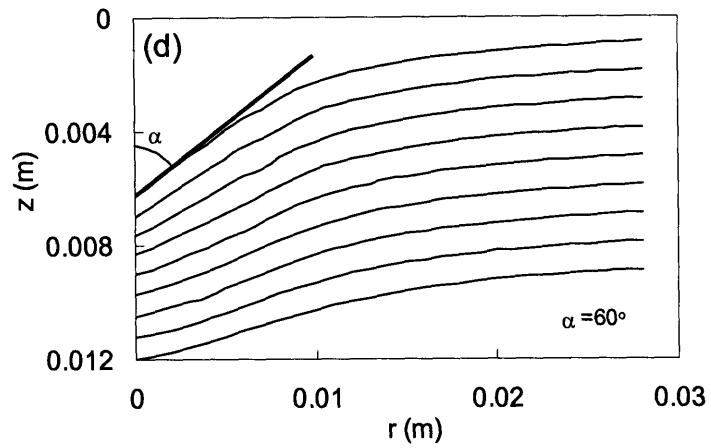
Figure 13. Comparison of the foam deflection (u_z) at different cone angles (a-e) and (f) with an equivalent spherical indenter.

6.4 Conclusions

Different size magnetite nanoparticles were produced using seed mediated growth. The size dependent magnetic properties of the nanoparticles were characterized in detail. SQUID studies confirmed the size based relaxation of these nanoaparticles. Field cooling experiments also indicated the size based dependence of the magnetization of the magnetic nanoparticle. Bilayer stabilization was utilized to transfer the nanoparticles from organic to aqueous phase but the nanoparticles could not be used in the LbL process due to the instability rendered to the nanoparticles. Ligand exchange method can be adopted to create more stable aqueous based nanoparticles. The drop ball test on foam impregnated with infinite Néel relaxation particles and the subsequent modeling suggested that indeed Néel relaxation behavior in nanoparticles can be exploited for energy absorption scenarios. This phenomenon can be used to create intelligent materials which would stiffen up only "on demand" (when the magnetic field is applied). The increase in stiffness scaled with the magnetization of the nanoparticles. Hence incorporating higher magnetizable nanoparticles can enhance the strength of the field responsive intelligent materials. The effect of a cone shape indenter on the amount of energy absorbed by the nanoparticle was also investigated. The strain profile generated by a 60° conical indenter resulted in the maximum energy absorption by the nanoparticles. This value was however lower that the energy absorbed by the nanoparticle when the foam was deflected with an equivalent spherical indenter. The spherical shape indenter deflects higher volume of the foam compared to the conical indenter leading to higher energy absorbed the nanoparticle.

Appendix

For the conical indenter the stress distribution on the surface, z = 0 is given by

$$\frac{\sigma_z}{p_m} = -\cosh^{-1}\frac{a}{r} \; ; \; r < a$$

$$\sigma_z = 0; \; r \geq a$$

$$\frac{\sigma_\theta}{p_m} = 2v\frac{\sigma_z}{p_m} - (1-2v)\frac{a}{r}J_0^1$$

$$\sigma_r = (1+2v)\sigma_z - \sigma_\theta$$

$$J_0^1 = \frac{a}{2r}\left[1-(1-r^2/a^2)^{1/2} + \frac{r^2}{a^2}\ln\frac{1+(1+r^2/a^2)^{1/2}}{r/a}\right]; \quad r < a$$

$$J_0^1 = \frac{a}{2r}; \quad r \geq a$$

Within the interior of the specimens the stresses are given by

$$\frac{\sigma_z}{p_m} = -\left[J_1^0 + \frac{z}{a}J_2^0\right]$$

$$\frac{\sigma_\theta}{p_m} = -\left[2vJ_1^0 + \frac{a}{r}\left((1-2v)J_0^1 - \frac{z}{a}J_1^1\right)\right]$$

$$\frac{\sigma_r}{p_m} = -\frac{2(1-v^2)}{(1-v)}J_1^0 - \frac{\sigma_z}{p_m} - \frac{\sigma_\theta}{p_m}$$

$$\frac{\tau_{rz}}{p_m} = -\frac{z}{a}J_2^1$$

$$J_2^0 = \left(\frac{r^2}{a^2} + \frac{z^2}{a^2}\right)^{-1/2} - \frac{\cos\varphi}{R}$$

$$J_1^1 = \frac{a}{r}\left[\left(\frac{r^2}{a^2} + \frac{z^2}{a^2}\right)^{1/2} - R\cos\varphi\right]$$

$$J_2^1 = \frac{a}{r}\left[\frac{(1+z^2/a^2)^{1/2}}{R}\cos(\theta-\varphi) - \frac{z}{a}\left(\frac{r^2}{a^2} + \frac{z^2}{a^2}\right)^{-1/2}\right]$$

$$J_1^0 = \frac{1}{2}\ln\left[\frac{R^2 + 2R(1+z^2/a^2)^{1/2}\cos(\theta-\varphi)+1+z^2/a^2}{(z/a+(r^2/a^2+z^2/a^2)^{1/2})^2}\right]$$

$$J_0^1 = \frac{1}{2}\left[\frac{r}{a}J_0^1 + \frac{a}{r}(1-R\sin\varphi) - \frac{z}{a}J_1^1\right]$$

$$R = \left[\left(\frac{r^2}{a^2}+\frac{z^2}{a^2}-1\right)^2 + 4\frac{z^2}{a^2}\right]^{1/4}$$

$$\tan\theta = \frac{a}{z}$$

$$\tan 2\varphi = 2\frac{z}{a}\left[\left(\frac{r^2}{a^2}+\frac{z^2}{a^2}-1\right)^{-1}\right]$$

Acknowledgements

6.5   References

1.   Debye, P., *Polar Molecules*. 1929, New York: The Chemical Catalog Co., Inc.

2.   Néel, L., Ann. Geophys., 1949. **5**(99).

3.   Sun, S.H., H. Zeng, D.B. Robinson, S. Raoux, P.M. Rice, S.X. Wang, and G.X. Li, *Monodisperse MFe2O4 (M = Fe, Co, Mn) nanoparticles.* Journal of the American Chemical Society, 2004. **126**(1): p. 273-279.

4.   Pellegrino, T., L. Manna, S. Kudera, T. Liedl, D. Koktysh, A.L. Rogach, S. Keller, J. Radler, G. Natile, and W.J. Parak, *Hydrophobic nanocrystals coated with an amphiphilic polymer shell: A general route to water soluble nanocrystals.* Nano Letters, 2004. **4**(4): p. 703-707.

5.   Rosenweig, R.E., *Ferrohydrodynamics*. 1985, New York: Cambridge University Press.

6.   Wang, A., H. Singh, T.A. Hatton, and G.C. Rutledge, *Field-responsive superparamagnetic composite nanofibers by electrospinning*. Polymer, 2004. **45**(16): p. 5505-5514.

7.   Morales, M.P., S. Veintemillas-Verdaguer, M.I. Montero, C.J. Serna, A. Roig, L. Casas, B. Martinez, and F. Sandiumenge, *Surface and internal spin canting in gamma-Fe2O3 nanoparticles*. Chemistry of Materials, 1999. **11**(11): p. 3058-3064.

8.   Shen, L.F., P.E. Laibinis, and T.A. Hatton, *Aqueous magnetic fluids stabilized by surfactant bilayers*. Journal of Magnetism and Magnetic Materials, 1999. **194**(1-3): p. 37-44.

9.   Lattuada, M., Hatton, T.A., *Functionalization of Monodisperse Magnetic Nanoparticles*. Manuscript in preparation.

10.   Cripps-Fischer, A., *Introduction to Contact Mechanics*. 2000: Springer.

11.   Timoshenko, S.P. and J.N. Goodier, *Theory of Elasticity*. 1951: McGraw-Hill.

12.   Hertz, H., *On the contact of Elastic Solids*. Tranlated and reprinted in English in Hertz's Miscellaneous Papers. 1881, London: Macmillan & Co.

Chapter 7

Field-responsive Superparamagnetic Composite Nanofibers by Electrospinning

7.1 Introduction

Energy absorbing materials which can dissipate impact energy have numerous applications in ballistics, sporting goods, protective equipment and vehicles [1]. The energy can be absorbed via elasticity, friction, viscoplasticity or plasticity mechanisms [2]. The recent trend is to make these structures more adaptive, where they can absorb energy in a large operating dynamic range, i.e. resilient under relatively low impact conditions and more rigid under high impact conditions [3-5]. In Chapter 6 we illustrated that incorporating high Néel relaxation nanoparticles in a matrix can enhance its strength. In this Chapter we will describe in detail a practical and scalable method to incorporate nanoparticles in polymeric fibers. Magnetic composite fibers, in which magnetic nanoparticles are embedded into a polymeric fiber matrix, are expected to exhibit interesting magnetic field-dependent mechanical behavior with potential applications in a range of areas. Such materials could, for instance, be used as 'intelligent' fibers and fabrics for protective clothing for military and first-response personnel, and in health care. Other potential applications include magnetic filters [6], sensors [7] and future generations of electronic, magnetic and/or photonic devices used for information storage, magnetic imaging, static and low frequency magnetic shielding and magnetic induction [8, 9]. Below approximately 100 nm in diameter, particles of ferromagnetic materials such as iron oxide no longer exhibit the cooperative phenomenon of ferromagnetism found in the bulk, due to thermal fluctuations sufficient to reorient the magnetization direction of entire particles. Instead, such nanoparticles are superparamagnetic, exhibiting strong paramagnetic properties with large susceptibility. In a uniform external magnetic field, such superparamagnetic nanoparticles within the fibers would be expected to align with their magnetic moments in the direction of the magnetic field such that when the fiber is deformed, extra energy is needed to disrupt this alignment of the

192

nanoparticles within the fiber if the time scale of the deformation is smaller than the relaxation time, resulting in its increased stiffness. In a nonuniform magnetic field, the magnetic nanofibers should also deform or bend in the direction of the gradient of the magnetic field. These changes in stiffness and shape should be completely reversible, since the particle magnetic moment and fiber orientations should relax to their original distributions on removal of stress and magnetic field. The relative magnitudes of the stiffness enhancement and fiber deformation are expected to increase as the diameter of the embedding polymer fiber is reduced, and, therefore, the question as to whether magnetic composite nanofibers (i.e. with diameters on the order of 100 nm or less) can be produced effectively is of considerable interest. We report here on the production and characterization of such superparamagnetic composite polymer/magnetite nanofibers, which we obtain using an electrospinning technique. Li et al. previously reported the production of magnetic ceramic nanofibers of nickel ferrite manufactured by calcination of electrospun PVP/metal alkoxide precursors; magnetic hysteresis was observed, but no mechanical properties were reported [10].

Electrospinning is an effective method for the production of polymeric nanofibers with diameters ranging from a few to several hundred nanometers. This technique has attracted interest over the last decade due to potential applications for nanofibers in such areas as reinforcing components in nanocomposites [11, 12], molecular electronics [13-15], membrane-based separation [16, 17], tissue engineering [18, 19], sensing and protective clothing [20]. In a typical electrospinning process, a polymer solution or melt is extruded through a capillary and forms a small droplet at the tip of the capillary. In the presence of an electric field, this droplet deforms into a conical shape. When the electrical field is strong enough, the charge density built up at the surface of the droplet overcomes surface tension, resulting in ejection of a charged jet from the apex of the cone. The jet is accelerated toward a grounded collecting device, traveling first as a steady jet for a certain distance, and then undergoing an electrostatically driven whipping instability [21-24] that bends and stretches the jet. The result of the whipping instability is a dramatic reduction in the diameter of the jet, typically by about 2 orders of magnitude, which allows for rapid solidification of the jet through solvent evaporation (for solution) or cooling (for melts). The solid fibers are deposited on an electrically

grounded collecting device in the form of threads [25] or as a nonwoven fabric. The feasibility of incorporation of nanoparticles into nanofibers has made this process very attractive for the production of composite nanofibers, simply by electrospinning the nanoparticle-filled polymer solution [26-29], although a major consideration in the processing of such composite nanofibers is the dispersion stability of the nanoparticles in the polymer solution.

In this Chapter, as proof of concept, we describe the formation of superparamagnetic nanofibers containing stably-dispersed superparamagnetic nanoparticles via electrospinning. The superparamagnetic nanoparticles are synthesized by an aqueous co-precipitation technique in the presence of a polymer that attaches to the particle surfaces and confers steric stabilization to the nanoparticle dispersion in the polymer solution. We incorporated these particles in the polymer solutions used in the electrospinning process to form polymeric nanofibers that we characterize in terms of both their magnetic and mechanical properties. However, the magnetite nanopaticles used had a polydisperse size distribution with an average size of 8 nm [30]. Néel relaxation of these particles is 10^{-8} s [31] and no increment in the strength of the fiber will be observed in the presence of an external magnetic field. We were unable to electrospin 25 nm iron nanoparticles (Chapter 6) due to dispersion problems. We were however able to synthesize high Néel relaxation magnetite nanoparticles which were electrospinnable. The magnetite nanoparticles were produced using organic route synthesis as explained in Chapter 6. A theoretical model for the estimation of the increment in stiffness of a nanofiber impregnated with high Néel relaxation magnetic nanoparticle is also discussed in this chapter.

7.2 Experiments

7.2.1 Materials

Poly(ethylene oxide) (PEO, M_v 2,000,000), poly(vinyl alcohol) (PVA, 87–89% hydrolyzed, M_w: 85–146k)and dodecyl sulfate, sodium salt (98%) (SDS) were obtained from Aldrich and used for making electrospinnable solutions. Poly(acrylic acid) (PAA; 50 wt% in water, M_w=5000), iron(III) chloride hexahydrate (97%), iron(II) chloride

194

tetrahydrate (99%), ammonium hydroxide (28 wt% in water), dimethyl formamide (DMF), iron (III) acetylacetonate (97%), benzyl ether (99%), 1-2 hexadecanediol (97%), ethanol, oleic acid (90%), oleylamine (70%), poly(methyl methyacrylate) (PMMA, M_w = 495,000), polyurethane (PU, M_w=145,000), tetrahydrofuran (THF), dimethyl formamide (DMF) , hexane and dicyclohexylcarbodiimide (CDI) were obtained from Aldrich (Milwaukee, WI) and used for synthesizing nanoparticles. Jeffamine XTJ-234 (PEO/PPO-NH$_2$, EO:PO=6.1:1, M_w=3000) is an amine-terminated random copolymer of ethylene oxide (EO) and propylene oxide (PO) repeat units with 6.1 EO units per PO unit. It was donated by Huntsman Corp. (Houston, TX) and has characteristics similar to that of pure PEO. All chemicals were used as received.

7.2.2 Preparation of aqueous magnetite nanoparticles

The graft copolymer was prepared by reacting the Jeffamine with the carboxyls on PAA via amidation chemistry as described elsewhere [32]. Only a small percentage (16%) of carboxyl groups were grafted with Jeffamine since free carboxyl groups are required for chelation with surface iron atoms and stabilization of the magnetite nanoparticles. In a typical procedure for the synthesis of the magnetite nanoparticles [32], an aqueous solution containing 2.35 g of iron(III) chloride hexahydrate, 0.86 g of iron(II) chloride tetrahydrate, and 1 g of graft copolymer was prepared by dissolving the reagents in 40 mL of deoxygenated water. Deoxygenation was achieved by bubbling with nitrogen under vigorous stirring for 30 min before reaction. The aqueous solution was heated to 80 °C, and 5 ml of 28 wt% of ammonium hydroxide was added to precipitate iron oxide in the form of magnetite. The growth of spherical nanoparticles was arrested by the polymer in the solution, which caps the magnetite nanoparticles as soon as they form and stabilizes them sterically against aggregation. The resulting mixture was then aged for 30 min at 80 °C. This procedure produces 1 g of magnetite in 40 mL of water, which is equivalent to a 2.5 wt% suspension of magnetite. The final magnetic fluid was washed in a centrifuge with an ultrafilter (Millipore, Centricon Plus 80, MWCO 100,000) to remove excess polymer and salts.

7.2.3 Preparation of monodisperse magnetic Nanoparticles

To synthesize 16 nm magnetite nanoparticles scheme of Sun et al. [33] was adopted as discussed in Chapter 6 (Section 6.2.2). In brief an organometallic precursor is decomposed in the presence of mixture of surfactants at high temperature resulting in monodisperse magnetite nanoparticles. 2 mmol of Iron (III) acetylacetonate, 10 mmol of 1,2 hexadecanediol, 6mmol of oleic acid , 6 mmol of oleylamine and 20 ml of benzyl ether were refluxed at 300 °C for 1 hr. The resulting black mixture was cooled down to room temperature, purified and resuspended in hexane and was used for seed mediated growth.

For synthesis of bigger nanoparticles, 2 mmol of Iron(III) acetylacetonate, 10 mmol of 1,2 hexadecanediol, 2mmol of oleic acid , 2 mmol of oleylamine , 20 ml of benzyl ether and 80 mg of seeds in 4 ml of hexane were mixed in a 3 neck flask and stirred continuously under a blanket of nitrogen. The mixture was kept at 100 °C for 30 mins and at 200 °C for 1h. Finally the mixture was refluxed at 300 °C for 30 mins. The magnetite was recovered using the procedure outlined above. The resulting magnetite nanoparticles can then be used as seeds for subsequent synthesis. In this manner stable nanoparticles up to 16 nm were synthesized in 3 cycles.

7.2.4 Preparation of spinning solutions

PEO solutions ranging from 1 to 3% by weight were prepared by directly adding the PEO polymer to deionized water. The solutions were stirred vigorously for at least 24 h at room temperature in order to obtain homogeneous solutions. PVA solutions ranging from 6.5 to 15% by weight were prepared by directly adding the polymer into distilled water, with vigorous stirring for at least 3–4 h at 70 °C.

Various concentrations of PEO/aqueous magnetite nanoparticle dispersions were prepared by adding the desired amount of PEO solution directly to the nanoparticle aqueous solution prepared as described above, with vigorous stirring for at least 24 h at room temperature. A range of PVA/magnetite nanoparticle suspensions was prepared similarly, and each was mixed using a vortex mixer (VWR Scientific Products) for at

least 10 min before spinning, as the particle suspension was not particularly stable against aggregation and settling.

Monodisperse nanoparticles synthesized using organic route were electrospun in PMMA and PU nanofibers. A 7.5 wt % PMMA solution containing 2.78wt % Fe_3O_4 in a mixture of THF and DMF (3:1) was prepared for electrospinning; A 10 wt% polyurethane solution containing 2.78% of Fe_3O_4 in a mixture of THF and DMF (3:1) was prepared for electrospinning.

7.2.5 Electrospinning experiments

The parallel-plate electrospinning apparatus used was similar to that described by Shin et al. [23] and Fridrikh et al. [34]. Briefly, two aluminum disks with diameters of 10 cm were arranged parallel at a distance of up to 30 cm apart. The fluid was pumped at a constant flow rate by a syringe pump (Harvard Apparatus PHD 2000) to a stainless steel capillary with inner diameter 1 mm located in the center of the upper disk. An electrical potential was applied to the upper disk by a high voltage power supply (Gamma High Voltage Research ES-30P). Current was measured by a Digital multimeter (Fluke85 III) as the voltage drop across a 1.0 MΩ resistor between the lower disk and ground. The electrical voltage, solution flow rate and distance between the two parallel plates were adjusted to obtain a stable jet.

7.3 Measurement and characterization

Viscosity was measured on an AR2000 Rheometer (TA Instruments) at 25 °C. A Kruss 10 tensiometer was used to determine surface tension, while conductivity was measured using a Cole Parmer 19820 conductivity meter.

7.3.1 Dynamic light scattering

Dynamic light scattering (DLS) was performed to determine the hydrodynamic diameters of the coated nanoparticles using a Brookhaven BI 200-SM system at a fixed angle of 90°. The autocorrelation function was fitted with an exponential curve to obtain

the diffusion coefficient, which was then used to calculate the hydrodynamic diameter via the Stokes–Einstein equation.

7.3.2 Scanning electron microscopy

Specimens for scanning electron microscopy (SEM) were prepared by direct deposition of the electrospun nanofibers on an aluminum foil and sputter-coating with gold using a Desk II cold sputter/etch unit (Denton Vacuum LLC, NJ). The images of the electrospun fiber were obtained using a JEOL-6060SEM (JEOL Ltd, Japan), and the fiber diameters were determined using AnalySIS image processing software (Soft Imaging System Corp., Lakewood, USA) by measuring 20 randomly selected fibers for each sample.

7.3.3 Transmission electron microscopy

For transmission electron microscopy (TEM), a dilute magnetite nanoparticle solution was dried on a carbon grid and visualized under the JEOL JEM200 CX TEM microscope (JEOL Ltd, Japan) to estimate the core sizes of the particles. The electrospun nanofibers were directly deposited onto a copper grid for TEM analysis.

7.3.4 Superconducting quantum interference device

The superconducting quantum interference device (SQUID) test was conducted using an MPMS XL magnetometer (Quantum Design Inc., San Diego) to measure the relaxation behavior and the magnetization curve for the magnetic Nanofibers.

7.3.5 Nanoindentation

Nanoindentation experiments were performed using a Nanoscope IV, Dimension™ 3100 AFM (Digital Instrument, Santa Barbara) with a RTESP single-beam silicon probe (Digital Instrument) (f_R=280–361 kHz, k=30–40 N/m). All the nanofibers were conditioned in a vacuum oven for at least 2 days before experiments, at room temperature for PEO and PEO/magnetite nanofibers and at 60 °C for PVA and PVA/magnetite nanofibers, respectively. During these AFM indentation tests, PVA and PVA/magnetite nanofibers were treated as a group, as were the PEO and PEO/magnetite

nanofibers. Within each group, the maximum indentation force, P_{max}, was the same. P_{max} for the PVA group was twice that for the PEO group. Within each group, mica and a flat reference sample of epoxy were indented using the same probe and parameters. The mica has an elastic modulus of ~171 GPa and Poisson ratio of ~0.3 [35-37]. The elastic modulus of the reference epoxy sample was determined independently using a Triboindenter with a Berkovich-type indentation tip (Hysitron Inc., Minneapolis). For each sample, at least 20 individual force curves were obtained.

7.3.6 Field responsiveness testing

A rectangular strip (length×width×thickness=1.8×0.555×0.004 cm) of electrospun nonwoven mat was placed on the surface of a table, with one end fixed by tape onto the table surface. A permanent laboratory magnet with a rectangular cross-section (1.8×0.6 cm) was suspended some distance away above the mat, and the response behavior of the nonwoven mat to the laboratory magnet was recorded by a digital camera.

7.4   Results and discussions

7.4.1   Characterization of magnetite nanoparticles

7.4.1.1 Aqueous Magnetite Nanoparticles

The size distribution of the aqueous route synthesized magnetite nanoparticles, as determined by DLS and shown in Figure 7-1, corresponds to a number average hydrodynamic diameter for the nanoparticles of 25 nm. An analysis of TEM images of the as-synthesized magnetite nanoparticles (Figure 7-2) indicates an average core diameter, assuming a log normal distribution, of 7.5±2.9 nm. Only the magnetite cores are visible in such TEM measurements because the very low contrast polymer coatings cannot be discerned in these images. The difference between the average hydrodynamic diameter and core size yields a thickness of about 9 nm for the polymer shell.
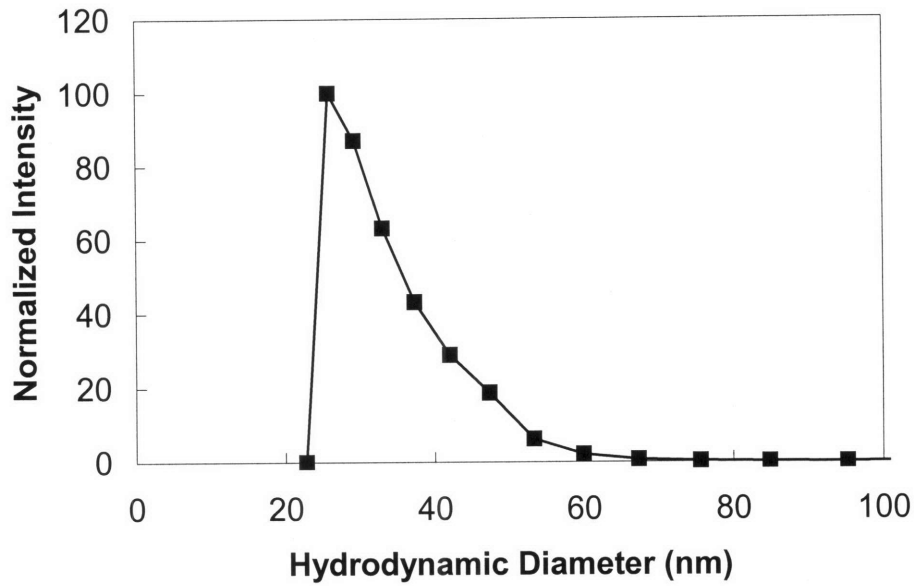
Figure 7-1. DLS curve for the 2.5 wt% magnetite nanoparticle solution.
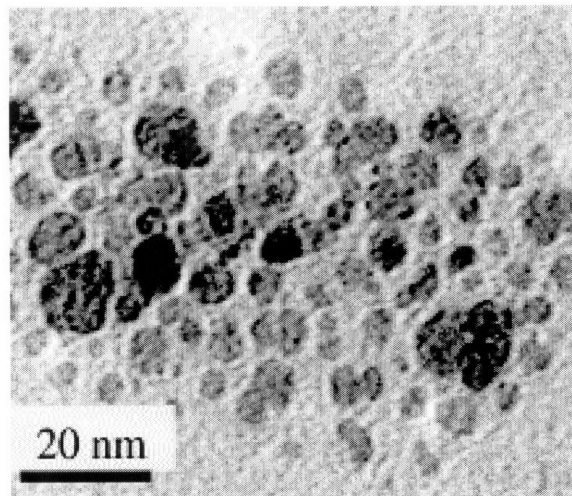
Figure 7-2. TEM image of the aqueous magnetic fluid.

The dependence of the magnetization, M, of the magnetite fluid on the applied magnetic field in the SQUID tests is shown in Figure 3. The magnetite nanoparticle suspension exhibits superparamagnetic behavior in that there is zero remnant magnetization at zero applied field. The saturation magnetization is approximately 0.5–0.7 T.
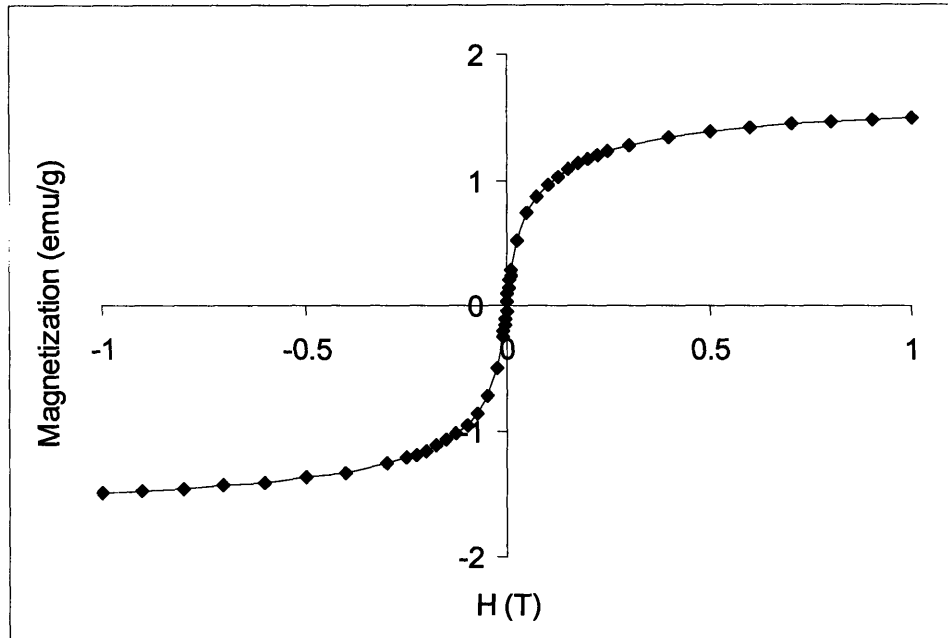
Figure 7-3. Magnetization (M) versus magnetic field (H) for the 2.5 wt% as-synthesized magnetite fluid at 25 °C.

7.4.1.2 Organic Magnetite Nanoparticles

The monodisperse nanoparticles are characterized in detail in Chapter 6. Monodisperse magnetite nanoparticles upto 16 nm in diameter were synthesized using this technique.

7.4.2 Electrospinning

7.4.2.1 PEO-magnetite nanofiber

The magnetite nanoparticles were readily dispersed as stable suspensions in PEO solutions, increasing their conductivity dramatically, as shown in Table 1. The preferred electrospinning parameters, also given in Table 7-1, are almost the same for PEO and PEO/magnetite solutions. Some representative SEM pictures of electrospun nanofibers of PEO and PEO/magnetite are shown in Figure 7-4. At low PEO concentration (1 wt%) in the absence of magnetite nanoparticles, the fibers adopted the bead-on-string morphology [38] (Figure 7-4(a)) while fibers with uniform diameters were obtained when 3.52 wt% magnetite nanoparticles were added to the spin solution (Figure 7-4(b)).

At higher concentrations (2–3 wt%) of PEO, uniform fiber morphologies were obtained for both PEO and PEO/magnetite solutions with little change in fiber diameters on the addition of magnetite nanoparticles, as shown in Figure 7-4(c) and (d).

Table 7-1. Solution properties and electrospinning processing parameters of some representative nanofibers.

		Conductivity (μS)	Viscosity (Pa·S)	Voltage (KV)	Flow Rate (ml/min)	Distance (cm)	Current (nA)	Fiber Diameter (nm)
PEO (2 wt%)		107.9	1.565	0.01	9.0	25	83	390±40
	Fe_3O_4 (0.75%)	1277	1.506	0.02	9.0	25	353	400±80
PVA (7.5%)		351	0.2905	0.01	29	25	412	170±40
	Fe_3O_4 (0.75%)	1372	0.3926	0.01	29	25	1534	320±40
	Fe_3O_4(0.75%)+SDS(1%)	2740	1.941	0.016	28.5	25	1050	140±30
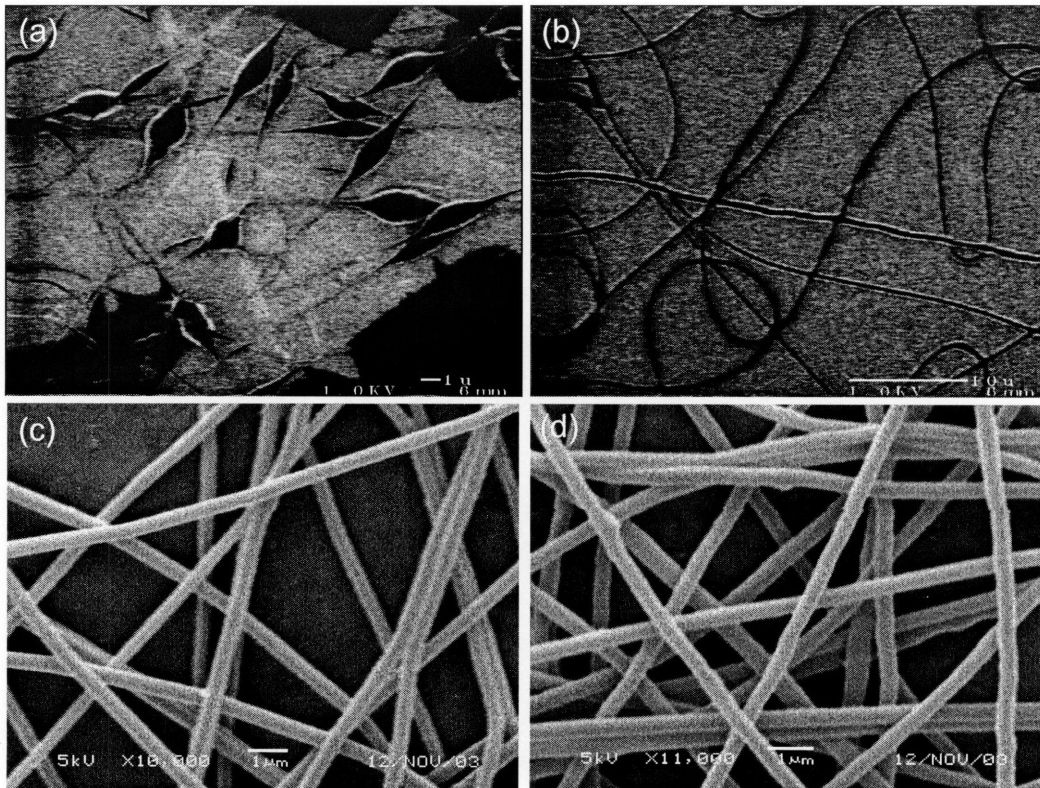
Figure 7-4. Some representative SEM images of PEO and PEO/magnetite nanofibers: (a) PEO (1%), (b) PEO (1%) +Fe_3O_4 (3.52%), (c) PEO (2%), (d) PEO (2%)+Fe_3O_4 (0.75%).

7.4.2.2 PVA-magnetite nanofiber

The magnetite nanoparticles were easily dispersed in PVA solutions, but these solutions were not as stable as in the PEO case, and the magnetite nanoparticles settled overnight. The reason for this settling of the suspension on standing is that the PEO-based shells around the nanoparticles are not as compatible with the PVA in solution as they are with PEO solutions. The PVA suspensions were easily homogenized, however, using a Vortex mixer for 10 min immediately before electrospinning. The presence of the magnetite nanoparticles in the PVA solutions increased the conductivity of these solutions (Table 7-1). Again, there was little change in the preferred electrospinning processing parameters for PVA solutions when magnetite nanoparticles were added (Table 7-1). SEM pictures of electrospun nanofibers using PVA and PVA/magnetite solutions (Figure 7-5) show that the magnetite nanoparticles lead to increased fiber diameters, but that addition of SDS to the solution counteracted this effect, as SDS generally reduces the fiber diameters (Table 7-1). The results of a detailed study of the effect of SDS on the PVA fiber morphology are shown in Table 7-2. The SDS increased both the conductivity and the viscosity of the solutions significantly, but had surprisingly little effect on the surface tension. The diameters of the nanofibers were decreased by adding 1 wt% SDS to various concentrations of PVA. At the lowest PVA concentration (6.5 wt%), the fiber morphology changed from bead-on-string (with no SDS) to uniform fibers on the addition of 1 wt% SDS.
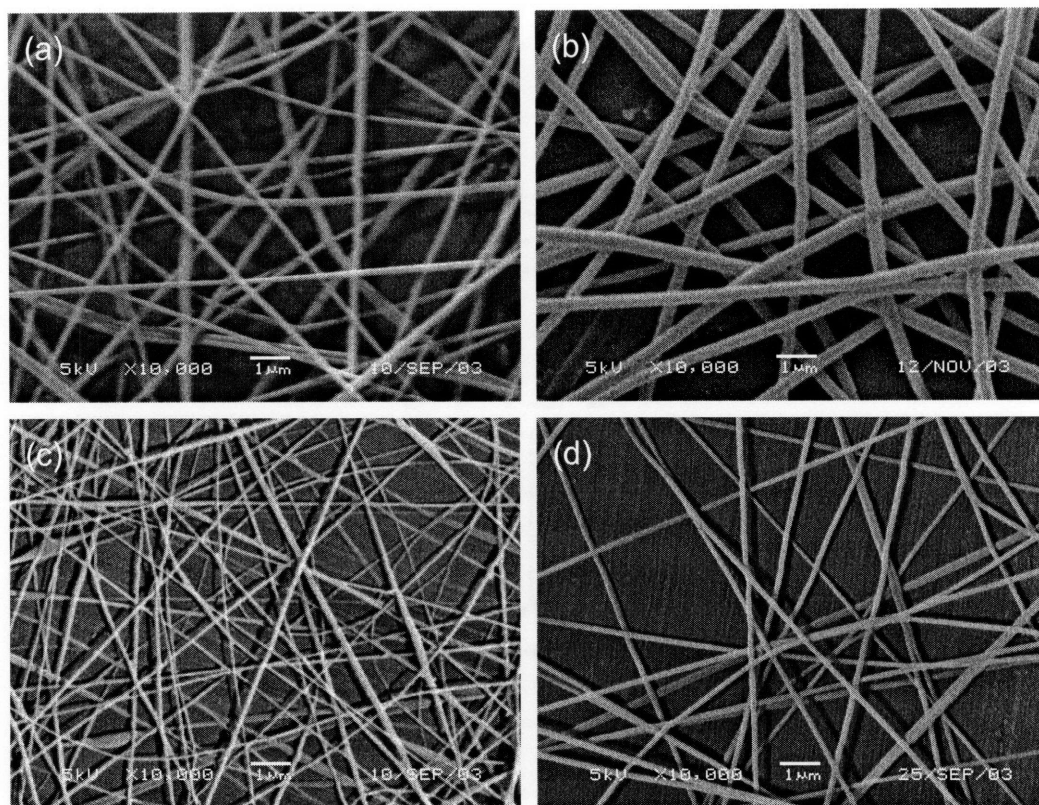
Figure 7-5. Some representative SEM images of PVA and PVA/magnetite nanofibers: (a) PVA (7.5%), (b) PVA (7.5%) + Fe_3O_4 (0.75%), (c) PVA (7.5%) +SDS (1%), (d) PVA (7.5%) +SDS (1%) +Fe_3O_4 (0.75%).

Table 7-2. Effect of SDS on the PVA solution properties and PVA fiber morphologies.

PVA (wt%)	Conductivity (μS)		Viscosity (Pa·S)		Surface Tension (mN/m)		Fiber Diameter (nm)	
	No SDS	SDS (1 wt%)	No SDS	SDS (1 wt%)	No SDS	SDS (1 wt%)	No SDS	SDS (wt1%)
6.5%	329	1223	0.1187	0.6456	41.58	42.04	Beaded	96.04±17.13
8%	315	1187	0.2905	1.375	39.5	42.42	146.67±10.90	73.72±14.51
10%	449	1156	0.8931	2.954	39.23	39.5	201.01±27.85	158.19±22.43
12%	496	1194	2.019	6.822	37.24	34.1	356.96±15.96	193.98±48.14
15%	515	1230	8.372	20.64	34.61	29.71	478.9±18.37	297.03±14.74

7.4.2.3 PMMA-Magnetite and PU-Magnetite Nanofibers

During the electrospinning process of the dispersion of 16 nm magnetite nanoparticles with PMMA in THF, the jet dried too fast at the capillary tip and continuous electrospinning was not possible. Adding 33 percent by volume of DMF to THF (a 3:1 THF:DMF solvent mixture) prior to dispersion, the jet became stable, and uniform fibers were obtained. A representative SEM picture of the electrospun PMMA fiber and PU fiber containing 16nm magnetite nanoparticles is shown in Figure 8-4. The preferred processing parameters are listed in Table 1. The inability to disperse high magnetization 25 nm iron nanoparticle (Chapter 6) in polymeric solution made their electrospinning impossible.

Table 7-3. Electrospinning parameters for PMMA and PU nanofibers

	Voltage (KV)	Flow rate (ml/min)	Distance (cm)	Current (nA)	Diameter
PMMA+Fe_3O_4	17.5	0.05	25	72.5	1.53±0.34
PU+ Fe_3O_4	17.2	0.02	35	32.5	1.45±0.76
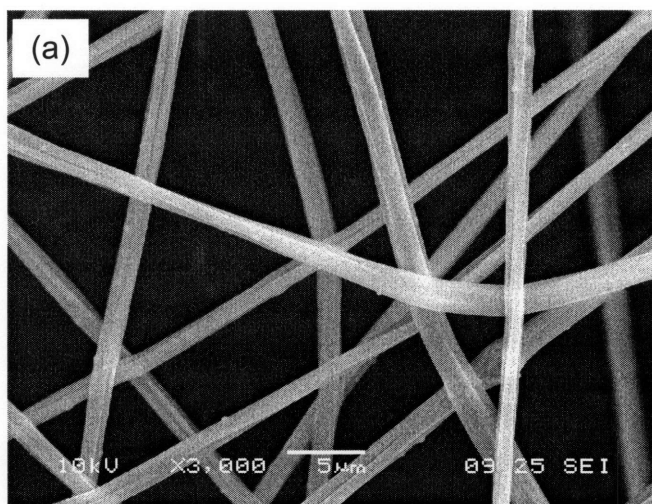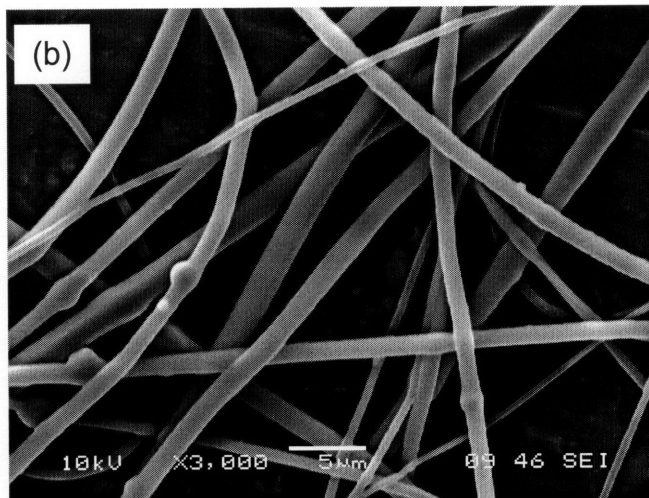
Figure 7-6. A representative SEM image of (a) PMMA and (b) polyurethane fibercontaining 37 wt% of 16 nm magnetite nanoparticles.

7.4.3 Characterization of the fibers

7.4.3.1 TEM analysis

Figure 7-6 shows TEM pictures of both PEO/magnetite and PVA/magnetite nanofibers. The weight percentages of magnetite nanoparticles within the fibers are 28%, and 8% for PEO/magnetite and PVA/magnetite nanofibers, respectively. The relatively large size of the PEO fiber and high content of nanoparticles within the fiber make it difficult to focus the TEM pictures, but the contour of the alignment of the nanoparticles into columns along the fiber axis direction is readily visible. For the PVA/magnetite fiber, it is clearer that the magnetite nanoparticles are aligned in columns parallel to the fiber axis direction within the fiber.

It was well known that magnetite nanoparticles can sometimes form chains in solution because of the magnetic coupling effects between the particles. The number of nanoparticles, n_0, in a chain in the fluid, at zero external field, can be estimated using the following formula [31]

$$n_o = \left[1 - \frac{2}{3}\left(\frac{\varphi}{\lambda^3}\right)e^{2\lambda}\right]^{-1} \tag{1}$$

Figure 7-7. TEM images of superparamagnetic Nanofibers: (a) PEO nanofiber with 28wt% magnetite nanoparticles. (b) PVA nanofiber with 8wt % magnetite nanoparticles.

where, ϕ is the volume fraction of particles in the fluid, and λ is the coupling coefficient, which measures the strength of the particle-particle interactions. λ is given by

$$\lambda = \frac{\mu_o M^2 V}{14kT} \qquad (2)$$

where, μ_0 is the permeability of free space, M is intensity of magnetization of the magnetic particles, V is the volume of the magnetic particles, k is Boltzmann's constant, and T is the absolute temperature in degrees Kelvin.

For magnetite particles 7.5 nm in diameter, λ<1 according to Equation (2), which means the particle-particle interaction energy is less than the thermal energy and no chains form in solution prior to electrospinning for any concentration of magnetite particles. We can infer, therefore, that the column alignment of magnetite nanoparticles within the fiber observed in Figure 6(b) is a result of the electrospinning process itself. Possible causes for this alignment may be hydrodynamics in the capillary, steady jet, or whipping jet regions, or induction by the local electric field.

7.4.3.2 Superconducting quantum interference device

SQUID magnetization curves for both 28% PEO/magnetite and 8% PVA/magnetite nanofibers show superparamagnetic behavior at room temperature as is evident in Figure 7-7. At low temperature (5 K), both systems are characterized by a narrow hysteresis and a small remnant magnetization at zero field. These can be explained by considering the magnetic relaxation of the nanoparticles. For 7.5 nm diameter particles, Neel relaxation dominates the Brownian rotation mechanism. The Neel relaxation time varies exponentially with inverse temperature [31, 39]. For example, at 300 K the Neel relaxation time for magnetite particles 8 nm in diameter in kerosene carrier is approximately 10^{-9} s [31], and increases to approximately 13 s at 5 K [39, 40]. At low temperature, when the applied field reached zero, the dipole moments of some nanoparticles were still polarized, and therefore, a small remnant magnetization was observed. The superparamagnetic behavior of the nanofibers at room temperature is especially useful for applications in which alternating nonuniform fields are needed, as this would reduce the dissipative energy in the device significantly.
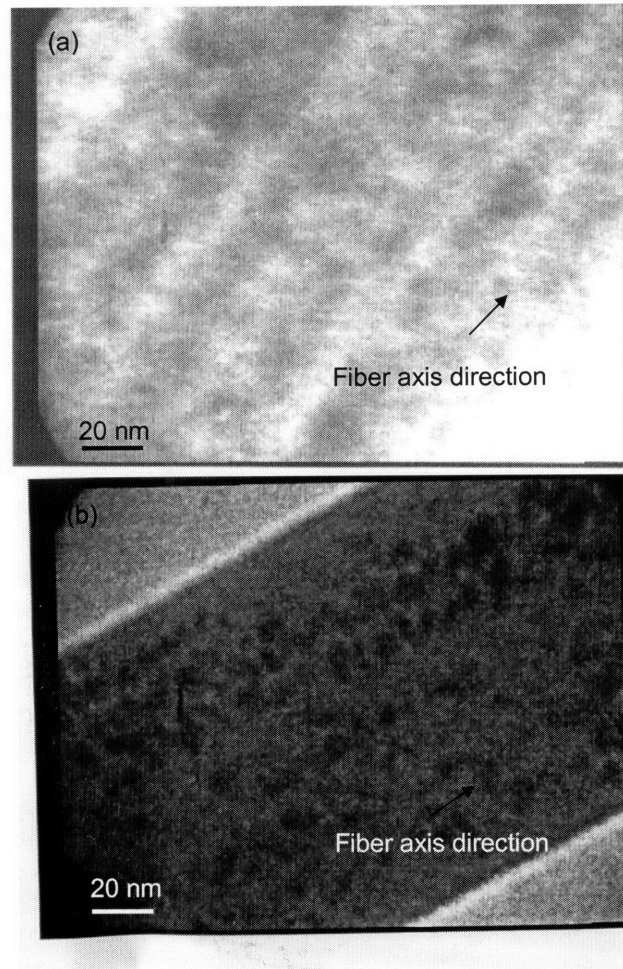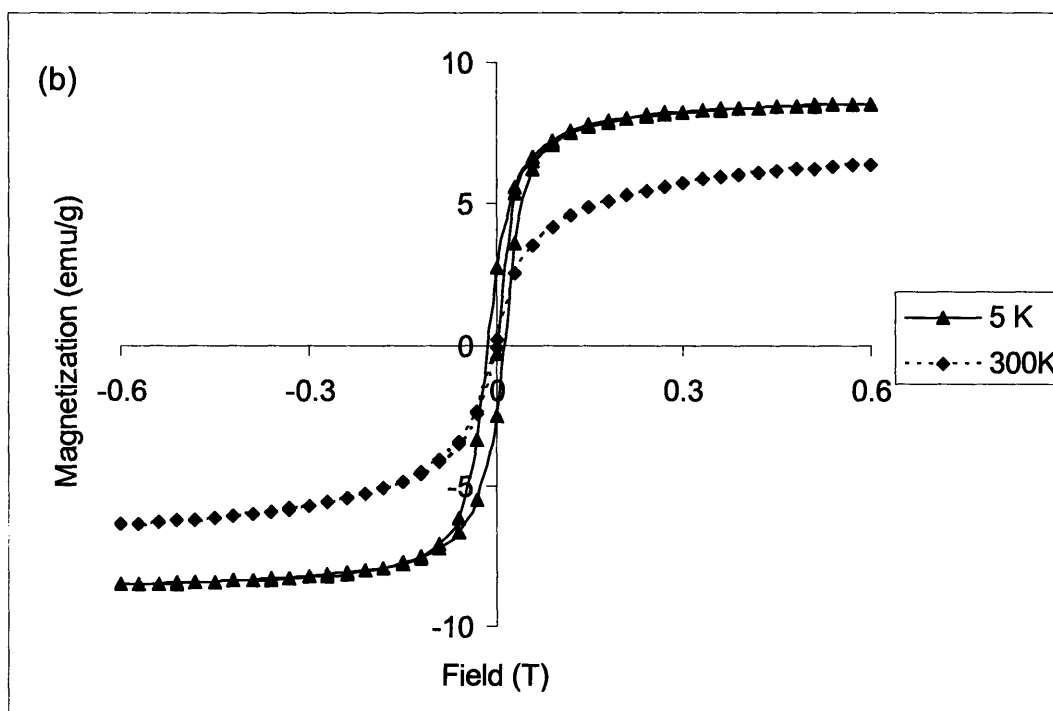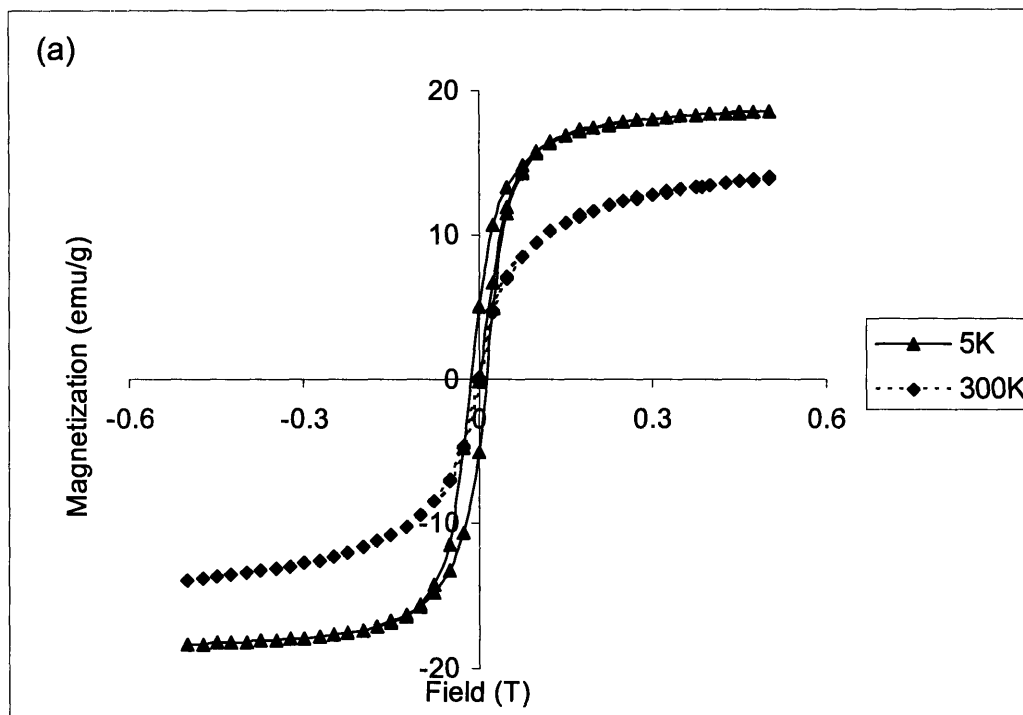
Figure 7-8. Magnetization curves of ferromagnetic nanofibers: (a) PEO nanofiber with (28 wt%) magnetite nanoparticles, (b) PVA nanofiber with (8 wt %) magnetite nanoparticles.

A SQUID magnetization curve for PMMA fiber containing 37% by weight of 6nm and 16 nm magnetite particles is shown in Figure 7-9a which is exactly similar to Figure 6-5. The fibers are superparamagnetic in nature like PEO/PVA magnetite fibers (Figure 7-7). However the relaxation studies of the fiber reflected the intrinsic difference between the 6nm and 16 nm embedded polymeric matrix. Figure 7-9b compares the relaxation curves for 6 nm and 16 nm PMMA/nanoparticle matrix. The experiment was performed at 5K. The sample were exposed to a pulse of 1000 Oe ($\sim$ 0.1T) magnetic field. The resultant decay in magnetization was then measured as a function of time. 16 nm nanoparticle relax very slowly compare to 6 nm particles. The experiment was performed at a low temperature (5K) to enhance the relaxation time of the particles thereby making it easy to measure. The above measurements are a definitive proof of nanoparticle relaxation in the polymeric matrix.
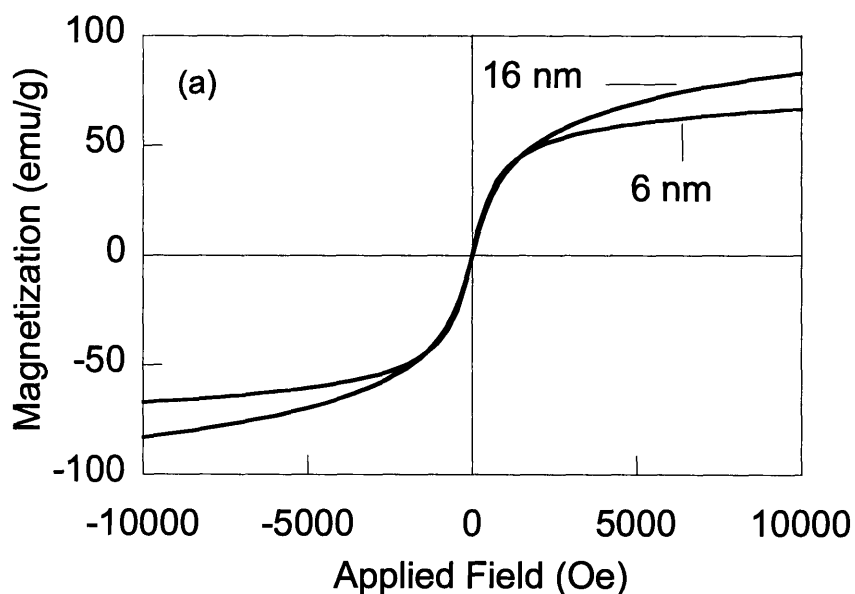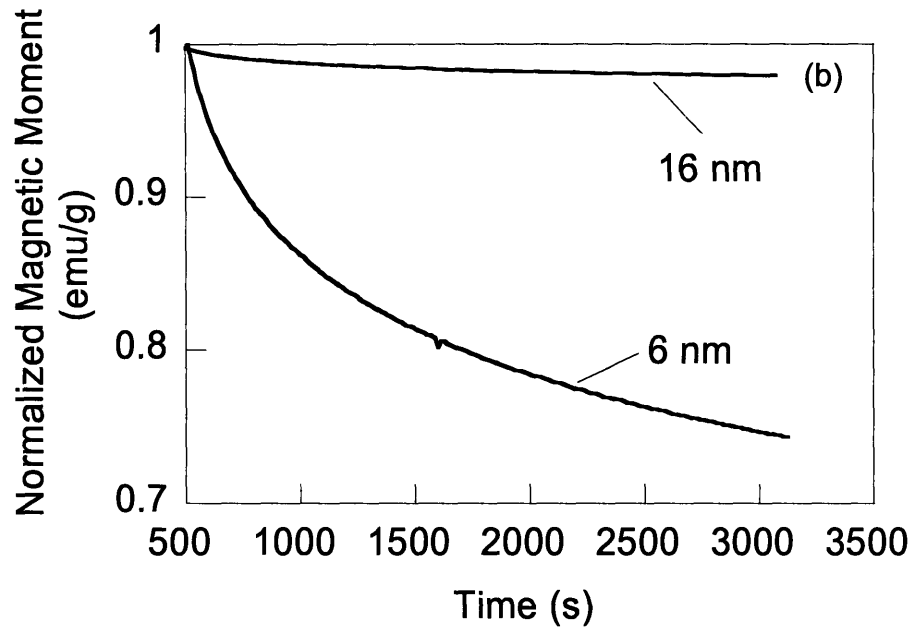
Figure 7-9. (a) Magnetization curve of the PMMA/6 nm and PMMA/16 nm magnetite nanoparticles at 300K. Notice the remnant magnetization is zero at zero field. (b) Relaxation curve of 6 nm and 16 nm nanoparticles embedded in polymeric matrix at 5K.

7.4.3.3 Nanoindentation analysis

The elastic modulus of the fibers was evaluated using an AFM indentation technique according to the following formula [41-45]

$$S = \frac{dP}{d\Delta Z_i}\bigg|_{P_{max}} = 2E^*\left(\frac{A}{\pi}\right)^{1/2} \tag{3}$$

Here, S is the slope of the unloading curve at P_{max}, P is the applied load, A is the contact area, ΔZ_i is the indentation depth, and E^* is the effective Young's modulus of the contact as defined by

$$\left(\frac{1}{E^*}\right) = \frac{1-v_s^2}{E_s} + \frac{1-v_t^2}{E_t} \tag{4}$$

In Equation (4), E_s and E_t are the elastic moduli, and v_s and v_t the Poisson ratios of the sample and the tip, respectively. The tip used was diamond with asymmetric

pyramidal geometry; indent size was characterized by the lateral distance from the apex to the base of the triangular impression [44]. E_t and ν_t are assumed to be 130 GPa and 0.2, respectively, corresponding to the bulk values of diamond [35-37]. The nanofibers were indented in the radial direction. A schematic of the tip-sample interaction during the indentation test is shown in Figure 7-8. The method is applicable here due to the fact that the diameters of the fibers (>150 nm) are much larger than the diameters of the contact area (<10 nm).
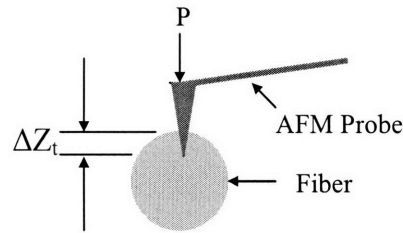
Figure 7-10. A schematic of tip-sample interaction during the indentation test.

The results of the indentation tests are shown in Figure 7-9 for PVA/magnetite nanofiber. Mica was also indented to evaluate the bending of the AFM cantilever, which was then subtracted from the raw PVA/magnetite data to get fiber properties. In these indentation tests, the slopes of the top portions of the unloading curves were used to evaluate the modulus of each sample. Assuming the tip geometry is the same for all the indentations, the relative changes in indent size are sufficient to relate contact areas; here, we equate the apex to base distance to a contact radius, r. The Poisson ratio, ν, is assumed to be the same for all fibers within each group. The ratio of modulus of different samples within each group can then be evaluated using the formula:

$$\frac{(dP/d\Delta Z_i)\big|_{P_{max,1}}}{(dP/d\Delta Z_i)\big|_{P_{max,2}}} = \frac{r_1 E_1}{r_2 E_2} \tag{5}$$

212
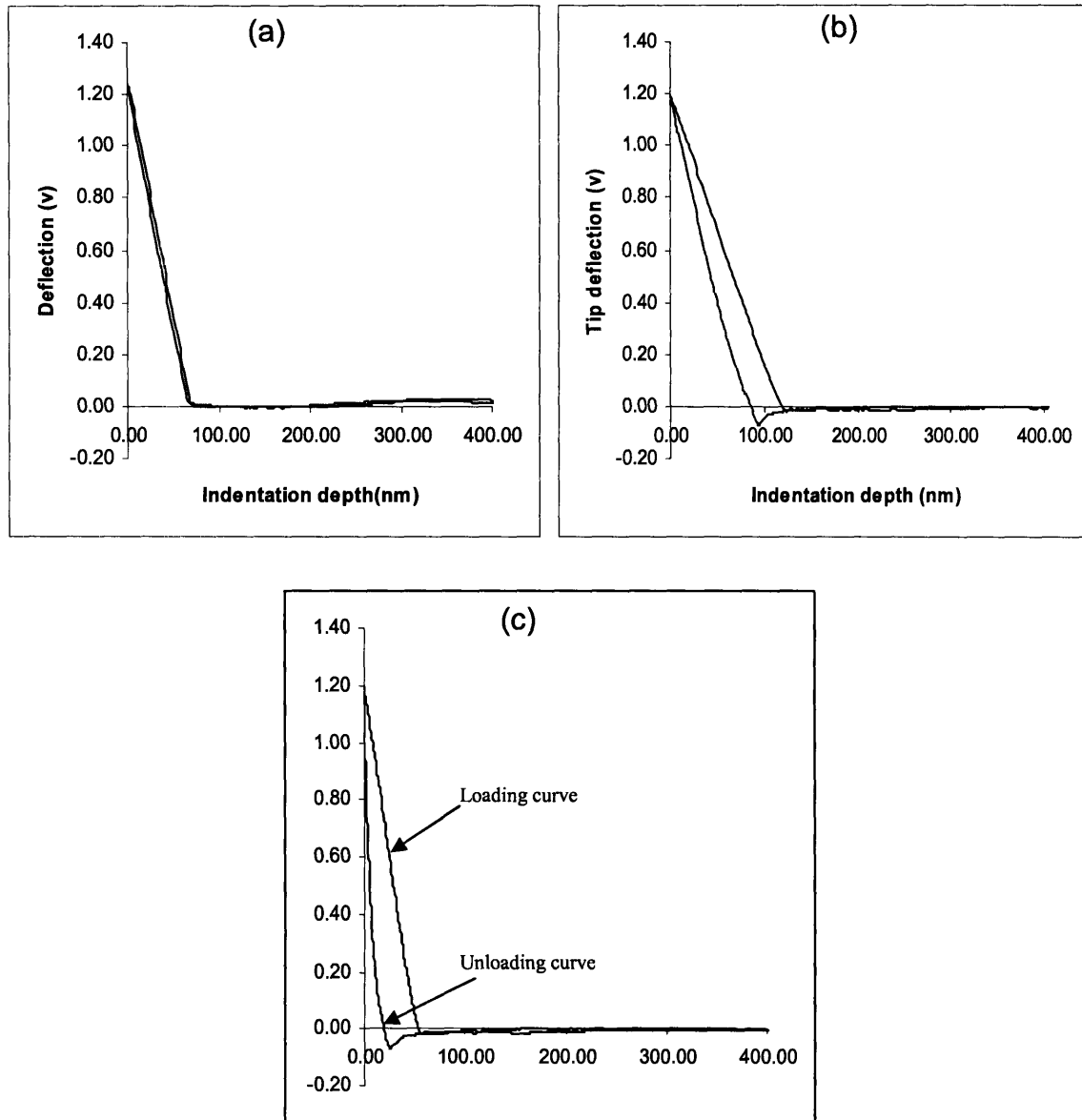
Figure 7-11. Indentation curves for PVA/magnetite(8 wt%) nanofiber: (a) calibration on hard surface (mica), cantilever bending without indentation; (b) indentation curve on PVA/magnetite nanofiber, cantilever bending and indent; (c) indentation curve on PVA/magnetite after subtracting the cantilever bending.

Table 3 shows the indentation data for all the nanofibers. ΔZ_i is the total displacement recovered from $P=P_{max}$ to $P=0$. ΔZ_t is the total indentation depth, which measures the penetration of the tip into the sample surface, including both the inelastic and elastic deformation of the material. The moduli were obtained by comparing with the reference epoxy sample within each group using Equation (5). The modulus of the

reference epoxy sample was determined to be 1.52 GPa using a Triboindenter. The indent size, r, was found to be 40 nm for the PEO and PEO/magnetite nanofibers, 10 nm for PVA and PVA/magnetite nanofibers, 20 and 10 nm for reference epoxy samples under conditions used to test the PVA group and PEO group, respectively. As shown inTable 3, after including magnetite nanoparticles (8 wt%) within PVA nanofibers, ΔZ_i was statistically the same, and ΔZ_t decreased. This indicates that the modulus of the PVA nanofibers was maintained and the inelastic deformation was decreased due to the reinforcement effect of magnetite nanoparticles. After including (28 wt%) magnetite nanoparticles within the PEO fiber, ΔZ_i decreased, but ΔZ_t increased showing that the modulus of PEO nanofibers was increased due to the reinforcement effect of magnetite nanoparticles. However, the increase in inelastic deformation of the PEO/magnetite nanofibers indicates that the short chains of polymeric shell around the nanoparticles were detrimental to the mechanical properties of the nanofibers and overwhelmed the effect of magnetite reinforcements as the concentration of the magnetite nanoparticles within the fibers increased from 8 to 28 wt%.

Table 7-4. Nanoindentation data of the nanofibers.

	PVA[a]	PVA+Fe$_3$O$_4$[a]	PEO[b]	PEO+ Fe$_3$O$_4$[b]	Epoxy[a]	Epoxy[b]
ΔE_i (nm)	12.33±4.46	14.55±2.67	9.36±1.41	5.92±0.68	22.14±1.42	10.92±0.35
ΔE_t (nm)	80.04±5.05	51.23±4.46	170.32±15.65	194.24±14.40	67.83±1.42	38.94±1.87
Modulus (GPa)	4.8 ±1.73	4.1 ±0.75	0.66 ±0.10	1.04 ±0.12	1.52±0.12*	1.52±0.12*

[a] Trigger setpoint of deflection signal of the cantilever is 1.2 V.
[b] Trigger setpoint of delfection signal of the cantilever is 0.6V.
[c] The modulus is determined independently by a triboindenter using a Berkovich tip.

7.4.3.4 Magnetic field-response behavior

The SQUID tests showed that the magnetite nanoparticles within the nanofibers were easily magnetized by an external magnetic field and the dipole moments of the nanoparticles were readily polarized in the direction of the external magnetic field. It is well known that the magnetic dipole experiences a torque in a uniform magnetic field and

a translational force in a magnetic field gradient. For the composite nanofibers containing magnetite particles in an external magnetic field gradient, the nanofibers will be deformed by the translational forces experienced by the embedded nanoparticles. Figure 7-10 shows the response of a strip of PVA/magnetite nonwoven mat to the field provided by a small laboratory magnet. One end of the nonwoven mat was fastened onto the surface of the table while the other end was free to move. In the absence of the magnetic field, the nonwoven mat lay flat on the surface of the table (Figure 10 (a)). When the magnet was placed above the nonwoven mat, the fabric was deflected by the translational forces in the direction of increasing magnetic field as shown in Figure 10 (b). As the magnet was brought closer to the fabric, the greater magnetic field gradients experienced by the nonwoven mat induced larger translational forces on the magnetite nanoparticles, causing a greater deflection of the free end of the mat towards the magnet (Figure 10(c)). The PEO/magnetite nonwoven mat showed similar response behavior to the laboratory magnet as the PVA/magnetite nonwoven mat. Clearly both superparamagnetic fabrics produced by the electrospinning technique exhibited field-responsive behavior.
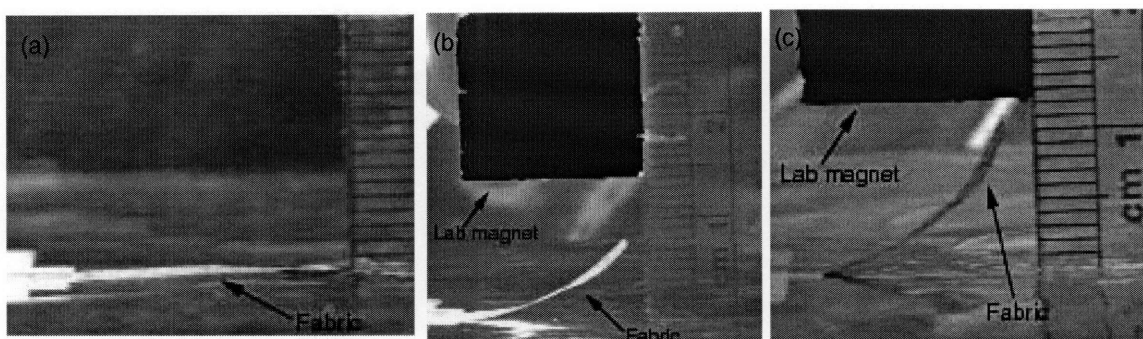
Figure 7-12. Field responsive behavior of PVA/magnetite fabric: (a) without magnetic field, (b) within low gradient of magnetic field, (c) within high gradient of magnetic field.

7.5 Model for the Deflection of a Single Fiber

Following ideas similar to those described in chapter 6, the increment in the modulus of the fiber due to the interaction of the nanoparticle with the external magnetic field was also modeled. Contributions from the dipole-field interactions and dipole-dipole interactions were considered, assuming the fiber can be treated as a bent cantilever

beam of length L, with circular cross section of diameter D, and constant radius of curvature, R. The nanoparticles of diameter d were assumed to be uniformly distributed in the fiber and initially aligned with the external magnetic field. We also assumed that the nanoparticles have an infinitely long relaxation time. So they achieve the configuration as shown in figure 8-1 when they are deflected.

(a)   (b)
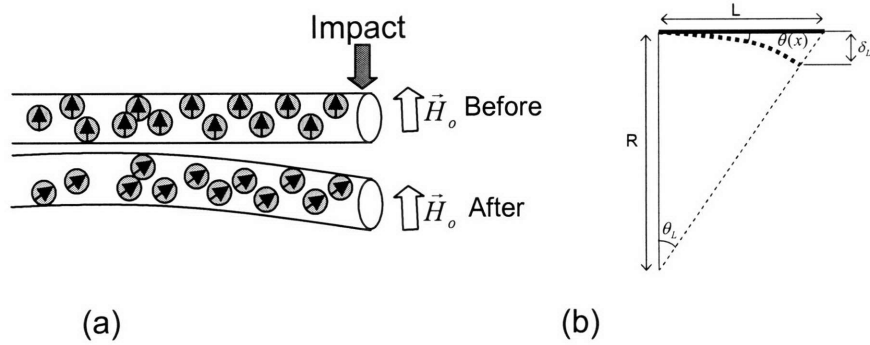
Figure 7-13. (a) Schematic of a fiber embedded with magnetic nanoparticles before and after deflection in a magnetic field. The adjacent figure (b) shows the modeling parameters.

For small deflections δ_L and $R \gg L$, we can approximate $\delta_L = L^2 / 2R$. $\theta(x)$ is the angle subtended by the distance x along the arc of the fiber, $\theta(x) = x/R = 2x\delta_L / L^2$. Normalizing both x and δ_L by the fiber length, L, we can write $\theta(x') = 2x'\delta_L'$ where $x' = x/L$ and $\delta_L' = \delta_L/L$

Net change in energy due to the deformation of the fiber under an external magnetic ΔE_t can be written as

$$\Delta E_t = \Delta E_h + \Delta E_p + \Delta E_f \qquad (1)$$

where ΔE_h is the contribution from the change in interaction energy of the magnetic dipole with the orientation with the external magnetic field , ΔE_p is the net change in the interparticle interaction energy, and ΔE_f is the energy change due to the bending of polymer fiber matrix component.

The resulting change in energy can be converted into change in bending modulus by the following relation

$$S = \frac{1}{\pi \left(\dfrac{D}{2}\right)^2 . L} \cdot \frac{\partial^2 \Delta E}{\partial \delta_L^{'2}}$$ (2)

ΔE_h for the whole length of the fiber can be written as

$$\Delta E_h = -\int_0^1 nmHL[\cos(\theta_i + \theta(x)) - \cos\theta_i] dx'$$ (3)

where ϕ is the volume fraction of nanoparticles in the fiber..

Double differentiation of ΔE_h yields

$$\frac{\partial^2 \Delta E_H}{\partial \delta_L^{'2}} = -\int_0^1 nmHL[\cos(\theta_i + \theta(x'))].(2x')^2 dx' = \frac{4}{3} nmHL$$ (4)

In this derivation we assumed that for small deflection $\theta(x') \rightarrow 0$. n is the linear density of the particle and is given by

$$n = \frac{3\phi D^2}{2d^3}$$ (5)

Substituting for m in the above equation we get

$$S_H = \frac{4}{3} \phi \mu_o M H_o$$ (6)

The calculation of ΔE_p was divided in two steps. In the first step the interaction of any arbitrary dipole was calculated with all the other dipoles in the fiber. Next this interaction energy was integrated over the whole fiber length. Overall interaction energy can be written as

$$\Delta E_p = \int_0^L \int_0^{t-a} \frac{n^2 m^2}{4\pi\mu_o} \cdot \frac{1}{(t-x)^3} \cdot [\cos(\theta(t) - \theta(x)) - 3\cos\phi(x)\cos\gamma(t)] dx dt +$$

$$\int_0^L \int_{t+a}^L \frac{n^2 m^2}{4\pi\mu_o} \cdot \frac{1}{(t-x)^3} \cdot [\cos(\theta(t) - \theta(x)) - 3\cos\phi(x)\cos\gamma(t)] dx dt$$

(7)

where $\theta(t)$, $\theta(x)$ are the angle by the which the dipole at position at t and x rotated due to bending of the fiber. $\phi(x)$ and $\gamma(t)$ is the angle which the respective dipole makes with the line joining the center of the two dipoles (See Figure 8-3).

Here a is the particle diameter. Non-dimensionalizing a, x and t with respect to L we can write the above equation as

$$\Delta E_p = \int_0^1 \int_0^{t'-a'} \frac{n^2 m^2}{4\pi\mu_o} \cdot \frac{1}{(t'-x')^3} \cdot [\cos(\theta(t') - \theta(x')) - 3\cos\phi(x')\cos\gamma(t')] dx' dt' +$$

$$\int_0^1 \int_{t'+a'}^1 \frac{n^2 m^2}{4\pi\mu_o} \cdot \frac{1}{(t'-x')^3} \cdot [\cos(\theta(t') - \theta(x')) - 3\cos\phi(x')\cos\gamma(t')] dx' dt'$$

(8)

$\theta(t)$, $\theta(x)$ are the angles by which the dipoles at position at t and x rotated due to bending of the fiber. $\phi(x)$ and $\gamma(t)$ is the angle which the respective dipole makes with the line joining the center of the two dipoles (See Figure 8-2).
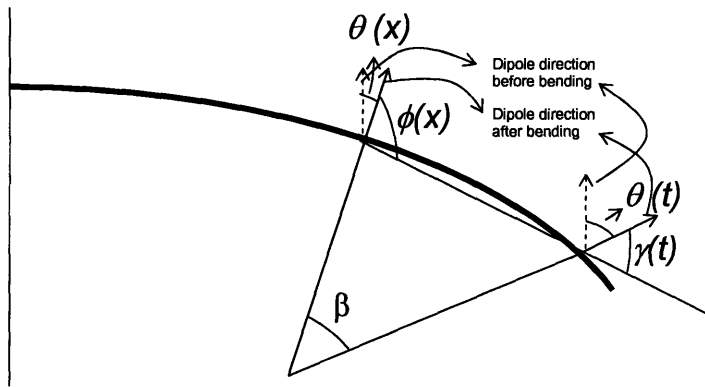
Figure 7-14. Schematic of the calculation in change in the dipolar interaction between two dipoles due to the bending of the fiber.

Simple trigonometrical analysis yielded

$$\beta(x) = [\theta(t) - \theta(x)]; \quad \phi(x) = [\pi/2 + \beta(x)/2]; \quad \gamma(t) = [\pi/2 - \beta(x)/2] \quad (9)$$

Solution of equation (11) for stiffness modulus gives

$$S_P = \frac{n^2 m^2}{\pi \mu_o L}(-1 - \ln(a')) = \frac{v^2 \mu_o M^2}{4}\left(\frac{D}{L}\right)^2 (-1 - \ln(a')) \quad (10)$$

where $a' = \dfrac{2d^3}{3vD^2 L}$

ΔE_f is the change in energy associated with the bending of the fiber itself and is given

by

$$\Delta E_F = \frac{1}{2}GI\int_0^1 \frac{L}{R^2}dx' \quad (11)$$

where G is the fiber modulus and I is the moment of inertia. Converting this energy

change into associated change in modulus gives

$$S_F = \frac{G}{4}\cdot\left(\frac{D}{L}\right)^2 \quad (12)$$

For ϕ = 10%, D = 200 nm, L= 200 μm, H $\sim$ 4 x 10^5 A/m and M $\sim$ 4.46 x 10^5 A/m

(saturation magnetization of magnetite), and G=200 MPa, the ratio of incremental change

in stiffness due to different interactions were calculated as follows

$$\frac{S_H}{S_F} \sim 600; \quad \frac{S_P}{S_F} \sim 10^{-4} \quad (13)$$

It can be seen that the bending stiffness of the magnetic fiber can be increased

significantly by the coupling interaction between the external magnetic field and

nanoparticles magnetic moment. The contribution of change in interparticle interaction

to the stiffness of the fiber is negligible.

219

The contribution of change in interparticle interaction to the stiffness of the fiber is negligible. The S_H in equation 26 depends on the volume fraction of the nanoparticle ϕ, magnetization M and field strength H. This corresponded to an increment in stiffness by 0.03 MPa for 37 wt% magneite/PU nanofiber assuming the dipoles of the magnetic nanoparticles are completely saturated (M = 4.46x10^5 A/m and H=0.5 T). This change in increment is too small to be able to observe physically. ϕ, M, or H can be increased to increase S_H. There is a practical upper limit on ϕ [31] as was reported before. Higher volume fraction of nanoparticles results in defects in the polymeric matrix which has a negative effect on the strength of the polymer. H_o can be increased but there are practical limitations because the weight of the setup to generate magnetic field scales exponentially with strength of the magnetic field. Increasing M is the only practical handle which can be used to increment the strength of the fiber. Hence incorporating higher magnetizable high Néel relaxation nanoparticles in the polymeric material can increase the stiffness significantly. Nanoparticles of the alloys of cobalt and iron have magnetization 3-4 times that of magnetite and their synthesis method is similar to that of the synthesis of organic route magnetite nanoparticles [46]. It should be possible to electrospin these nanoparticles and this will be explored in future.

7.6 Conclusions

Superparamagnetic polymer nanofibers ranging in diameter from 140 to 400 nm were obtained via the electrospinning of polymer-stabilized magnetite nanoparticle suspensions in PEO and PVA solutions. The nanoparticles were observed to line up within the fibers in columns parallel to the fiber axis direction, apparently induced by the electrospinning process. Both sets of fibers were superparamagnetic at room temperature, and responded to an externally-applied magnetic field by deflecting in the direction of increasing field gradient. Nanoindentation tests showed that magnetite nanoparticles reinforced the mechanical properties of nanofibers, although the significant amount of short-chain polymer adsorbed to the nanoparticles to ensure their suspension stability increased the inelastic deformation of the nanofibers.

A mathematical model to predict the change in stiffness of a magnetic fiber doped with high Néel relaxation particle under an applied magnetic field was developed. The bending modulus of magnetic fibers was predicted to increase significantly due to the interaction between the dipole moment of nanoparticles and the external magnetic field. Different size magnetite nanoparticles were produced using seed mediated growth and a general scheme to electrospin these organic based nanoaprticles in nanofibers was devised. The increase in stiffness scales with the magnetization of the nanoparticles. Hence incorporating high magnetizable nanoparticles can enhance the strength of the field responsive intelligent materials.

Acknowledgements

7.7   References

1.   Kanianthra, J.N., *Side Impact Energy Adsorber*. 1996: US Patent 5,564,535.

2.   Deshmukh, S. and G.H. McKinley, *Adaptive Energy-Absorbing Materials Using Field-Responsive Fluid-Impregnated Cellular Solids*. Adv. Funct. Mat. **submitted**.

3.   Gooding, E., *Adaptive Energy Absrobing Strucutre*. 1999: US Patent 5,915,819.

4.   Cheeseman, B.A. and T.A. Bogetti, *Ballistic impact into fabric and compliant composite laminates*. Composite Structures, 2003. **61**(1-2): p. 161.

5.   Courtney, W.A. and S.O. Oyadiji, *Preliminary investigations into the mechanical properties of a novel shock absorbing elastomeric composite*. Journal of Materials Processing Technology, 2001. **119**(1-3): p. 379.

6. Pinchuk, L.S., L.V. Markova, Y.V. Gromyko, E.M. Markov, and U.S. Choi, *Polymeric magnetic fibrous filters.* Journal Of Materials Processing Technology, 1995. **55**(3-4): p. 345-350.

7. Epstein, A.J. and J.S. Miller, *Molecule- and polymer-based magnets, a new frontier.* Synthetic Metals, 1996. **80**(2): p. 231-237.

8. Dikeakos, M., L.D. Tung, T. Veres, A. Stancu, L. Spinu, and F. Normandin, *Fabrication and characterization of tunable magnetic nanocomposite materials.* Materials Research Society Symposium - Proceedings, 2003. **734**: p. 315.

9. Jones, F.G., T.R. Shrout, S.-J. Jang, and M.T. Lanagan, *Microwave properties of ferroelectric ceramic/polymer 0-3 composites.* 90 IEEE 7 Int Symp Appl Ferroelectr; Published by Publ by IEEE, Piscataway, NJ, USA, 1992: p. 455.

10. Li, D., T. Herricks, and Y. Xia, *Magnetic nanofibers of nickel ferrite prepared by electrospinning.* Applied Physics Letters. **83**(22): p. 4586.

11. Bergshoef, M.M. and G.J. Vancso, *Transparent nanocomposites with ultrathin, electrospun nylon-4,6 fiber reinforcement.* Advanced Materials, 1999. **11**(16): p. 1362.

12. Kim, J.-S. and D.H. Reneker, *Mechanical properties of composites using ultrafine electrospun fibers.* Polymer Composites, 1999. **20**(1): p. 124.

13. MacDiarmid, A.G., W.E. JonesJr, I.D. Norris, J. Gao, A.T. JohnsonJr, N.J. Pinto, J. Hone, B. Han, F.K. Ko, H. Okuzaki, and M. Llaguno, *Electrostatically-generated nanofibers of electronic polymers.* Synthetic Metals, 2001. **119**(1-3): p. 27.

14. Norris, I.D., M.M. Shaker, F.K. Ko, and A.G. MacDiarmid, *Electrostatic fabrication of ultrafine conducting fibers: polyaniline/polyethylene oxide blends.* Synthetic Metals, 2000. **114**(2): p. 109.

15. Reneker, D.H. and I. Chun, *Nanometre diameter fibres of polymer, produced by electrospinning.* Nanotechnology, 1996. **7**(3): p. 216.

16. Demir, M.M., I. Yilgor, E. Yilgor, and B. Erman, *Electrospinning of polyurethane fibers.* Polymer, 2002. **43**(11): p. 3303.

17. Tsai, P.P., H. Schreuder-Gibson, and P. Gibson, *Different electrostatic methods for making electret filters.* Journal of Electrostatics, 2002. **54**(3-4): p. 333.

18. Huang, L., R.A. McMillan, R.P. Apkarian, B. Pourdeyhimi, V.P. Conticello, and E.L. Chaikof, *Generation of synthetic elastin-mimetic small diameter fibers and fiber networks.* Macromolecules, 2000. **33**(8): p. 2989.

19. Jin, H.J., S.V. Fridrikh, G.C. Rutledge, and D.L. Kaplan, *Electrospinning Bombyx mori silk with poly(ethylene oxide).* Biomacromolecules, 2002. **3**(6): p. 1233.

20. Gibson, P.W., H.L. Schreuder-Gibson, and D. Rivin, *Electrospun Fiber Mats: Transport Properties.* AIChE Journal, 1999. **45**(1): p. 190.

21. Hohman, M.M., M. Shin, G. Rutledge, and M.P. Brenner, *Electrospinning and electrically forced jets. I. Stability theory.* Physics of Fluids, 2001. **13**(8): p. 2201.

22. Hohman, M.M., M. Shin, G. Rutledge, and M.P. Brenner, *Electrospinning and electrically forced jets. II. Applications.* Physics of Fluids, 2001. **13**(8): p. 2221.

23. Shin, Y.M., M.M. Hohman, M.P. Brenner, and G.C. Rutledge, *Electrospinning: A whipping fluid jet generates submicron polymer fibers.* Applied Physics Letters, 2001. **78**(8): p. 1149-1151.

24. Yarin, A.L., S. Koombhongse, and D.H. Reneker, *Bending instability in electrospinning of nanofibers.* Journal of Applied Physics, 2001. **89**(5): p. 3018.

25. Theron, A., E. Zussman, and A.L. Yarin, *Electrostatic field-assisted alignment of electrospun nanofibres.* Nanotechnology, 2001. **12**(3): p. 384.

26. Dai, H., J. Gong, H. Kim, and D. Lee, *A novel method for preparing ultra-fine alumina-borate oxide fibres via an electrospinning technique.* Nanotechnology. **13**(5): p. 674.

27. Ko, F., Y. Gogotsi, A. Ali, N. Naguib, H. Ye, G. Yang, C. Li, and P. Willis, *Electrospinning of continuous carbon nanotube-filled nanofiber yarns.* Advanced Materials. **15**(14): p. 1161.

28. Shao, C., H.-Y. Kim, J. Gong, B. Ding, D.-R. Lee, and S.-J. Park, *Fiber mats of poly(vinyl alcohol)/silica composite via electrospinning.* Materials Letters, 2003. **57**(9-10): p. 1579.

29. Yang, Q.B., D.M. Li, Y.L. Hong, Z.Y. Li, C. Wang, S.L. Qiu, and Y. Wei, *Preparation and Characterization of a PAN nanofibre containing Ag Nanoparticles via electrospinning.* Synthetic Metals, 2003. **137**(1-3): p. 973.

30. Wang, M., H. Singh, T.A. Hatton, and G.C. Rutledge, *Field-responsive superparamagnetic composite nanofibers by electrospinning*. Polymer, 2004. **45**(16): p. 5505.

31. Rosenweig, R.E., *Ferrohydrodynamics*. 1985, New York: Cambridge University Press.

32. Moeser, G.D., K.A. Roach, W.H. Green, P.E. Laibinis, and T.A. Hatton, *Water-based magnetic fluids as extractants for synthetic organic compounds*. Industrial and Engineering Chemistry Research, 2002. **41**(19): p. 4739.

33. Sun, S.H., H. Zeng, D.B. Robinson, S. Raoux, P.M. Rice, S.X. Wang, and G.X. Li, *Monodisperse MFe2O4 (M = Fe, Co, Mn) nanoparticles*. Journal of the American Chemical Society, 2004. **126**(1): p. 273-279.

34. Fridrikh, S.V., J.H. Yu, M.P. Brenner, and G.C. Rutledge, *Controlling the Fiber Diameter during Electrospinning*. Physical Review Letters, 2003. **90**(14): p. 144502.

35. Klapperich, C., K. Komvopoulos, and L. Pruitt, *Nanomechanical properties of polymers determined from nanoindentation experiments*. Transactions of the ASME. Journal of Tribology, 2001. **123**(3): p. 624.

36. Kracke, B. and B. Damaschke, *Measurement of nanohardness and nanoelasticity of thin gold films with scanning force microscope*. Applied Physics Letters, 2000. **77**(3): p. 361.

37. Vanlandingham, M.R., S.H. McKnight, G.R. Palmese, R.F. Eduljee, J.W. Gillespie, Jr., and R.L. McCulough, *Relating elastic modulus to indentation response using atomic force microscopy*. Journal of Materials Science Letters, 1997. **16**(2): p. 117.

38. Fong, H., I. Chun, and D.H. Reneker, *Beaded nanofibers formed during electrospinning*. Polymer, 1999. **40**(16): p. 4585.

39. McNab, T.K., R.A. Fox, and A.J.F. Boyle, *Some magnetic properties of magnetite (Fe3O4) microcrystals*. Journal of Applied Physics, 1968. **39**(12): p. 5703.

40. Martinet, A., *Thermomechanics of Magnetic Fluids*, ed. B.M. Berkovskii. 1978, Washington DC: Hemisphere. 97-114.

41. Drechsler, D., A. Karbach, and H. Fuchs, *Nanoindentation on polycarbonate/polymethyl methacrylate blends.* Applied Physics A (Materials Science Processing), 1998. **66**(Supplement, Part 1-2Part 1-2): p. S825.

42. Pharr, G.M., W.C. Oliver, and F.R. Brotzen, *On The Generality Of The Relationship Among Contact Stiffness, Contact Area, And Elastic-Modulus During Indentation.* Journal Of Materials Research, 1992. **7**(3): p. 613-617.

43. Sneddon, J.N., International Journal of Engineering Science, 1965. **3**(1965): p. 47-56.

44. VanLandingham, M.R., R.R. Dagastine, R.F. Eduljee, R.L. McCullough, and J.W. Gillespie, *Characterization of nanoscale property variations in polymer composite systems: 1. Experimental results.* Composites Part A-Applied Science And Manufacturing, 1999. **30**(1): p. 75-83.

45. Vanlandingham, M.R., S.H. McKnight, G.R. Palmese, J.R. Elings, X. Huang, T.A. Bogetti, R.F. Eduljee, and J.W. Gillespie, *Nanoscale indentation of polymer systems using the atomic force microscope.* Journal Of Adhesion, 1997. **64**(1-4): p. 31-59.

46. Hutten, A., D. Sudfeld, I. Ennen, G. Reiss, W. Hachmann, U. Heinzmann, K. Wojczykowski, P. Jutzi, W. Saikaly, and G. Thomas, *New magnetic nanoparticles for biotechnology.* Journal Of Biotechnology, 2004. **112**(1-2): p. 47-63.

Chapter 8

Conclusions and Future Work

8.1 Summary of Research

Magnetic Nanoparticles were used as building blocks to create 3D magneto-responsive structures. A Template based technique coupled with an electrostatic based adsorption was exploited to create higher order magnetic structures. The behavior of the structures under the applied magnetic field was further exploited to create novel complex structures.

The layer-by-layer technique was used to coat polystyrene beads with polyelectrolytes of alternating charge and with charged magnetic nanoparticles [1]. An inexpensive and versatile approach was developed for the synthesis of monodisperse magnetoresponsive rods of desired diameter, length and magnetic susceptibility based on the confined alignment of magnetic beads in microchannels of selected channel height, followed by localized hydrolysis of sol-gel precursors within polyelectrolyte shells adsorbed on the beads [2]. The polystyrene cores could be removed either by solvent dissolution or by calcination to form hollow shelled chains. The reorientation dynamics of single and clustered chains following the application of an external magnetic field was evaluated theoretically, with favorable comparisons with the experimental data.

The magnetic response of the core-shell bead was compared to the commercially available matrix-type beads in which the nanoparticles are distributed in the bead core. A theoretical and experimental study of the interactions of magnetic nanoparticles within planar structured arrays was performed [3]. The results indicated that the magnetization curves for these arrays depend on their orientations relative to externally-applied magnetic fields. When the layers and the magnetic field are co-directional, the apparent magnetic susceptibilities are enhanced, but a decrease is seen when the field is normal to the nanoparticle array. The magnetic response of a core-shell type bead coated with one or more ordered layers of magnetic nanoparticles was evaluated by treating the particles

at any position on the surface as being in a planar array tangent to the surface of the bead at that position; the effective magnetic susceptibilities of the beads were estimated by integration over the bead surface of the orientation-dependent responses of these layers to the applied magnetic field. The effective susceptibility of magnetite nanoparticle monolayer-covered beads can increase by up to about 30 percent, but the effects are reduced as the number of layers increase.

Next we developed an efficient, one-step method to create magnetic nanowires consisting of permanently-linked chains of magnetic beads of varying flexibility tethered to a patterned glass surface using simple amidation chemistry [4]. The flexibility of the nanowire was governed by the molecular weight of the molecule used to covalently link the beads, and its length by the height of the microchannel in which it was synthesized. The nanowire diameter was determined both by the bead size, and by the number of beads adhering to each dot in the microstamped, patterned array. Longer nanowires can form loops attached at two points on the glass surface. Both single flexible chains and flexible loops can adopt different configurations (straight, hairpin, S-shaped, etc.) when subjected to magnetic fields, the configurations depending on the directions of these fields. Shorter, less flexible nanowires align with the field always and do not exhibit the more exotic configurations seen for long, flexible chains and loops. The chains were also tethered in a microchannel. These magnetic nanowires can have potential use in microfluidic pumping and mixing processes and in microparticle manipulation.

The use of soft charged templates was also explored to create magnetic rings and magnetic icosahedra-shaped clusters. The modeling of the behavior of the magnetic rings in a magnetic field predicted that the rings will aggregate to form links. A mixture of surfactants which self-assembled into discs and icosahedras was utilized [5, 6]. It was found that the charge difference between the edge and the surface of the surfactant structures formed was not sufficient to aid selective adsorption of the nanoparticles on the edges.

Radiation crosslinking served as an efficient route to create "templateless" clusters [7-9]. Poly (ethylene) oxide coated magnetic nanoparticles were synthesized and

were crosslinked *in situ.* The extent of crosslinking was controlled by the dosage rate. Excessive crosslinking resulted in the formation of magnetic gels.

Lastly, the effect of magnetic nanoparticle size was studied. An organic route synthesis was adopted to make fairly monodisperse magnetite nanoparticles up to 16 nm. 16 nm particles exhibited measurable Néel relaxation [10]. Modeling suggested that the incorporation of high Néel relaxation nanoparticles in a structure can improve its energy absorbing capacity/modulus of the structure under an applied magnetic field. This was experimentally verified with a drop ball test on foam impregnated with 25 nm iron nanoparticles which have inifinite Néel relaxation. For practical applications magnetic nanoparticles were embedded in polymeric nanofibers. As a proof of concept, first superparamagnetic polymeric nanofibers were produced via an electrospinning technique from colloidally-stable suspensions of magnetite nanoparticles in polyethylene oxide and polyvinyl alcohol solutions [11]. The magnetite nanoparticles were aligned in columns parallel to the fiber axis direction within the fiber by the electrospinning process. The polymer/magnetite nanofibers exhibited superparamagnetic behavior at room temperature, and deflected in the presence of an applied magnetic field. The mechanical properties of the nanofibers were maintained or improved after incorporating the magnetite nanoparticles. Finally high Néel relaxation magnetite nanoparticles synthesized using the organic route were electrospun in PMMA and PU nanofibers. Their magnetic response was modeled. These fibers can have potential application as adaptive energy absorbing material.

8.2   Future Research Directions

Applications of the flexible chain for micropumping and micromixing [12] uses in microfluidic channels should be studied. This would require use of a rotating magnetic field. Preliminary results have shown that the tethered chains grown in a microchannel respond to the rotating field and can be used as micropumps for pumping small beads in a microfluidic channel. This should be explored further. Also the effect of a variable magnetic field on the response of the tethered chains can generate different motions of the chains and can have interesting applications [13].

Self assembly of differently shaped magneto-responsive structures under an applied field is another rich area for further study. Technique of Dendukadi et al. [14] can be used to create charged templates of different shapes which can then be coated with magnetic nanoparticles. Some preliminary work was also done where ring shaped templates were used and the results were very encouraging.

"Smart Nanofibers" which can adsorb high energy under an applied magnetic field can be made a reality if we can synthesize high Néel relaxation, high magnetization nanoparticles. Nanoparticles of alloys of cobalt and iron are promising candidates for this application [15].

8.3 References

1. Caruso, F., R.A. Caruso, and H. Mohwald, *Nanoengineering of Inorganic and Hybrid Hollow Spheres by Colloidal Templating.* Science, 1998. **282**(5391): p. 1111-1114.

2. Singh, H., P.E. Laibinis, and T.A. Hatton, *Rigid, superparamagnetic chains of permanently linked beads coated with magnetic nanoparticles. Synthesis and rotational dynamics under applied magnetic fields.* Langmuir, 2005. **21**(24): p. 11500-11509.

3. Singh, H. and T.A. Hatton, *Orientational Dependence of Apparent Magnetic Susceptibilities of Superparamagnetic Nanoparticles in Planar Structured Arrays: Effect on Magnetic Moments of Nanoparticle-Coated Core-Shell Magnetic Beads.* Sumbitted to Journal of Magnetism and Magnetic Materials, 2006.

4. Singh, H., P.E. Laibinis, and T.A. Hatton, *Synthesis of flexible magnetic nanowires of permanently linked core-shell magnetic beads tethered to a glass surface patterned by microcontact printing.* Nano Letters, 2005. **5**(11): p. 2149-2154.

5. M. Dubois (1), L.B., Th. Zemb (1), B. Demé (2), Th. Gulik-Krzywick(3), *Formation of rigid nanodiscs: edge formation and molecular separation.* Progress in Colloid and Polymer Science, 2000. **115**: p. 238-242.

6.   Zemb, T., M. Dubois, B. Deme, and T. Gulik-Krzywicki, *Self-assembly of flat nanodiscs in salt-free catanionic surfactant solutions.* Science, 1999. **283**(5403): p. 816-819.

7.   Cooper, W.J., R.D. Curry, and K.E., *Environmental Applications of Ionizing Radiation.* 1998: Wiley-Interscience.

8.   Stringer, J.L. and N.A. Peppas, *Diffusion of small molecular weight drugs in radiation- crosslinked poly(ethylene oxide) hydrogels.* Journal of Controlled Release, 1996. **42**(2): p. 195-202.

9.   Park, M.-K., S. Deng, and R.C. Advincula, *Sustained release control via photo-crosslinking of polyelectrolyte layer-by-layer hollow capsules.* Langmuir, 2005. **21**(12): p. 5272-5277.

10.   Rosenweig, R.E., *Ferrohydrodynamics.* 1985, New York: Cambridge University Press.

11.   Wang, A., H. Singh, T.A. Hatton, and G.C. Rutledge, *Field-responsive superparamagnetic composite nanofibers by electrospinning.* Polymer, 2004. **45**(16): p. 5505-5514.

12.   Biswal, S.L. and A.P. Gast, *Micromixing with linked chains of paramagnetic particles.* Analytical Chemistry, 2004. **76**(21): p. 6448-6455.

13.   Dreyfus, R., J. Baudry, M.L. Roper, M. Fermigier, H.A. Stone, and J. Bibette, *Microscopic artificial swimmers.* Nature, 2005. **437**(7060): p. 862-865.

14.   Dendukuri, D., D.C. Pregibon, J. Collins, T.A. Hatton, and P.S. Doyle, *Continuous-flow lithography for high-throughput microparticle synthesis.* Nature Materials, 2006. **5**(5): p. 365-369.

15.   Hutten, A., D. Sudfeld, I. Ennen, G. Reiss, W. Hachmann, U. Heinzmann, K. Wojczykowski, P. Jutzi, W. Saikaly, and G. Thomas, *New magnetic nanoparticles for biotechnology.* Journal of Biotechnology, 2004. **112**(1-2): p. 47-63.